

UNIVERSIDAD COMPLUTENSE DE MADRID

FACULTAD DE CIENCIAS FÍSICAS



TESIS DOCTORAL

Estancamiento atmosférico en la región euromediterránea:
variabilidad espaciotemporal e impacto en la calidad del aire

Air stagnation in the Euro-Mediterranean región:
spatiotemporal variability and impact on air quality

MEMORIA PARA OPTAR AL GRADO DE DOCTOR

PRESENTADA POR

José Manuel Garrido Pérez

DIRECTORES

Ricardo Francisco García Herrera
Carlos Ordóñez García

UNIVERSIDAD COMPLUTENSE DE MADRID
FACULTAD DE CIENCIAS FÍSICAS



TESIS DOCTORAL

**Estancamiento atmosférico en la región euromediterránea:
variabilidad espaciotemporal e impacto en la calidad del aire**

**Air stagnation in the Euro-Mediterranean region:
spatiotemporal variability and impact on air quality**

MEMORIA PARA OPTAR AL GRADO DE DOCTOR EN FÍSICA

Presentada por
José Manuel Garrido Pérez

Directores
Ricardo Francisco García Herrera
Carlos Ordóñez García

Madrid, 2022



U N I V E R S I D A D
COMPLUTENSE
M A D R I D

DECLARACIÓN DE AUTORÍA Y ORIGINALIDAD DE LA TESIS PRESENTADA PARA OBTENER EL TÍTULO DE DOCTOR

D./Dña. José Manuel Garrido Pérez,
estudiante en el Programa de Doctorado en Física,
de la Facultad de Ciencias Físicas de la Universidad Complutense de
Madrid, como autor/a de la tesis presentada para la obtención del título de Doctor y
titulada:

Estancamiento atmosférico en la región euromediterránea: variabilidad espaciotemporal e impacto en la calidad del aire
Air stagnation in the Euro-Mediterranean region: spatiotemporal variability and impact on air quality

y dirigida por: Ricardo García Herrera y Carlos Ordóñez García

DECLARO QUE:

La tesis es una obra original que no infringe los derechos de propiedad intelectual ni los derechos de propiedad industrial u otros, de acuerdo con el ordenamiento jurídico vigente, en particular, la Ley de Propiedad Intelectual (R.D. legislativo 1/1996, de 12 de abril, por el que se aprueba el texto refundido de la Ley de Propiedad Intelectual, modificado por la Ley 2/2019, de 1 de marzo, regularizando, aclarando y armonizando las disposiciones legales vigentes sobre la materia), en particular, las disposiciones referidas al derecho de cita.

Del mismo modo, asumo frente a la Universidad cualquier responsabilidad que pudiera derivarse de la autoría o falta de originalidad del contenido de la tesis presentada de conformidad con el ordenamiento jurídico vigente.

En Madrid, a 22 de marzo de 2022

**GARRIDO
PEREZ JOSE
MANUEL -
80075191R**

Fdo.:

Firmado digitalmente por
GARRIDO PEREZ JOSE
MANUEL - 80075191R
DN: cn=GARRIDO PEREZ JOSE
MANUEL - 80075191R, c=ES,
email=jmgarridoperez@gmail.com
Fecha: 2022.03.22 13:49:02
+01'00'

Esta DECLARACIÓN DE AUTORÍA Y ORIGINALIDAD debe ser insertada en
la primera página de la tesis presentada para la obtención del título de Doctor.

*Dedicado a
mi familia*

Agradecimientos

Ha llegado el momento de escribir las líneas más difíciles de toda la tesis, puesto que supone reconocer el fin de una época muy feliz en mi vida. Y esto sólo ha sido posible gracias a un grupo especial de personas a las que me gustaría agradecerse.

La etapa predoctoral puede ser un quebradero de cabeza importante, quemando a quien pasa por ella debido a su precariedad laboral, alta exigencia, escasa perspectiva de futuro, ... Sin embargo, todo esto pasa a un segundo plano cuando formas parte del grupo humano con el que he tenido la suerte de trabajar: el grupo STREAM. Nunca podré agradecer lo suficiente a mis directores Carlos y Ricardo el trabajo que han hecho conmigo, guiándome a cada paso del camino. Y a David, quien siempre hace que todo sea más fácil. Los tres formáis un dream team. Pese a que sabéis que tengo muchos ídolos de barro, vosotros sois el espejo en el que me miro.

Gracias también al resto del grupo STREAM: Álvaro, Antonio, Blanca, Dana, Fernando, Jacob, Javi, Leo, Maddalen, Marie, Marina, Marta, Natalia, Samu, Solange y Vero. Lo que más he echado de menos durante la pandemia de la COVID-19 ha sido comer con vosotros cada día. Y en especial, gracias a Froila. Espero algún día poder volver a compartir despacho contigo.

Tampoco me gustaría dejar pasar la oportunidad de declarar mi gratitud a la ciudad de Madrid, a la que ya considero mi casa. En un principio era escéptico ante la idea de vivir aquí, pero pronto encontré que es una ciudad integradora, ejemplo de acogida y encuentro. Y esto fue posible gracias a las personas que aquí he conocido. Gracias a mis compañeros de los Másteres de Energía y del Profesorado, al grupo “Comer en la Uni”, al resto de complutenses FPU, y a todos y cada uno de los integrantes del Instituto de Geociencias y del departamento de Física de la Tierra y Astrofísica. Gracias por las experiencias vividas, habéis hecho que me sienta como en casa. Y este sentimiento se junta con el orgullo de mis orígenes extremeños, el cual proclamo allá por donde paso. Y

que no corresponde a un himno o una bandera, sino a mis amigos de toda la vida. Aunque cada uno estemos en un sitio, mi patria está donde estéis vosotros.

También me gustaría agradecer a mi familia por el continuo apoyo que me ha dado a lo largo de todo este tiempo. Me encanta mi rutina, pero más aún romperla para pasar tiempo con vosotros. Y en especial quiero utilizar estas líneas para agradecer a mis padres todo lo han hecho y siguen haciendo por mí. Sin vosotros el resto no tendría sentido. Aunque sea un poco despegado, agradezco inmensamente saber que puedo contar con vosotros para todo.

Y finalmente gracias a Adriana. Poco antes de empezar el doctorado escribí que eras “la invariante que no cambia pese al conjunto de transformaciones de mi pensamiento”, y creo que ahora esa afirmación está más vigente que nunca.

Gracias a todos. Espero no haberme pasado de zalamero.

Este trabajo ha sido financiado por la ayuda para la formación de profesorado universitario (FPU16/01972) otorgada por el Ministerio de Educación, Cultura y Deportes.

Contents

Acronyms and chemical formulae

Resumen	1
Summary	5
1 Introduction	9
1.1 Air stagnation	9
1.2 Influence of stagnation on air pollution	16
1.2.1 Particulate Matter	16
1.2.2 Ozone	21
1.3 Objectives	26
2 Data	29
2.1 Meteorological observations	29
2.2 Meteorological reanalysis	31
2.3 CMIP6 meteorological data	33
2.4 Air quality observations	34
2.5 Catalogue of blocks and ridges	36
3 Air stagnation in Europe:	
Spatiotemporal variability and impact on air quality	41
3.1 Annual occurrence of air stagnation in observations and reanalysis	42
3.2 Spatiotemporal variability of air stagnation	46
3.2.1 Regionalization of air stagnation	46
3.2.2 Temporal variability of air stagnation	47
3.3 Synoptic patterns leading to stagnation	53
3.4 Impact of stagnation on air quality	56
3.5 Main findings and discussion	64

4	Assessing the value of air stagnation indices to reproduce PM_{10} variability in Europe	67
4.1	Air stagnation indices	68
4.2	Comparison of ASIs	69
4.3	Statistical modelling of daily PM_{10} as a function of stagnation components	81
4.4	Main findings and discussion	87
5	Strong signatures of high-latitude blocks and subtropical ridges in winter PM_{10} over Europe	91
5.1	Impact of blocks and ridges on winter mean PM_{10}	91
5.2	Impact of EUR blocks and ATL ridges on winter PM_{10} extremes	100
5.3	Impact of EUR blocks and ATL ridges on the interannual variability of winter PM_{10}	101
5.4	Analysis of southern Germany	103
5.4.1	Transport pathways of air masses on days with EUR blocks and ATL ridges	103
5.4.2	Changes in the PM_{10} distribution and effect of synoptic persistence	107
5.4.3	Interannual variability	110
5.5	Main findings and discussion	112
6	The differing impact of air stagnation on summer ozone across Europe	115
6.1	Relationship between $MDA8\ O_3$, temperature and stagnation	116
6.2	Impact of stagnation on the O_3 diurnal cycle	126
6.3	Main findings and discussion	133
7	A storyline view of the projected role of remote drivers on summer air stagnation in Europe and the US	137
7.1	The computation of the air stagnation index in climate models	138
7.2	Regionalization of air stagnation	141
7.3	Spatial and inter-model variability of projected changes in air stagnation occurrence	144
7.4	Remote driver responses and sensitivity of stagnation	146

7.5	Storylines of future regional changes in air stagnation	155
7.6	Main findings and discussion	160
8	Conclusions and outlook	163
8.1	Main conclusions	163
8.2	Outlook	168
9	Publications	171
	Bibliography	175
	Annex	204

Contents

Acronyms and chemical formulae

AirBase	EEA's air quality database
AMOC	Atlantic Meridional Overturning Circulation
AOD	Aerosol optical depth
API	Air pollution index
AQ	Air quality
ASI	Air stagnation index
ATL	Atlantic
BALT	Baltic region
BLH	Boundary layer height
BRIT	British Isles
CAPE	Convective available potential energy
CCM	Chemistry–climate model
CEU	Central Europe
CH_4	Methane
CIN	Convective inhibition
CO	Carbon monoxide
CMIP5	Coupled Model Intercomparison Project Phase 5
CMIP6	Coupled Model Intercomparison Project Phase 6
CSB	Climate Services Branch
CTM	Chemical transport model
DD	Dry Day
DJF	December-January-February

ECAD	European Climate Assessment and Dataset
ECMWF	European Centre for Medium-Range Weather Forecasts
EE	Eastern Europe
EEA	European Environment Agency
EMEP	European Monitoring and Evaluation Programme
E-OBS	ECAD gridded dataset
ERA5	Fifth generation ECMWF Interim reanalysis
ERA-Interim	Fourth generation ECMWF Interim reanalysis
ESM	Earth System Model
EU	European Union
EUR	European
GAM	Generalized Additive Model
GDAS	Global Data Assimilation System
GW	Global warming
HO _{ASI}	Horton's air stagnation index
HO_x	Hydrogen oxide radicals
HU _{ASI}	Huang's air stagnation index
HYSPLIT	Hybrid Single-Particle Lagrangian Integrated Trajectory
IBE	Iberian Peninsula
IGRA	Integrated Global Radiosonde Archive
IPCC	Intergovernmental Panel on Climate Change
IPR	Integrated Process Rate
IQR	Interquartile range
ISD	Integrated Surface Database

JJA	June-July-August
<i>MDA8 O₃</i>	Maximum daily 8-h running average near-surface ozone
MB	Mean bias
NAO	North Atlantic Oscillation
NATL	North Atlantic warming
NCAR	National Center for Atmospheric Research
NCDC	National Climatic Data Center
NCE	Northern-central Europe
NCEI	National Centers for Environmental Information
NCEP	National Centers for Environmental Prediction
NEU	Northern Europe
<i>NMVOC</i>	Non-methane volatile organic compound
<i>NO</i>	Nitrogen monoxide
<i>NO₂</i>	Nitrogen dioxide
NOAA	National Oceanic and Atmospheric Administration
<i>NO_x</i>	Nitrogen oxides
NPAC	North Pacific warming
NSC	Northern Scandinavia
<i>O</i>	Oxygen atom
<i>O₃</i>	Ozone
<i>OH</i>	Hydroxyl radical
<i>PAN</i>	Peroxyacetyl nitrate
PBL	Planetary boundary layer
PDF	Probability density function

PDO	Pacific Decadal Oscillation
PDP	Partial dependence plot
PM	Particulate matter
PM_{10}	PM with aerodynamic diameter $\leq 10\mu m$
$PM_{2.5}$	PM with aerodynamic diameter $\leq 2.5\mu m$
PTD	Potential thunderstorm day
Q1	First quartile
Q2	Second quartile = median
Q3	Third quartile
R	Pearson correlation coefficient
R^2	Coefficient of determination
RTAW	Ratio between the tropical and Arctic warming
RCP	Representative Concentration Pathway
RMSE	Root mean squared error
RUS	Russian
SCAN	Scandinavia
SCE	Southern-central Europe
SD	Standard deviation
SE	South East Europe
SLP	Sea level pressure
SST	Sea surface temperature
SW	South West Europe
Tmax	Daily maximum temperature at 2 m
Twsp	Transport wind speed

UK	United Kingdom
US	United States
UTC	Coordinated Universal Time
ν_{eff}	Effective number of degrees of freedom
Vent	Ventilation
VIF	Variance Inflation Factor
WA_ASI	Wang's air stagnation index
WE	Western Europe
Wsp10	Wind speed at 10 m
Wsp500	Wind speed at 500 hPa
Wsp850	Wind speed at 850 hPa
Z500	500 hPa geopotential height

Resumen

Introducción

El estancamiento atmosférico se caracteriza por condiciones atmosféricas estables, vientos débiles en la troposfera media y baja, y ausencia de precipitación. Estas condiciones minimizan la dispersión horizontal y la mezcla vertical de masas de aire, favoreciendo la acumulación de contaminantes cerca de la superficie de la Tierra (ej. Leibensperger et al., 2008; Jacob and Winner, 2009; Tai et al., 2010; Dawson et al., 2014).

En los últimos años, varios estudios han desarrollado índices meteorológicos para identificar las condiciones de estancamiento que podrían desencadenar episodios de contaminación atmosférica (Wang and Angell, 1999; Horton et al., 2012, 2014; Wang et al., 2016, 2018; Cai et al., 2017; Zou et al., 2017; Feng et al., 2018, 2020; Huang et al., 2018). Pese a compartir características comunes, estos índices se definen a partir de diferentes variables meteorológicas y su aplicabilidad podría depender del lugar. En el momento actual, la mayoría de los estudios sobre las situaciones de estancamiento se han realizado a escala global o hemisférica (Horton et al., 2012, 2014; Wang et al., 2018) o se han centrado en los Estados Unidos (Wang and Angell, 1999; Leibensperger et al., 2008; Tai et al., 2010) y China (Huang et al., 2017, 2018; Wang et al., 2016; Zou et al., 2020). Sin embargo, pese a que las proyecciones climáticas indican que el entorno Mediterráneo podría ser una de las zonas con un mayor aumento del estancamiento en el futuro (Horton et al., 2014), no se ha llevado a cabo un análisis sistemático sobre el mismo para esta región.

Objetivos

Esta tesis pretende llevar a cabo el primer análisis exhaustivo del estancamiento en la región euromediterránea y evaluar su impacto en la calidad del aire. En particular, esta tesis:

1. Caracterizará la variabilidad espaciotemporal del estancamiento en la región euromediterránea.
2. Evaluará en qué medida un reanálisis meteorológico puede reproducir los patrones climatológicos observados para el estancamiento.
3. Identificará los patrones sinópticos asociados con extremos estacionales de estancamiento.
4. Examinará la relación entre las partículas en suspensión y el estancamiento determinado a partir de tres índices.
5. Evaluará el potencial del estancamiento para explicar la variabilidad del ozono durante el verano.
6. Realizará un análisis cuantitativo de los cambios futuros en el estancamiento para diferentes *storylines* y niveles de calentamiento.

Datos y métodos

En esta tesis se ha usado el índice definido por Horton et al. (2012) para identificar las situaciones de estancamiento. Además, se han empleado otros dos índices de estancamiento adaptados específicamente para las partículas en suspensión (Wang et al., 2016, 2018; Huang et al., 2018). Para calcular estos índices se han usado principalmente datos de los reanálisis de ECMWF, así como observaciones meteorológicas de las bases de datos E-OBS, IGRA y ISD. Las observaciones de concentraciones de contaminantes se han obtenido de las bases de datos AirBase y EMEP. Las proyecciones futuras han sido extraídas de modelos CMIP6.

Resultados

1. Los patrones espaciales del estancamiento en el área de estudio son muy heterogéneos, mostrando una mayor frecuencia de estancamiento en el sur y centro de Europa que en el norte del continente. Se han identificado cinco regiones con comportamientos coherentes: Escandinavia (SCAN), Norte de Europa (NEU), Centroeuropa (CEU), Suroeste de Europa (SW) y Sureste de Europa (SE). Las regiones más septentrionales (SCAN y NEU) presentan menor frecuencia y variabilidad temporal que las del sur (SW y SE). En general, se han encontrado tendencias ascendentes en el período 1979–2016 para una región al norte del Mediterráneo similar a aquella para la que Horton et al. (2014) proyectaron un aumento del estancamiento hacia finales del siglo XXI.
2. Existe un acuerdo razonable entre la frecuencia de estancamiento determinada a partir de datos de reanálisis y de observaciones. Las principales diferencias provienen del viento en superficie, puesto que este campo depende de las condiciones locales y está afectado por las imperfectas parametrizaciones usadas en los reanálisis.
3. En general, para la mayoría de las regiones, los inviernos y veranos con mayor frecuencia de estancamiento presentan anomalías positivas de geopotencial a 500 hPa sobre la región afectada. Sin embargo, durante los inviernos con más estancamiento en SCAN y NEU, se han observado anomalías negativas del geopotencial a 500 hPa y un desplazamiento de la corriente en chorro extratropical hacia el sur.
4. Los eventos persistentes de estancamiento favorecen al aumento de las concentraciones de partículas de suspensión. Sin embargo, la magnitud de ese aumento varía según el índice que se considere. En invierno, las anomalías positivas bajo condiciones de estancamiento son muy similares para los tres índices utilizados. En verano, las anomalías son considerablemente más pequeñas que en invierno y éstas presentan los valores más altos para un índice concreto. Los resultados también indican que la circulación a gran escala tiene un gran impacto en la variabilidad de las concentraciones de partículas en suspensión.

5. Durante los meses de verano las concentraciones de ozono no responden al estancamiento de manera uniforme en Europa. En el centro/sur del continente, el estancamiento es un buen predictor de ozono y tiende a amplificar los ciclos diurnos de este contaminante. Sin embargo, éste no es siempre el caso en las regiones más septentrionales. Durante los días sin estancamiento y con temperaturas moderadamente altas ($20^{\circ} - 25^{\circ}\text{C}$), el norte de Europa suele estar bajo la influencia de advección del sur que trae masas de aire con concentraciones relativamente altas de ozono.
6. La diversidad de los cambios proyectados de estancamiento depende de la respuesta forzada de *drivers* remotos. En Europa, encontramos diferencias de ~ 2 días por grado de calentamiento global para el verano entre las diferentes combinaciones de *storylines*. Además, las *storylines* obtenidas también muestran que el peor escenario para una región puede ser el mejor para otra. Por ejemplo, la *storyline* caracterizada por la combinación de un ratio alto entre los calentamientos Tropical y Ártico con un calentamiento alto del Atlántico Norte da lugar al mayor incremento de estancamiento para el suroeste de Europa y el menor en el resto del continente.

Summary

Introduction

Air stagnation occurs under stable weather conditions, weak winds in the lower to mid-troposphere and absence of precipitation. These conditions minimize the horizontal dispersion and vertical mixing of air masses as well as the scavenging of air pollutants, favouring their accumulation in the lower atmospheric layers (e.g. Leibensperger et al., 2008; Jacob and Winner, 2009; Tai et al., 2010; Dawson et al., 2014).

In the last few years, several studies have developed meteorological indices to identify stagnant conditions conducive to enhanced air pollution (Wang and Angell, 1999; Horton et al., 2012, 2014; Wang et al., 2016, 2018; Cai et al., 2017; Zou et al., 2017; Feng et al., 2018, 2020; Huang et al., 2018). Despite sharing common features, such so-called air stagnation indices (ASIs) are defined based on different meteorological variables and their applicability may be geographically dependent. Most previous studies on air stagnation have either been conducted on global and hemispheric scales (Horton et al., 2012, 2014; Wang et al., 2018), or have been confined to the US (Wang and Angell, 1999; Leibensperger et al., 2008; Tai et al., 2010) or China (Huang et al., 2017, 2018; Wang et al., 2016; Zou et al., 2020). However, although southern Europe has been identified as a climate hot spot where climate models project strong increases in air stagnation frequency (Horton et al., 2014), a systematic analysis of air stagnation and its impact on air quality has not been carried out hitherto for Europe and the Mediterranean region.

Objectives

In this thesis we aim to perform the first comprehensive analysis of air stagnation in the Euro-Mediterranean region and examine its impact on air quality. In particular, we will:

1. Characterize the spatiotemporal variability of stagnation over the Euro-Mediterranean area.
2. Assess the degree of consistency between the climatological features of air stagnation as derived from a meteorological reanalysis and observations.
3. Identify the synoptic patterns associated with seasonal regional stagnation extremes in Europe.
4. Assess the relationship between air stagnation and PM concentrations separately for three different ASIs.
5. Evaluate the potential of stagnation as a driver of summer ozone pollution over different regions of Europe.
6. Provide a quantitative analysis of future changes in stagnation for different storylines and levels of warming.

Data and methods

We have used the simplified ASI defined by Horton et al. (2012) to identify air stagnation situations. In addition, two alternative ASIs specifically adapted to PM (Wang et al., 2016, 2018; Huang et al., 2018) have also been used for comparative purposes. The computation of all indices is mostly based on data from the ECMWF reanalyses and meteorological observations from the E-OBS, IGRA and ISD datasets. Air quality observations have been obtained from the AirBase and EMEP databases, while future projections have been extracted from CMIP6 models.

Results

1. There is considerable spatial heterogeneity in stagnation patterns over the study area, with higher stagnation frequency in southern and central Europe than in the north of the continent. We have identified five regions where stagnation presents coherent spatiotemporal patterns: Scandinavia (SCAN), Northern-Europe (NEU), Central-Europe (CEU), South-West (SW) and South-East (SE). The northern regions (SCAN and NEU) present low frequency and temporal variability compared to the southern regions (SW and SE). Overall, we have found upward trends for the period 1979–2016 over a region north of the Mediterranean where stagnation has also been projected to increase towards the end of the 21st century (Horton et al., 2014), suggesting that such increases have already started.
2. There is fair agreement between stagnation as derived from reanalysis and observations. The main differences arise from the surface wind speed, as this field depends on the local setting of the observational sites and imperfect parameterizations within the reanalysis model.
3. The winters and summers with the highest stagnation frequency often concur with positive 500 hPa geopotential height anomalies over the regions, with the exception of negative anomalies and a displacement of the extratropical jet to the south in the case of SCAN and NEU during winter.
4. The application of a simplified ASI indicates that persistent and widespread stagnation events favour the build-up of PM over most of the continent. However, the magnitude of the PM concentration enhancements under stagnant conditions varies with the ASI. Positive PM anomalies under stagnant conditions are of the same order of magnitude for the three ASIs tested here during winter. The anomalies are considerably smaller in summer, when one of the indices outperforms the others at most locations. The results also indicate that the consideration of the large-scale circulation consistently contributes to reproducing PM_{10} variability. We have also identified some potential improvements that could be made to two of the ASIs.

5. We have found differing responses of summer near-surface ozone to the occurrence of air stagnation accross Europe. In central/southern Europe, stagnation is a good predictor of ozone and tends to amplify the diurnal cycles of this pollutant. However, this is not always the case for the northern regions. Under non-stagnant conditions and moderately high temperatures ($20^{\circ} - 25^{\circ}\text{C}$), northern Europe is often affected by southerly advection that brings warm, aged air masses with elevated ozone mixing ratios. This regional dependency of the ozone - stagnation relationship across Europe indicates that climate model projections of increases in stagnation should not directly be translated into degraded air quality without a proper assessment of the regional impacts.

6. The diversity of projected stagnation changes depends on the forced response of remote drivers in individual models. In Europe, differences of ~ 2 stagnant days per degree of global warming are found for summer amongst the different storyline combinations. In addition, the resulting storylines have also shown that the worst-case scenario for one region can be the best-case scenario for another. For example, the storyline characterized by the combination of a high ratio between tropical and Arctic warming with high North Atlantic warming is associated with the highest stagnation increase in southwest Europe and the lowest in the rest of the continent.

1 Introduction

1.1 Air stagnation

In the mid-latitudes, atmospheric circulation is often modulated by transient synoptic disturbances, which determine the trajectory of weather systems and therefore the occurrence of precipitation and the variability of wind speed. However, there are occasions when the circulation is interrupted and the atmospheric flow is weak, leading to stagnation. The *American Meteorological Society* Glossary of Meteorology (<https://glossary.ametsoc.org/wiki/Welcome>) defines a stagnation area as:

“An air pollution term for an anticyclonic region of subsidence and light winds that tends to trap pollutants near the ground where concentrations can become large.”

Air stagnation situations are characterized by stable weather, weak winds in the lower to mid-troposphere and absence of precipitation. They occur under the presence of high-pressure anticyclones and weak sea level pressure (SLP) gradients with undetermined flow at the lower levels. These conditions impede the horizontal dispersion and vertical mixing of air masses in the lower troposphere as well as the washout of pollutants, favouring the occurrence of poor air quality (AQ) and low visibility events (e.g. Leibensperger et al., 2008; Tai et al., 2010; Dawson et al., 2014; Wang et al., 2016, 2018). The influence

of stagnation on air pollution will be introduced in more depth in Section 1.2. On the other hand, both air stagnation and air pollution episodes are also associated with the occurrence of heat waves, cold spells and droughts (Bedi and Parthasarathy, 1967; Edwards et al., 1991; Schnell and Prather, 2017; Sun et al., 2017; Demetillo et al., 2019; Vautard et al., 2018). As an illustration, Schnell and Prather (2017) found high correlations between air stagnation frequency and extreme daily maximum temperature over eastern North America, whereas Demetillo et al. (2019) suggested that stagnation may also be relevant to understand the enhancement of ozone under drought conditions in California. Although these extreme events are characterized by different meteorological drivers, many of them are connected and often co-occur or appear slightly offset in space or time. Note that they are more likely to occur under the persistent anticyclones associated with a wavy jet (Francis and Vavrus, 2015) that trigger stagnation in mid-latitude regions. For all these reasons, air stagnation poses a serious risk not only to human health but also to environment and socio-economic development.

In the last few years, several indices have been developed in the literature to track the meteorological conditions conducive to air mass stagnation. Air stagnation indices (ASIs) are usually determined by using predefined thresholds for different daily meteorological fields. Wang and Angell (1999) considered that there is stagnation if three conditions are simultaneously met for at least four days: sea level geostrophic wind speed $< 8 \text{ ms}^{-1}$, 500-hPa wind speed (Wsp500) $< 13 \text{ ms}^{-1}$ and no precipitation (for practical purposes, daily accumulated precipitation below 1 mm). The United States (US) National Oceanic and Atmospheric Administration (NOAA) National Climatic Data Center (NCDC) uses this ASI to monitor the meteorological situations which potentially favour the accumulation of air pollutants (<https://www.ncdc.noaa.gov/societal-impacts/air-stagnation/overview>). As an illustration, Figure 1.1 shows stagnation conditions provided by NOAA NCDC for August 2019. This index is an objective measure of synoptic-scale stagnation over the US, but the dependence of the geostrophic wind on the latitude might limit its application to other regions of the globe. Wang and Angell (1999) showed that the ratio between the sea level geostrophic wind speed and the 10 m wind speed (Wsp10) is on average around 2.5 and is not geographically dependent

over the US. Therefore, the 8 ms^{-1} sea level geostrophic wind condition is approximately equivalent to a 3.2 ms^{-1} threshold for Wsp10. Following those analyses, Horton et al. (2012, 2014) introduced a simplified ASI (hereafter, referred to as HO_ASI), where Wsp10 is used with a threshold of 3.2 ms^{-1} . HO_ASI has the advantage that it is based on three fields – Wsp10, Wsp500 and precipitation – which are provided by most meteorological reanalyses and climate models. However, as detailed in Section 1.2, this index presents some limitations to assess the impact of meteorology on AQ (Kerr and Waugh, 2018). Other studies have discussed the adequacy of Wsp500 to determine stagnant days under certain conditions. For instance, Dawson et al. (2014) claimed that the $\text{Wsp500} < 13 \text{ ms}^{-1}$ condition is mainly relevant for multiday warm weather stagnation episodes, while Huang et al. (2017) adapted it to account for the influence of the orography in China. Moreover, Huang et al. (2018) found that Wsp500 is stronger than 13 ms^{-1} on 75% of the most polluted days in Beijing (Figure 1.2), suggesting that air pollution is not necessarily linked to weak mid-tropospheric wind speed.

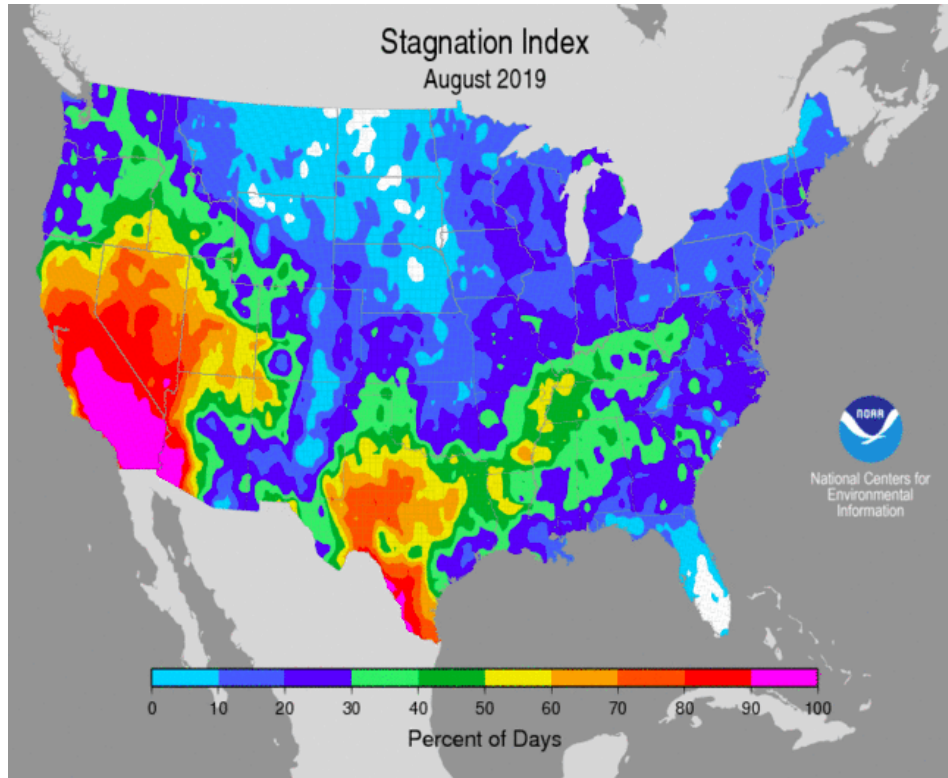


Figure 1.1: Air stagnation frequency map for August 2019. Provided by the NOAA NCDC based on the work of Wang and Angell (1999). From <https://www.ncdc.noaa.gov/societal-impacts/air-stagnation/maps/201908>.

In order to address some of the limitations of HO_ASI, Wang et al. (2016, 2018) and Huang et al. (2018) have proposed alternative ASIs (referred to as WA_ASI and HU_ASI, respectively, from now on) specifically adapted to particulate matter and with a potential to be applied worldwide. Wang et al. (2016, 2018) excluded the Wsp500 condition and used the atmospheric boundary layer height (BLH) to characterize the vertical mixing of pollutants. Huang et al. (2018) replaced both Wsp10 and Wsp500 by the ventilation (defined as the integral of the horizontal wind speed in the boundary layer), and added an extra condition based on the convective available potential energy (CAPE) and the convective inhibition (CIN) to consider the latent instability of the lower atmosphere. More precise details on the calculation of these indices are given in Chapter 4. Other stagnation indices have also been developed, but some of them include information on circulation patterns which are specific to certain regions (e.g. Cai et al., 2017) or consider spatial averages of meteorological fields over large regions (e.g. Zou et al., 2017), which limits their applicability to different areas of the globe.

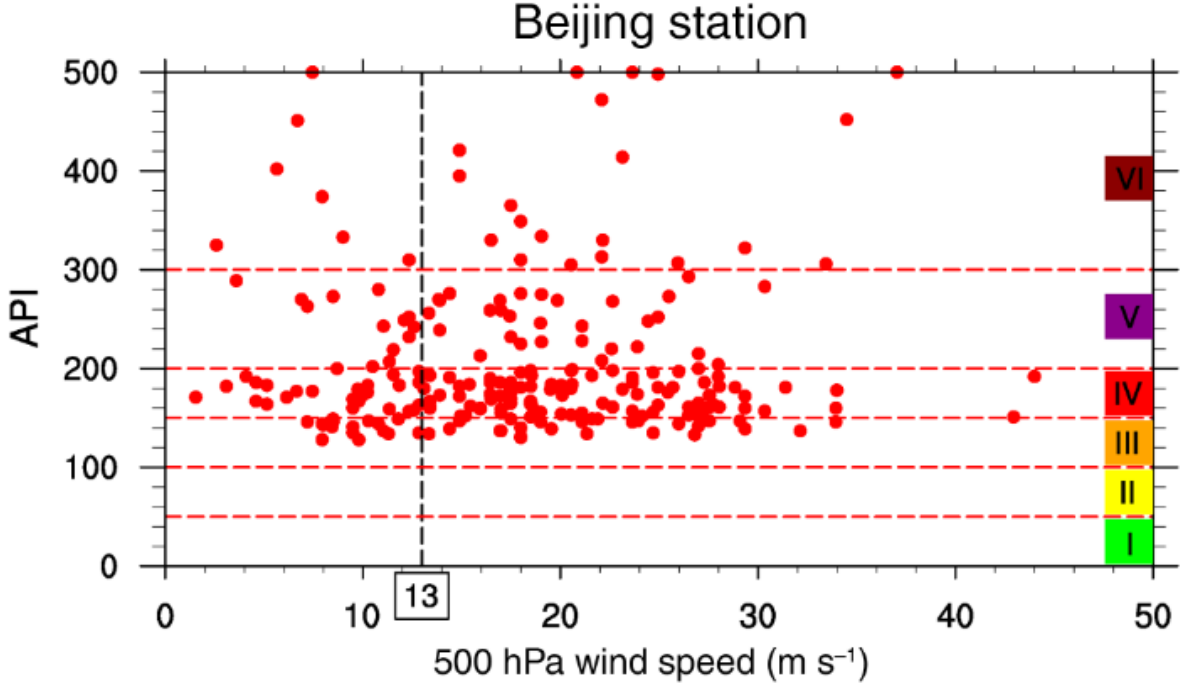


Figure 1.2: Relationship between the air pollution index (API) and Wsp500 on most polluted winter days ($> 90^{th}$ percentile) during 2000–2012 in Beijing. Air pollution is classified into six levels (I–VI), indicating excellent, good, slightly polluted, moderately polluted, heavily polluted and severely polluted conditions, respectively. From Huang et al. (2018).

It should be borne in mind that some of the meteorological variables used to define the previously mentioned ASIs are strongly influenced by complex local conditions at the Earth's surface (e.g. orography, surface roughness). Due to the sparsity of observations, stagnation studies have often used output from meteorological reanalyses or climate models, where those meteorological variables are generated from imperfect parameterizations of the boundary layer physics. However, the potential biases between reanalysis or model data and observations might be a problem for accurately reproducing stagnation. In particular, the representation of near-surface wind speed might be especially problematic since it is used in the definition of most existing ASIs. Vautard et al. (2010) showed that observed surface wind speeds have declined over continental areas of the northern mid-latitudes, while meteorological reanalysis datasets do not exhibit such trend. Furthermore, reanalyses also suffer from significant precipitation biases over some regions (Bosilovich et al., 2008; Nogueira, 2020), forcing some studies to adapt the precipitation threshold to local conditions (e.g. Dawson et al., 2014). This could advise against the use of reanalysis data for the characterization of air stagnation. To our knowledge, only few studies have analysed stagnation based on observations over large regions (e.g. Huang et al., 2017, 2018, for China), but the consistency between ASIs derived from reanalysis and observations has not been assessed so far. This will be an objective of this work.

Previous studies on air stagnation have either been conducted on global and hemispheric scales with a focus on future and past changes (Horton et al., 2012, 2014; Wang et al., 2018), or have been confined to the US (Wang and Angell, 1999; Leibensperger et al., 2008; Tai et al., 2010), China (Huang et al., 2017, 2018; Wang et al., 2016; Zou et al., 2020) and specific regions in Europe (Russo et al., 2016; Caserini et al., 2017). As an illustration, it has been shown that the low frequency of summertime mid-latitude cyclones and frontal passages are strong predictors of stagnation in the US (Leibensperger et al., 2008; Tai et al., 2010). Huang et al. (2017) conducted a comprehensive investigation of the spatiotemporal patterns of air stagnation in China for a 30-year period, while Zou et al. (2020) demonstrated the role of atmospheric teleconnection processes in linking Arctic sea ice decline with winter air stagnation over that region. Russo et al. (2016) identified links between circulation patterns and stagnation events in Portugal. Nonetheless,

a systematic analysis of air stagnation has not been carried out for Europe. To address this issue, in this thesis we perform the first comprehensive study of the past variability in air stagnation over the Euro-Mediterranean region. This provides a benchmark for the evaluation of past stagnation in historical simulations of climate models as a necessary step prior to attempting to improve the confidence in future model projections of regional climate.

Previous studies have projected an increase in the occurrence (total number of days per year) and persistence (average length of events) of air stagnation over some of the most populated areas of the globe if the emissions of greenhouse gases are not reduced (Leung and Gustafson, 2005; Horton et al., 2012, 2014; Caserini et al., 2017; Cai et al., 2017; Han et al., 2017; Hong et al., 2019; Gao et al., 2020; Lee et al., 2020). In particular, Mediterranean Europe is one of the regions where air stagnation has been projected to increase towards the end of the 21st century (Figure 1.3). This may be especially important in summer, when the Mediterranean region is under the influence of subtropical high-pressure ridges which favour the occurrence of subsidence and elevated temperatures, while also inhibiting precipitation (García-Herrera and Barriopedro, 2018). However, although these probabilistic multi-model ensemble projections of future climatic change have been considered a community best practice, recent work has suggested that regional projections based on multi-model ensemble means should be considered with care due to low confidence and high uncertainty in the forced response of atmospheric dynamics, which exerts a strong control on regional climates (Shepherd, 2014).

As an alternative to probabilistic projection, the identification of “storylines”, or plausible and physically self-consistent combinations of climate change responses in well-known drivers of regional climate, can be used to characterize uncertainties within multi-model ensembles (Shepherd et al., 2018; Zappa, 2019; Mindlin et al., 2020). This approach simplifies the spread of atmospheric circulation responses into a few plausible dynamically-driven scenarios, allowing for a better understanding of the changes simulated by the multi-model ensemble. Zappa and Shepherd (2017) followed this approach to show that the severity of the decline in Mediterranean winter precipitation and the

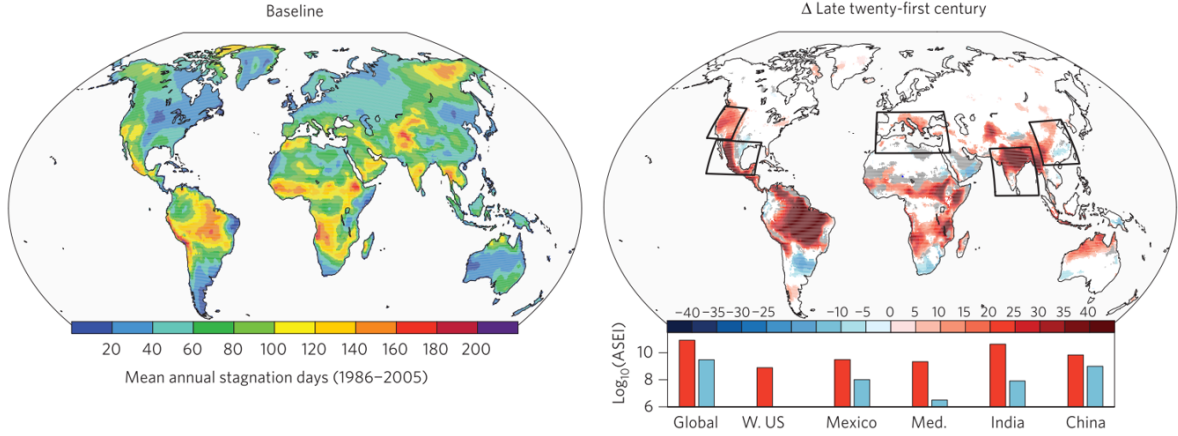


Figure 1.3: Left panel: Mean annual baseline (1986–2005) stagnation days from the bias-corrected historical ensemble of the Coupled Model Intercomparison Project Phase 5 (CMIP5). Right panel: Change in mean annual stagnation days from baseline to future period 2080–2099 under the Representative Concentration Pathway (RCP) 8.5 scenario. White represents non-significant change; grey represents that ensemble members do not agree on the change direction; blue (decreasing) and red (increasing) represent significant change. Bar plots show logarithmic values of the air stagnation exposure index for the baseline (blue) and future (red) periods. This index is a metric that captures the potential human exposure to changes in stagnant conditions. From Horton et al. (2014).

increase in central European windiness projected by the models of the Climate Model Intercomparison Project Phase 5 (CMIP5) strongly depend on a few remote drivers of the atmospheric circulation in the Euro-Atlantic sector. Likewise, Peings et al. (2018) dissected climate projections of different features of the winter eddy-driven jet over the North Atlantic and found that changes in the ratio between upper tropospheric tropical warming and lower tropospheric Arctic warming can explain a considerable fraction of the multi-model spread. Models with the largest change in this ratio projected a reinforcement and slight poleward shift of the jet, while a significant reduction in the westerlies on the poleward flank of the jet occurred in models with the smallest change in ratio. Kornhuber and Tamarin-Brodsky (2021) classified CMIP5 models by the sign of the trend in their future equator-to-pole temperature gradient to investigate different regional patterns of summer weather persistence, namely the zonal propagation speeds of anticyclones and warm temperature anomalies. They found the best agreement between both subsets over southern North America, whereas the sign of the projections strongly disagreed over Europe. In this thesis, we apply the storyline approach to 21st century projections of sum-

mer air stagnation. We use a CMIP6 ensemble to generate stagnation storylines based on the forced response of three remote drivers of the Northern Hemisphere mid-latitude atmospheric circulation.

1.2 Influence of stagnation on air pollution

Air pollution is the presence in the air of substances at a concentration or for a duration high above their normal levels to produce a measurable effect on human beings or the environment (Seinfeld and Pandis, 2016). Although pollution levels mainly depend on emissions (from both anthropogenic and natural sources), meteorological factors also exert great influence on the variability of atmospheric pollutant concentrations. In particular, air stagnation is one of the most important meteorological phenomena to take into account in order to understand the accumulation of pollutants in the lower atmospheric layers (Jacob et al., 1993; Leibensperger et al., 2008; Tai et al., 2010; Dawson et al., 2014). The absence of precipitation and poor ventilation associated with stagnant conditions impede the scavenging and dispersion of pollutants, resulting in poor air quality close to the emission sources. In recent years, there has been a considerable amount of literature on the impact of air stagnation on AQ, especially for two of the main pollutants linked to serious health impacts: particulate matter and ozone.

1.2.1 Particulate Matter

Particulate matter (PM) is a complex mixture of solid and liquid aerosol particles suspended in the air. It includes particles of both organic and inorganic origin, with varied chemical and physical properties which determine their interaction with radiation at different wavelengths. Some of these particles are primarily emitted while others are formed through gas-to-particle conversion. Once inhaled, they can cause serious health effects. The impact of elevated PM concentrations on human health has been addressed through the combination of epidemiological studies and model projections (e.g. Pope III et al., 2002; Nel, 2005; Sacks et al., 2011; Shindell et al., 2012; Janssen et al., 2013; Cohen et al., 2017). Despite the reduction of anthropogenic emissions of PM and its precursors

in Europe (Barnpadimos et al., 2012; Guerreiro et al., 2014) and the US (Cohen et al., 2017; McClure and Jaffe, 2018) over the last decades as a result of the implementation of AQ legislation, the atmospheric concentrations of PM remain worrisome. In Europe, more than 400,000 premature deaths have been attributed to this pollutant during 2016 (EEA, 2019).

In general, the smaller the size of the particle, the longer its residence time in the atmosphere and the greater the impact on human health. Therefore, for AQ regulatory purposes, PM is often classified in two groups, $PM_{2.5}$ and PM_{10} , based on the aerodynamic diameter of the particles (up to 2.5 and 10 μm , respectively) (e.g. EU, 2008). $PM_{2.5}$ is mainly composed of primary combustion particles as well as secondary inorganic and organic aerosols, whereas PM_{10} also includes larger particles like dust, pollen or marine aerosols (e.g. Putaud et al., 2010). A schematic representation of the portions of the mass particle size distributions is shown in Figure 1.4. Since each component comes from diverse sources and may respond differently to meteorological changes, unlike most other air pollutants, PM cannot be characterized by the variability of a single compound. Consequently, PM concentrations are particularly difficult to predict.

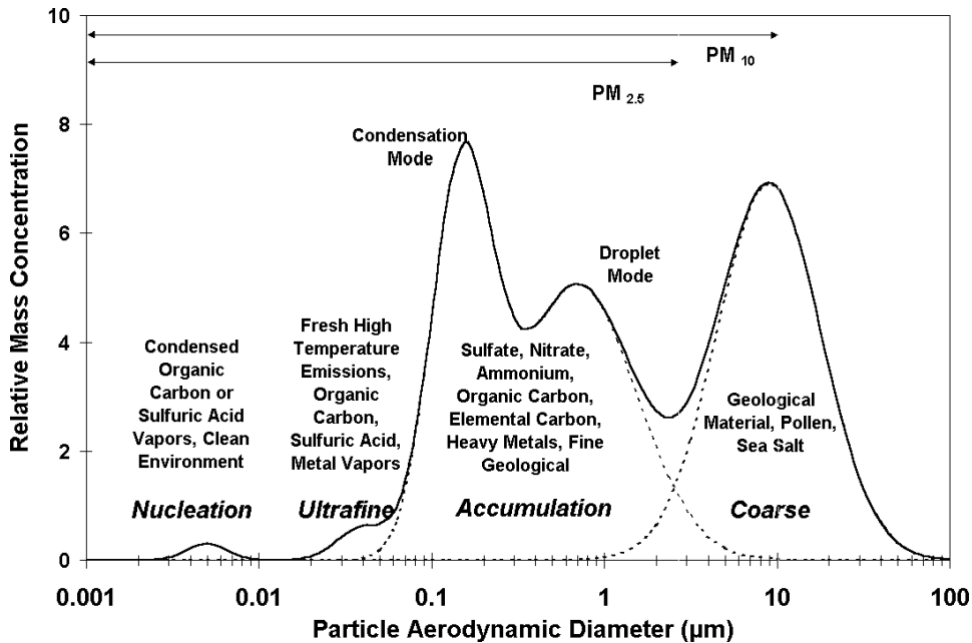


Figure 1.4: Idealized diagram representing the portions of the mass particle size distributions. From Watson (2002).

The dependence of $PM_{2.5}$ and PM_{10} on meteorological conditions has been subject of comprehensive analyses (Jacob and Winner, 2009; Querol et al., 2009; Tai et al., 2010; Barmpadimos et al., 2012; Fiore et al., 2012; Dawson et al., 2014; Wang et al., 2016). In general, PM concentrations decrease with precipitation as wet deposition provides the main sink for aerosol particles. PM concentrations also tend to increase with humidity, although the different components of PM may respond differently to humidity changes, leading to compensation effects (Jacob and Winner, 2009; Tai et al., 2010). Other processes such as long-range transport of dust and biomass burning plumes can also increase the PM concentrations during specific episodes (e.g. Begum et al., 2011; Kollanus et al., 2016; Guo et al., 2017). The accumulation of PM in the planetary boundary layer (PBL) is favoured by stagnation and poor ventilation (e.g. low winds and shallow mixing depth), which inhibit the dispersion of pollutants (e.g. Tai et al., 2010; Liao et al., 2018). Despite this, the applicability of the different ASIs to PM studies has not been demonstrated for many regions of the globe. In Europe, WA-ASI has been the only ASI used to assess the impact of stagnation on PM (Wang et al., 2018). Hence, it is unclear which ASI best fits the European climate and orography. This issue will be addressed in this work.

As indicated above, numerous meteorological fields (e.g. wind speeds at different heights, precipitation, BLH, CAPE and CIN) have been used to construct ASIs. However, some uncertainty exists about the most appropriate stagnation variables to include in the definition of an ASI to maximize its ability to capture the conditions conducive to elevated PM. This is due to the geographical dependence of PM concentrations on meteorology and the few observational studies available at the continental scale. In Europe, (Barmpadimos et al., 2012) constructed generalized additive models at seven background stations in five European countries, finding the boundary layer height, wind speed, wind direction, temperature, precipitation and synoptic weather pattern as the most important meteorological factors affecting PM concentrations. Table 1.1 shows the most frequently chosen explanatory variables for each season. Other studies have also examined similar dependencies at local or regional scales (e.g. Gietl and Klemm, 2009; Sfetsos and Vlachogiannis, 2010; Barmpadimos et al., 2011; Pateraki et al., 2012; Dimitriou, 2015), but they mainly focus on standard meteorological variables and overlook some of the stagna-

tion components included in existing ASIs.

Table 1.1: List of explanatory variables for $PM_{2.5}$ at seven background stations in five European countries. Positive signs (+) next to variable names indicate a positive relationship between $PM_{2.5}$ and the explanatory variable, whereas negative signs (-) represent the opposite. Use of both signs (+/-) indicates relationships with turning points or variables whose behaviour depends on the station. More frequently chosen variables are displayed first. From Barmapadimos et al. (2012).

Winter	Spring	Summer	Autumn	Year
BLH (-)	BLH (-)	Wind speed (-)	BLH (-)	BLH (-)
Wind direction (+/-)	Wind direction (+/-)	Julian day (+/-)	Wind speed (-)	Wind direction (+/-)
Wind speed (-)	Wind speed (-)	Temperature (+)	Temperature (+)	Wind speed (-)
Prec (-)	Julian day (+/-)	BLH (-)	Wind direction (+/-)	Season
Weather Regime	Prec (-)	Weather Regime	Weather Regime	Temperature (+)
Pressure (+)	Temperature (+)	Wind direction (+/-)	Prec (-)	Julian day (+/-)
Temperature (-)	Previous day Prec (-)		Relative humidity (+/-)	Prec (-)
				Previous day Prec (-)

On the other hand, the inclusion of meteorological variables representing the large-scale flow in the ASIs might also be appropriate in view of the strong relationship between the large-scale circulation and PM concentrations found by some studies. Tai et al. (2010, 2012b) found that the correlations of $PM_{2.5}$ with some meteorological variables such as temperature and relative humidity over the US arise to a large extent not from direct dependence but from covariations with synoptic transport. As a consequence, Tai et al. (2012a,b) focused on the synoptic scale to establish the main meteorological modes of variability for $PM_{2.5}$ in different regions of the US. A follow-on study by Leung et al. (2018) used the same methodology to study the relationship of $PM_{2.5}$ with synoptic weather patterns in different regions of China across various timescales. Some studies have used other approaches to evaluate the impact of the synoptic and large-scale atmospheric circulation on the PM concentrations or on aerosol optical depth (AOD), which can be used as a proxy for atmospheric aerosols. For instance, Fortelli et al. (2016) quantified the relationship between synoptic/local meteorological patterns and the PM concentrations at a coastal site in Italy, Pey et al. (2013) and Salvador et al. (2014) examined the transport mechanisms dominating African dust outbreaks and their contribution to PM over the Mediterranean, Lecoecur et al. (2014) estimated present and future PM concentrations in

Europe based on a weather-type representation of the meteorology, and Jia et al. (2015) addressed the role of the Siberian High in the interannual variability of AOD over northern China. Some analyses have investigated links to modes of climate variability, such as the relationship of the North Atlantic Oscillation (NAO) with winter PM (Pausata et al., 2013) and Saharan dust intrusions (Pey et al., 2013; Salvador et al., 2014) in Europe, or the impact of the 2015 El Niño event on winter PM in China (Chang et al., 2016).

Among the synoptic features which are expected to impact PM and other air pollutants in the midlatitudes, one can mention the frequency and persistence of high-pressure systems with an anticyclonic circulation such as subtropical ridges and high-latitude blocks. Although sometimes these systems associated with stable weather conditions induce similar anomalies in the surface climate (e.g. Barriopedro et al., 2010; Sousa et al., 2016), there are conceptual differences in the definition of blocking and subtropical ridge patterns. Atmospheric blocking is associated with persistent, slow-moving high pressure systems that interrupt the prevailing westerly winds and therefore the eastward progress of extratropical storm systems at middle and high latitudes (Rex, 1950). Blocking events produce strong meteorological anomalies that can favour the conditions leading to air stagnation over northern and central Europe in all seasons (Sousa et al., 2016, 2017; Ordóñez et al., 2017). In addition, changes in the frequency and duration of blocking events have a significant impact on both temperature and precipitation in winter (Fraedrich et al., 1993; Trigo et al., 2004; Masato et al., 2012; Sousa et al., 2016). Subtropical ridges are low latitude structures manifested as relatively narrow bands of positive geopotential height anomalies extending from sub-tropical latitudes towards extra-tropical regions and often reaching higher latitudes (Santos et al., 2009). The impact of these patterns on near-surface ozone in Europe has been analysed previously (Ordóñez et al., 2017). Among other results, they found that winter ozone in north-western Europe responds differently to the occurrence of blocks (ozone decrease) and ridges (ozone increase). The stable atmospheric conditions during blocking events impede the arrival of ozone-rich background air masses from the Atlantic, while also favouring the accumulation of primary pollutants in the PBL and therefore the loss of ozone by titration with nitrogen monoxide (NO) at this time of the year. Ridges are associated with above-average ventilation of the PBL

over that region, which contributes to the dilution of primary pollutants and inhibits the loss of ozone by titration. Following these results, Ordóñez et al. (2017) suggested that the response of primary pollutants and PM might be the opposite to that of ozone in that season, but this has not been investigated yet. Only some studies have addressed similar problems over short temporal scales or for small spatial domains. For instance, Hamburger et al. (2011) found enhanced aerosol loadings in the PBL of north-western and central Europe during an anticyclonic blocking event, while Webber et al. (2017) reported increases in the PM_{10} concentrations in the United Kingdom (UK) Midlands following the occurrence of Rossby wave breaking over the northeast Atlantic–European region. In this thesis we will provide further insights into the impact of blocks and ridges on PM.

1.2.2 Ozone

As illustrated in Figure 1.5, ozone (O_3) can be transported from the stratosphere and produced in the troposphere by photochemical oxidation of non-methane volatile organic compounds (*NMVOCS*), carbon monoxide (CO) and methane (CH_4), catalysed by nitrogen oxides (NO_x) and hydrogen oxide radicals (HO_x). Anthropogenic emissions are the main source of O_3 precursors, but the contribution of biogenic *NMVOCS* is also significant. Elevated O_3 concentrations pose a serious threat to human health, the environment and climate (Felzer et al., 2007; Myhre et al., 2013; REVIHAAP, 2013). To reduce some of these impacts, the European Union has implemented AQ legislation over the last decades (Fowler et al., 2013; EU, 2016). Consequently, observational studies have shown a general decrease in the concentrations of ozone precursors over Europe (e.g. Georgoulias et al. 2019, for nitrogen dioxide (NO_2); Worden et al. 2013, for CO ; Waked et al. 2016, and references therein, for *NMVOCS*). This does not necessarily result in reduced near-surface O_3 concentrations because the response of this pollutant to precursor emissions is non-linear. Overall, decreases in annual mean ozone concentrations have been reported at rural stations over the last years, associated with the reductions in NO_x and *NMVOCS* emissions. On the other hand, ozone levels have risen at urban sites at least partly because of the reduced titration by NO following the emission reductions. This has led to a convergence of ozone pollution for the different types of sites in Europe, although

the concentrations remain higher at rural than at urban background sites (Sicard et al., 2013; Paoletti et al., 2014; Monks et al., 2015; Boleti et al., 2018).

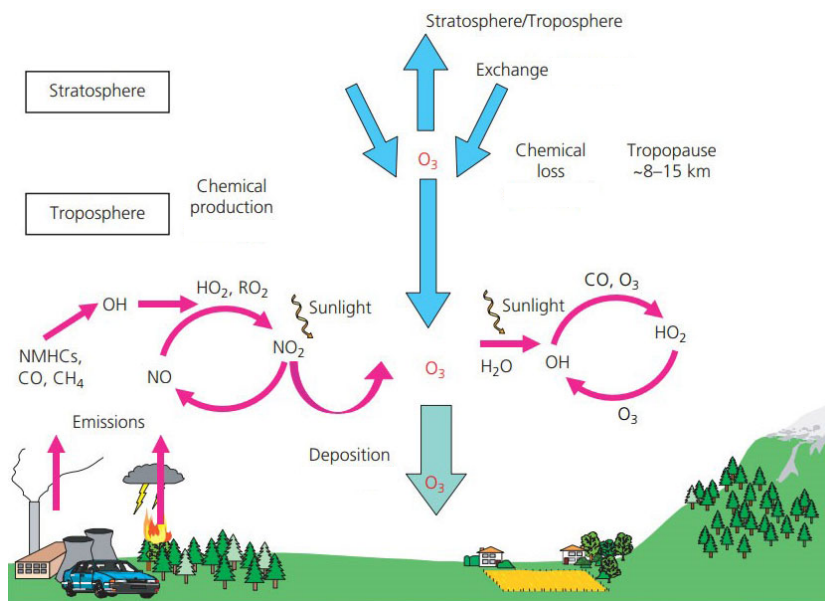


Figure 1.5: Schematic representation of the sources and sinks of ozone in the troposphere. The fluxes of ozone include stratosphere to troposphere exchange, chemical production and loss in the troposphere, and the deposition flux to terrestrial and marine surfaces. From the UK Air Pollution Information System (http://www.apis.ac.uk/overview/pollutants/overview_o3.htm).

Observational studies have shown strong relationships of O_3 with meteorological parameters. Understanding such relationships is often complicated by the covariance of the meteorological variables as well as by the effect of short- and long-term emission changes. Ambient air temperature is the most correlated variable with daily ozone maxima in summer (Bloomfield et al., 1996; Xu et al., 1996; Kuebler et al., 2001; Tarasova and Karpetchko, 2003; Ordóñez et al., 2005). The relationship between both variables is driven by several well-known temperature-dependent mechanisms: the thermal decomposition of the NO_x reservoir species peroxyacetyl nitrate (PAN , $CH_3COO_2NO_2$) (Orlando et al., 1992), the temperature-dependent emissions of both $NM VOCs$ from vegetation and NO_x from soil (Fehsenfeld et al., 1992; Simpson, 1995), the extra evaporation of anthropogenic $NM VOCs$ at high temperatures (Vautard et al., 2005), or the high stomatal resistance at elevated temperatures, which limits the dry deposition of ozone to vegetation (Wesely, 1989). Nevertheless, the temperature – O_3 relationship is complex and can only partially

be explained by the mentioned processes. As an example, Porter and Heald (2019) have estimated that the covariance of temperature with other meteorological variables explains over 40% of the ozone–temperature correlation in the US and up to 60% in Europe (Figure 1.6). For instance, the positive temperature – O_3 relationship may partly reflect association of high temperatures with air mass origin and regional stagnation (Jacob et al., 1993; Jacob and Winner, 2009, and references therein).

There are also a number of relevant meteorological processes that may alter the ozone–temperature relationship at a given location. . As an illustration, wind speed can influence O_3 concentration in a number of ways (Jacob and Winner, 2009, and references therein). For instance, weak wind speeds in moderately polluted regions often yield ozone increases, as would be expected from a long reaction time of ozone precursors and increased aerodynamic resistance to dry deposition. However, in urban areas, the accumulation of primary pollutants close to the surface under reduced wind speeds should result in increased ozone loss by reaction with NO . On the other hand, strong wind speeds may be associated with enhanced vertical mixing, which favours the entrainment of ozone-rich air from the free troposphere into the boundary layer. These kinds of competing effects are also found for other meteorological parameters such as humidity. At the global scale, relative humidity has a negative relationship with O_3 , because water vapour leads to O_3 depletion through the reaction $O_3 + h\nu \rightarrow O(^1D) + O_2$ followed by $O(^1D) + H_2O \rightarrow 2OH$. However, the OH radicals formed through these reactions oxidize CO and $NMVOC$ s, leading to increased O_3 mixing ratios under moderately high NO_x conditions. On the other hand, in the mid-latitudes, high relative humidity is often linked to weather conditions that do not favour O_3 formation.

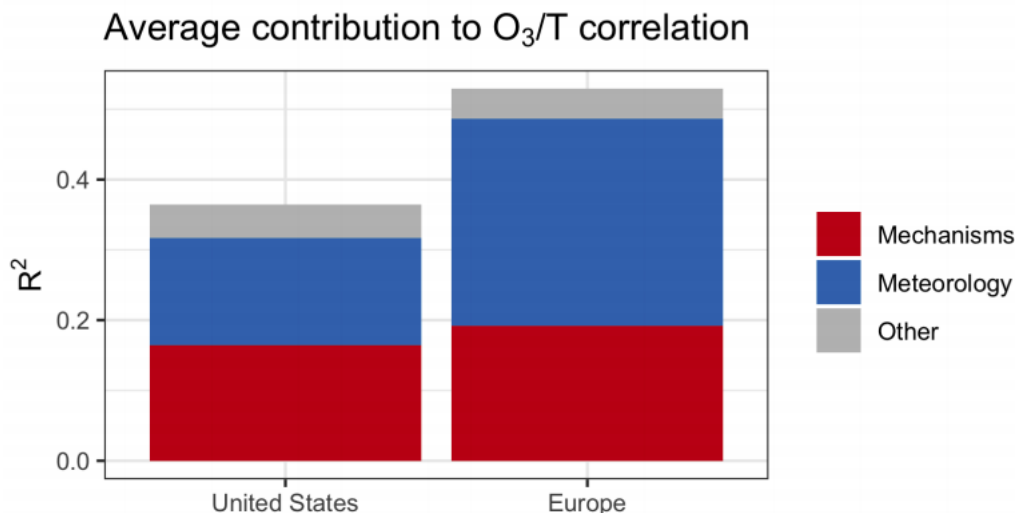


Figure 1.6: Contribution of modelled temperature-related mechanisms (red) and other meteorological variables (blue) to the total O_3 –temperature correlation. From Porter and Heald (2019).

Air stagnation is another relevant meteorological phenomenon for ozone as it is characterized by stable weather conditions with poor ventilation, leading to the accumulation of pollutants close to the surface (Jacob et al., 1993; Jacob and Winner, 2009; Dawson et al., 2014; Fiore et al., 2015). Enhanced ozone concentrations under stagnant conditions have been documented for the US (Leibensperger et al., 2008; Schnell and Prather, 2017). The relationship among stagnation, temperature and O_3 has been closely examined by some studies for the US. Sun et al. (2017) found that the probability of high O_3 days increases with the co-occurrence of high temperature and stagnation, and that the occurrence of successive stagnation days further enhances this likelihood (Figure 1.7). Schnell and Prather (2017) showed that air stagnation, O_3 extremes and temperature extremes tend to co-occur in large-scale, multiday, spatially coherent structures. These evidences are in line with the hypothesis of Horton et al. (2012), who projected 21st century increases in stagnation frequency over several highly populated regions of the globe and suggested a potential to enhance the accumulation of both near-surface ozone and PM close to the surface. However, the relationship between stagnation and summer ozone has been reported to be weak over some regions of the US (Kerr and Waugh, 2018). That study noted the limited skill of HO-ASI to explain air pollution events and indicated an erratic overlap between stagnation and pollutant extremes in the US, especially in the

Northeast. Consequently, they advised against the use of this common index as a metric to examine pollution events and recommended testing new indices considering other meteorological predictors such as BLH and temperature. Thus, much uncertainty still exists about how air stagnation impacts O_3 and its relationship with temperature. The Euro-Mediterranean region has been identified as a climate change hot spot (Diffenbaugh and Giorgi, 2012; de Sherbinin, 2014) where model simulations under climate change scenarios project strong increases both in temperature (Giorgi and Lionello, 2008; Barkhordarian et al., 2012) and in the occurrence of stagnation (Horton et al., 2012, 2014). Understanding the complementarity of temperature and stagnation in driving the variability of O_3 becomes highly relevant, as will be analysed later in this thesis.

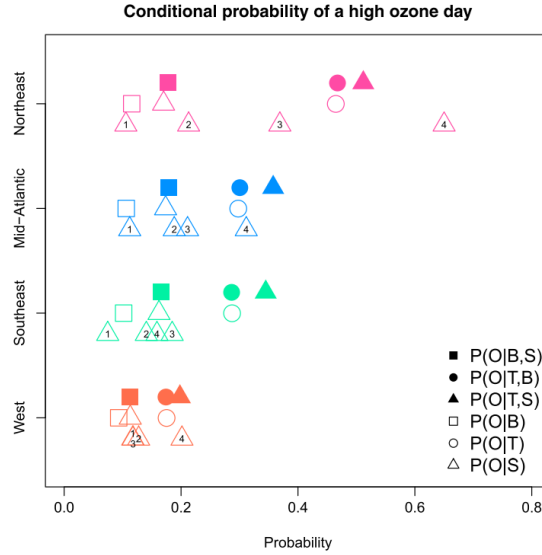


Figure 1.7: Conditional probability of a high ozone day (referred as O) under a high-temperature day (T), a stagnation day (S) and an anticyclonic day (B) (open symbols) and combinations of the above (closed symbols) for four regions of the US. The triangles with numbers represent the probability of occurrence of a high ozone day after a number of consecutive stagnation days (duration denoted by number in the triangle). From Sun et al. (2017).

1.3 Objectives

In this thesis we will fill some of the gaps described above for the Euro-Mediterranean region. We aim to perform the first comprehensive analysis of air stagnation and examine its impact on the airborne concentrations of two of the main pollutants linked to serious health impacts, PM_{10} and O_3 . In particular, we will:

1. Characterize the spatiotemporal variability of stagnation over the Euro-Mediterranean area.
2. Assess the degree of consistency between the climatological features of air stagnation as derived from a meteorological reanalysis and observations.
3. Identify the synoptic patterns associated with seasonal regional stagnation extremes in Europe.
4. Assess the relationship between air stagnation and PM_{10} concentrations separately for three different ASIs and identify the most important stagnation-related meteorological fields that explain PM_{10} variability.
5. Evaluate the potential of stagnation as a driver of summer ozone pollution over different regions of Europe.
6. Provide a quantitative analysis of future changes in stagnation for different storylines and levels of warming.

Chapter 2 introduces the reanalysis and observational data sources used throughout this PhD thesis. Chapter 3 presents the climatology of stagnation days, events (defined as the sequence of one or more consecutive stagnation days) and their duration using HO_ASI both for reanalysis and observations. In addition, it provides a regionalization of stagnation over Europe, and investigates its temporal variability and the synoptic patterns leading to seasonal stagnation extremes in the different regions (Garrido-Perez et al., 2018). Chapter 4 undertakes a comparative analysis of the relationships of PM_{10} with three ASIs (HO_ASI, WA_ASI and HU_ASI) and characterizes the dependence of this

pollutant on the most important meteorological variables related to stagnation using generalized additive models (Garrido-Perez et al., 2021). Chapter 5 provides further insights into the relationship between atmospheric circulation and PM_{10} . In particular, it examines the regional responses of winter PM_{10} to the occurrence, position and persistence of blocks and ridges (Garrido-Perez et al., 2017). Chapter 6 evaluates whether the relationship between maximum daily 8-h running average near-surface ozone ($MDA8\ O_3$) and temperature differs under stagnant and non-stagnant situations. Moreover, the diurnal cycle of O_3 is analysed in order to understand the response of this pollutant to stagnation and the mechanisms involved (Garrido-Perez et al., 2019). Chapter 7 develops plausible storylines of atmospheric circulation change to examine uncertainties in future regional changes in air stagnation over the contiguous United States and Europe (Garrido-Perez et al., 2022). Finally, Chapter 8 summarizes and discusses the main conclusions, and provides some outlook for future work.

2 Data

To achieve the objectives set in the previous chapter, we have used observational, reanalysis and simulated datasets that provide information related to the meteorology and AQ in Europe. This section presents an overview of these datasets. For the sake of clarity, the data used in each of the next chapters is summarized in Table 2.1.

Table 2.1: Summary of the datasets used in each chapter.

	Chapter 3	Chapter 4	Chapter 5	Chapter 6	Chapter 7
Meteorological observations	E-OBS, IGRA & ISD	-	E-OBS	-	-
Meteorological reanalysis	ERA-Interim & NCEP	ERA5	ERA-Interim & NCEP	ERA-Interim	ERA5
AQ observations	Airbase & EMEP	Airbase	Airbase	Airbase & EMEP	-
Climate models	-	-	-	-	CMIP6

2.1 Meteorological observations

Meteorological observations are used in Chapter 3 to characterize air stagnation and compare its climatological features to those derived from a meteorological reanalysis. As mentioned previously, air stagnation is often defined by three meteorological variables: precipitation, upper-air wind speed and near-surface wind speed. However, there is no observational database providing them simultaneously for Europe. Therefore, we have

used three different databases covering the period 1979–2016.

Daily precipitation was obtained from the E-OBS gridded dataset (Haylock et al., 2008) at $0.25^\circ \times 0.25^\circ$ horizontal resolution, which is provided by the European Climate Assessment and Dataset (ECAD) (<http://www.ecad.eu/download/ensembles/download.php>). These data have also been analysed in Chapter 5, as precipitation is known to impact PM concentrations and its regional distribution is affected by the presence of both blocks and ridges.

Upper-air wind data were obtained from the Integrated Global Radiosonde Archive (IGRA) (Durre et al., 2006) (<https://www.ncdc.noaa.gov/data-access/weather-balloon/integrated-global-radiosonde-archive>) provided by the NOAA’s National Centers for Environmental Information (NCEI). This dataset has been tested by the data provider through a comprehensive set of quality control procedures to remove gross errors. We have only used the standard level of 500 hPa and averaged all the available measurements within a single day (often two soundings) to calculate daily average Wsp500 for each location.

Daily average Wsp10 observations were obtained from the Integrated Surface Database (ISD) (Smith et al., 2011) (<https://www.ncdc.noaa.gov/isd/data-access>) which is provided by the NCDC’s Climate Services Branch (CSB). The data supplier controls the quality of the dataset by means of algorithms that check format, extreme values and limits, consistency between parameters and continuity between observations.

Even though some IGRA radiosondes also include Wsp10 data, we opted to use the ISD database. The reason lies in the greater amount of data available in the latter. This allows averaging Wsp10 from a number of ISD stations located within 50 km around each IGRA’s radiosonde location, in a similar way as Vautard et al. (2010). This way local effects that affect surface wind speed are smoothed. The radiosonde site is eliminated from the study if no ISD stations can be found in the proximities. We have finally used 91 IGRA sites distributed homogeneously throughout the area of study as well as 583 ISD stations (Figure 2.1). The number of ISD sites used for each IGRA location is irregular, ranging from only 1 to 24. Previous studies have used the IGRA and ISD databases

simultaneously both for wind (e.g. Gatey et al., 2011) and for other variables such as humidity or cloud cover data (e.g. Nygård et al., 2014). Finally, daily precipitation is taken from the closest grid of the E-OBS dataset in relation to the IGRA’s radiosonde location. These two datasets have previously been used simultaneously for the evaluation of the meteorological performance of coupled chemistry-meteorology simulations over Europe and the US (Brunner et al., 2015). Thus, the joint use of three different datasets should not have a significant impact on our results.

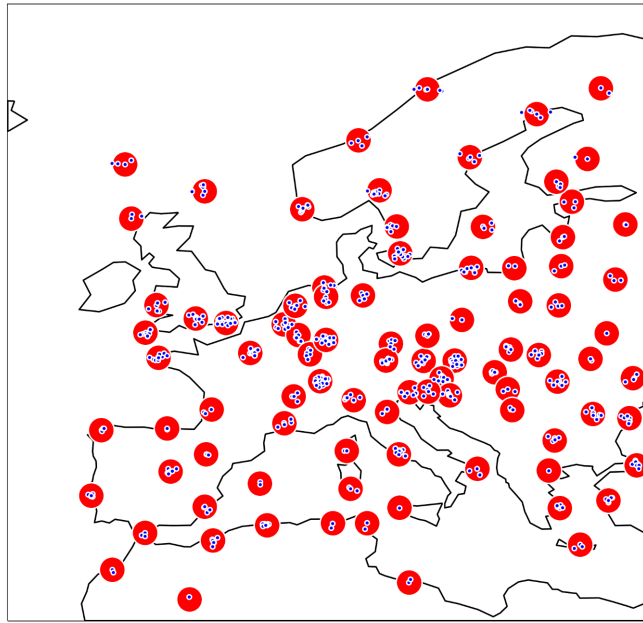


Figure 2.1: Spatial distribution of the 91 IGRA (red) and 583 ISD (blue) locations. The red circles represent the approximate area around each IGRA station where data from nearby ISD sites are averaged.

2.2 Meteorological reanalysis

We have used two reanalysis products provided by the European Centre for Medium-Range Weather Forecasts (ECMWF): ERA-Interim (Dee et al., 2011) and ERA5 (Hersbach et al., 2020). While the former has extensively been used throughout this PhD thesis (Chapters 3, 5 and 6), the latter has been employed for the most recent analyses presented here (Chapter 4) following its launch in 2019. Note that the change from ERA-Interim to ERA5 has resulted in a substantial improvement in weather and climate data. Among other advantages, ERA 5 has much higher spatial and temporal resolu-

tion, improved numerical model and data assimilation schemes, better global balance of precipitation and evaporation and more consistent sea surface temperature and sea ice (<https://confluence.ecmwf.int/pages/viewpage.action?pageId=74764925>).

On the one hand, we use daily mean fields of SLP, 500 hPa geopotential height (Z500), 10 m (Wsp10), 850 hPa (Wsp850) and 500 hPa (Wsp500) wind; daily accumulated precipitation (Prec); daily maximum temperature at 2 m (Tmax), and BLH from the ECMWF ERA-Interim reanalysis at $0.75^\circ \times 0.75^\circ$ horizontal resolution. Prec has been calculated by summing the 12-h accumulated precipitation forecast at 00 and 12 UTC. Tmax has been computed as the maximum from all the temperature values forecast for each day. Daily values of BLH correspond to those at 12 UTC. Daily averages of any other meteorological variables are calculated by averaging four analysis values at 00:00, 06:00, 12:00 and 18:00 for each day.

SLP, Z500, wind speed at different heights, 2m temperature, 1000 hPa relative humidity, Prec, BLH, CAPE and CIN have also been obtained from the ERA5 reanalysis product at $0.75^\circ \times 0.75^\circ$ horizontal resolution. However, in this case daily precipitation has been computed as the sum of 1-h accumulated precipitation forecast for twenty-four time intervals on each day. In addition, while the daily values of BLH, CAPE and CIN correspond to those at 12 UTC, daily maximum ventilation is computed as the highest value at the standard meteorological hours 00, 06, 12 and 18. Daily averages of wind speed, SLP, Z500, temperature at 2m and relative humidity have also been calculated by averaging four analysis values at the standard meteorological hours 00, 06, 12 and 18 for each day.

We have also used the National Centers for Environmental Prediction (NCEP) / National Center for Atmospheric Research (NCAR) reanalysis (Kalnay et al., 1996) for some of the analyses carried out here. The results were similar to those obtained from ERA-Interim and ERA5, indicating that they are robust regardless of the reanalysis. They are not included here for the sake of brevity.

2.3 CMIP6 meteorological data

Model-based meteorological data are used in Chapter 7 to investigate changes in regional air stagnation due to the forced response of remote drivers in a multi-model ensemble. Meteorological variables, including daily 500hPa wind speed, near-surface wind speed, and precipitation, as well as monthly 2m, 850hPa and 250hPa temperatures, and sea surface temperatures (SSTs) were obtained from a 22-member CMIP6 ensemble of opportunity (Table 2.2; Eyring et al. (2016)). All simulated data have been interpolated to a common grid with $2.5^\circ \times 2.5^\circ$ horizontal resolution. For each individual model realization, the end-of-century climate change response is defined as the 2071–2100 mean in the shared socioeconomic pathway SSP5-8.5 scenario minus the 1981–2010 mean in the historical simulation. Although realization of this high emission scenario is considered unlikely, the corresponding simulated climate futures cannot be ruled out (IPCC, 2021).

Table 2.2: CMIP6 models and modelling groups included in this thesis.

Institute ID	Model version	Atmospheric resolution (Lon \times Lat, Levels)	Variant level
CSIRO-ARCCSS, Australia	ACCESS-CM2	192 \times 145, L85	r1i1p1f1
=	ACCESS-ESM1-5	192 \times 145, L38	r1i1p1f1
BCC, China	BCC-CSM2-MR	320 \times 160, L46	r1i1p1f1
CCCma, Canada	CANESM5	128 \times 64, L49	r1i1p2f1
NCAR, United States	CESM2	288 \times 192, L32	r4i1p1f1
=	CESM2-WACCM	288 \times 192, L70	r1i1p1f1
CMCC, Italy	CMCC-CM2-SR5	288 \times 192, L30	r1i1p1f1
EC-Earth-Consortium, Europe	EC-EARTH3	512 \times 256, L91	r1i1p1f1
CAS, China	FGOALS-G3	180 \times 80, L26	r1i1p1f1
NOAA-GFDL, United States	GFDL-CM4	360 \times 180, L33	r1i1p1f1
MOHC, UK	HADGEM3-GC31-LL	192 \times 144, L85	r1i1p1f3
=	HADGEM3-GC31-MM	432 \times 324, L85	r1i1p1f3
INM, Russia	INM-CM4-8	180 \times 120, L21	r1i1p1f1
=	INM-CM5-0	180 \times 120, L73	r1i1p1f1
AORI/NIES/JAMSTEC, Japan	MIROC6	256 \times 128, L81	r1i1p1f1
=	MIROC-ES2L	128 \times 64, L40	r1i1p1f2
MPIM, Germany	MPI-ESM1-2-HR	384 \times 192, L95	r1i1p1f1
=	MPI-ESM1-2-LR	192 \times 96, L47	r1i1p1f1
MRI, Japan	MRI-ESM2-0	320 \times 160, L80	r1i1p1f1
NCC, Norway	NorESM2-LM	144 \times 96, L32	r1i1p1f1
=	NorESM2-MM	288 \times 192, L32	r1i1p1f1
MOHC-NERC, UK	UKESM1-0-LL	192 \times 144, L85	r1i1p1f2

2.4 Air quality observations

AQ is quantified through two of the most relevant pollutants in Europe: PM_{10} (Chapters 3 to 5) and O_3 (Chapters 3 and 6). The concentrations of both pollutants have been obtained from two databases: the European Environment Agency’s air quality database (AirBase) (<http://www.eea.europa.eu/data-and-maps/data/airbase-the-european-air-quality-database-8>) and the European Monitoring and Evaluation Programme (EMEP) (Tørseth et al., 2012) (<http://ebas.nilu.no/>).

We have used daily average PM_{10} for each monitoring station during time periods up to 13 years. The use of daily averages is appropriate to evaluate the impact of stagnation and atmospheric circulation on the day-to-day variability of PM_{10} . Moreover, this coincides with the averaging period used to assess the short-term health impacts of this pollutant on the basis of epidemiological studies ($50 \mu g m^{-3}$ limit value averaged over 24 hours (EU, 2008)). These data have also been employed to understand the influence of large-scale circulation on PM_{10} in Europe (Ordóñez et al., 2019). The selection of sites has been done based on the data availability ($>75\%$ for each period of analysis) and the resulting dataset includes ~ 500 stations of various categories. They can be classified according to the type of area (urban/suburban/rural) and the predominant source of pollution (traffic/industrial/background). Since pollution levels are heavily dependent on the type of station, some analyses will only use background stations in order to filter out local phenomena as much as possible. This will be indicated in each chapter. Figure 2.2 illustrates the summer and winter means of PM_{10} at each background location (~ 300 stations). The average over all sites ranges from $20.5 \mu g m^{-3}$ in summer to $28.6 \mu g m^{-3}$ in winter, but there are considerable regional differences. The highest concentrations are found for eastern Europe, northern Italy and some sites in the Iberian Peninsula, where the winter averages exceed $40 \mu g m^{-3}$. Winter mean concentrations of $\sim 30 \mu g m^{-3}$ are also common to many sites in Benelux, southeastern France, Switzerland and southern Germany, whereas they are lower over other regions. Similar patterns, although with lower concentrations, are found in summer. Note that we examined the availability of $PM_{2.5}$ observations from AirBase and EMEP, but finally opted for PM_{10} as it presents

much better temporal and spatial coverage.

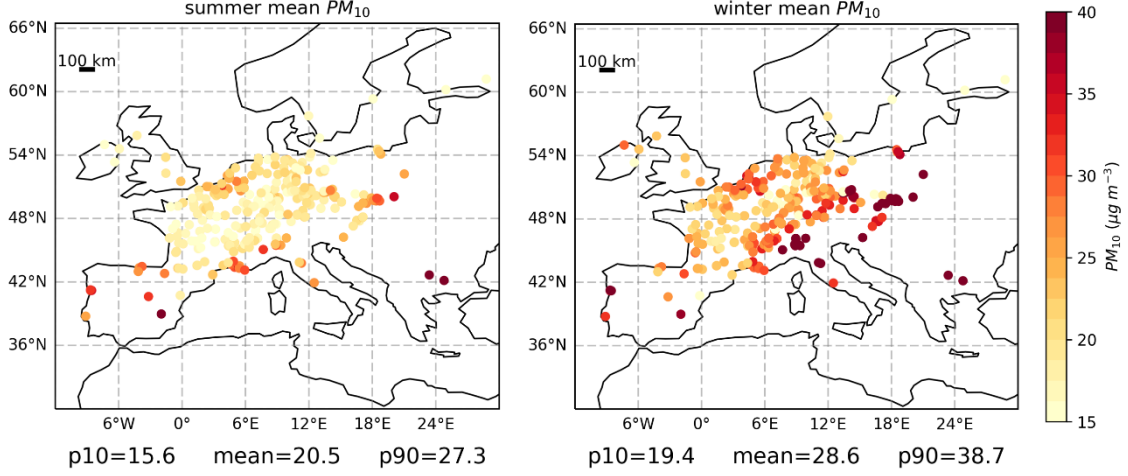


Figure 2.2: Summer (left) and winter (right) average background PM_{10} concentrations ($\mu\text{g m}^{-3}$) during the 2000–2012 period. The numbers below the panels respectively indicate the 10th percentile (p10), mean and 90th percentile (p90) across all sites.

On the other hand, we have used interpolated datasets of observed $MDA8 O_3$ and hourly ozone volume mixing ratios over Europe at $1.0^\circ \times 1.0^\circ$ resolution covering periods up to 18 years. We focus on summer data for this pollutant as it is the season when the concentrations maximize over large parts of Europe. The summer means of $MDA8 O_3$ from these datasets are illustrated in Figure 2.3 (left panel). The data have been generated by merging non-traffic observations obtained from AirBase and EMEP with the objective mapping algorithm developed by Schnell et al. (2014, 2015). These data have also been used by several studies (Otero et al., 2016, 2018; Carro-Calvo et al., 2017; Ordóñez et al., 2017) to understand the meteorological drivers of ozone in Europe. In particular, Carro-Calvo et al. (2017) applied the k-means clustering technique to obtain nine regions where summer O_3 shows coherent spatiotemporal patterns. The regions from that study will be used in this thesis to examine the relationship among air stagnation, temperature and O_3 in a consistent way (Chapter 6). From west to east and from north to south, the regions analysed here roughly cover the British Isles (BRIT), northern-central Europe (NCE), northern Scandinavia (NSC), the Baltic region (BALT), the Iberian Peninsula (IBE), western Europe (WE), southern-central Europe (SCE) and eastern Europe (EE). This regionalization is displayed on Figure 2.3 (right panel).

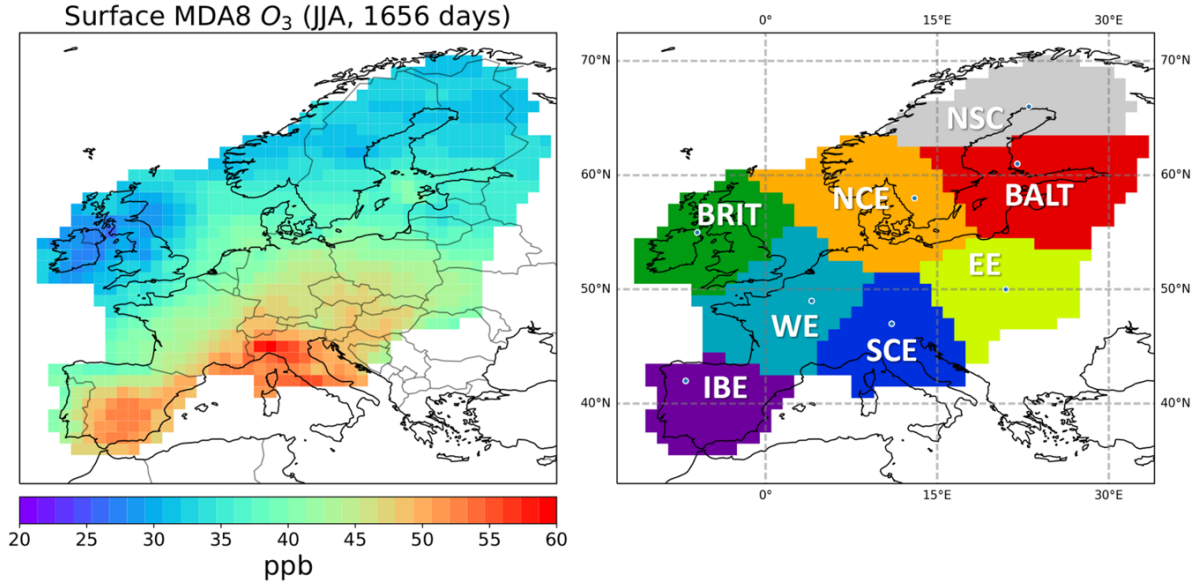


Figure 2.3: Left panel: Composite of the summer (JJA) mean of maximum daily 8 h running average near-surface ozone ($MDA8 O_3$) expressed in parts per billion by volume (ppb) during the 1998 – 2015 period. Right panel: Regionalization of summer $MDA8 O_3$. Adapted from Carro-Calvo et al. (2017). From west to east and from north to south the regions roughly correspond to the British Isles (BRIT), northern-central Europe (NCE), northern Scandinavia (NSC), the Baltic region (BALT), the Iberian Peninsula (IBE), western Europe (WE), southern-central Europe (SCE) and eastern Europe (EE). Blue circles represent the land grid cells where the correlations between the standardized anomalies of the $MDA8 O_3$ time series and those of the respective centroid maximize (see details in Chapter 6).

2.5 Catalogue of blocks and ridges

We have used the catalogue of high-latitude blocks and subtropical ridges developed by Sousa et al. (2016, 2017). The NCEP/NCAR meteorological reanalysis at $2.5^\circ \times 2.5^\circ$ was used to create the catalogue. This horizontal resolution is coarser than that of other reanalysis datasets, but it is appropriate to characterise large-scale phenomena such as blocks and ridges. The same catalogue has been used by Ordóñez et al. (2017) to analyse the response of European near-surface ozone to blocks and ridges.

To identify blocks and ridges and avoid their overlap, the detection algorithms set some north/south boxes with latitudinal limits at 45° N during winter, based on sensitivity analyses by Sousa et al. (2017). Blocking centres are detected north of that

line and ridges in the south. The detection of blocks applies a simplified version of the method described by Barriopedro et al. (2006), where they are defined as large-scale reversals of the Z500 meridional gradient. The algorithm considers that reversals must have a minimum longitudinal extension of 12.5° during their whole lifetime and a minimum duration of 5 days. Two conditions are imposed for the detection of subtropical ridges: a ridge is detected in a southern box if (i) at least 75 % of the grid points are above the 80th percentile of the specific 31-day moving average Z500 climatology during the period 1950 – 2012 and (ii) no more than 50 % of the grid points in the northern box are above the same threshold.

Three longitudinal sectors of 30° width with two boxes each (north/south) were used by Sousa et al. (2017) and Ordóñez et al. (2017) to catalogue high-latitude blocks and subtropical ridges regionally according to the position of their centres: Atlantic (ATL, 30° – 0° W), European (EUR, 0° – 30° E), and Russian (RUS, 30° – 60° E). Only blocking and ridge centres within the first two sectors (ATL, EUR) have been used here, as the occurrence of these patterns in the RUS sector has a limited impact on the pollutant concentrations over the area of study. These two longitudinal sectors are used to assess how the location of blocks and ridges as well as their residence times impact PM_{10} concentrations over different areas of the European continent (Chapter 5). Note, however, that some blocks and ridges can have their centres in more than one sector during their lifetimes, since they tend to move eastwards.

The average blocking duration is ~ 8 – 10 days, longer in winter than in summer. Nevertheless, their residence time in a given sector is more relevant than their lifetime to assess their effects on PM_{10} . We have identified a total of 174 days with block centres in the ATL sector, 138 days with blocks in the EUR sector, 128 with ridges in the ATL sector and 151 with ridges in the EUR sector during the winter months (DJF) of the period Jan 2000 – Feb 2010, as displayed on the top of the panels in Figure 5.1. The interannual variability of the number of days with block and ridge centres over a given sector can be rather large, as shown in Figure 2.4.

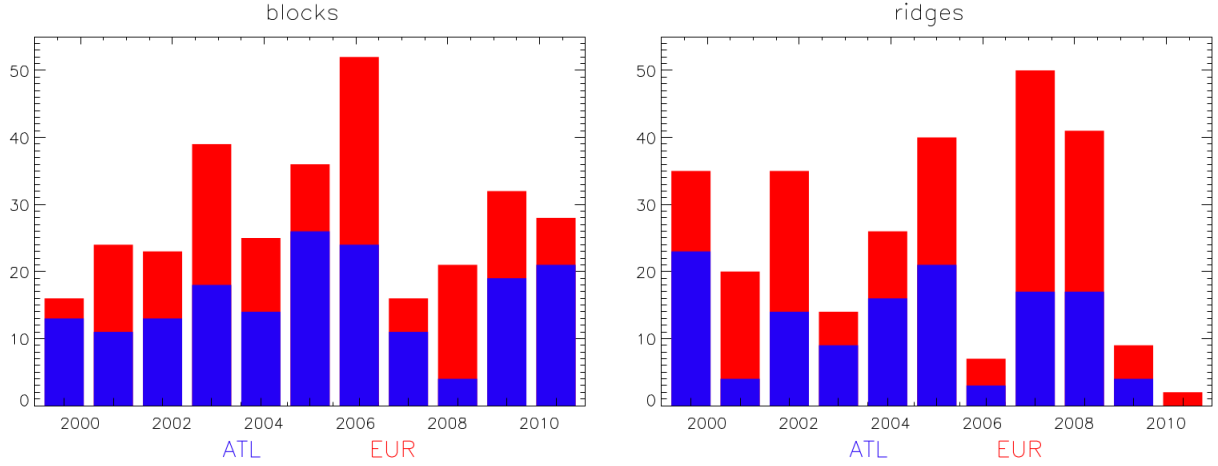


Figure 2.4: Interannual variability of the number of days with block (left panel) and ridge (right panel) centres detected over each sector (Atlantic, ATL; European, EUR) during the winter (DJF) months of the Jan 2000 – Feb 2010 period.

The seasonal composites of the anomalies (with respect to the climatology) and absolute values for the daily Z500 fields, considering days with blocking and ridge centres in each sector over a ~ 60 -year period as well as a more recent 15-year period, can be found in Sousa et al. (2016, 2017) and Ordóñez et al. (2017), respectively. Figure 2.5 illustrates the composites of the anomalies (with respect to days without blocks or ridges in the specific sector) and absolute values of Z500 for the winter months (DJF) of the 2000–2010 period analysed here. Stippling indicates statistically significant anomalies at the 5% level (determined through a bootstrap resampling method). The highest values of the absolute Z500 field (black contour lines) and the positive Z500 anomalies (shaded areas) are centred in the respective sector. Significantly positive anomalies dominate the northern latitudes in the case of blocks and the low latitudes in the case of ridges, being larger for blocks than for ridges.

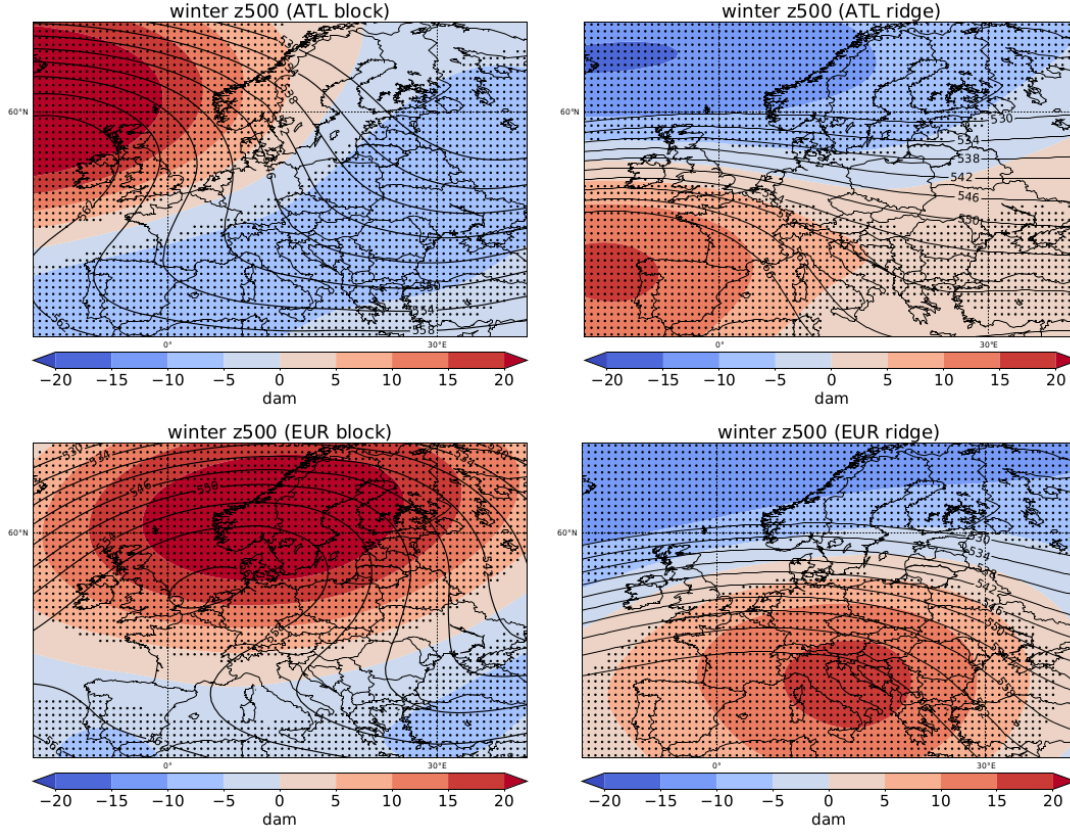


Figure 2.5: Composites of the daily anomalies (shaded areas) as well as absolute values (black contour lines) of Z500 for blocking (left) and ridge (right) centres within the Atlantic (top) and European (bottom) sectors. Anomalies are calculated as deviations from the data without blocks / ridges in the respective sector during winter 2000–2010. Stippling (density is proportional to grid spacing) indicates regions with statistically significant anomalies at the 95 % (determined through a bootstrap resampling method). All values are in decametres (dam).

The composites shown by Sousa et al. (2016, 2017) and Ordóñez et al. (2017) were calculated for Z500 data from the NCEP/NCAR reanalysis, while fields from the ERA-Interim reanalysis have been used for Figure 2.5 and for all the analyses in Chapter 5. One important reason for using ERA-Interim data is that, unlike NCEP/NCAR, it includes output for the boundary layer height. As documented by many studies, this parameter has a strong impact on the surface PM concentrations (e.g. Jacob and Winner, 2009; Fiore et al., 2012). Moreover, the anomalies of Z500 and other meteorological fields on days with blocks/ridges shown here for ERA-Interim are consistent with those of the previous studies. Analyses carried out by Sousa et al. (2017) also confirm the low sensitivity of the results to the reanalysis dataset.

3 Air stagnation in Europe:

Spatiotemporal variability and impact on air quality

This chapter characterizes the spatiotemporal variability of air stagnation over the Euro-Mediterranean area for the 1979–2016 period by using a simplified air stagnation index: HO-ASI (Horton et al., 2012). According to this index, a day is considered as stagnant for a given location when three conditions are fulfilled simultaneously: daily mean Wsp10 is lower than 3.2 m/s , Wsp500 is below 13.0 m/s and daily total precipitation is under 1.0 mm (i.e. a dry day). For each location, this yields a time series filled with ones (stagnant day) and zeros (no stagnation), which can be aggregated into monthly frequencies of stagnation days. Unlike the previous index by Wang and Angell (1999), this ASI adaptation places no length requirements on stagnation events and considers them as any sequence of consecutive days meeting the previous conditions, without any minimum threshold for duration. This is appropriate for our region of study due to the presence of some areas where stagnation frequency and average duration are relatively low, as will be shown later.

Despite the existence of more complex meteorological indices which may better represent the conditions favourable to the occurrence of elevated PM concentrations over some regions (e.g. WA_ASI and HU_ASI), the choice of a simplified index in this chapter is motivated by the following reasons. First, it minimizes the potential discrepancies between reanalysis and observations by reducing the number of variables that strongly depend on the model physics (e.g. PBL). Second, this index has been widely employed in the literature, being a good indicator of AQ episodes related to both PM and O_3 in other regions of the globe. Hence, in principle it allows us to evaluate simultaneously the impact of stagnation on pollutants affected by different meteorological mechanisms. Furthermore, previous analyses using this index have projected future increases in air stagnation over the north of the Mediterranean (Horton et al., 2014), but the ability of the index to reflect the weather conditions triggering poor AQ in the region needs to be investigated.

Air stagnation will be analysed for the whole year, while the assessment of its impacts on AQ will be restricted to the seasons with the highest concentrations of those pollutants: winter (December-January-February, DJF) for PM_{10} and summer (June-July-August, JJA) for O_3 (e.g. Laurila, 1999; Koelemeijer et al., 2006; Schnell et al., 2015). The results of this chapter have been reported in Garrido-Perez et al. (2018).

3.1 Annual occurrence of air stagnation in observations and reanalysis

We have first examined the ability of the ERA-Interim reanalysis to reproduce the observed air stagnation climatology by comparing a series of benchmarks: annual frequency of stagnation days, number of events and their duration. For simplicity, in these comparisons each of the 91 locations with observations (see Section 2.1) is matched to the closest reanalysis grid cell. We are aware that more complex spatial verification methods are available in the literature, but the improvement that they bring is more relevant for cases that require higher resolution than ours (Brown et al., 2012).

Figure 3.1 shows the annually averaged percentage of air stagnation days (% , left), the average number of events per year (middle) and the average event duration (number of days, right). Generally, the spatial distribution of the calculated values compares relatively well between reanalysis and observations. Considering the whole dataset of 91 observational sites, we obtain a Pearson correlation coefficient (R) over 0.70 (p -value < 0.01) for both stagnation days and events, although only slightly above 0.55 for the average event duration. Mean biases (MB) for stagnation days and events are relatively low in the reanalysis compared to the observations (-1.4 % and 2.1 events per year, respectively), with root mean squared errors (RMSE) close to 7 % for the stagnation days and 7 in the case of the events. As expected, these values are lower for the mean event duration, with zero bias and RMSE = 0.4 days. There are, however, some locations where the differences in the frequency of stagnation days between reanalysis and observations (Figure 3.1, left) are high enough to indicate that further analyses are needed. In order to investigate this, we have done some additional comparisons for the three meteorological variables included in the HO_ASI calculation.

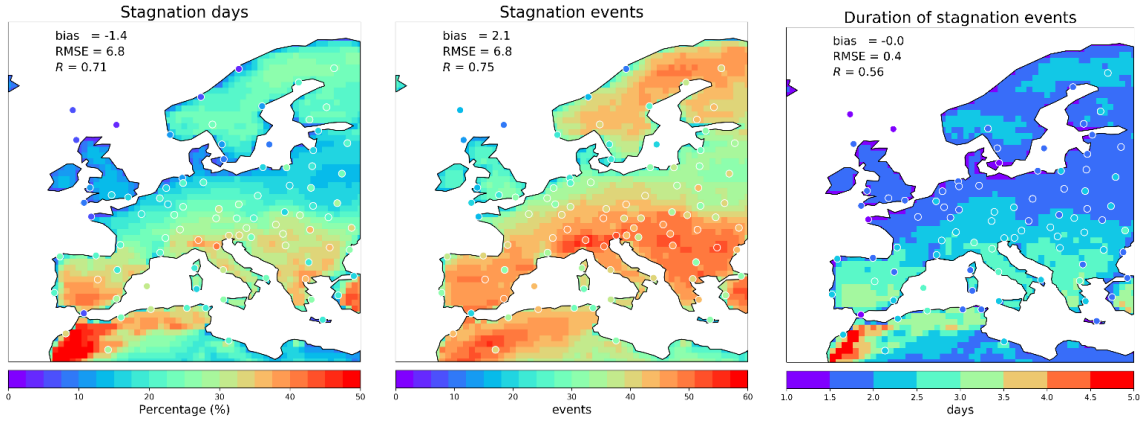


Figure 3.1: Percentage of stagnation days (% , left) per year, average number of stagnation events per year (middle) and mean event duration (number of days, right) during the period 1979–2016. Shaded colours represent reanalysis data and coloured circles observations. Mean bias (MB), root mean square error (RMSE) and Pearson correlation coefficient (R) are obtained from the two samples considering only the grid cells of the reanalysis which are closest to the observational sites.

Figure 3.2 displays the percentage of days that stagnation conditions are met separately for each component used in the HO_ASI definition: precipitation below 1 mm (i.e. dry day, DD), Wsp10 below 3.2 m/s and Wsp500 below 13 m/s . The comparison of

reanalysis with observations for precipitation (Figure 3.2, left) and upper air wind speed (Figure 3.2, right) shows consistent patterns between both datasets, with R values of 0.95 and 0.93 respectively. The magnitude of the mean bias and RMSE is smaller for the upper-air wind speed than for precipitation, whose occurrence is overestimated by the reanalysis leading to reduced stagnation ($MB = -7.2\%$). The main discrepancies between reanalysis and observations arise from Wsp10, for which $R = 0.64$ and $RMSE = \sim 18\%$. This can be explained by the strong influence of orography together with the insufficient horizontal resolution and imperfect boundary layer parameterizations of the reanalysis model, as well as the impact of the local settings on observations. Furthermore, there are a considerable number of coastal sites, which could yield higher observed wind speeds compared to those in the reanalysis over some regions. In spite of this, the reanalysis underestimates the overall number of days fulfilling the 10 m wind condition for air stagnation ($MB = -3.6\%$). In conclusion, keeping in mind the reasonably fair agreement between the regional patterns of air stagnation in reanalysis and observations (Figure 3.1, left), and that the main differences emerging from surface winds are highly local, it seems reasonable to use the reanalysis to analyse regional-scale variability of air stagnation. In the following, we will focus on the analysis of air stagnation as obtained from the reanalysis dataset, unless otherwise stated.

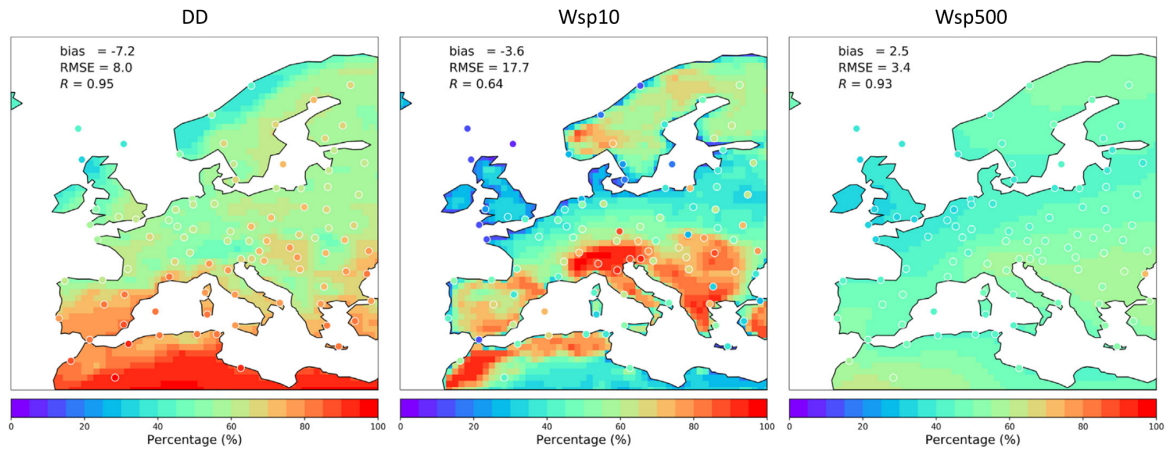


Figure 3.2: Annual percentage of days that fulfil the stagnation condition for precipitation (left), 10 m wind speed (middle) and upper-air wind speed (right) during the period 1979–2016. Shaded colours represent reanalysis and coloured circles observations. Mean bias (%), root mean square error (RMSE, %) and correlation coefficient (R) are obtained from the two samples considering only the grid cells of the reanalysis which are closest to the observations.

Similarly as found by Horton et al. (2012) for the whole globe and Huang et al. (2017) for China, annual air stagnation days are distributed with considerable regional heterogeneity across Europe. The highest stagnation centres are located over southern Europe and northern Africa, where stagnant conditions are met more than 40 % of the days over some locations (Figure 3.1, left). Coastal areas show less stagnation than continental areas, as can be expected due to the land-sea contrast and the overall minor presence of topographic barriers compared to inland locations, which results in increased wind speed and therefore reduced air stagnation. The spatial distribution of air stagnation events resembles that of stagnation days (Figure 3.1, middle), with ~ 50 events per year over large areas in the proximity of the Mediterranean and Black Seas, above 40 events in Scandinavia and considerably fewer events in the British Isles, the North European Plain and the Baltic countries. Stagnation events tend to last longer in areas with more stagnation days (Figure 3.1, right). Their average length reaches 5 days in some areas of Morocco and around 3 days north of the Mediterranean, and decreases to around 2 days or less further north.

As expected, the spatial distribution of the percentage of days that fulfil the Wsp10 condition for air stagnation shows substantial regional heterogeneity (Figure 3.2, middle). This is the HO_ASI component showing the most similar spatial pattern to that of the frequency of air stagnation (Figure 3.1, left), with a correlation coefficient of 0.95, although the occurrence of dry days may be more relevant to explain the north-south gradient in stagnation (Figure 3.2, left). As latitude decreases, so does the occurrence of precipitation and therefore the number of dry days increases. The upper-air wind speed presents considerable spatial homogeneity, fulfilling the stagnation condition in a range between 40 and 60% of the days for most of the study area. These values are considerably low compared to those found for the other two fields over specific regions, in particular for the southern half of the domain. Accordingly, upper-air wind speed may be the main limiting factor in the occurrence of stagnation over some regions of southern Europe, while precipitation and 10 m wind speed would restrict it in Scandinavia and the regions around the North European Plain, respectively. A more detailed regional assessment is presented in the next section.

3.2 Spatiotemporal variability of air stagnation

3.2.1 Regionalization of air stagnation

A regionalization of air stagnation has been made by means of the k-means iterative optimization process. This technique is based on the Voronoi partition (Aurenhammer, 1991) and has been widely used to generate spatial divisions of meteorological and AQ fields (e.g. Bador et al., 2015; Carvalho et al., 2016; Lyapina et al., 2016; Carro-Calvo et al., 2017). It allows the generation of clusters from a multidimensional dataset. In this case, we have applied the k-means clustering technique on the gridded monthly frequency of stagnation days over Europe for 1979–2016 obtained from reanalysis data. The stagnation dataset consists of a matrix filled with the number of stagnant days per month in each grid cell of the reanalysis, considering only the continental areas within the range $33^{\circ}N - 75^{\circ}N$ and $12^{\circ}W - 26.25^{\circ}E$. This covers a region smaller than that shown in Figure 3.1, as we have preferred to limit the analyses to regions with reasonably good coverage of PM_{10} and O_3 observations. The algorithm allows obtaining regions or clusters where air stagnation presents consistent temporal patterns. After some testing, we have set the number of seeds (i.e. initial cluster centres) to 30 and the maximum number of iterations to 300; these choices ensure repeatability and reproducibility of the clustering results. This has resulted in a spatial division of five regions as displayed on Figure 3.3. The choice of the final number of clusters has been made as a compromise between the spatial extension and the representativeness of the regions.

From north to south and from west to east, the clusters roughly cover Scandinavia (SCAN), Northern Europe (NEU), Central Europe (CEU), the South West (SW) and South East (SE) of the domain. In general, these regions seem to be consistent with the spatial distribution of air stagnation frequency shown in Figure 3.1 (left). SW (Iberian Peninsula and northern Africa) and SE (Italy and Balkans) cover a large part of the Mediterranean region, where stagnation is most frequent. NEU is basically made up by the British Isles, Benelux, Denmark and the Baltic countries, the area with the minimum frequency of stagnation. Overall, SCAN corresponds to the geographical location of the

Scandinavian Peninsula, where air stagnation frequency is moderate. This is also the case for CEU, which is mainly located inside continental Europe. Note that some grid cells belonging to NEU (dark blue) and CEU (orange) are farther from their respective centroids than from others with more stagnation. This occurs because most of these cells are located close to the sea, where surface wind speed tends to be high, limiting the occurrence of stagnation compared to the surrounding regions.

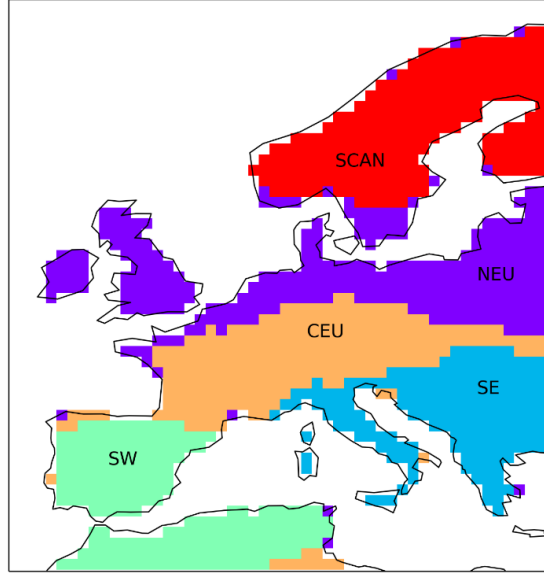


Figure 3.3: Regionalization of the monthly frequency of air stagnation during 1979–2016, as derived from the ERA-Interim reanalysis. Coloured shading identifies the clustered regions, which broadly correspond to Scandinavia (SCAN), Northern Europe (NEU), Central Europe (CEU), South West (SW) and South East (SE).

3.2.2 Temporal variability of air stagnation

Once we have regionalized the area of study, we will first compare the seasonal cycles in each region as obtained separately from the reanalysis and the observations. This will provide further insights into the consistency between the regional features derived from reanalysis and from the embedded observational sites. In addition, we will examine the long-term variability of air stagnation in each region.

Seasonal cycle

Figure 3.4 shows the seasonal cycles of the number of stagnant days for each cluster, considering the observations (red), the reanalysis grid cells closest to observational sites (blue) and the cluster centroids which include all reanalysis grid cells (green) within these regions. The intervals defined by one standard deviation from the mean overlap when only grid cells around the observational sites are considered (red and blue), confirming a reasonably good agreement between reanalysis and observations. The largest discrepancy is found for the SW region in summer, where the differences in the mean values are up to 3 days per month. Moreover, if we consider every reanalysis grid cell within the cluster (green), the number of days with stagnation increases considerably in that region. This result strongly suggests that the 10 observational stations available for SW do not represent the behaviour of air stagnation in this cluster. Many of these stations are located in coastal areas as can be seen in Figure 3.1, which can explain the reduced stagnation when only those locations are considered. The discrepancies when the nearest grid cells in the reanalysis are used (red and blue) may partly occur because such cells cover land and sea areas, but they are also related to the biases reported previously for the three components of HO₂ASI in reanalysis and observations. The rest of clusters seem to include representative enough stations, although the number of sites per region varies substantially, from only 8 in SCAN to 25 in NEU. Due to these limitations in the number and representativeness of the observational sites, the cluster centroid (i.e. the average monthly frequency of stagnant days for all reanalysis grid cells within the region) will be used for the regional analysis of the temporal variability of stagnation in the reminder part of this section. Seasonal and annual series of stagnation frequency will be derived for each region by adding up the monthly frequencies of the corresponding period.

All the reanalysis seasonal cycles (green) are characterized by a common maximum around summer (often in August). Nevertheless, the month with minimum air stagnation is clearly dependent on the region, as it varies from October (SCAN) to June (CEU). The largest amplitude (defined as the difference between the maximum and the minimum) is found for SW and SE, with about 9 and 7 days, while it is below 4 days for the rest of

the clusters. This is due to the strong seasonality of both precipitation and wind in these regions.

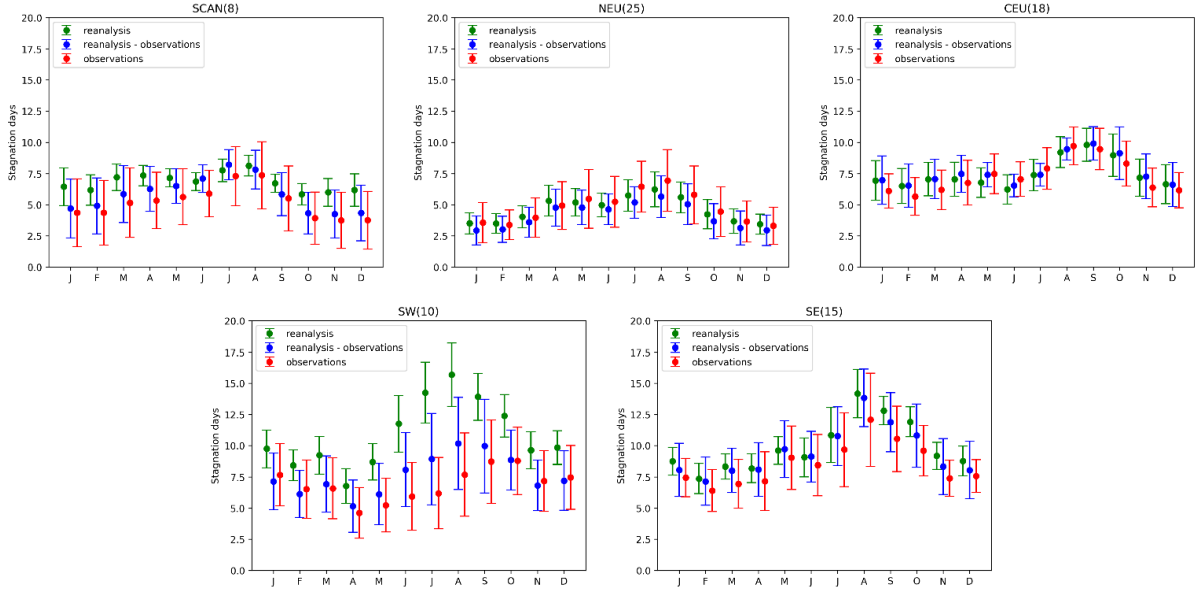


Figure 3.4: Seasonal cycles of the monthly frequency of stagnation days for each of the clusters shown in Figure 3.3. They are calculated from observations (red), reanalysis considering the closest grid cells to observations (blue) and all the grid cells (green) for a given region. The filled circles represent the mean values and the error bars extend from the mean to show the range of the data \pm one standard deviation (SD). Each SD has been calculated for the 38 monthly values of each location during the period of analysis (1979–2016). The numbers in brackets represent the number of stations considered in each cluster.

Interannual variability

The interannual variability differs for the five regions. The monthly standard deviations in Figure 3.4 (green bars) evidence SW and SE as the regions with the largest interannual variability. The seasons when interannual variability reaches its maximum are also different depending on the region: summer for the southern regions (SW and SE) and winter for SCAN.

To better understand the influence of the three components of HO_{ASI} in the interannual variability, we have evaluated which of them controls the temporal patterns of air stagnation over each region. For this purpose, we have computed the correlation coefficients between the regional time series of stagnant days and those resulting from

each component separately. Table 3.1 shows the individual air stagnation component that presents the highest correlation on a seasonal and yearly basis.

Table 3.1: Component whose occurrence of stagnant conditions yields the highest R (in brackets) with the frequency of air stagnation days in each region. All correlations shown in the table are significant at the 95% confidence level (two-tailed t-test). Wsp10: near-surface wind stagnation; Wsp500: upper wind stagnation; DD: dry days.

Region/Period	Spring	Summer	Autumn	Winter	Year
SCAN	Wsp10 (0.86)	Wsp10 (0.66)	DD (0.85)	Wsp10 (0.88)	Wsp10/Wsp500 (0.80)
NEU	DD (0.75)	DD (0.78)	Wsp10 (0.85)	Wsp10 (0.90)	DD (0.77)
CEU	DD (0.84)	Wsp500 (0.81)	Wsp500 (0.88)	DD/Wsp500 (0.83)	DD (0.83)
SW	Wsp500 (0.91)	Wsp500 (0.94)	Wsp500 (0.93)	Wsp500 (0.96)	Wsp500 (0.93)
SE	Wsp500 (0.70)	Wsp500/DD (0.53)	Wsp500 (0.90)	DD (0.75)	Wsp500 (0.70)

The table indicates that no HO_ASI component controls uniformly the interannual variability of stagnant days in Europe, but it depends on the considered latitude. To a large extent, Wsp500 drives the interannual variability of stagnation in southern Europe (SW and SE), while DD is more relevant in central regions (CEU and NEU) and Wsp10 over the northernmost part of Europe (SCAN). The main driver of interannual variability does not seem to be seasonally dependent in the south of the continent, since Wsp500 is selected in all seasons (with $R > 0.90$) for SW and 3 out of 4 seasons in SE. This latter region and CEU share Wsp500 and DD as the main drivers of interannual variability. DD is also the dominant driver in NEU, in particular during spring-summer, while Wsp10 controls the interannual variability during autumn-winter there and during most seasons in SCAN. Note that, while these are the general patterns, in some cases the correlation coefficients are not too different for the three HO_ASI components. As an example, Wsp500 has not been selected as the main driver of interannual variability in any season over SCAN but yields high correlations all year round, which results in this variable being selected (together with Wsp10) as the main driver of variability on an annual basis. We also stress that, with the exception of the southern regions, the main drivers of interannual variability do not necessarily correspond to the major limiting factors to the climatological occurrence of stagnant days (Figure 3.2).

Finally, in order to understand the interannual variability of air stagnation at different time scales, all regions have also been tested for significant periodicities by means of a wavelet analysis (Torrence and Compo, 1998) applied to the time series of monthly air stagnation days. The wavelet power spectra have not revealed significant periodicities, apart from the expected presence of the annual cycle for all regions (Figure A1).

Long-term trends

Linear trends in the annual and seasonal number of air stagnation days have been calculated for the 1979–2016 period by using ordinary least squares regression. The results are summarized in Table 3.2. A large area spanning NEU, CEU and SE has undergone an upward annual trend (statistically significant at the 90% only for the first region), while weak trends are found for SCAN and SW. These trends are seasonally dependent. Over CEU there is a large (although not significant) annual trend of 2.38 days decade⁻¹, with the largest contribution in spring (1.28 days decade⁻¹). In the case of NEU, the annual increase (1.48 days decade⁻¹) is distributed into two seasons with positive trends: autumn (1.21 days decade⁻¹) and spring (0.49 days decade⁻¹). Significantly positive trends are also found for SE in summer (1.71 days decade⁻¹) and SCAN in autumn (1.44 days decade⁻¹). There are some negative trends, in particular for winter, but they are not significant for any region and season.

Table 3.2: Seasonal and annual trends in the frequency of air stagnation (days decade⁻¹) for each region during 1979–2016. Significant trends at the 90% confidence level (t-test) are highlighted in bold.

Region	Spring	Summer	Autumn	Winter	Annual
SCAN	0.53	0.05	1.44	-0.31	0.18
NEU	0.49	-0.10	1.21	-0.15	1.48
CEU	1.28	0.43	0.51	-0.37	2.38
SW	0.32	0.02	-0.95	-0.66	-0.46
SE	-0.26	1.71	-0.09	-0.27	1.37

Horton et al. (2014) reported a significant increase in air stagnation over some areas of the globe throughout the 21st century if greenhouse emissions remain unabated. One of the affected regions would be an area north of the Mediterranean covering most of SE and part of CEU, where we have also found upward trends. This suggests that an increase in stagnation may already have begun in some parts of Europe. According to that study, future increases in stagnation over the Mediterranean will result from more frequent dry days and stagnant 10 m wind occurrences, the first being associated with enhanced mid-tropospheric subsidence. We have also tried to assess the contribution of each individual HO_ASI component to past annual trends by separately examining long-term changes in the occurrence of days when each individual component is below its stagnation threshold (Table 3.3). The contribution to the significant trends in CEU comes from the three HO_ASI components, for which the occurrence of stagnant conditions has also experienced upward annual trends. For NEU there is only a significant rise in the occurrence of stagnant Wsp10. In the case of SE, the significant increase in the number of days with Wsp500 below 13.0 m/s has led to an overall upward trend in stagnation, but this is partially counterbalanced by a substantial downward trend in DD. Similarly, the regions with weak trends (SCAN and SW) show changes of opposite signs in their individual components and such changes tend to cancel out. Summarizing, from the three HO_ASI components, only the occurrence of Wsp500 stagnant conditions has increased over most regions, and CEU and NEU are the only regions with upward trends in the three components. Nevertheless, the diverging results found for the different components and regions do not allow establishing clear conclusions on the drivers of long-term trends in stagnation over the whole area of study.

Table 3.3: Trends in the annual occurrence (days decade⁻¹) of near-surface wind stagnation (Wsp10), upper wind stagnation (Wsp500) and dry days (DD) for each region during the period 1979–2016. Significant trends at the 90% confidence level (t-test) are highlighted in bold.

	SCAN	NEU	CEU	SW	SE
Wsp10	0.08	3.39	2.23	-2.23	-0.33
Wsp500	2.52	2.08	3.34	-0.12	4.82
DD	-2.52	0.88	3.30	0.90	-2.23

3.3 Synoptic patterns leading to stagnation

We have examined the synoptic patterns associated with stagnation in each cluster separately for summer and winter. Only summer and winter are analysed given that they are the seasons with the highest and lowest stagnation, as well as with the highest concentrations of O_3 and PM_{10} over most regions, respectively. Figure 3.5 displays the average Z500 anomalies for the five summers (left) and winters (right) with the largest number of stagnation days in each region. Likewise, SLP anomalies are shown in Figure 3.6. There are at least five summers and winters when the number of stagnant days exceeds the seasonal mean plus one standard deviation for each region, which justifies the choice of the number of cases in each composite.

Different Z500 and SLP anomaly distributions can lead to above average stagnation, although we have identified two main patterns. Firstly, pattern H (high) is characterized by significantly positive anomalies in at least one of these fields over the region. This blocks the westerly flow, decreasing both near-surface and upper-air wind speed; concurrently, precipitation is also reduced within the region. Therefore, the three stagnation components more easily fulfil the air stagnation threshold condition when pattern H occurs. In Figures 3.5 and 3.6, this pattern can be identified in summer (left panels) for all regions with the exception of SW, and in winter for the central and southern regions (CEU, SW and SE). A second pattern denominated L (low) has been found for SCAN and NEU in winter. It consists of significantly negative anomalies of Z500 and SLP located south of the regions, together with significantly positive anomalies of Z500 over Greenland. This may displace the position of the Atlantic jet stream and consequently the storm tracks to the south, and, accordingly, yield an increase in stagnation over the north of the continent.

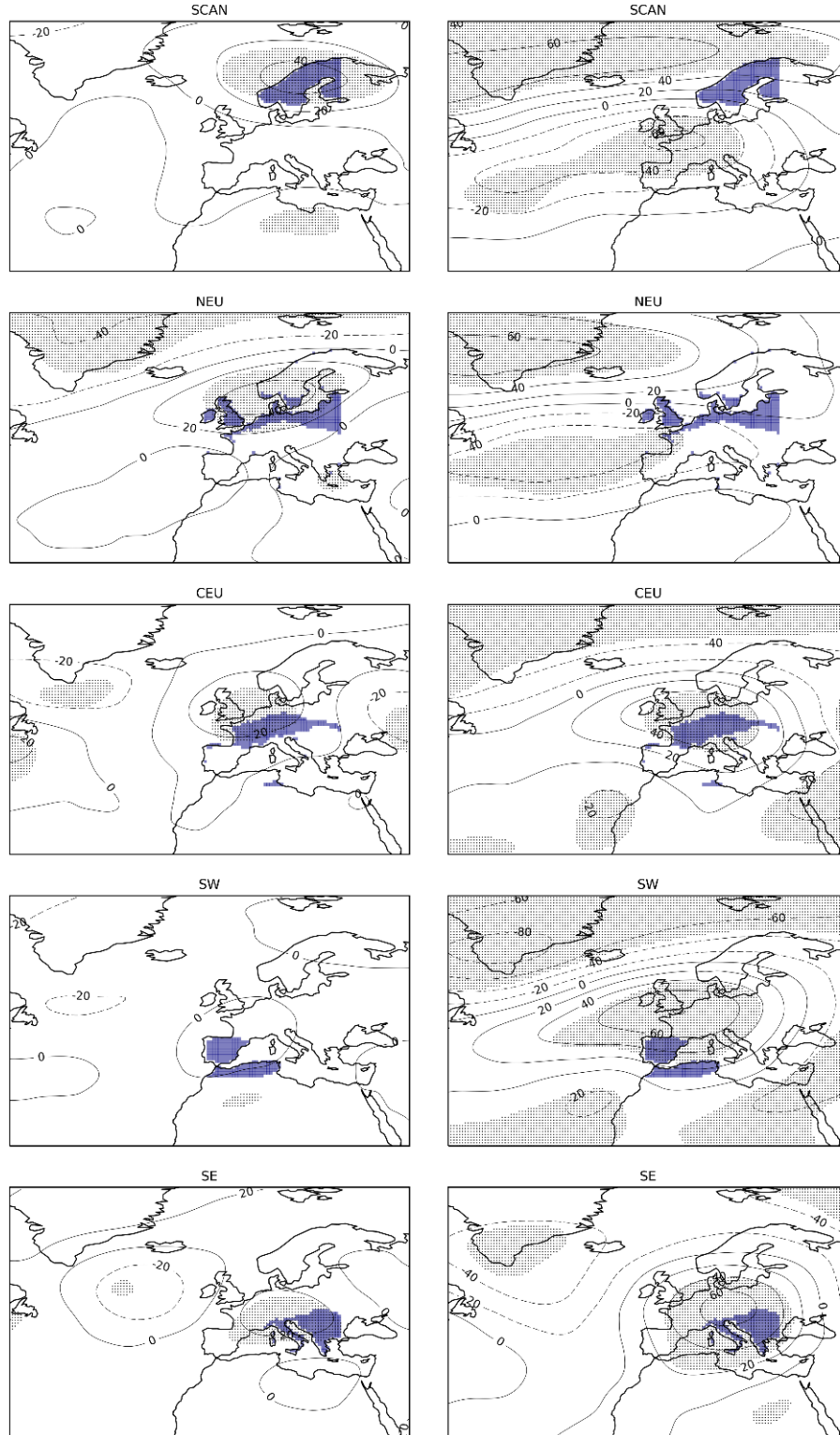


Figure 3.5: Composite anomalies of Z500 (m; lines) for the 5 summers (left) and winters (right) with the largest number of stagnation days in each region. The regions, from top to bottom, are SCAN, NEU, CEU, SW and SE. Blue shading depicts the location of the region and stippling the areas where anomalies are significant at the 95% confidence level. Anomalies have been calculated with respect to the seasonal climatology during the 1979–2016 period.

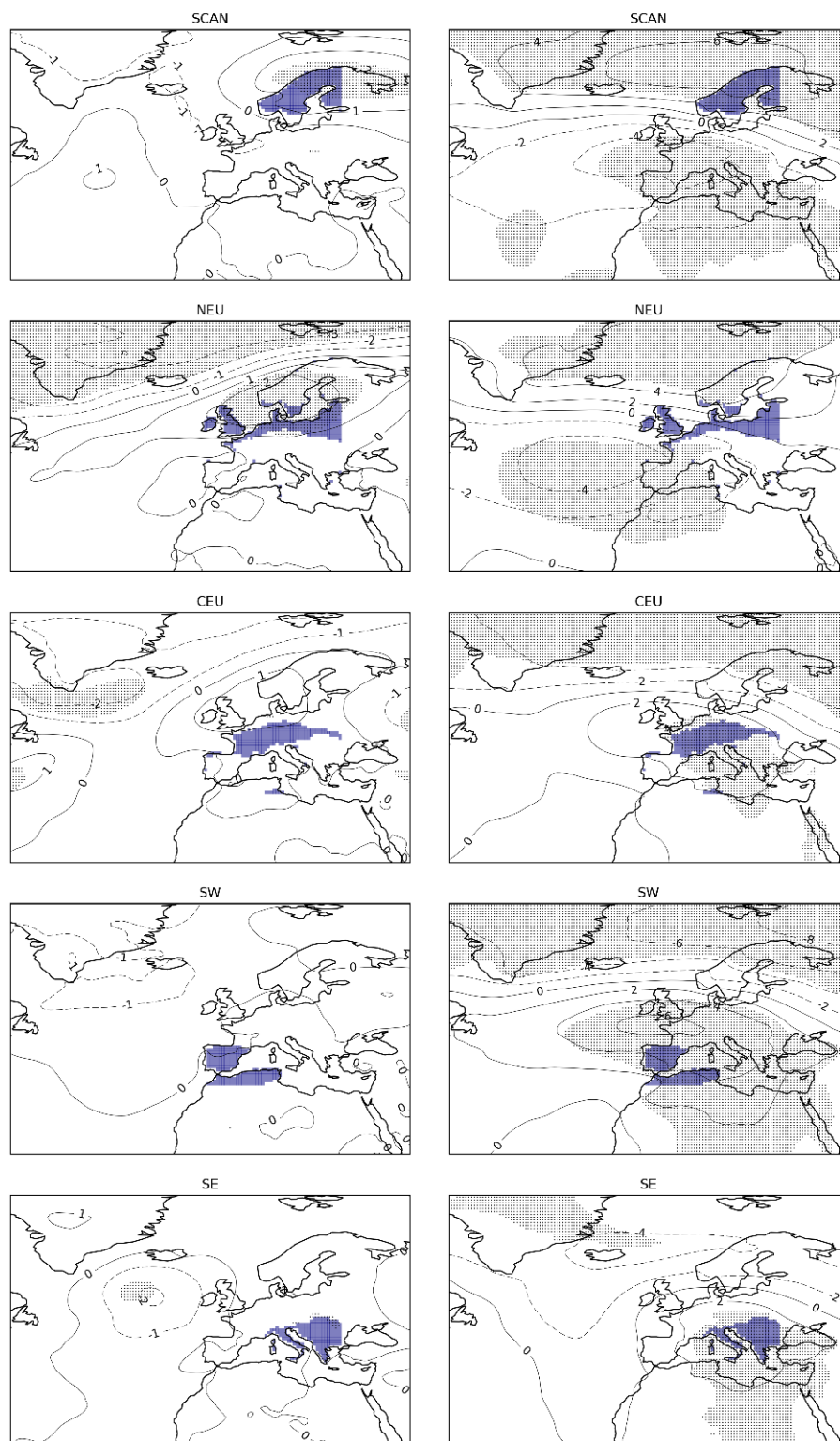


Figure 3.6: As Figure 3.5 but for SLP, represented by line contours at 1 hPa intervals in summer and 2 hPa in winter.

The latitudinal position of the extratropical jet has been studied in more depth to better explain the effects of pattern L associated with stagnation. To do so, we have catalogued each day by using the daily jet latitudinal index of Woollings et al. (2010) applied to NCEP/NCAR reanalysis data with a spatial resolution of 2.5° . The algorithm zonally averages the low-pass filtered, lower-tropospheric (925–700 hPa) daily mean zonal wind in the longitudes ranging from 0° to 60° W. The latitude where the zonal wind reaches its maximum is assigned to one of the latitudinal ranges corresponding to the modal positions of the jet over the Atlantic during winter: southern (15° – 44° N), central (44° – 53° N) and northern (53° – 75° N). Note that the reanalysis resolution is sufficient taking into account the large area considered to identify the position of the jet. Following this, we have checked that during the five winters with maximum stagnation over SCAN / NEU, the number of days with northern jet locations (53° – 75° N) correspond to the 24th / 30th percentile of their winter climatology while the number of days with the jet in lower latitudes (15° – 44° N) correspond to the 69th / 71st percentile, confirming that the enhanced stagnation over the north of the continent associated with pattern L results from the displacement of the position of the Atlantic jet stream.

Finally, we have not found any clear synoptic pattern associated with maximum stagnation over SW in summer. The Z500 anomaly maps for the five summers with most air stagnation in this region exhibit completely different patterns (i.e. anomalies are not spatially coincident), resulting in no clear pattern when the Z500 field is averaged for those summers.

3.4 Impact of stagnation on air quality

We have assessed the impact of air stagnation as measured by HO₂ASI on AQ, focusing on winter daily average PM_{10} and summer $MDA8$ O_3 . As the period with good data availability is different for both pollutants, we have evaluated PM_{10} from December 2002 to February 2011 and O_3 from 1998 to 2012. Only stations with at least 75% of the winter data available for the period of analyses have been used for PM_{10} , selecting a total of 535 sites. Considering the types of measurement sites, the selected locations

can be classified as follows: 68.6% are background, 23.0% traffic and 8.4% industrial sites. For the first exploratory analyses shown in Figure 3.7, the PM_{10} station data and the O_3 grid cells have been associated with the closest air stagnation grid cells at the nominal resolution of the reanalysis. The figure displays the difference between the seasonal concentrations of winter PM_{10} (left) and summer O_3 (right) for days with and without stagnation. These anomalies are only shown when they are significant at the 95% confidence level (two-tailed t-test). As expected, there are widespread positive anomalies across the continent for both pollutants, although their magnitude varies depending on the region.

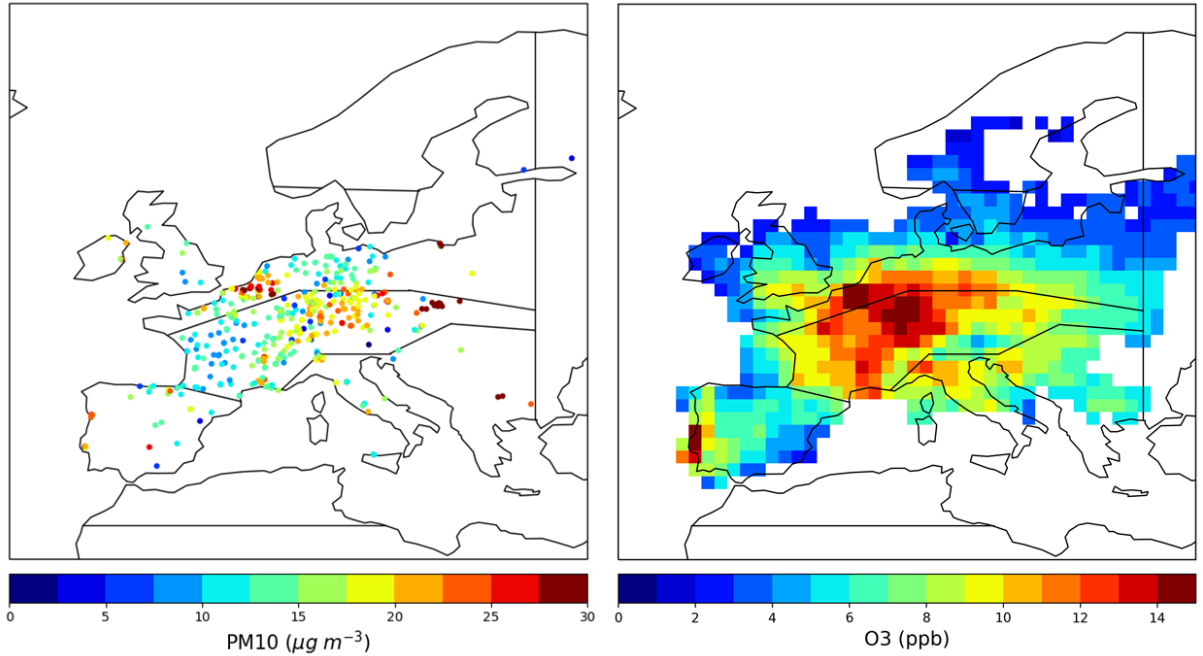


Figure 3.7: Composites of winter PM_{10} ($\mu g m^{-3}$, left) and summer MDA8 O_3 (ppb, right) concentration anomalies on days with stagnation, with respect to the days without stagnation during the same season. PM_{10} data have been evaluated for Dec 2002 – Feb 2011 and O_3 for 1998–2012. Anomalies are only shown when they are statistically significant at the 95% confidence level (determined through a two-tailed t-test). The boundaries on the maps roughly correspond to those of the five clusters: SCAN, NEU, CEU, SW and SE.

In the following, we will present some additional analyses to better understand the overall impact on the regions defined in Figure 3.3. In these analyses, all grid cells within the region are considered for O_3 and only the background sites for PM_{10} , in order

to avoid any potential biases in regions with a high proportion of traffic sites. It is known that the O_3 gridded dataset has some inhomogeneities around the Balkans before 2004 (Carro-Calvo et al., 2017); therefore, O_3 data within SE have only been considered since that year. The average anomalies (absolute values and percentages) of the pollutant concentrations on stagnant vs. non-stagnant days are summarized for each region in Table 3.4.

Table 3.4: Average concentration anomalies for winter PM_{10} and summer $MDA8 O_3$ in each region, defined as the difference in the seasonal concentrations considering days with and without air stagnation. Absolute anomalies are reported in $\mu g m^{-3}$ for PM_{10} and ppb for O_3 . Relative anomalies (%) have been calculated as the ratio between the absolute anomalies and the seasonal means. The numbers in parentheses represent the number of background stations / grid cells considered for PM_{10} / O_3 . No PM_{10} results are reported for SCAN due to the lack of observations in that region.

		SCAN	NEU	CEU	SW	SE
Winter PM_{10}	Absolute ($\mu g m^{-3}$)	– (0)	16.3 (88)	16.0 (232)	10.3 (9)	16.1 (11)
	Relative (%)	–	58	56	45	31
Summer O_3	Absolute (ppb)	1.5 (149)	6.1 (177)	10.3 (132)	6.0 (103)	6.9 (100)
	Relative (%)	5	16	23	13	14

We first focus on the impact of air stagnation on winter PM_{10} (left panel of Figure 3.7 and Table 3.4). The strongest effect is found for NEU and CEU. On average, PM_{10} concentrations are $16 \mu g m^{-3}$ higher on stagnant than on non-stagnant days in these clusters, which corresponds to more than half (58 and 56%) of the seasonal mean concentrations. The relative anomalies for the southern clusters (SW and SE) are above 30%, but these results should be treated with care due to the low number of sites. The impact over SCAN has not been considered due to the lack of PM_{10} data in this region.

Summer average O_3 anomalies (right panel of Figure 3.7 and Table 3.4) are around 10 ppb ($\sim 20 \mu g m^{-3}$) in CEU and above 5 ppb for three of the other four regions (NEU, SW and SE). These anomalies correspond to at least 13 % of the summer mean mixing ratios in each region (up to 23% in CEU). Such values are of the same order of magnitude as those reported by Ordóñez et al. (2017) for O_3 in different locations of Europe under the influence of high-latitude blocks and subtropical ridges. However, the ozone anomalies

over SCAN on stagnant days are relatively small (5%) and lower than those found by that study under the influence of European blocks. The main reason for the relatively low anomalies of O_3 compared to those of PM_{10} during stagnant days most probably lies in the longer lifetime of the former, which implies a substantial contribution of transport processes and background concentrations to the atmospheric levels of this pollutant. It is also known that O_3 mixing ratios are enhanced over some regions of northern Europe following the advection of southern air masses (Carro-Calvo et al., 2017), which seems to be consistent with the moderate impact of stagnation found for SCAN and, to a lesser extent, NEU, in comparison to CEU. This will be examined in Chapter 6. In addition, a number of studies have attributed large-scale downward transport of ozone-rich air masses to elevated summer ozone in the lower troposphere over the Mediterranean (e.g. Velchev et al., 2011; Doche et al., 2014). This could be relevant for the SW and SE regions, but HO_ASI does not implicitly include information on subsidence.

Taking these considerations into account, it is expected that the frequency distributions of both pollutants will also be affected by air stagnation. Figure 3.8 displays the probability density function (PDF) of daily PM_{10} (left) and O_3 (right) for the region most influenced by stagnation, i.e. CEU, considering all seasonal data (grey bars) as well as days with stagnation (red line). Both PDFs are displaced to the right on days with stagnation. There exists a reduction of the lower tails for both pollutants as well as an increase in the occurrence of daily PM_{10} concentrations above $30 \mu g m^{-3}$ and MDA8 O_3 mixing ratios above 45 ppb. This enlargement of the upper tails by air stagnation has clear implications for the number of exceedances of the $50 \mu g m^{-3}$ and $120 \mu g m^{-3}$ (~ 60 ppb) AQ limit values for these pollutants (indicated by vertical blue lines on both panels). Similar results, albeit with a more moderate impact, have been found for most of the other regions (see Annex Figures A2 and A3).

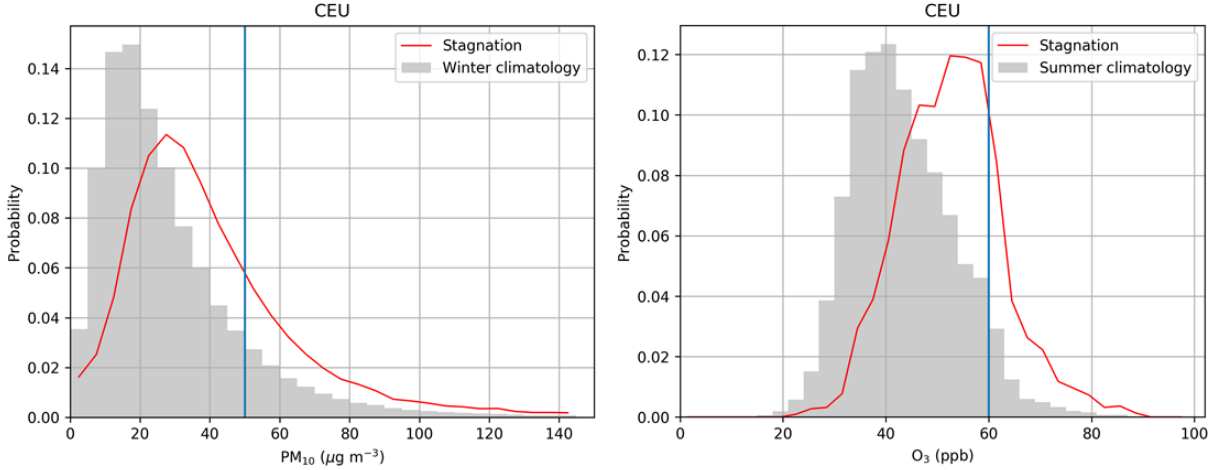


Figure 3.8: Probability density functions (PDFs) of daily winter background PM_{10} concentrations ($\mu g m^{-3}$, left) and summer MDA8 ozone mixing ratios (ppb, right) for CEU. Grey bars correspond to the histogram considering all seasonal data. Red lines represent the distribution considering only days with stagnation. These PDFs are significantly different at the 95% confidence level for both pollutants (determined through a two-sample Kolmogorov-Smirnov test; see e.g. Smirnov, 1939; Young, 1977; Wilks, 2011). Each bin covers a range of 5 $\mu g m^{-3}$ for PM_{10} and 3 ppb for O_3 . The vertical lines at 50 $\mu g m^{-3}$ and 60 ppb represent the AQ targets for PM_{10} averaged over 24 h and for MDA8 O_3 , respectively.

We have also examined the build-up of the pollutant concentrations during the most widespread stagnation events found in each region and season. To simplify the analyses, we have focused on the first five days of the ten episodes with the largest areal extent fulfilling stagnation conditions within each region and season (winter 2002–2011 and summer 1998–2012). We consider all background PM_{10} sites and O_3 grid cells within the region regardless of whether they are under stagnant conditions on those days. For illustration purposes, Figure 3.9 shows composites of the evolution of winter PM_{10} (top) and summer O_3 (bottom) during those episodes for CEU (left) and NEU (right). The first two boxes in each panel represent the distribution of the pollutant concentrations during the two days before the beginning of the episode (day 0-2, day 0-1) and the remaining boxes correspond to the first five days of the event (day 0, day 0+1, day 0+2, day 0+3, day 0+4). As the extension of the stagnant area increases day after day for some of the ten episodes considered and decreases for others, this may result in large spread in the data and even decreases in the median concentrations during the life cycles of these episodes.

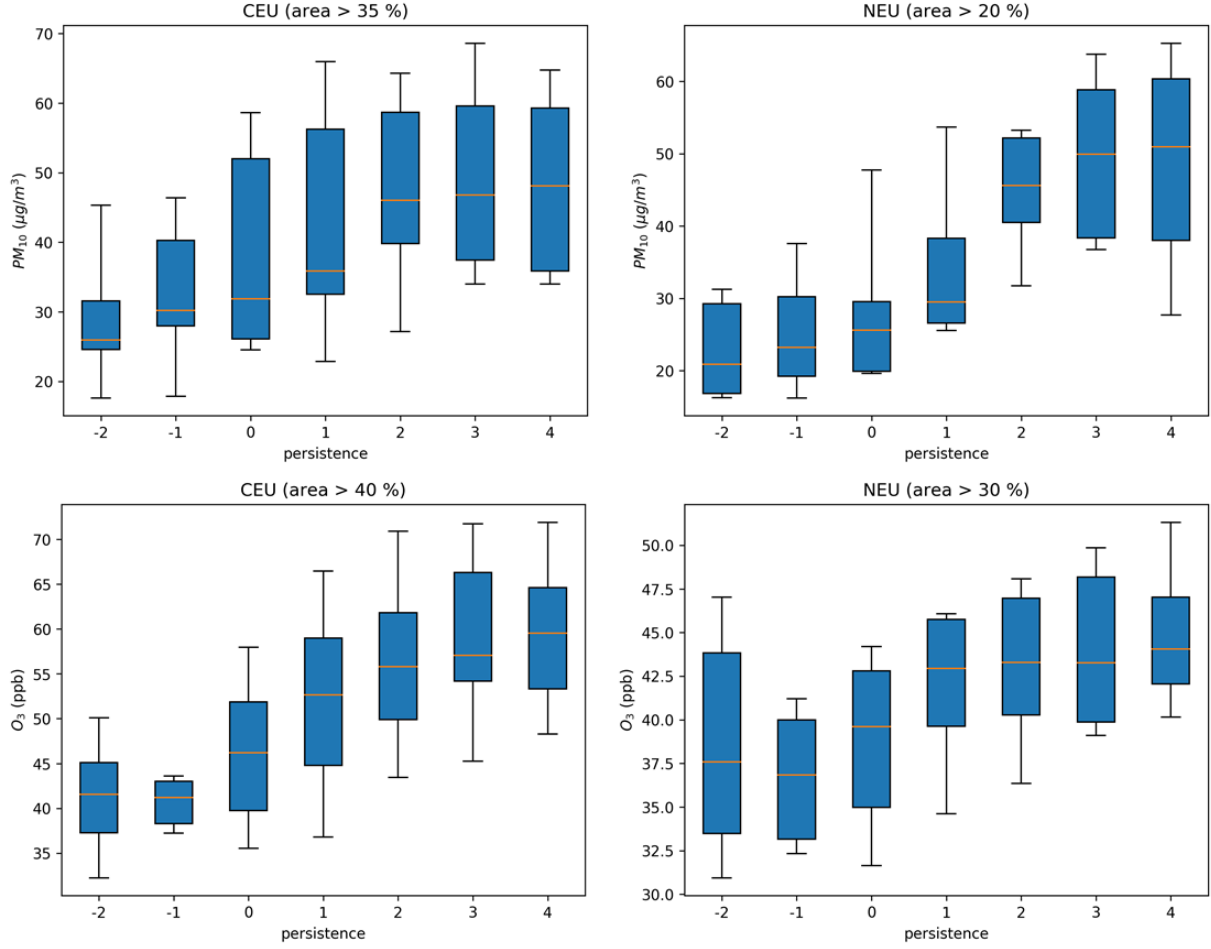


Figure 3.9: Average evolution of air pollutant concentrations during the most widespread stagnation events over CEU (left) and NEU (right). Results are separately shown for daily background PM_{10} (top) and $MDA8$ O_3 (bottom) during the 10 stagnation events with the largest area coverage in winter 2002–2011 and summer 1998–2012, respectively. The ticks on the x-axes represent the last two days before the event (-2, -1), the first day of the event (0) and the four following days (1, 2, 3, 4). The boxes extend from the lower (Q1) to the upper (Q3) quartile values of the data, with a horizontal line indicating the position of the median concentrations. The whiskers extend from the boxes to show the range of the data between the 10th and 90th percentiles.

The PM_{10} build-up during the winter episodes (Figure 3.9, top) is particularly pronounced for NEU, even though only slightly above 20% of the region is under stagnant conditions during those events, compared to above 35% for CEU. The median of the PM_{10} concentrations increases by nearly $20 \mu g m^{-3}$ from day 0-2 to day 0+3 in CEU, while there is a stronger build-up of $\sim 20 \mu g m^{-3}$ during the first three days (day 0 to day 0+2) in NEU. Nevertheless, the upper quartiles (top of the boxes) considerably exceed

50 $\mu\text{g m}^{-3}$ during the five days of the episodes in CEU, indicating that at least 25% of the background sites in the region breach the AQ target for this pollutant. This also occurs in NEU, but only from the third day of the episodes (day 0+2 to day 0+4). In the case of summer O_3 (Figure 3.9, bottom), the percentage of the region under stagnant conditions during the selected events is above 40 % in CEU and 30 % in NEU. There is a strong increase (> 15 ppb) in the median O_3 concentrations over CEU from day 0-1 to day 0+4 and the upper quartiles, i.e. 25% of the sites, exceed the 60 ppb threshold from day 0+2 to day 0+4. The build-up of O_3 over NEU is not as strong, with a steady increase in the median concentrations of ~ 6 ppb only from day 0-1 to day 0+1. In both cases there is also a remarkable rise in the low percentiles (lower whiskers) throughout the episodes, indicating a widespread impact of air stagnation on the sites with the lowest O_3 concentrations within these two regions. Overall, similar life cycles, although with a more moderate impact, have been found for PM_{10} and O_3 during stagnation episodes in the other regions (Figures A4 and A5). Consequently, persistent air stagnation conditions facilitate the build-up of both pollutants in the area of study.

Finally, we have investigated whether the frequency of occurrence of air stagnation can determine the interannual variability of summer O_3 extremes (defined as the 95th percentiles of the seasonal concentrations), in a similar way as done by Schnell and Prather (2017) for eastern US. The analysis has been conducted only for the regions with good spatiotemporal coverage of O_3 (i.e. all regions except for SE). We have not considered PM_{10} due to the relatively short time series (9 winters) available for this pollutant as compared with ozone (15 summers). The time series have been detrended by subtracting the year-to-year change expected from a linear trend (using ordinary least squares regression). The coefficients of correlation are 0.54 for SCAN, 0.72 for NEU, 0.81 for CEU and 0.58 for SW. Overall, the link between the interannual variability of air stagnation and O_3 extremes in Europe is similar to that reported by Schnell and Prather (2017) for a larger region in the US during the extended summer season, with R values of 0.79. This is particularly the case for O_3 in CEU and NEU. The corresponding time series are shown in Figure 3.10. It is worthwhile to mention the high percentage of stagnation days in the summers with the highest ozone levels: summer 2003 for CEU and summer 2006 in NEU.

These two summers were indeed periods of exceptionally hot weather and extreme air pollution over different parts of Europe, as reported by other studies (e.g. Schnell et al., 2014; Carro-Calvo et al., 2017, and references therein). Therefore, our results demonstrate that a simple linear model on the frequency of stagnant days can explain a considerable fraction of the interannual variability of summer ozone extremes, and suggest that air stagnation may also be a good indicator of some meteorological extremes such as heat-waves. This is in line with previous studies that have highlighted the joint association of high ozone and temperature with stagnation. While it has been consistently observed that summer ozone correlates with temperature, this is not only driven by the impact of temperature on photochemical ozone production (e.g. through the thermal decomposition of the reservoir species PAN and the increase in emissions of biogenic isoprene at high temperatures), as it also reflects the association of high temperatures with air mass origin and regional stagnation (Jacob et al., 1993; Jacob and Winner, 2009, and references therein). This subject will be analysed in more detail in Chapter 6.

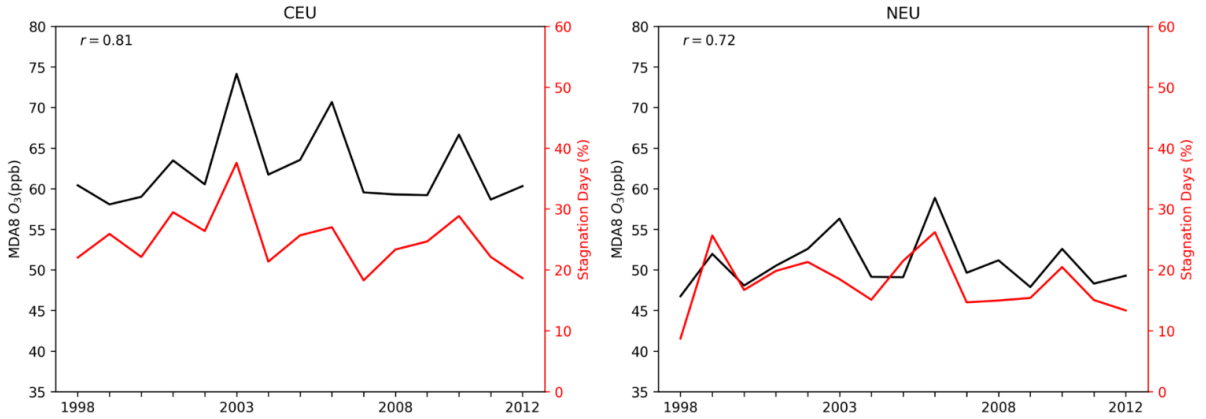


Figure 3.10: Summer time series (1998–2012) of the 95th percentiles of detrended *MDA8 O₃* (ppb, black line and left y-axis) and the detrended frequency of stagnation days (%), for CEU (left) and NEU (right). The upper left corner of each panel shows the correlation coefficient *R* between both series.

3.5 Main findings and discussion

This chapter presents the first comparison of stagnation as derived both from observations and reanalysis that can be found in the literature. Our findings indicate a reasonably good agreement between reanalysis and observations in the representation of the frequency and variability of stagnation days and events at the regional scale. Overall, both the occurrence of dry days and stagnant upper air wind speed are consistent between reanalysis and observations, while the 10 m wind speed is responsible for the main differences due to its dependence on local factors, including the orography and surface roughness, as well as the insufficient horizontal resolution and imperfect parameterizations of the reanalysis.

There is considerable spatial heterogeneity across Europe, with more stagnation in the south than in the north. We have identified five regions with different behaviour: Scandinavia (SCAN), Northern Europe (NEU), Central Europe (CEU), South West (SW) and South East (SE). The temporal variability, the associated large-scale circulation patterns and the impact on the atmospheric concentrations of two pollutants (PM_{10} and O_3) have then been studied separately for each region. Table 3.5 summarizes this information for winter and summer.

Table 3.5: Characteristic features of air stagnation for each cluster in winter / summer.

Clusters	Interannual Variability	Dominant variable	Synoptic Pattern	Winter PM_{10} / summer O_3
SCAN	** / *	Wsp10/Wsp10	L/H	No data / =
NEU	* / **	Wsp10/DD	L / H	+++ / +
CEU	** / **	DD & Wsp500 / Wsp500	H / H	+++ / ++
SW	*** / ****	Wsp500 / Wsp500	H / U	+++ / +
SE	** / ***	DD / Wsp500 & DD	H / H	+++ / +

*The names of the clusters, as displayed on Figure 3.3, are given in the first column. The second column summarizes the interannual variability, according to the seasonal cycles from Figure 3.4: * indicates that the seasonal averages of the monthly standard deviation for the number of stagnation days are lower than 1 day, ** between 1 and 1.5 days, *** between 1.5 and 2, and **** higher than 2 days. Column 3 indicates the meteorological component from HO_ASI which better explains the interannual variability of the number of stagnant days within the region, according to Table 3.1. Column 4 summarizes the synoptic patterns associated with the 5 winters/summers with maximum stagnation, following Figure 3.5: H (high, positive Z500 anomalies in the region); L (low, negative Z500 anomalies south of the region), and U (undetermined). The last column indicates the impact on the winter PM_{10} /summer O_3 concentrations (following Table 3.4): = for concentration anomalies under 10%; + between 10 and 20%; ++ between 20 and 30%; +++ over 30%.*

The regions located at higher latitudes, SCAN and NEU, present the lowest stagnation frequency. Ample precipitation and high 10 m winds are respectively the limiting factors to the occurrence of stagnation in these regions. The role of 10 m winds is particularly relevant in the case of NEU as it includes the regions around the North and Baltic Seas, where near-surface westerlies prevail. Both regions share some common features such as small amplitude of the seasonal cycle and low interannual variability. The synoptic patterns that maximize stagnation are also common to both regions. In summer, they are characterized by positive anomalies of Z500 over the region (labelled as pattern H). Unlike other regions, the winter synoptic patterns ruling stagnation display positive Z500 anomalies over Greenland and a southward displacement of the jet (pattern L). Air stagnation is associated with strong positive anomalies of winter PM_{10} in NEU and moderate summer O_3 anomalies in both regions, standing out as a relatively good indicator for interannual variability of extreme ozone events, with correlations of 0.54 and 0.72 for SCAN and NEU, respectively.

The highest frequency of stagnation occurs over the Mediterranean area, where the seasonal cycle is characterized by a maximum in summer and high interannual variability. This area is comprised of two distinct regions (SW and SE), for which upper wind speed is the major limiting factor to the occurrence of stagnation. This component also drives part of the interannual variability of stagnation in both regions, in particular over SW. Despite these similarities, the frequency of dry days is lower in SE and therefore considerably contributes to the interannual variability of stagnation in this region. On seasonal scales, maximum stagnation in these regions is often associated with pattern H, although no clear synoptic pattern has been found for SW in summer. The impact on AQ is noteworthy but somewhat weaker than in other European regions. Nevertheless, some caution is required due to the limited number of sites for both regions.

Finally, CEU is a region that covers a large part of continental Europe and presents moderate stagnation. The interannual variability is relatively small, as does the seasonal cycle, with a slight rise in autumn. CEU is a transition region between the south and the north. As such, different components (namely, upper air winds and dry days) dominate

the interannual variability of stagnation. This is also the region with the largest annual trends ($+2.38$ days decade⁻¹) and similar upward values are separately found for the three HO_ASI components. CEU also stands out as the region where stagnation has the largest impact on AQ, with relative anomalies above 20% for summer O_3 and 50% for winter PM_{10} . Furthermore, exceedances of AQ targets for these two pollutants are more likely to occur on stagnant days. In particular, the stronger impact on the first pollutant in CEU compared to the remaining clusters might be related to the fact that other factors are known to contribute to elevated summer ozone in those regions, namely southerly advection in northern Europe (Carro-Calvo et al., 2017) and large scale subsidence in the proximity of the Mediterranean (e.g. Velchev et al., 2011; Doche et al., 2014; Zanis et al., 2014). A better understanding of these dynamical processes would be useful to develop more sophisticated meteorological indices for those regions. In spite of that, our analyses have proved that persistent, widespread stagnation events favour the build-up of both O_3 and PM_{10} over most of the continent.

In short, our results demonstrate the usefulness of a simple ASI to characterize the spatiotemporal variability of air stagnation and represent the conditions favourable for the accumulation of PM and O_3 over the Euro-Mediterranean area. We have been able to identify regions where stagnation behaves differently and consequently so do features such as the temporal variability, the associated large-scale circulation patterns and the impact on AQ. These findings confirm that air stagnation triggers elevated concentrations of air pollutants over most regions of Europe, including the occurrence of AQ episodes.

4 Assessing the value of air stagnation indices to reproduce PM_{10} variability in Europe

In the previous chapter, we have shown the impact of stagnation on winter PM_{10} using HO_ASI. However, as indicated in the Introduction, different ASIs have been proposed in recent years to measure the atmospheric diffusion conditions. Accordingly, this chapter undertakes a comparative analysis of three ASIs and explores their ability to capture the conditions conducive to elevated PM_{10} in Europe for the winter and summer months of 2000–2012. The dependence of the PM_{10} concentrations on the ASI components is also evaluated by using correlations and generalized additive models. The results of this chapter can be found in Garrido-Perez et al. (2021).

4.1 Air stagnation indices

We have used these ASIs: HO_ASI (Horton et al., 2012, 2014), WA_ASI (Wang et al., 2016, 2018) and HU_ASI (Huang et al., 2018). The three indices are based on predefined thresholds of daily meteorological fields and are binary, i.e. they can only take two values (stagnant/non-stagnant). As indicated in the previous chapter, HO_ASI considers that a location is stagnant on a given day if three conditions are simultaneously met: daily average Wsp10 below 3.2 m/s, daily average Wsp500 below 13.0 m/s and Prec below 1 mm (i.e. dry day).

WA_ASI requires that Prec is below 1 mm and that BLH is below a threshold that depends on the Wsp10 field and the season, following Equations 4.1 to 4.4:

$$\text{Spring :} \quad BLH = 3.57 * 10^3 * \exp(-3.35 * W_{sp10}) + 0.352 \quad (4.1)$$

$$\text{Summer :} \quad BLH = 7.66 * 10 * \exp(-2.12 * W_{sp10}) + 0.443 \quad (4.2)$$

$$\text{Autumn :} \quad BLH = 1.88 * 10^4 * \exp(-5.15 * W_{sp10}) + 0.440 \quad (4.3)$$

$$\text{Winter :} \quad BLH = 0.759 * \exp(-0.6 * W_{sp10}) + 0.264 \quad (4.4)$$

These equations have been derived by fitting Wps10 and BLH on dry days with normalized PM concentrations close to 100% at sites distributed throughout China, the US and Europe (for more detail see Wang et al. (2018)).

HU_ASI considers a location as stagnant if three conditions are met on a given day. First, Prec must be below 1 mm. Second, daily maximum ventilation (Vent), defined as the integral of the horizontal wind speed within the boundary layer (see Equation 4.5), must be below 6000 m² s⁻¹.

$$Vent = \int_0^{BLH} W_{sp}(z) dz \quad (4.5)$$

where

z is the height above the surface

$W_{sp}(z)$ is the wind speed at a height of z .

Finally, this index uses two thermodynamic parameters, CAPE and CIN, to provide additional information on the strength of atmospheric convection in some areas of China. According to Huang et al. (2018), stagnation can only occur if the value of CAPE is below that of CIN. We have adapted that condition to Europe, following the work by Taszarek et al. (2018). Consequently, here the occurrence of stagnation excludes potential thunderstorm days (PTDs), i.e. those with $\text{CAPE} > 100 \text{ J/kg}$ and $\text{CIN} > -50 \text{ J/kg}$. Summarising, our adaptation of the index by Huang et al. (2018) for Europe considers that there is stagnation if there is a dry day ($\text{Prec} < 1 \text{ mm}$), $\text{Vent} < 6000 \text{ m}^2 \text{ s}^{-1}$ and there is no potential thunderstorm day (non-PTD).

4.2 Comparison of ASIs

We have first compared the spatiotemporal variability of air stagnation frequency over Europe for the three different ASIs. Figure 4.1 shows the annual average percentage of air stagnation days (%) for each of these indices. The spatial patterns share some common features, with considerable spatial heterogeneity across Europe. As already described for HO_ASI in Chapter 3, the highest stagnation frequency occurs over the Mediterranean area, whereas the lowest stagnation centres are located at higher latitudes, specifically over the British Isles, northwestern France, Benelux, northern Germany, Denmark, Poland and the Baltic states. These spatial patterns resemble those of the average number of events (defined as the sequence of one or more consecutive stagnation days) per year and the average event duration (Figure 4.2). However, the absolute values and the seasonal cycles differ among the ASIs. HO_ASI is characterized by a winter minimum and a summer maximum, whereas the opposite occurs for HU_ASI, as seen in Figure 4.3 and also reported by Huang et al. (2018) for China. On the other hand, WA_ASI presents the smallest seasonal dependence.

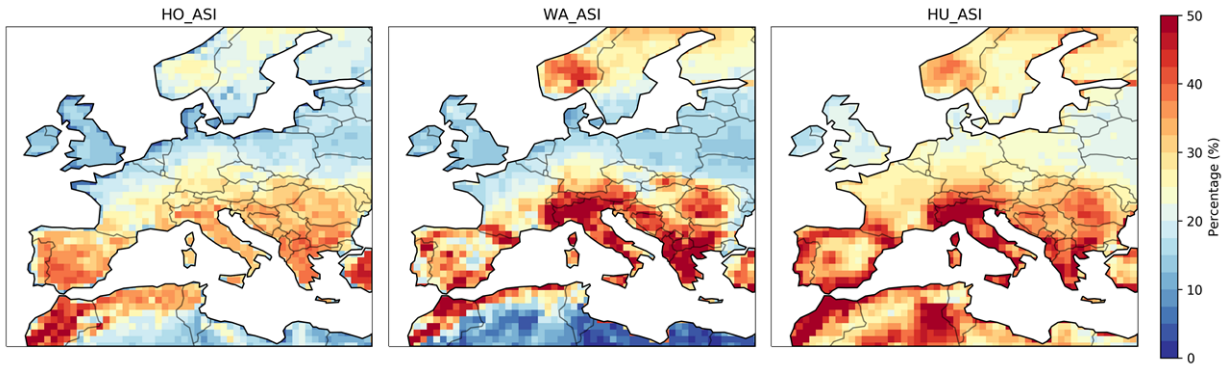


Figure 4.1: Annual average percentage of stagnation days (%) during the period 1981–2010 for HO_ASI (left), WA_ASI (middle) and HU_ASI (right).

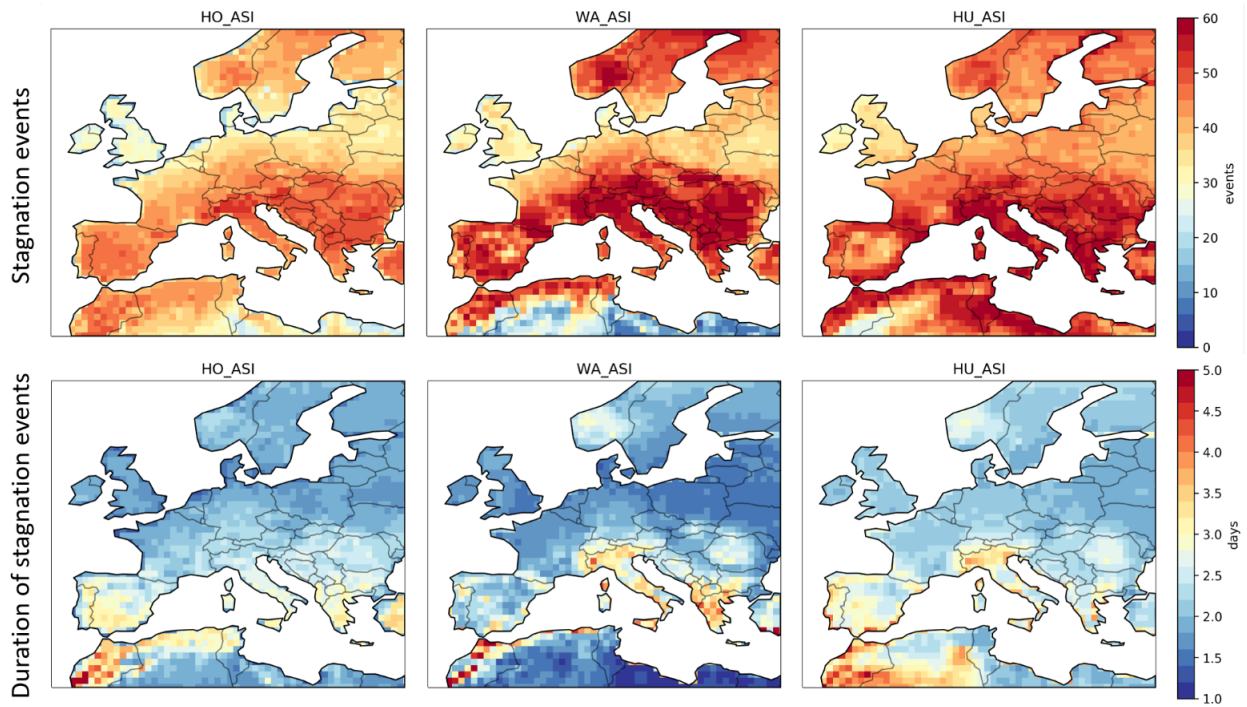


Figure 4.2: Average number of air stagnation events per year (top) and mean event duration (bottom; number of days) during the period 1981–2010 for HO_ASI (left), WA_ASI (middle) and HU_ASI (right).

4. Assessing the value of ASIs to reproduce particulate matter variability

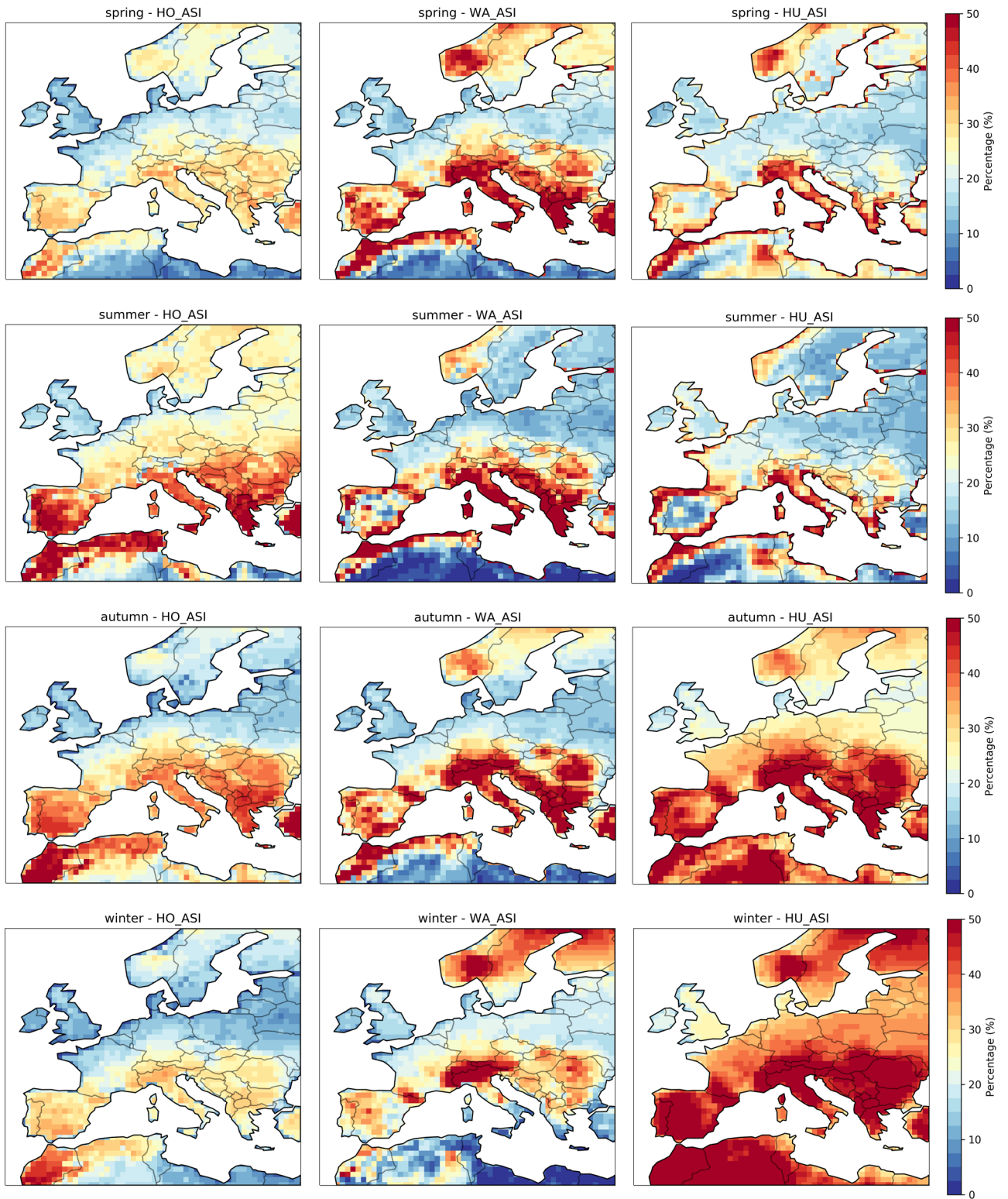


Figure 4.3: As Figure 4.1 but for each season.

The differences in the temporal variability of stagnation among ASIs must be attributable to the distinct conditions used in the definition of each index. Therefore, we have examined how often stagnation conditions are met separately for each component (Figure 4.4), in a similar way as done in Chapter 3 for HO_ASI (Figure 3.2). Note that although panels a), d) and g) of Figure 4.4 represent almost the same as Figure 3.2, they are repeated here for comparison purposes. First, the occurrence of dry days (top panels) exceeds 50% for most of the study area and increases gradually as latitude decreases to around 80% at some locations of southern Europe, explaining to a certain extent the north-south gradient in stagnation. The use of this precipitation condition as an indicator of the washout of pollutants is common to all indices, but the approaches to characterize the atmospheric horizontal dispersion capability and vertical mixing are different. HO_ASI uses two wind speed conditions at 10 m (Figure 4.4d) and 500 hPa (Figure 4.4g). The former condition presents considerable regional heterogeneity, with spatial patterns that closely resemble those of the frequency of stagnation over most regions, indicating the relevance of this meteorological variable. However, as noted in Chapter 3, the 500 hPa wind speed might be the limiting factor in the occurrence of stagnation over large parts of Europe since it fulfils the stagnation conditions less frequently than the rest of components over most regions. Anyway, both wind speed conditions are more/less likely to be met in summer/winter due to the weak/strong climatological winds in these seasons (Figures 4.5 and 4.6), explaining the seasonality of this ASI. Note also that Wsp500 is a rather smooth field because it is hardly influenced by processes in the boundary layer. As a consequence, the frequency of stagnation is more spatially uniform for HO_ASI than for the other two indices over some regions such as the Iberian Peninsula and Scandinavia (Figure 4.1).

As mentioned above, the seasonal cycle is reversed in the case of HU_ASI compared to HO_ASI. The reason lies in the dependence of Vent on BLH (see Equation 4.5), which maximizes in summer and minimizes in winter (Figure 4.7). This implies that the Vent condition, whose spatial pattern (Figure 4.4f) resembles to some extent that of the 10 m wind speed condition of HO_ASI (Figure 4.4d), is more likely to be met in winter than in summer (Figure 4.8), leading to a seasonal cycle of HU_ASI characterized by a maximum in winter and a minimum in summer. Note that the occurrence of PTDs does not limit

that of stagnation since they are highly unusual (Figure 4.4h). This condition is mainly relevant over some regions in summer. On the other hand, WA_ASI is defined based on a Wsp10–BLH condition which shows similar spatial patterns to those of the Vent condition and, to a lesser extent, those of Wsp10 (Figure 4.4d-f). However, the Wsp10–BLH condition is less often met than the Vent condition of HU_ASI over the British Isles and the Great European Plain, resulting in somewhat lower stagnation frequency for WA_ASI in those regions (Figure 4.1). Finally, the inter-seasonal variability of stagnation is considerably smaller for this index than for the rest of ASIs, because of the season-specific formulation used to construct the Wsp10–BLH condition (Equations 4.1 to 4.4).

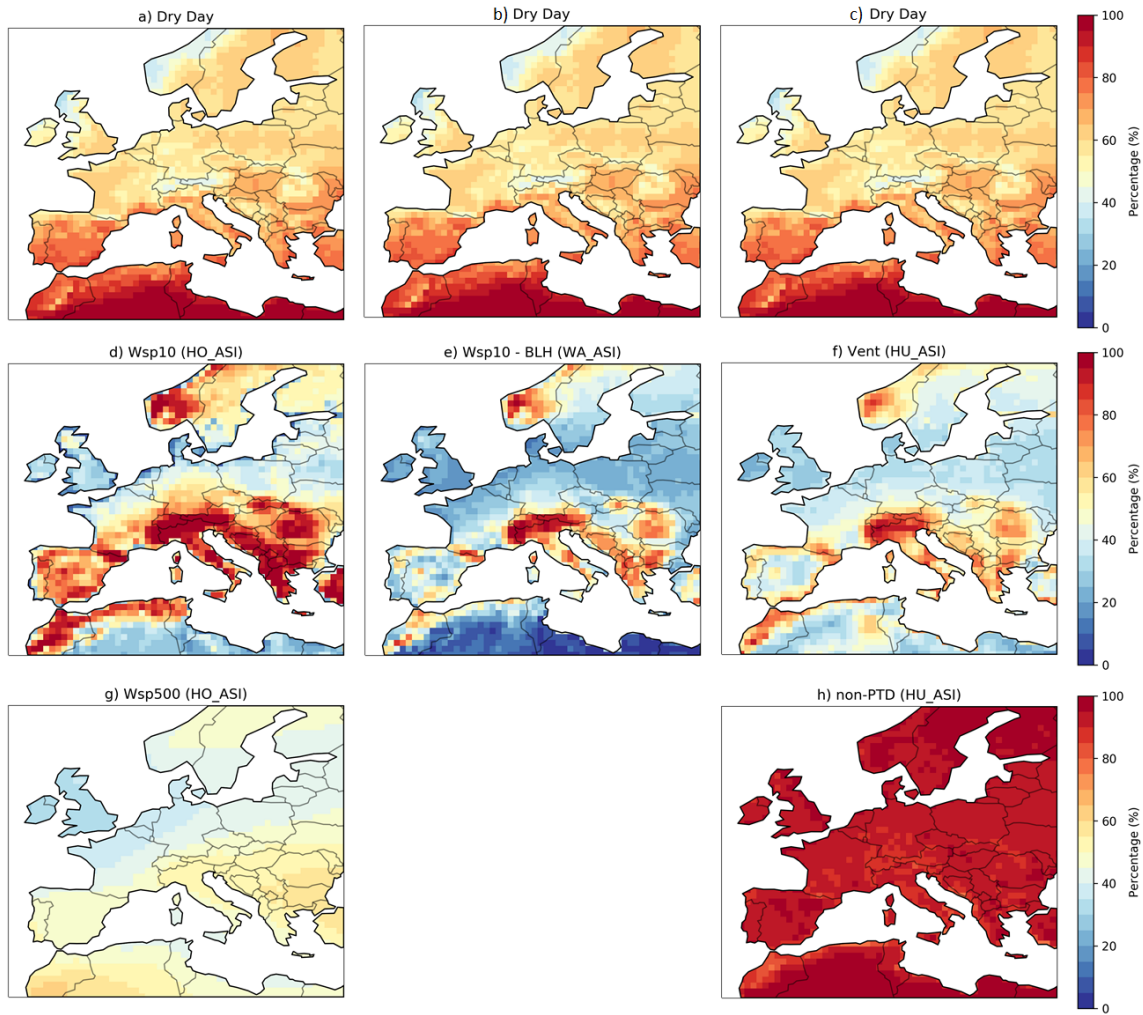


Figure 4.4: Annual percentage of days that fulfil stagnation conditions for the different components of HO_ASI (a,d,g), WA_ASI (b,e) and HU_ASI (c,f,h) during the period 1981–2010. Full details of these conditions are given in Section 4.1.

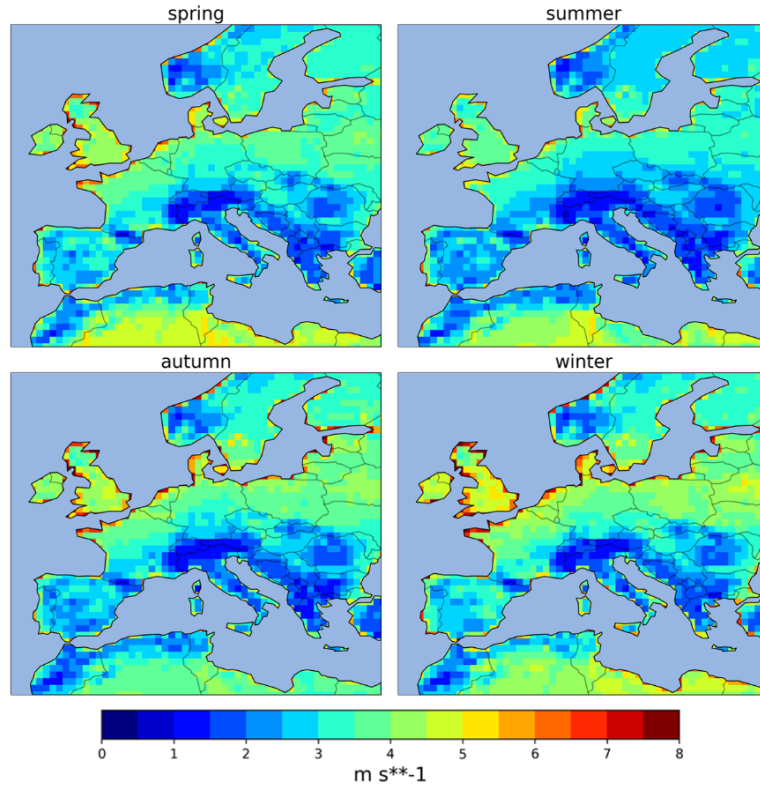


Figure 4.5: Seasonal means of the surface wind speed (m/s) during 1981–2010.

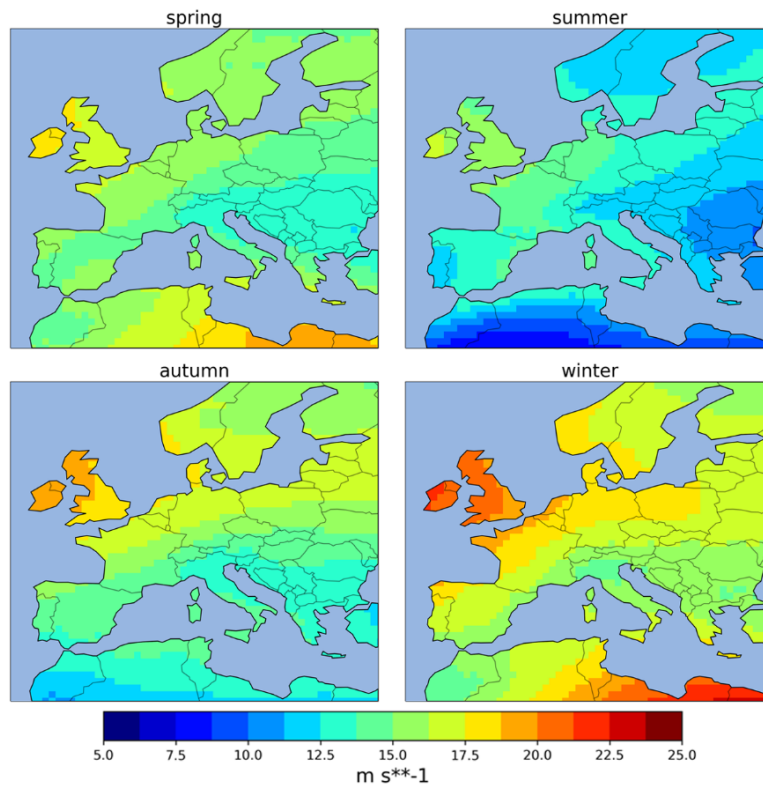


Figure 4.6: Seasonal means of the wind speed at 500 hPa (m/s) during 1981–2010.

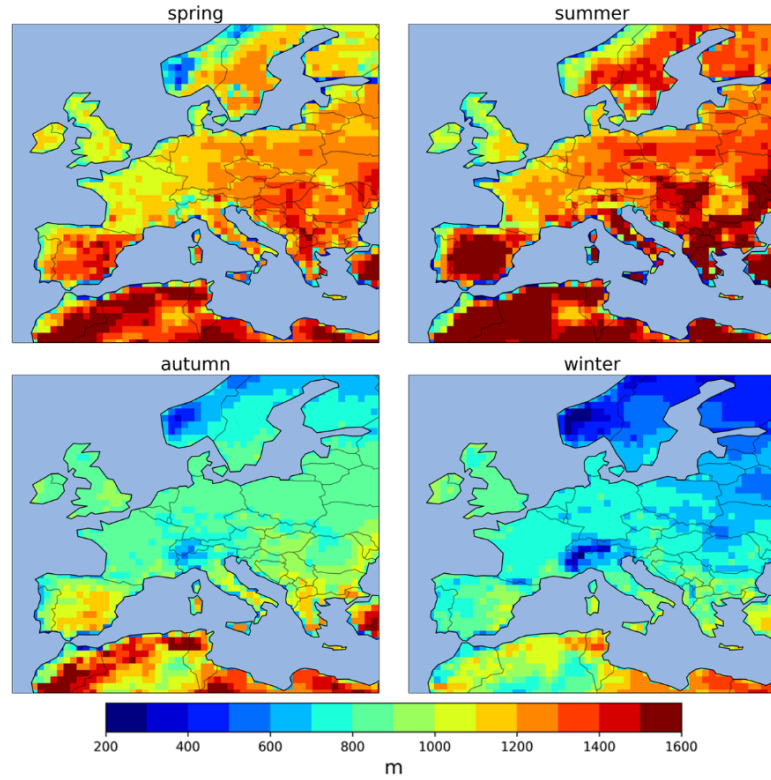


Figure 4.7: Seasonal means of the boundary layer height (m) during 1981–2010.

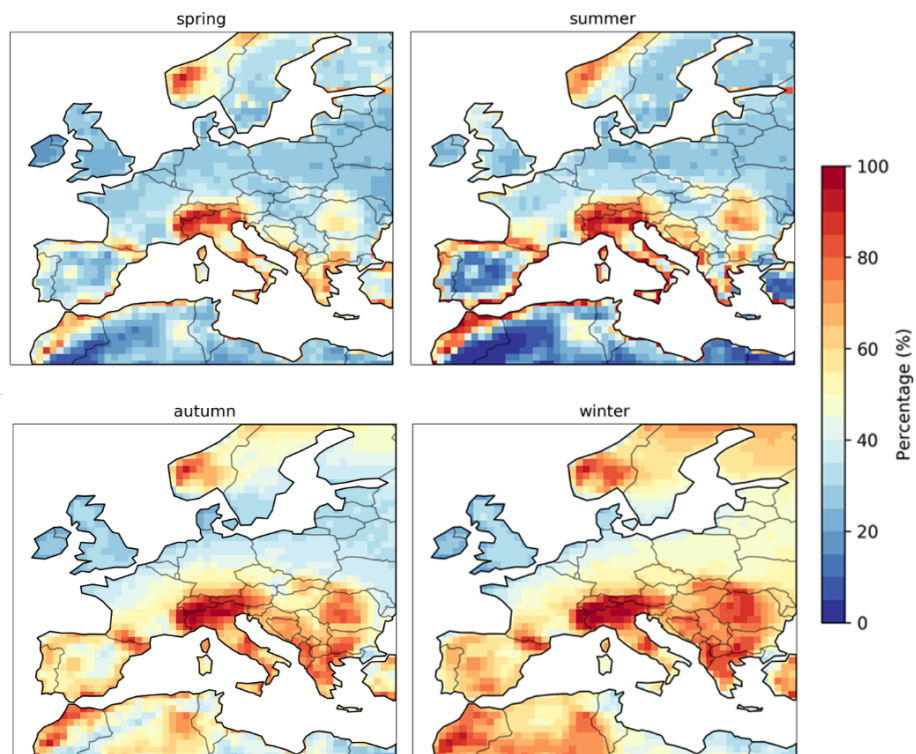


Figure 4.8: Seasonal percentage of days that fulfil the ventilation condition of HU_ASI during the period 1981–2010.

Next we examine the dependence of PM_{10} on each ASI by computing PM_{10} anomalies as the differences of the mean concentrations between days with and without stagnation at each site. This has been done separately for winter and summer. Note that only stations catalogued as background with at least 75% of the data available separately during the summer and winter months of the period of analysis have been considered, selecting a total of 306 sites. Winter (top) and summer (bottom) PM_{10} anomalies are shown in Figure 4.9 when they are statistically significant at the 95% confidence level (two-tailed t-test). As expected, stagnation enhances the PM_{10} concentrations at all sites in winter, but its impact is small over some regions in summer. The strongest effect is found over Benelux and the inner part of the continent (including eastern France, Switzerland, the southern half Germany, the Czech Republic and Poland) for both seasons. The lowest anomalies are located over western and central France, Spain and northern Germany, as well as in Italy during summer. The magnitude of these anomalies also varies with the ASI. In winter, the response of PM_{10} to stagnation is quite similar among the three indices, with average concentration anomalies between 17.2 and $18.6 \mu g m^{-3}$. This corresponds to $\sim 60\%$ of the seasonal mean concentrations (see top panels of Figure 4.10, where PM_{10} anomalies have been normalized by the seasonal mean concentrations at each location). Moreover, there are anomalies over $25 \mu g m^{-3}$ at some locations for all indices. In summer, HO_ASI shows the largest PM_{10} anomalies, with an average of $5.7 \mu g m^{-3}$ compared with 4.6 and $3.8 \mu g m^{-3}$ for WA_ASI and HU_ASI, respectively. While this difference may seem small in absolute terms, it still represents a considerable portion of the seasonal mean (see Figure 4.10, bottom panels). The average normalized anomalies increase from 19 and 22 % for HU_ASI and WA_ASI, respectively, to 28 % for HO_ASI, confirming the higher specificity of the latter in this season. Nevertheless, these anomalies are less than half of those found in winter for all indices.

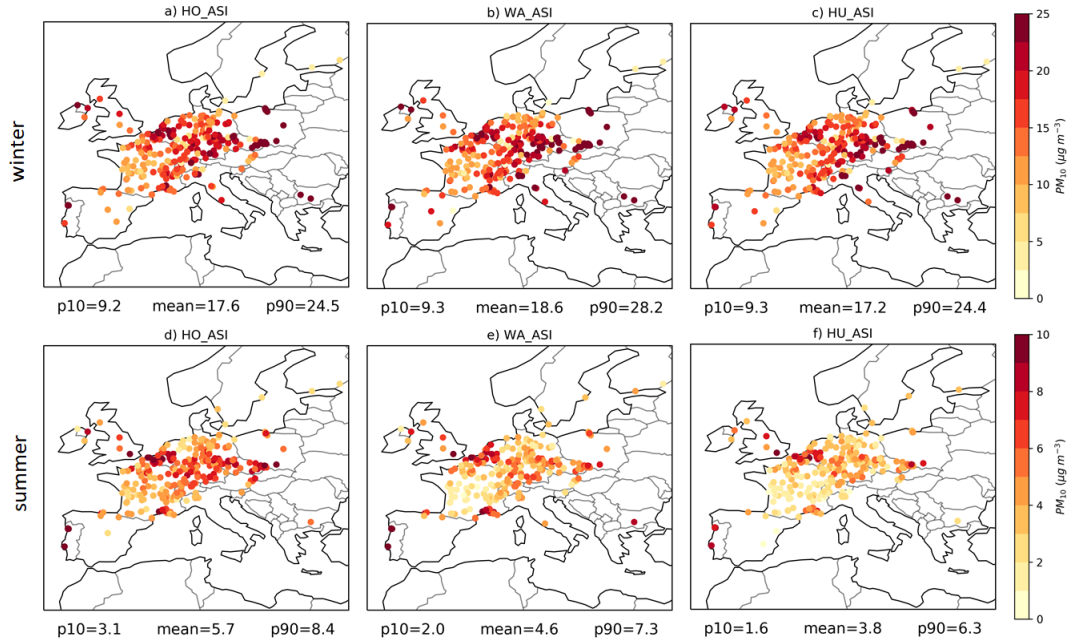


Figure 4.9: Composites of winter (top) and summer (bottom) PM_{10} concentration anomalies ($\mu g m^{-3}$) on days with stagnation with respect to days without stagnation for HO_ASI (left), WA_ASI (middle) and HU_ASI (right) during the period 2000–2012. Anomalies are only shown when they are statistically significant at the 95% (determined through a two-tailed t-test). Note the differences in the colour scales, indicating considerably higher anomalies in winter than in summer. The numbers below the panels respectively indicate the 10th percentile (p10), mean and 90th percentile (p90) across all sites.

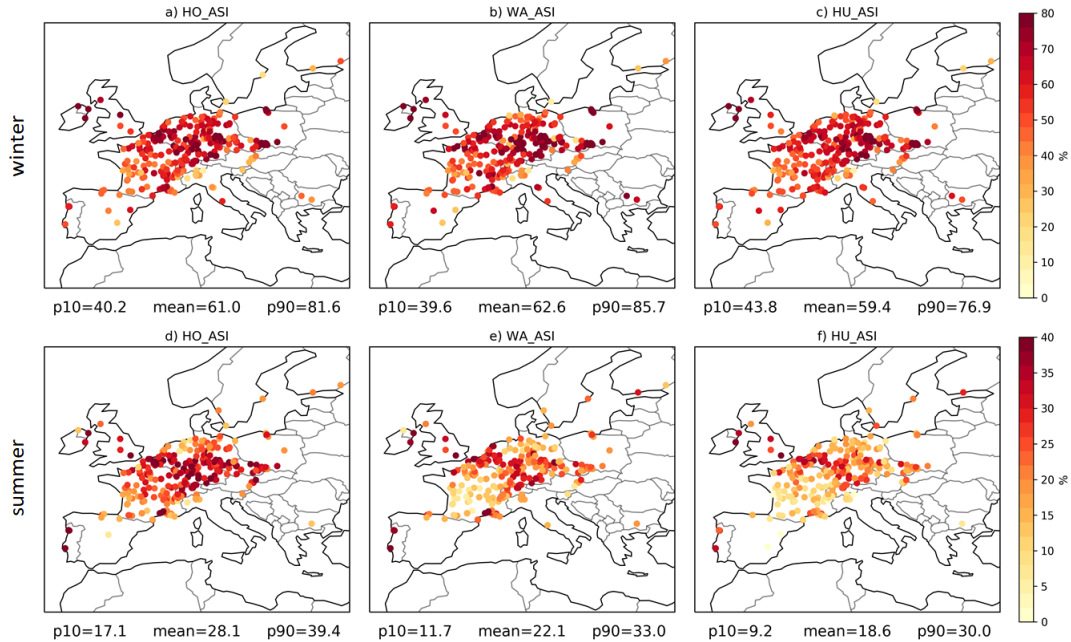


Figure 4.10: As Figure 4.9 but normalized by the respective seasonal mean concentrations (%).

We have also identified the ASI yielding the highest PM_{10} anomaly at each location (Figure 4.11). In winter, WA_ASI outperforms the other indices for almost half of the sites (137), whereas HO_ASI and HU_ASI are selected for 103 and 66 sites, respectively. Nevertheless, no clear spatial patterns have been identified as the ASI selection seems to be more specific to the local settings of the stations than to the geographical regions, with the exception of some relatively small regional clusters (e.g. HU_ASI tends to be selected in some areas of northern Germany and western Austria). Conversely, HO_ASI is associated with the highest PM_{10} anomalies in summer at 263 sites, compared to only 43 sites for the other two ASIs. While HO_ASI clearly beats the other two indices over most of the continent in summer, WA_ASI performs best at coastal sites.

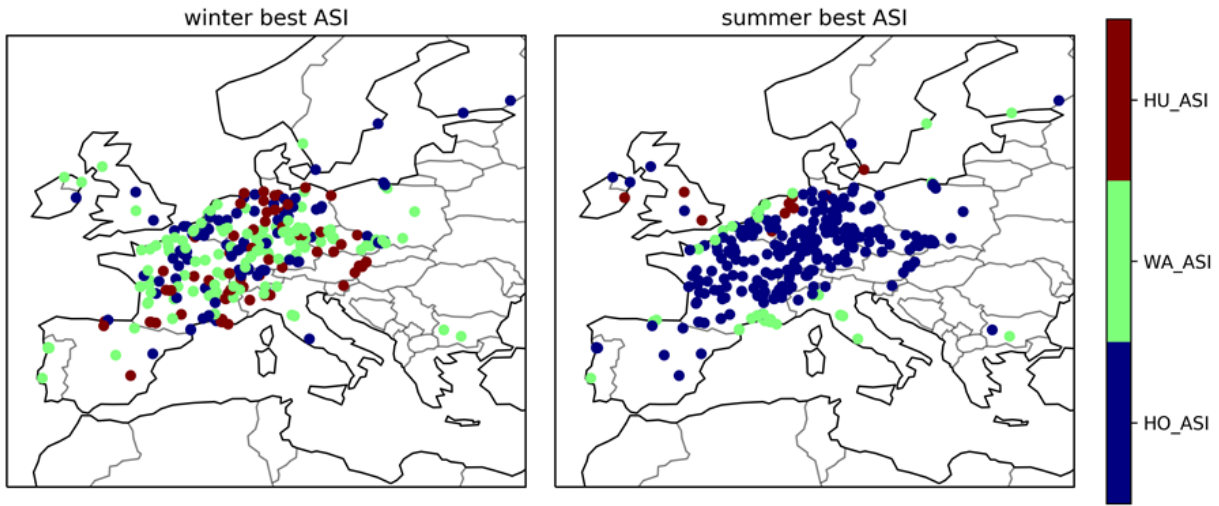


Figure 4.11: Spatial distribution of the ASIs with the highest PM_{10} anomalies in Figure 4.9.

The previous results indicate that the relationships between each ASI and the PM_{10} concentrations vary with location and season. Therefore, a more detailed assessment of the impact of each stagnation component on this pollutant is required to better understand the spatiotemporal responses of PM_{10} to each ASI. In order to do so, we have computed Spearman's rank correlation coefficients between the daily time series of PM_{10} concentrations and the daily values of Wsp10, Wsp500, Vent, BLH and Transport wind speed (Twsp). Twsp is a parameter that takes into account Vent and BLH simultaneously ($Twsp = Vent/BLH$) to measure the average strength of horizontal dilution within the

boundary layer (Huang et al., 2018). Only these meteorological variables have been considered in this analysis because the characterization of the atmospheric dilution capacity is the main difference among the three ASIs. Note also that Spearman’s correlation measures the strength of monotonic relationships (whether linear or not) between variables. Figure 4.12 shows the first, second and third most correlated variables with PM_{10} in winter (top) and summer (bottom). In winter, Vent and Wsp10 are the fields that best explain the day-to-day variability of PM_{10} , besides BLH in some parts of northern Europe. Moreover, Twsp seems to be a better predictor than Wsp500, as it is often selected as the variable with the second and third best correlations. These results seem to be inconsistent with the fact that the application of HU_ASI yields the lowest winter PM_{10} anomalies on stagnant days (although by a low margin), as it is the only ASI defined based on Vent. In fact, HO_ASI results in slightly higher PM_{10} anomalies than HU_ASI despite the lowest correlations found for Wsp500 in this season. This could be due to non-linear relationships between the meteorological variables and PM_{10} concentrations. Since ASIs are defined based on fixed thresholds, they cannot take this into account as does the Spearman’s rank correlation coefficient. We have repeated the analysis shown in Figure 4.12 but using the Pearson’s correlation coefficient, which assesses linear relationships, instead of Spearman (Figure 4.13). In this case, Wsp10 is the field with the highest correlations at most sites in winter, while the correlations for Vent and Twsp decrease compared to those of other variables, which now seems consistent with the somewhat smaller PM_{10} anomalies found for HU_ASI than for the other two indices.

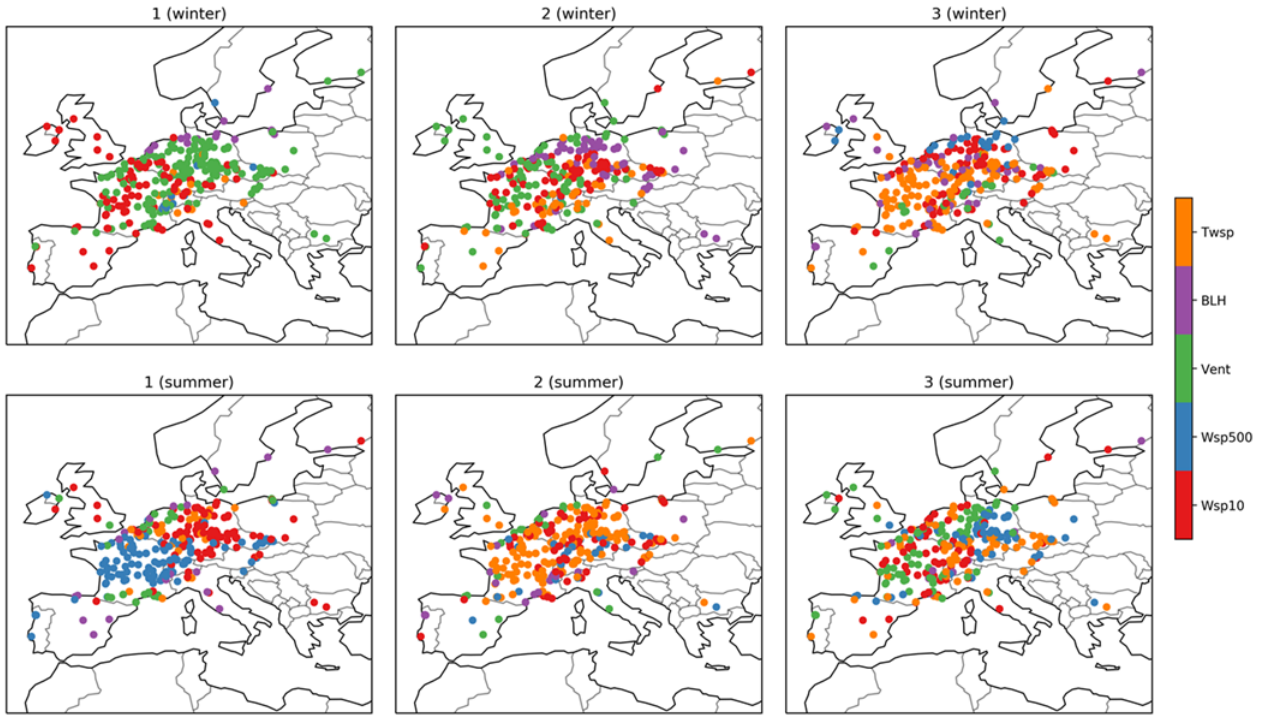


Figure 4.12: First (left), second (middle) and third (right) most correlated meteorological variables (either positively or negatively) with daily PM_{10} concentrations, using the Spearman rank correlation coefficient for all stations in winter (top) and summer (bottom) of 2000–2012.

More marked spatial patterns are found in summer for both Spearman and Pearson correlation coefficients, with Wsp500 presenting the highest correlations over most of France and Wsp10 in other regions, consistent with the highest PM_{10} anomalies reported for HO_ASI in this season. In addition, BLH has been selected at some of the coastal sites where WA_ASI outperformed the other two indices. Finally, it must be noted that Twsp is the field with the second best correlations at many sites in summer. As expected, unlike winter, this field becomes more relevant than Vent, with the exception of some coastal locations. While subsidence under stagnant clear-sky anticyclonic conditions limits the dilution capacity of the lower atmosphere, yielding the accumulation of pollutants close to the surface, Vent values can still be high because the strong radiative and surface heat fluxes favour the development of the boundary layer over continental areas under such situations in summer. This suggests that replacing the ventilation condition by another one based on an appropriate Twsp threshold in the definition of HU_ASI could improve the performance of the index for Europe in summer.

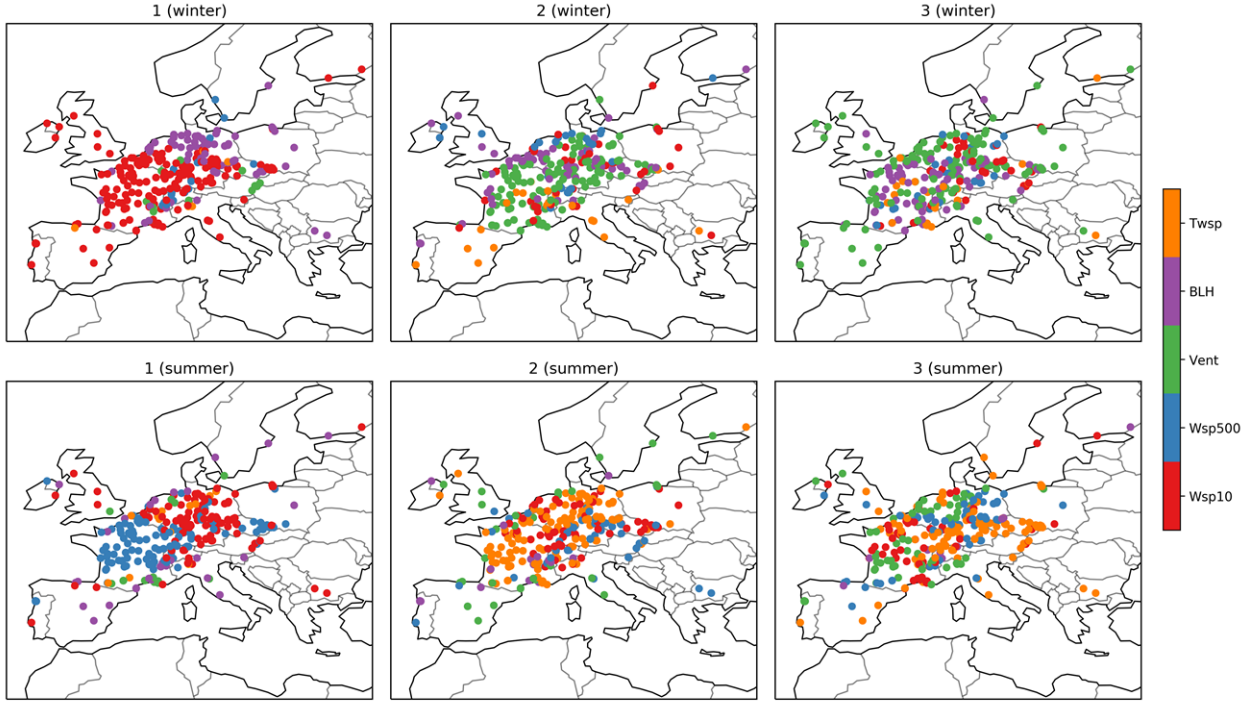


Figure 4.13: As Figure 4.12 but using the Pearson correlation coefficient.

4.3 Statistical modelling of daily PM_{10} as a function of stagnation components

None of the three ASIs tested seems to clearly outperform the others all year round when examining PM_{10} anomalies under stagnant vs. non-stagnant days (Figure 4.11). Moreover, our correlation analyses have raised contrasting responses of the PM_{10} concentrations to some of the ASI components depending on the location and season (Figure 4.12). While some of those components are expected to show some collinearity, others may have an additive effect on the PM_{10} concentrations. Consequently, we have constructed Generalized Additive Models (GAMs) to explore the relationships between the PM_{10} concentrations and the ASI components at each location separately for summer and winter.

GAMs are effective tools to conduct non-linear regression analysis of air pollutant time series (Dominici et al., 2002; Barmpadimos et al., 2011, 2012; Boleti et al., 2018;

Ordóñez et al., 2020). They are semi-parametric extensions of the generalized linear model that assume that there is an additive effect of the predictors on the predictant. We have applied this statistical technique, provided by the pyGAM Python module (Servén and Brummitt, 2018), to each station and season separately in order to explore the relationships between the PM_{10} concentrations and a pool of potential meteorological drivers. Factor and spline smoothing functions have been used to model the pollutant response to categorical and continuous variables, respectively. The factor function fixes constant values for each categorical attribute, while the spline function constructs the response curve from several polynomial segments that connect smoothly at their joints. In particular, we have used a regression spline known as penalized B-spline or P-spline. This technique imposes smoothness by directly penalizing the differences between adjacent coefficients, avoiding overfitting. Model fitting is achieved by maximum likelihood estimation. Details can be found in Wood (2017) and references therein. In addition, it is well known that PM concentrations follow a lognormal distribution (Bencala and Seinfeld, 1976). Therefore, like Barmpadimos et al. (2011, 2012), we have used the log-transformed daily concentrations of PM_{10} in order to achieve normally distributed residuals and improve the homoscedasticity of the model. The general form of the model is as follows:

$$\log(PM_{10}) = \beta_0 + \sum_x s_x(A_x) + \sum_y f_y(B_y) \quad (4.6)$$

where

β_0 : intercept of the model

$s_x(A_x)$: smoothing spline function on continuous feature A_x

$f_y(B_y)$: factor function on categorical feature B_y

Note that, with the exception of dry day and non-PTD, which are treated as discrete variables, we do not use the threshold exceedance of the other ASI components but their actual daily values in the models. We have also included Z500 and SLP among the potential drivers to account for synoptically-driven variability of PM_{10} in Europe (Ordóñez et al., 2019). A stepwise procedure has been used for the selection of the best set of predictors from the pool of meteorological variables. The algorithm is similar to that

applied in previous studies to model the atmospheric concentrations of the OH radical, PM or ozone (Jackson et al., 2009; Barmadimos et al., 2011; Otero et al., 2016). It consists of the following five steps: 1) We evaluate the strength of the regression between the pollutant and each of the potential predictors. The explanatory variable with the highest deviance explained by the GAM is selected. 2) We recompute the GAMs using each of the remaining potential predictors separately together with the previously selected variable. The combination with the highest deviance explained is considered as the pool of selected variables. 3) We check the choice from the first step. The variable selected in that step is ignored and each of the remaining potential predictors are separately added to the model together with the variable selected in the second step. If any of these combinations performs better than that of the second step, then it is considered as the new pool of selected variables. 4) We test the collinearity between the selected variables to avoid redundancy and oversensitivity of the model to the data. For that purpose, we have computed the Variance Inflation Factor (VIF; Freund and Wilson, 1998) for each pair of selected variables. Following Barmadimos et al. (2011), if VIF exceeds 2.5 for a pair of predictors, the collinear variable with the smallest contribution is excluded from the screening process. This threshold is quite restrictive compared to the values used by other analyses (e.g. VIF=10 in Otero et al. (2016)), restricting the collinearity of the variables included in the model. 5) The procedure is repeated from steps 2 to 4 until the inclusion of a new variable in the pool of selected predictors results in an increase of the deviance explained below one percent or if all the potential explanatory variables have already been selected.

The resulting combinations of explanatory variables are shown in Tables A1 and A2 for winter and summer, respectively. Table 4.1 also summarizes how often each variable is selected over all sites. The precipitation condition (dry day), which is common to all three ASIs, is the most used predictor in winter and the second least selected one in summer. The other discrete variable, i.e. non-PTD, is selected at only 5% of the sites in winter, as expected, rising to 11% in summer. This indicates a weak relationship with PM_{10} and a low added value of this field as a result of the low frequency of occurrence of PTD in the region of study (Figure 4.4h).

Table 4.1: Percentage of sites (out of a total of 306) for which each predictor was selected by the backward stepwise regression in winter and summer.

	Wsp10	Wsp500	Vent	BLH	Twsp	Prec	non-PTD	Z500	SLP
Winter	43	78	57	31	43	82	5	76	69
Summer	65	85	42	62	30	13	11	100	89

Among the stagnation components that characterize the atmospheric horizontal dispersion and vertical mixing of air masses, Wsp500 is the most used predictor in both seasons. This does not necessarily mean that it is the most important variable in reproducing PM_{10} variability, but that it is the one that best complements the rest of meteorological drivers tested in the model. The moderate selection frequency of Wsp10, Vent, BLH and Twsp is due to their close relationship. Since Vent and Twsp depend on both wind speed and BLH, the inclusion of these fields in the model accounts for both the horizontal and vertical dilution capacity of the atmosphere. Therefore, these four variables are highly correlated and are often removed from the optimal set of predictors to avoid multicollinearity. In fact, their simultaneous inclusion occurs in less than 2% of the stations for both seasons, while any combination of three of them remains below 15%. It is noteworthy the fact that Vent is preferred over Wsp10 and BLH in winter, which is in line with the Spearman's correlations reported in Section 4.2 (Figure 4.12) but not with the Pearson's correlations (Figure 4.13). This suggests that the consideration of non-linear relationships between the variables that characterize the dilution capacity of the atmosphere and PM_{10} concentrations is key to understand the additive contribution of each explanatory variable.

An example of the non-linear dependence of PM_{10} on Vent and other fields at a representative station in southern Germany can be seen in Figure 4.14. Partial dependence plots (PDP) are graphical representations of the marginal effect that the explanatory variables included in the model have on PM_{10} , accounting for the average effects of all other predictors (Friedman, 2001). This helps understand the importance of each feature in the model and illustrates how PM_{10} concentrations vary when a driver changes, showing if their relationship is linear or more complex. As expected, an increase in Vent results in a decrease of the PM_{10} concentrations, but this trend is much steeper for low values

of Vent. The figure also shows that PM_{10} concentrations are enhanced on days with low mid-tropospheric winds and no rain. On the other hand, the relationship between PM_{10} and Z500, with a maximum at around 550 dam, is clearly non-linear. This occurs because the regional response of PM_{10} to anticyclonic systems not only depends on their intensity but also on their position, as will be seen in Chapter 5. The evaluation of Z500 and SLP provides information on the relative importance of the synoptic conditions. The selection frequency of these variables is high in both seasons, especially in summer (89% for SLP and 100% for Z500). In addition, their simultaneous inclusion occurs at 51% and 90% of the stations in winter and summer, respectively. This, together with the high selection frequency of Wsp500, suggests that the inclusion of a meteorological variable representing the large-scale flow in the ASI definition is particularly useful in summer, which is in line with the highest skill of HO_ASI during this season. Wsp500 also seems to be of value in winter, although the 13 m/s threshold used for this field might need to be relaxed because of the strong climatological wind speeds in that season (see Figure 4.6).

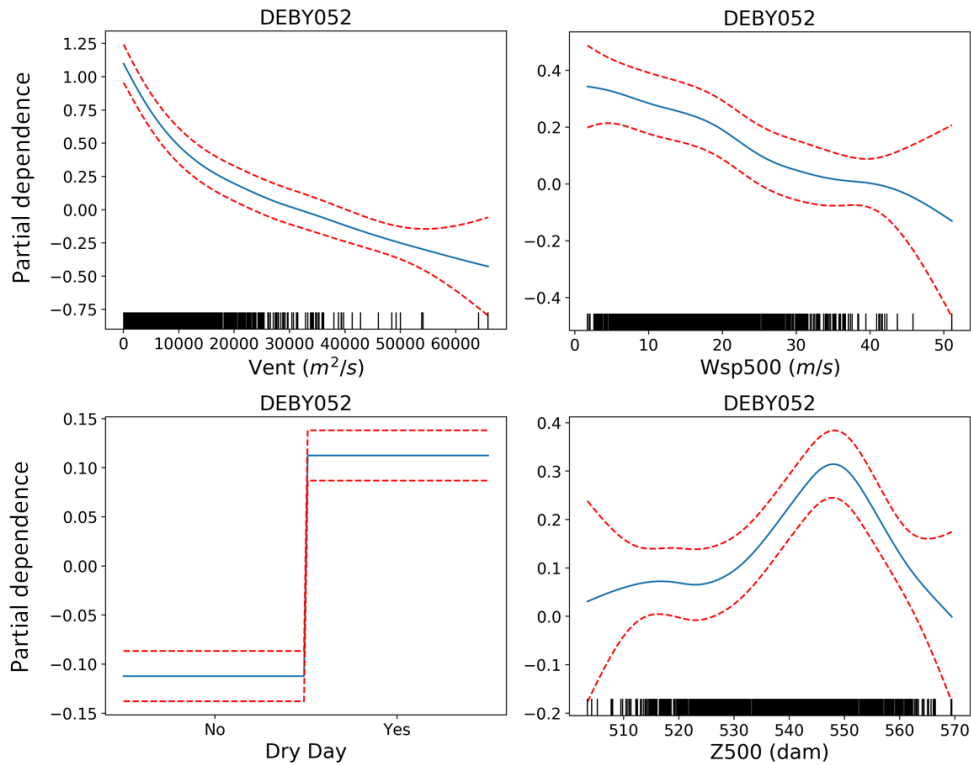


Figure 4.14: Partial dependence plots of the predictors used in the GAM model for DEBY052 site (Germany, [48.4° N, 10.0° E]) in winter. Red dotted lines indicate the 95% confidence intervals for the estimated functions (blue solid lines). The distribution of the data is indicated by the vertical marks along the x-axis for the continuous variables (rug plot).

Finally, Figure 4.15 displays the spatial distribution of the deviance explained by the GAMs using the resulting combinations of explanatory variables for winter and summer. The models explain a larger fraction of the day-to-day variability of PM_{10} in the former season, with average deviance explained over all sites ranging from 0.37 in summer to 0.43 in winter. The best performance is found over Benelux and the inner part of the continent, with values up to ~ 0.6 in winter and ~ 0.5 in summer at some sites of eastern France, Switzerland, southern Germany and the Czech Republic. These are among the European regions where the PM_{10} concentrations are most influenced by large-scale patterns such as anticyclonic systems or the North Atlantic jet (e.g. Ordóñez et al., 2019), indicating the importance of the synoptic conditions to capture inter-daily variations of PM_{10} .

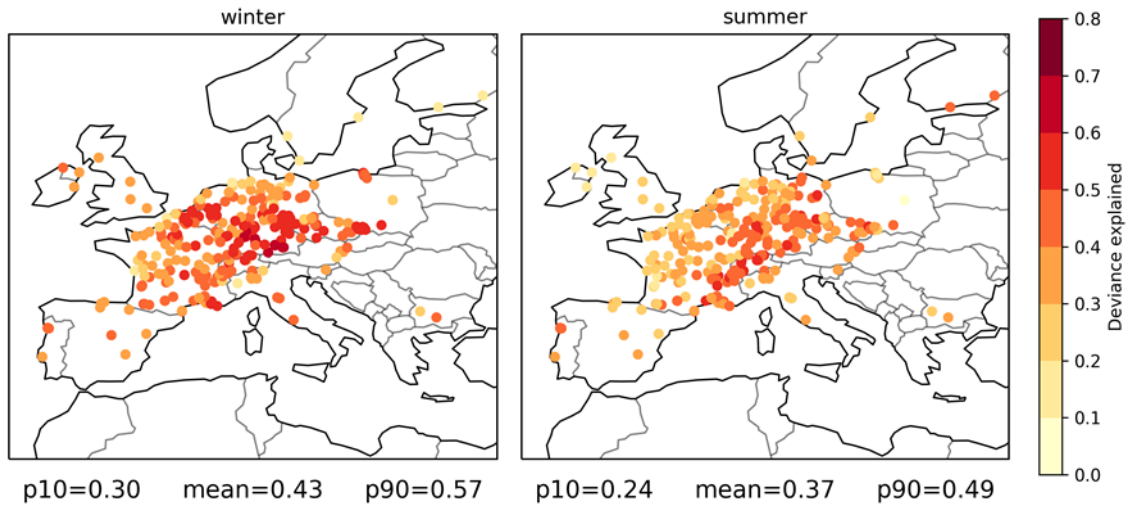


Figure 4.15: Deviance explained by the GAMs for all stations in winter (left) and summer (right) during the period 2000–2012. The list of variables considered as potential predictors is available in Table 4.1.

4.4 Main findings and discussion

The main findings from the analyses presented so far in this chapter are summarized below:

- The application of the three ASIs results in similar spatial patterns of stagnation frequency, but also in important differences in the seasonal cycles. According to HO_ASI, the frequency of stagnation in Europe presents a summer maximum and a winter minimum, while the opposite is the case for HU_ASI. This occurs because HO_ASI uses predefined thresholds of wind speeds at 10 m and 500 hPa, whose values decrease in summer and increase in winter, whereas HU_ASI sets a threshold on the ventilation, which is higher in summer than in winter. On the other hand, the definition of WA_ASI considers different 10-m wind speed – boundary layer height conditions for each season, limiting the seasonal variability of this index.
- The response of the PM_{10} concentrations to stagnation varies with the ASI and also depends on the location and season. In winter, the application of the three ASIs yields similar positive PM_{10} anomalies (calculated as composite differences between the mean concentrations for stagnant and non-stagnant days), with averages over all sites ranging from 17.2 to 18.6 $\mu g m^{-3}$. In summer, the highest PM_{10} anomalies are found for HO_ASI over most of the area of study (on average 5.7 $\mu g m^{-3}$, considerably smaller than in winter). The main exceptions occur in coastal areas, where WA_ASI seems to be more powerful than the other ASIs.
- The consideration of the large-scale circulation consistently contributes to reproducing PM_{10} variability. Z500, SLP and wind speed at 500 hPa are among the most selected variables by the screening process used to find the best set of meteorological predictors. The selection frequency is especially high in summer, explaining the highest skill of HO_ASI during this season.
- There is some room for improving the performance of HO_ASI and HU_ASI over Europe. This might require adapting the 500 hPa wind speed threshold to the season for the former and replacing the ventilation condition by an appropriate transport

wind speed threshold in the latter.

- ASIs provide an incomplete description of the relationships between PM_{10} and meteorology. Since the three ASIs evaluated here are based on fixed thresholds of meteorological fields, they cannot deal with non-linear relationships, which limits their ability to explain PM_{10} variability. In addition, PM_{10} concentrations also respond to changes in some other meteorological fields such as temperature and relative humidity which are not indicators of stagnation.

The deviance explained by the GAMs is moderate for most locations, ranging from an average of 0.37 in summer to 0.43 in winter (Figure 4.15). However, there is still room for improvement since we have not considered some meteorological variables and factors that affect PM. For instance, the effect of the persistence (defined as the concentrations of air pollutants on the previous day) is well known from previous studies (e.g. Vlachogianni et al. (2011), for NO_x ; Otero et al. (2016), for ozone; Ordóñez et al. (2019), for PM_{10}). Increases in relative humidity are related to wet conditions with reduced suspension of dust (Wise and Comrie, 2005), but also to the formation of ammonium nitrate (Liao et al., 2006; Lecoeur and Seigneur, 2013). Changes in temperature have also been reported to influence PM concentrations showing multiple competing effects. On the one hand, high temperatures increase the rate of SO_2 oxidation and promote the emission of biogenic volatile organic compounds, resulting in enhanced sulphate concentrations and production of secondary organic aerosols, respectively (Dawson et al., 2007; Heald et al., 2008; Jacob and Winner, 2009; Tai et al., 2010). On the other hand, high temperatures lead to the volatilization of ammonium nitrate and semi-volatile organic aerosols, reducing the concentrations of PM (Dawson et al., 2007; Aksoyoglu et al., 2011; Jiménez-Guerrero et al., 2012). In an attempt to consider some of these complex relationships, in addition to the well-known covariation of temperature and humidity with other meteorological variables affecting PM (Tai et al., 2010, 2012b), we have rebuilt the GAMs including the persistence, temperature and relative humidity among the potential explanatory variables.

The deviance explained by the new models rises to an average of 0.66 in winter and 0.60 in summer, exceeding 0.80 at some locations of central Europe in the former season (Figure 4.16). This is a considerable improvement compared to the values reported for the same seasons in Figure 4.15. Persistence is selected for all sites both in winter and in summer, temperature is respectively chosen at 74% and 49% of the sites in winter and summer, and relative humidity at 72% and 54% of the sites in the same seasons. Furthermore, if persistence was the only new field added to the pool of potential predictors, the average deviance explained would be 0.60 for both seasons. While we have not quantified the changes in the collinearity of the predictors for the different models, the results provide evidence for the strong effect of persistence compared to that of temperature and relative humidity. Overall, the use of the persistence together with meteorological fields related to stagnation suffices to obtain explained deviances of ~ 0.60 in both seasons, while the inclusion of other fields such as temperature and relative humidity contributes to raising those values in winter but not in summer.

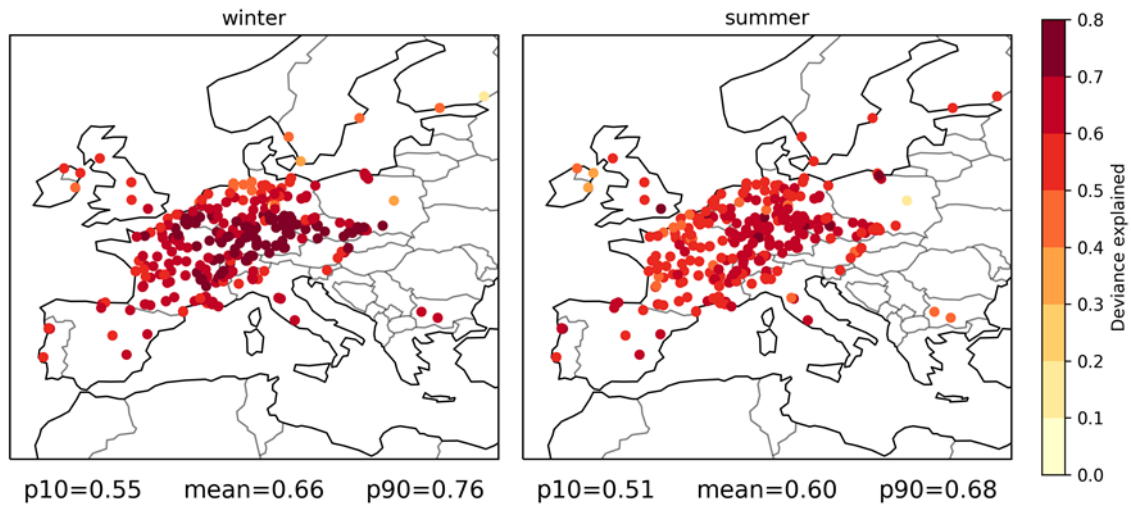


Figure 4.16: As Figure 4.15 but considering the persistence (defined as the mean PM_{10} concentration of the previous day), temperature and relative humidity as potential explanatory variables of PM_{10} .

While our analyses have proven the value of stagnation-related meteorological fields to identify conditions conducive to enhanced PM pollution, they also point to some potential limitations of the three ASIs evaluated here. These indices are based on fixed thresholds and cannot easily deal with non-linear relationships. In addition, ASIs dis-

regard some relevant meteorological fields such as temperature and relative humidity. Consequently, statistical models based on the local selection of pollution-related variables might be more suited to reproduce the day-to-day variability of PM than ASIs. Nevertheless, it must be borne in mind that ASIs are qualitative indicators of air pollution potential and their usefulness goes beyond their ability to explain the variability of a specific air pollutant. In addition, the main advantages of these indices lie in their simplicity and in the fact that they often use common output variables that are provided by global and regional models (Horton et al., 2012, 2014; Caserini et al., 2017; Gao et al., 2020; Lee et al., 2020). This has clear implications for the long-term climatological assessment of air pollution potential. In this sense, the consideration of large-scale meteorological variables seems to be particularly relevant since future changes in regional climates are strongly driven by the atmospheric circulation (Woollings, 2010). Moreover, large-scale circulation anomalies generally arise as part of teleconnections linked to anomalies in other regions of the globe (e.g. Zappa and Shepherd, 2017). Therefore, special attention should be given to remote drivers of regional circulation and their impact on air pollution. For instance, recent studies have reported the influence of changes in Arctic sea ice and Eurasian snow cover on air pollution in East Asia (Zou et al., 2017; Zhao et al., 2018; Kim et al., 2019), but these issues remain unexplored for Europe. The strong relationship between large-scale circulation and pollutant concentrations found in this thesis and other studies (Ordóñez et al., 2017, 2019) suggests that remote drivers might also play a key role in the long-term variability of air pollutant concentrations in Europe. In particular, the tropical and Arctic amplification of global warming as well as changes in stratospheric vortex strength are potential candidates to be investigated in future work, since they shape different aspects of European climate such as precipitation and windiness, at least during the extended winter season (Zappa and Shepherd, 2017). This issue will be addressed in Chapter 7.

5 Strong signatures of high-latitude blocks and subtropical ridges in winter PM_{10} over Europe

In the previous chapter we have provided evidence that air stagnation can partly explain the variability of the PM_{10} concentrations in Europe. Accordingly, this chapter delves deeper into this matter and examines the regional responses of winter PM_{10} to the occurrence, position and persistence of blocks and ridges, presumably two of the large-scale patterns more closely associated with stagnation in the midlatitudes, for the winter period of 2000–2010. The results of this chapter can be found in Garrido-Perez et al. (2017).

5.1 Impact of blocks and ridges on winter mean PM_{10}

Most analyses carried out in this chapter are based on composites of the PM_{10} concentrations at each AirBase site and meteorological fields over the European domain, separating data for those days when blocks and ridges have their centres in the ATL and EUR sectors. Note that only stations with at least 75% of the winter data avail-

able for the period of analysis have been used for PM_{10} , selecting a total of 500 sites located in 20 different European countries. Considering the types of measurement sites, the selected locations can be classified as follows: 9.2 % are industrial, 23.0 % traffic sites and 67.8 % background, of which 54.3 % are urban background, 28.0 % suburban background, 16.2 % rural background and the remaining 1.5 % unknown. Firstly, concentration/meteorological anomalies are calculated as the differences of the mean field between days with and without blocks or ridges in a given sector. Figure 5.1 displays the winter PM_{10} concentration anomalies on days when these patterns are identified in the ATL and EUR sectors. Anomalies are only shown when they are statistically significant at the 95 %. Significance is evaluated by means of a bootstrap resampling method, which generates random samples of winter PM_{10} concentrations for the whole period of analysis. Each random sample includes as many days as the synoptic pattern of interest (i.e. blocks or ridges in a given sector). Since these patterns are often identified during consecutive days, the random sample is grouped in episodes of the same length as the blocks or ridges registered. Then an anomaly is calculated as the difference between the mean of the sample and that of the rest of the data. This procedure is repeated 1000 times to create a random distribution of winter PM_{10} concentration anomalies. Sensitivity analyses indicate that this number is sufficient to produce a stable distribution. Following this, the composite anomalies calculated for the days when blocks or ridges were identified are compared with the distribution of PM_{10} anomalies. Finally, they are considered significantly negative or positive when they are below or above the 2.5 % and 97.5 % tails, respectively.

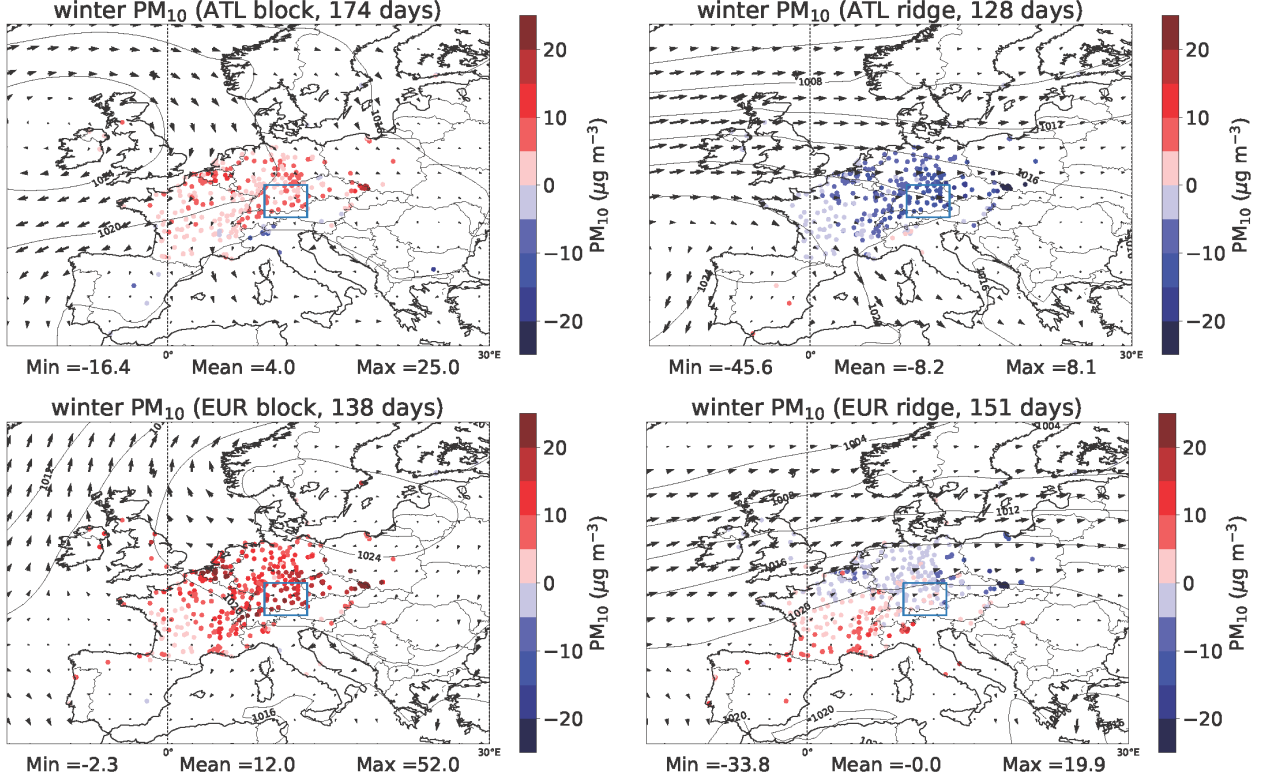


Figure 5.1: Composites of winter PM_{10} concentration anomalies on days with blocks (left) and ridges (right) over the ATL (top) and EUR (bottom) sectors in winter 2000–2010. Anomalies are only shown when they are statistically significant at the 95 % (determined through a bootstrap resampling method, see main text). The black contour lines and arrows respectively represent mean SLP (hPa) and horizontal winds at 10 m. The vertical line at 0° longitude separates the ATL (30°–0°W, only partially shown) and EUR (0°–30°E) sectors.

We first focus on the average impact of blocks on PM_{10} (left hand side panels of Figure 5.1). The strongest effect is found when blocks are situated over the EUR sector (Figure 5.1, lower left), with high positive anomalies especially over two areas: the Benelux (in particular Belgium) and the inner part of the continent (including Switzerland, southern Germany and the Czech Republic). On average, the concentration anomaly for EUR blocks is $12.0 \mu g m^{-3}$. The effect is acute at some locations where anomalies can exceed $50 \mu g m^{-3}$. These large positive anomalies are caused by a combination of poor ventilation and vertical mixing as well as a reduction in the precipitation associated with the anticyclonic centre located in northern Europe. This can be seen from the negative anomalies in PBL height and wind speed as well as the strong decrease in precipitation frequency over most areas with positive PM_{10} anomalies (Figure 5.2, right).

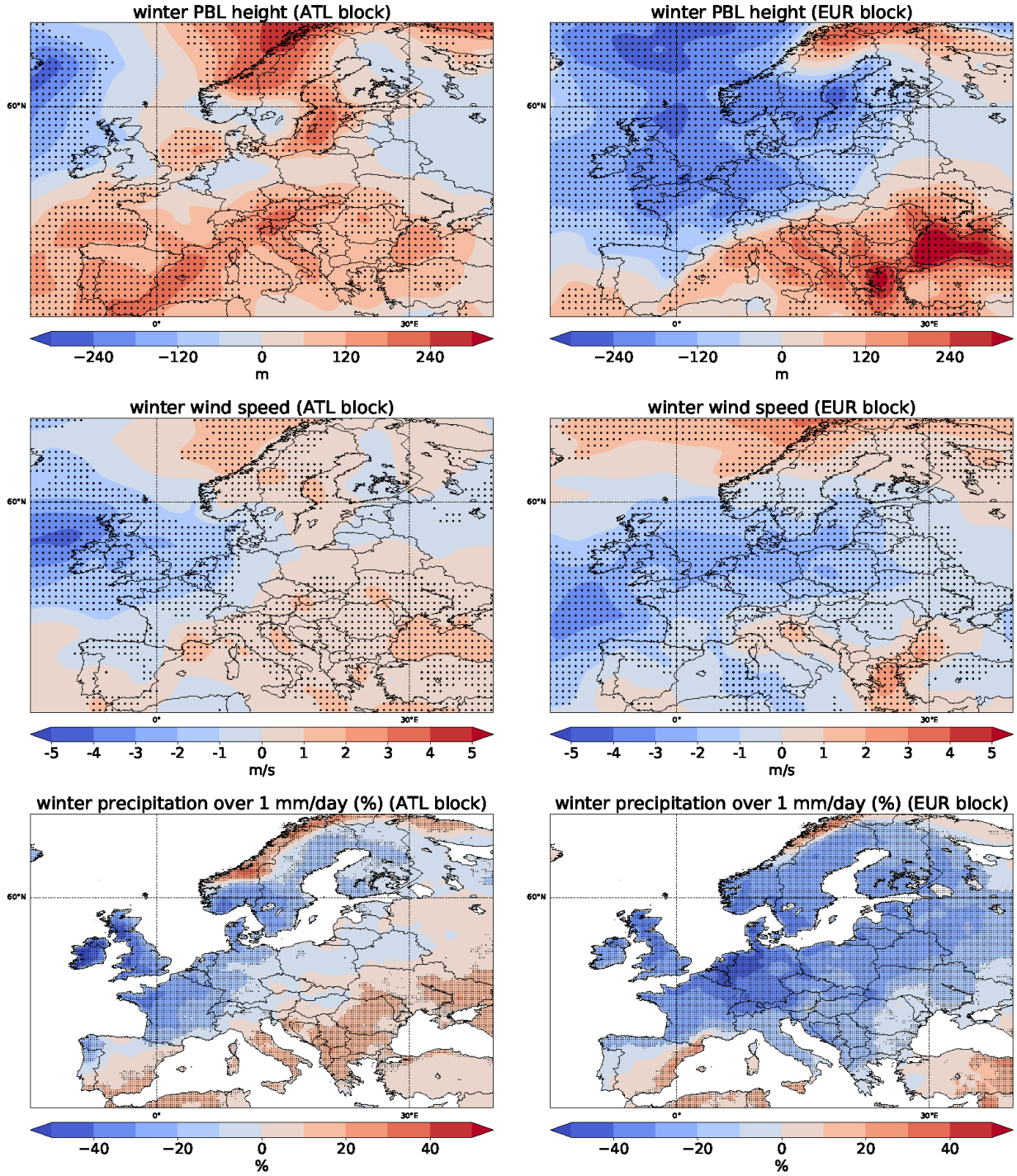


Figure 5.2: Anomalies of boundary layer height (m, top), 10 m wind speed (m/s , middle) and frequency of precipitation above 1 mm day^{-1} (% , bottom) on days with blocks over the EUR sector (left) and ridges over the ATL sector (right) during the winter periods from Jan 2000 to Feb 2010. Stippling (density is proportional to grid spacing) indicates regions where anomalies are statistically significant at the 95 % (determined through a bootstrap resampling method).

When blocks are situated in the ATL sector (Figure 5.1, upper left panel), the PM_{10} anomalies are weaker, being significantly positive in the central and northern parts of the continent. Conversely, anomalies tend to be negative in southern Europe but they are significant only at few sites. A reason for the moderate anomalies in the north could be that two opposing effects act simultaneously: the potential stagnation of air masses associated with the anticyclone located over the British Isles and the inflow of clean Atlantic air masses from the north. A closer examination of the meteorological fields (left panels of Figure 5.2) also points to the interplay of some contrasting effects. First, whereas southern and central Europe experience positive anomalies in the PBL height, there is not a clear pattern over northern Europe. Moreover, wind anomalies are negative close to the western coast of the continent but become positive inland and in the Nordic countries, and the reduction in the precipitation frequency is less marked than in the case of EUR blocks (Figure 5.2, lower right panel). On the other hand, the generally small negative PM_{10} anomalies observed for some sites in southern Europe are concurrent with an overall increase in PBL height, while the increases in wind speed and precipitation frequency are not so marked for all regions.

The strongest impact of ridges on PM_{10} (right hand side of Figure 5.1) is seen when they are situated over the ATL sector (upper right panel), with a significant decrease in the concentrations over most regions where blocks produce an increase, as well as relatively small positive anomalies (only significant at very few locations) in Iberia and northern Italy. The average reduction considering all sites is around $-8 \mu g m^{-3}$ and the highest negative anomaly is around $-46 \mu g m^{-3}$. Therefore, the impact of ATL ridges is notable but somewhat lower and of opposite sign than that of EUR blocks. The negative anomalies may be partly related to the enhanced zonal flow from the Atlantic around $50^{\circ}-60^{\circ}N$, which brings clean air masses and favours the horizontal and vertical dispersion of pollution. This is apparent from the observed increase in PBL height and wind speed over most of those regions, which act in the same direction as the increase in precipitation frequency since the latter favours the washout of pollutants (Figure 5.3, left). The situation is reversed for southern Europe, where there are decreases in PBL height and precipitation frequency over some areas.

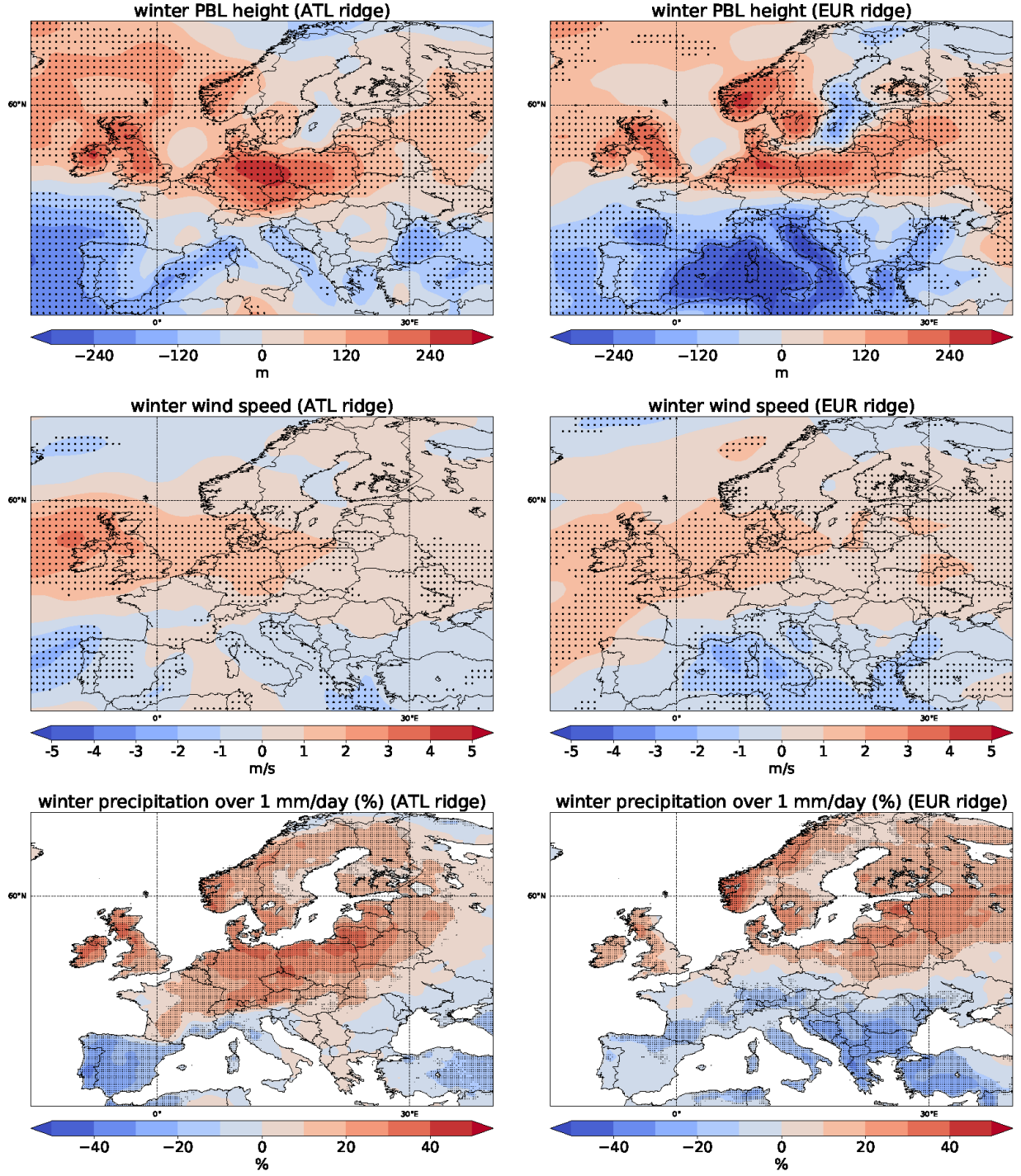


Figure 5.3: As Figure 5.2, but for days with blocks over the ATL sector (left) and ridges over the EUR sector (right).

EUR ridges are associated with a clear contrast in the PM_{10} concentration anomalies (lower right panel of Figure 5.1), with decreases north of around 50°N and increases in the south. The negative anomalies in central and northern Europe are considerably smaller than those found for ATL ridges but obey to some of the same reasons, in particular the overall increase in PBL height and wind speeds (top and middle right panels of Figure 5.3). The positive PM_{10} anomalies in the south found for EUR ridges may be partly caused by the stagnation of air masses associated with low mean SLP gradients in the area. There are more locations with significantly positive PM_{10} anomalies in southern Europe on days with EUR ridges than on days with ATL ridges, probably due to the more widespread reduction in PBL heights in the first case. As expected, the reduction in the frequency of precipitation is very marked over Iberia with ATL ridges (lower left panel of Figure 5.3) and extends to other regions of southern Europe, including Italy and the Balkans, on days with EUR ridges (lower right panel of Figure 5.3). Nonetheless, there is not a clear link between the geographic locations of precipitation and PM_{10} anomalies in the south, as the latter tend to be significantly positive only under the presence of EUR ridges. We have not examined whether the intrusion of Saharan dust into southern Europe might be favoured under the presence of ridges, although previous studies have reported a moderate contribution of these types of events to the winter PM_{10} concentrations in the region (e.g. Querol et al., 2009).

It is worthwhile to mention the potential effect of varying anthropogenic emissions under changing meteorological conditions on the observed PM_{10} concentration anomalies. Sousa et al. (2017) reported considerably colder than average winter temperatures over large regions of Europe during blocking days and warmer than average on ridge days. As a consequence, emissions from residential heating should increase on blocking days while the opposite effect is expected for days with ridges. Hence, in addition to the meteorological anomalies already discussed, changes in emissions will likely contribute to the magnitude of the positive PM_{10} anomalies found for EUR blocks and the negative PM_{10} anomalies for ATL ridges.

The previous results might also be sensitive to the methodology used for the calculation of the meteorological and concentration anomalies. As indicated above, these have been calculated at a given location as the difference between all data averaged on days with blocks or ridges in a given sector and the data averaged over the rest of the days. We have investigated whether the seasonal cycle of the PM_{10} concentrations and the meteorological fields may introduce any biases in the results. For that purpose, we have repeated the analyses shown in Figures 5.1 to 5.3, but considering the anomalies at each location as deviations from the daily climatology of the field of interest during the 11-year period. This means that the differences in the fields between days with and without blocks or ridges in a given sector have been calculated separately for each day of the winter months and then averaged over the whole period. Overall, only relatively minor changes have been found in the magnitude and spatial distribution of the anomalies, indicating that the results are not very sensitive to the seasonal cycle.

We have done some additional tests to assess the sensitivity of our analyses to the selection of sites and to the PM_{10} concentrations at each location. This has been done in two different ways. Firstly, we have repeated all the analyses considering only background sites (~ 68 % of the total). The regional patterns and typical values of the PM_{10} anomalies found for them hardly differ from those of Figure 5.1, indicating a minor impact of the station typology on the conclusions presented above. Therefore, the subsequent analyses will continue to include data from the whole dataset, which mixes stations of different types but ensures the best possible data coverage. Secondly, we have normalized the PM_{10} anomalies presented in Figure 5.1 by dividing them by the winter mean concentration at each site (Figure 5.4). The resulting patterns resemble those of the absolute anomalies for most locations, which again indicates that the previous results are not very sensitive to the PM_{10} levels at each site. Nevertheless, the normalized anomalies are relatively larger for some sites in France where the average winter PM_{10} concentrations are generally low (Figure 5.1). As expected, the largest impact, with average positive anomalies of 38 %, is found for EUR blocks, followed by that of ATL ridges, with average negative anomalies of -27% over all sites.

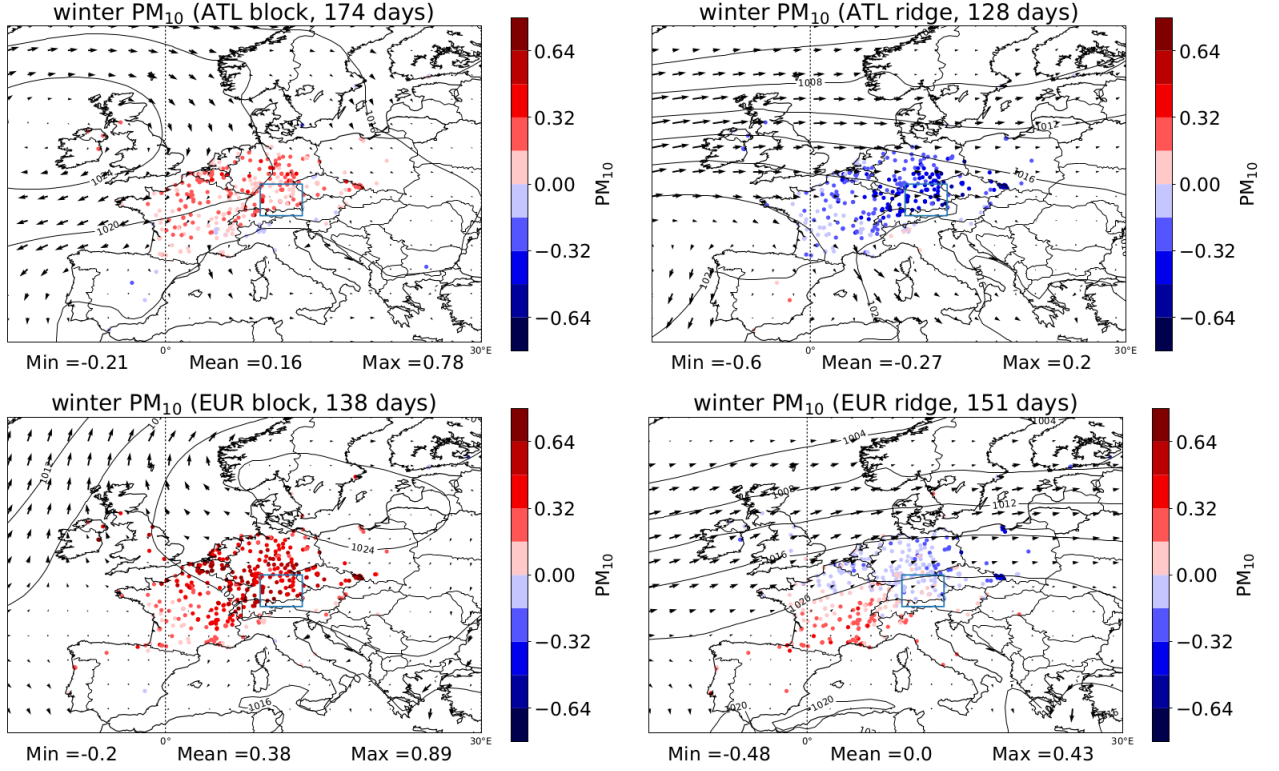


Figure 5.4: Composites of winter PM_{10} normalized concentration anomalies on days with blocks (left) and ridges (right) over the ATL (top) and EUR (bottom) sectors in winter 2000–2010. Results are only shown for statistically significant anomalies (bootstrap resampling method, $p < 0.05$) in Figure 5.1.

Finally, we would like to note that the impact of EUR blocks and ATL ridges is not restricted to winter, as they produce similar effects on the PM_{10} concentrations during the other seasons; however, the anomalies are of smaller magnitude in those seasons than in winter.

5.2 Impact of EUR blocks and ATL ridges on winter PM_{10} extremes

As the strongest influence on the PM_{10} concentrations has been found for EUR blocks (positive anomalies) and ATL ridges (negative anomalies), we will now examine the impact of these two synoptic situations on the highest (90th) and lowest (10th) percentiles of PM_{10} , respectively. In order to do so, we have calculated the percentage of EUR blocking days with PM_{10} concentrations above the 90th percentile of the daily PM_{10} distribution for each site in winter as well as the percentage of ATL ridge days with PM_{10} below the 10th percentile. One would expect that 10 % of the days should show concentrations both above the 90th and below the 10th percentile if these synoptic patterns did not have any impact, but that is clearly not the case as seen in Figure 5.5. The signal is particularly strong for days with EUR blocks (Figure 5.5, left), when the local 90th percentile is exceeded on more than 35 % of the days at many sites in Belgium, some parts of Eastern France, most of Switzerland, the southern half of Germany and the Czech Republic. The number of days with PM_{10} concentrations above the local seasonal 90th percentile even exceeds 50 % at some sites. The influence of ATL ridges on low PM_{10} extremes is not very strong, but there is a region that includes the central-southern part of Germany and the neighbouring countries where the PM_{10} concentrations are below the 10th percentile on more than 25 % of the days with ATL ridges (Figure 5.5, right). Thus, the strongest sensitivity of the average and extreme PM_{10} concentrations to these synoptic patterns is found for central Europe.

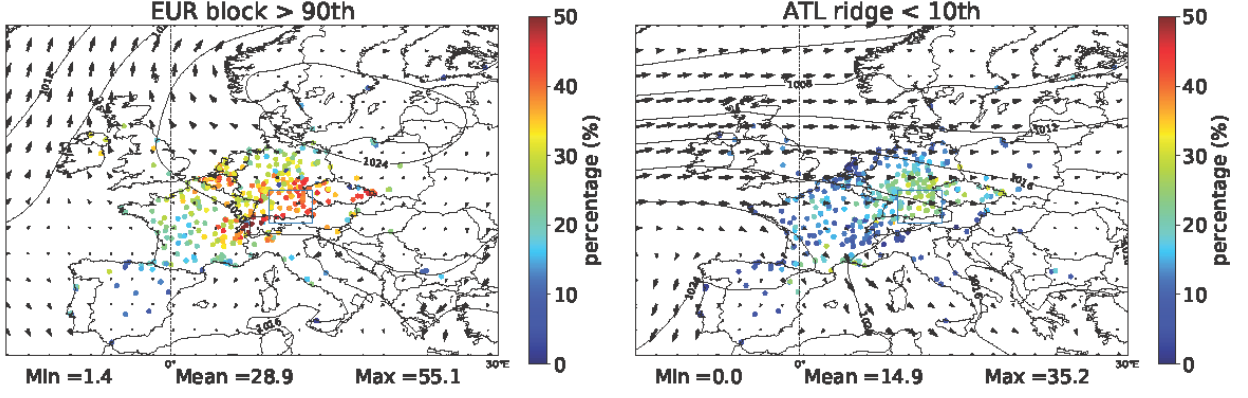


Figure 5.5: Percentage of EUR block days when the 24-h average PM_{10} concentration at each site exceeds the local 90th percentile (left) and percentage of ATL ridge days with 24-h PM_{10} below the local 10th percentile (right) in winter. The black contour lines and arrows respectively represent mean SLP (hPa) and horizontal winds at 10 m.

5.3 Impact of EUR blocks and ATL ridges on the interannual variability of winter PM_{10}

In the previous sections we have quantified the influence that blocks and ridges exert on the average and extreme PM_{10} concentrations at short time scales (daily). Now we will examine whether the frequency of occurrence of these synoptic patterns can also drive the interannual variability of winter PM_{10} . For this purpose, we have modelled the winter mean PM_{10} concentrations at each location as a multiple linear fit on the number of EUR blocks ($nEUR_{blocks}$) and ATL ridges ($nATL_{ridges}$) during each winter:

$$PM_{10} = a + b \cdot nEUR_{blocks} + c \cdot nATL_{ridges} + \epsilon \quad (5.1)$$

where

a: intercept of the model

b, c: coefficients of the total number of blocks/ridges

ϵ : random error

For each specific site we evaluate the significance of both coefficients and only keep $nEUR_{blocks}$ and $nATL_{ridges}$ in the model when the corresponding coefficient is significant ($p < 0.05$). This way we can determine the regions where both synoptic patterns significantly contribute to the interannual variability of PM_{10} and those where only one of them is relevant. The results of the coefficient of determination (R^2) for the sites where there is a significant regression relationship are shown in Figure 5.6.

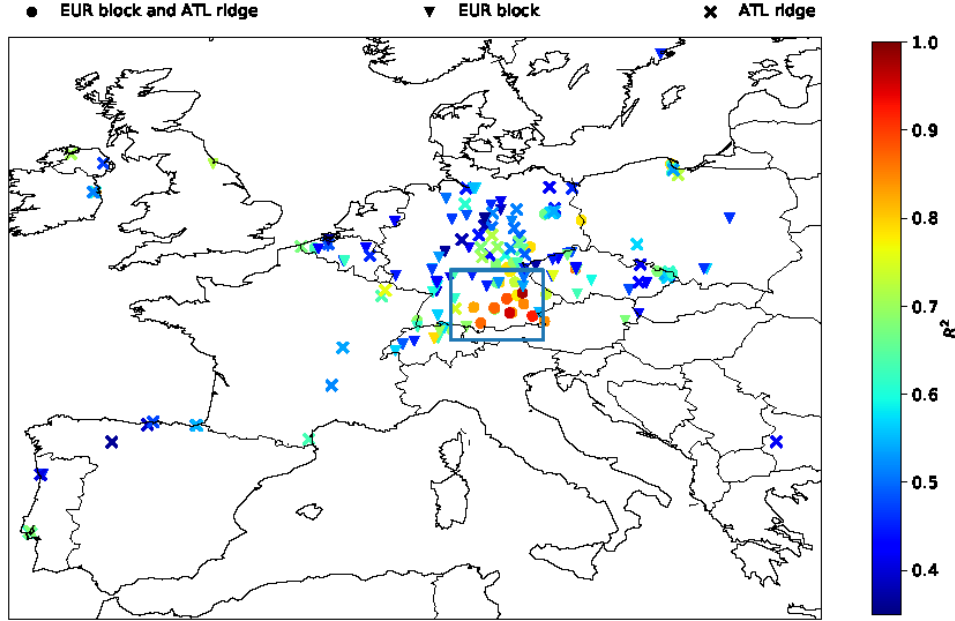


Figure 5.6: Coefficient of determination (R^2) of a multiple linear model fitting the winter mean PM_{10} concentrations at each site on the frequency of occurrence of EUR blocks and ATL ridges during winter 2000–2010 (see Equation 5.1). Circles indicate the locations where both coefficients associated with EUR blocks and ATL ridges are significant. Down triangles are used for sites where only the EUR block coefficient is significant while crosses indicate locations where only ATL ridges are significant. The locations where neither of them is selected by the model are not shown. Significance of the linear regression relationship has been assessed through an analysis of variance ($p < 0.05$). The blue square indicates the location of a region in southern Germany where the response of PM_{10} to blocks and ridges will be analysed in more detail.

As seen from the figure, combining the occurrence of EUR blocks and ATL ridges explains a large fraction of the interannual variability of PM_{10} (circles) for more than half the sites within the blue box in southern Germany, with R^2 values often above 80 %. The impact of EUR blocks is also significant (down triangles) at many sites in western Germany, Switzerland and the Czech Republic, with R^2 values within the range 40–70 %

for most locations. ATL ridges also control the interannual variability of PM_{10} (crosses) at a considerable number of sites in northern and eastern Germany, and have a more moderate impact at some locations in the west of the continent (Ireland, west and north of Iberia, and eastern France).

5.4 Analysis of southern Germany

The previous sections have shown that the winter mean and extreme PM_{10} concentrations in southern Germany (indicated by the blue box in Figure 5.6) experience a particularly strong response to both EUR blocks and ATL ridges at daily and interannual timescales. Following this, in this section we conduct more in-depth analyses for this region. First, we use backward trajectories to investigate the transport pathways of the air masses arriving in the region on days with EUR blocks and ATL ridges. Then we examine changes in the probability density function (PDF) of daily PM_{10} over the whole area under the influence of these patterns as well as the effect of synoptic persistence on the PM_{10} concentrations. Finally, we assess the separate and joint impact of blocks and ridges on the interannual variability of PM_{10} .

5.4.1 Transport pathways of air masses on days with EUR blocks and ATL ridges

The HYSPLIT (Hybrid Single-Particle Lagrangian Integrated Trajectory) version 4.0 dispersion model (Stein et al., 2015), driven by the GDAS (Global Data Assimilation System) meteorological dataset from NCEP, is used in order to investigate the origin of the air masses arriving in the boundary layer of southern Germany on days with EUR blocks and ATL ridges. In particular, we have calculated 5-day backward trajectories at 1 h time steps for Augsburg, Germany (48.37°N, 10.90°E), at 0 meters over the terrain for each winter (DJF) day registering these synoptic patterns during the period December 2004 – February 2010. This site is of urban background type, it is located close to the centre of the blue box from Figure 5.6 and presents a mean PM_{10} concentration of $31.3 \mu g m^{-3}$. On average it experiences a PM_{10} increase of $21.7 \mu g m^{-3}$ (decrease of 16.0

$\mu\text{g m}^{-3}$) on days with EUR blocks (ATL ridges), which indicates the strong contrast that these synoptic patterns exert on the PM concentration at this site. Figure 5.7 shows the residence times (left) and heights (right) of air masses arriving at Augsburg considering only days with EUR blocks (top) and ATL ridges (bottom). The corresponding 5-day backward trajectories can be seen in Figure 5.8.

On days with EUR blocks air masses stay longer over the south-east corner of Germany (see area in red colour in the upper left panel of Figure 5.7) and the transport pathways do not strongly suggest any prevailing wind direction, with a moderate preference for easterly advection (see darker orange colours over Austria and the Czech Republic). On days with ATL ridges there is a prevailing westerly advection, as seen from the higher residence times of the air masses over the south-west of Germany, Switzerland and eastern France (darker orange and red colours in lower left panel of the figure). The western origin of air masses for the ATL ridge case is also evident from the bottom panel of Figure 5.8. In addition, the median heights of the trajectories five days back in time (right panels of Figure 5.7) are above 500 m for ATL ridges and only ~ 100 m for EUR blocks. The differences in the 75th percentiles of the trajectory heights are also considerable: ~ 1750 m for ATL ridges and ~ 700 m for EUR blocks. These results show that on days with EUR blocks air masses arriving in Augsburg have resided within the European boundary for several days, while there is more ventilation and inflow from the Atlantic on days with ATL ridges. The results are in line with the PBL height and 10 m wind speed anomalies reported in Section 5.1 and thus reinforce the previous findings. Note also that, as shown previously, the precipitation anomalies over the region are negative on days with EUR blocks and positive for ATL ridges (lower panels of Figure 5.2 and Figure 5.3). This indicates that washout processes will contribute less than average to a reduction in the lifetime of PM_{10} within the PBL in the case of EUR blocks and more in the case of ATL ridges.

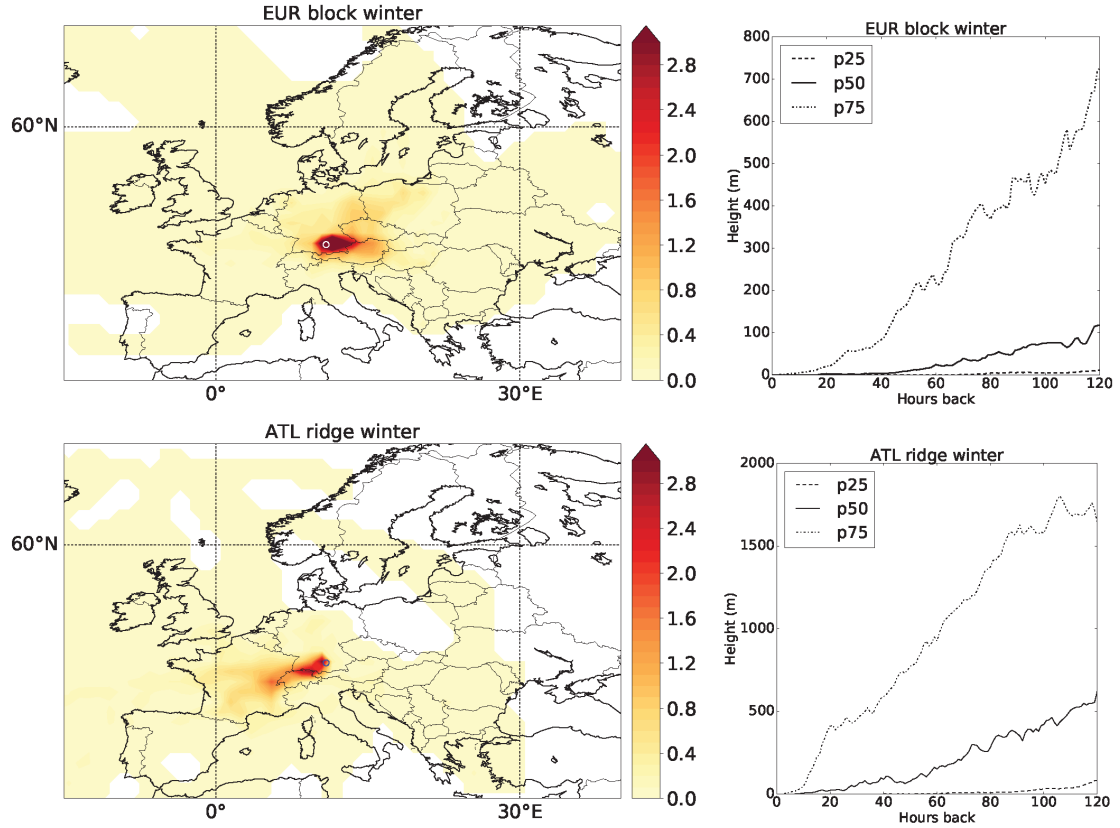


Figure 5.7: Residence times and transport pathways (left) of 5-day backward air masses arriving at Augsburg, Germany, and corresponding trajectory heights (right). The trajectories are separately shown for days with EUR blocks (top) and ATL ridges (bottom) in winter. The circle on the left panels represents the end point of the trajectories and the colour bars indicate residence times (%). The trajectory heights on the right panels correspond to the 75th, 50th (median) and 25th percentiles for each hourly time step. The corresponding 5-day backward trajectories can be seen in Figure 5.8.

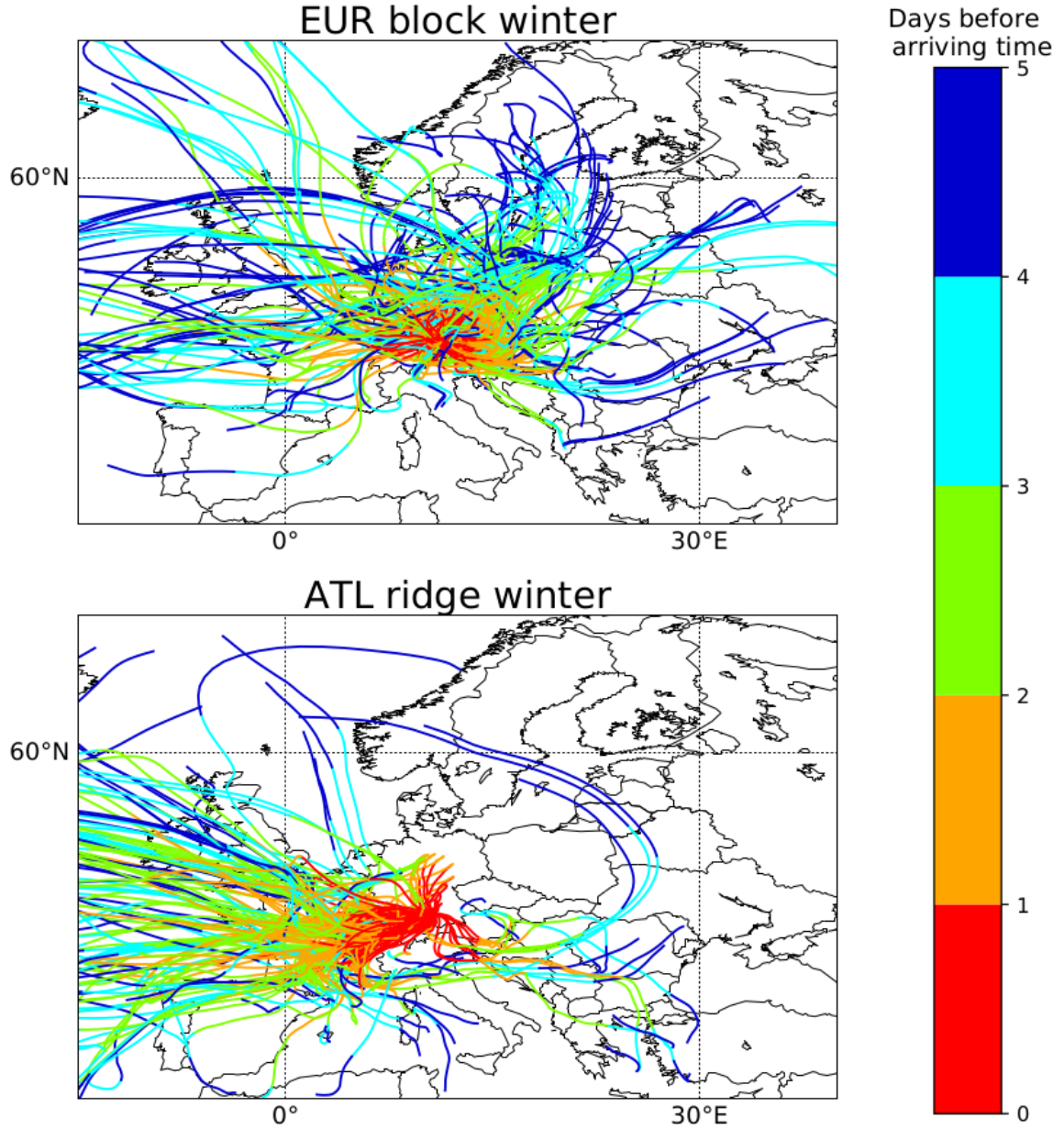


Figure 5.8: 5-day back trajectories corresponding to the residence times seen in Figure 5.7. The colour code indicates the number of days before the arrival of the air masses at Augsburg, Germany, on days with EUR blocks (top) and ATL ridges (bottom). As the panels display the same region as Figure 5.7, the whole trajectory pathways starting 5-days back in time are not shown. Nevertheless, the figure clearly illustrates the more marked continental origin of the air masses on EUR blocking days compared to ATL ridge days.

5.4.2 Changes in the PM_{10} distribution and effect of synoptic persistence

As both the mean and extreme PM_{10} concentrations in the region respond strongly to the presence of EUR blocks and ATL ridges (see Figures 5.1 and 5.5) it is expected that these synoptic patterns affect the whole frequency distribution of PM_{10} . In order to examine this in more detail for southern Germany, Figure 5.9 displays the PDFs of the daily PM_{10} concentrations in that area, considering all winter data (grey bars) as well as winter days with EUR blocks (red line) and ATL ridges (blue line). On days with EUR blocks there exists a reduction in the occurrence of PM_{10} concentrations below $30 \mu g m^{-3}$ and an increase within the range $40\text{--}100 \mu g m^{-3}$, with potential implications for the number of exceedances of the $50 \mu g m^{-3}$ limit value for this pollutant (indicated by a vertical dashed line in the figure). In fact, we have found that, on average over the 35 measurement sites considered in the region, there are around 10 days with exceedances of that threshold during each winter, and that 30 % and 24 % of them correspond to days with blocking centres in the EUR and ATL sectors, respectively. Thus, more than half the winter exceedances occur on days with blocks. On the other hand, under the influence of ATL ridges, the occurrence of very low PM_{10} concentrations ($< 5 \mu g m^{-3}$) increases by a factor of three, but the strongest impact of this synoptic pattern is a reduction in the exceedances of the $50 \mu g m^{-3}$ threshold. The shape of the PDF gets narrower for ATL ridges, while it becomes wider and is displaced to the right on days with EUR blocks, being significantly different from the climatological PDF, with p values well below 0.0001 (two-sample Kolmogorov-Smirnov test). Hence, these two synoptic patterns significantly affect the tails of the distribution of the daily PM_{10} concentrations, with the blocks enlarging and the ridges reducing the upper tail.

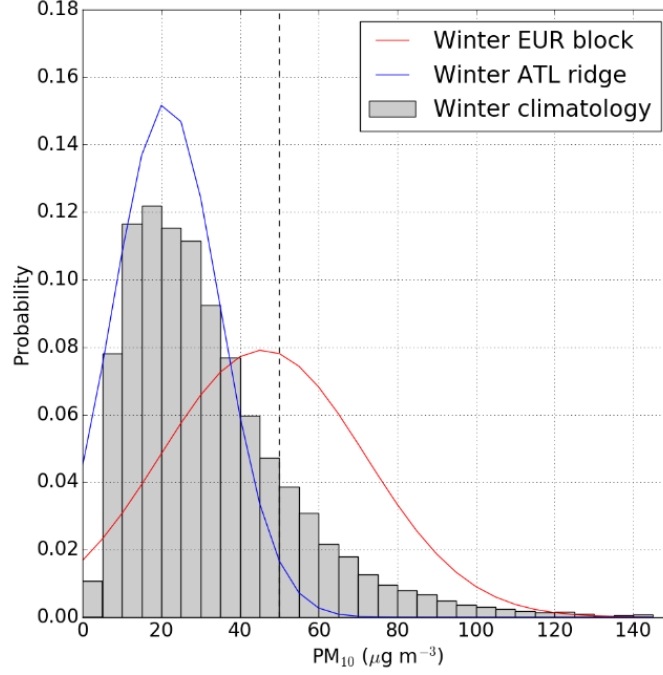


Figure 5.9: Probability density functions (PDFs) of 24-h average PM_{10} concentrations in winter for the 35 measurement stations located inside the blue box from Figure 5.6. Grey bars correspond to the histogram considering all winter days. Red and blue lines represent fits to the data for days with EUR blocks and ATL ridges, respectively. Each bin covers a range of $5 \mu g m^{-3}$. The vertical line at $50 \mu g m^{-3}$ represents the AQ target for PM_{10} averaged over 24 hours.

Both the occurrence and the persistence of blocks and ridges may impact the PM_{10} concentrations. To assess the effect of synoptic persistence in the region, we have evaluated the typical evolution of PM_{10} following the passage of blocks and ridges over a given longitudinal sector. To account for this, the observations have been separately pooled considering the number of days EUR blocks and ATL ridges have stayed in their respective sector. Note that as these synoptic patterns tend to move eastwards, they do not necessarily stay over the same sector during their whole lifetime. Therefore the number of cases considered will decrease day after day. The results are only shown for EUR blocks in Figure 5.10. There is an overall build-up of PM_{10} in the area during the days blocks stay in the EUR sector, with increases in the median values from $30 \mu g m^{-3}$ on day 1 to more than $45 \mu g m^{-3}$ on day 5. The PM_{10} median concentration for EUR blocks is clearly higher than the climatological median (horizontal full line) and even exceeds the climatological 75th percentile (horizontal dash-dotted line) from the second day on. Conversely, the PM_{10} median concentration on days with ATL ridges is below the

climatological 25th percentile from the first day, but the impact of persistence is almost negligible in this case (Figure A6). Our results for winter PM_{10} are in the same line as previous analyses which found a strong build-up of the surface ozone concentrations during summer under the influence of blocks compared to ridges (Ordóñez et al., 2017). The reason for this may lie in the nature of blocks and ridges, as the first are persistent, quasi-stationary anticyclonic structures, while the latter tend to be more transient. In addition, for the particular case of winter PM_{10} analysed here, it is expected that the dilution of the pollutant concentrations, as a consequence of above-average ventilation, in the case of ridges has a weaker dependence on persistence than the gradual build-up of pollution under stable blocking conditions.

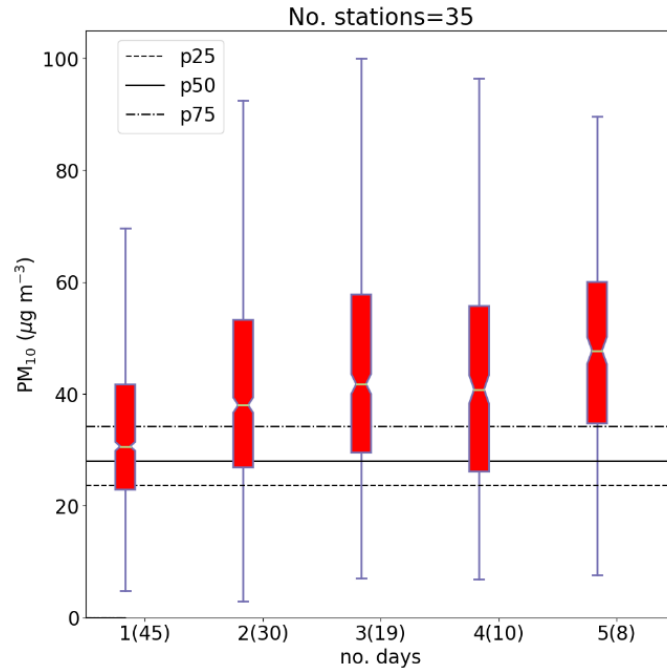


Figure 5.10: Evolution of the winter daily PM_{10} concentrations considering all stations within the blue box in Figure 5.6 under the influence of EUR blocks. The PM_{10} data are separately pooled considering the number of days (from one to five, see x axis) blocks stay over the EUR sector, in order to illustrate the effect of synoptic persistence on the day-to-day evolution of the PM_{10} concentrations. The numbers in brackets represent the number of days considered in each case. The boxes extend from the lower (Q1) to upper (Q3) quartile values of the data, with a line indicating the position of the median. The whiskers extend from the box to show the range of the data, from (Q1-1.5 IQR) to (Q3+1.5 IQR) (IQR = Interquartile range). The horizontal lines represent Q1, median (Q2) and Q3 of the winter PM_{10} concentrations considering all data.

5.4.3 Interannual variability

In Section 5.3 we showed that the combined effect of EUR blocks and ATL ridges seems to control a large fraction of the interannual variability of PM_{10} at many locations in southern Germany during the 11-year period of analysis. In fact, this is the only region where the joint effect of both patterns tends to be significant, with high R^2 values even exceeding 80 % at some sites (see orange and red circles within blue square of Figure 5.6). Following this, first we will separately compare the interannual variability of winter mean PM_{10} averaged over this region to that of EUR blocks and ATL ridges, to later examine the combined effect of these patterns. For these analyses, the seasonal mean has been removed to focus on synoptic-scale correlations. The resulting seasonal anomalies have then been detrended by subtracting the year-to-year change expected from a linear trend (using ordinary least squares regression), in order to minimize the potential influence of changing anthropogenic emissions on the PM concentrations.

The left panel of Figure 5.11 strongly suggests that the interannual variability of winter PM_{10} (black line) is linked to the frequency of occurrence of EUR blocks (red line, $R^2 = 73\%$) and, to a lesser extent, to that of ATL ridges (blue line, $R^2 = 50\%$). As expected, these synoptic patterns have an opposite impact on the interannual variability of PM_{10} . The highest PM_{10} concentrations are found in winters with high occurrence of blocks and low occurrence of ridges (e.g. 2003 and 2006), while the lowest concentrations often coincide with low occurrence of blocks and high occurrence of ridges (e.g. 2000 and 2007). Consequently, even though blocks exert a stronger influence, both patterns contribute to determining the occurrence of years with anomalously high or low PM_{10} concentrations. This is not surprising as the presence of both EUR blocks and ATL ridges affects the whole frequency distribution of daily PM_{10} over the region (Figure 5.9).

The joint effect of EUR blocks and ATL ridges has been examined by fitting the anomalies of the winter PM_{10} concentrations on those of the frequency of occurrence of these patterns through a multiple linear model like that of Equation 5.1. The intercept and coefficients of the model have then been used to reproduce the interannual variability

of PM_{10} . The right panel of Figure 5.11 displays the time series of the observed (solid line) and modelled (dashed line) PM_{10} anomalies. The model reproduces the observations remarkably well for most years and the coefficient of determination ($R^2 = 0.86$) is within the range of values observed for individual sites (see blue square in Figure 5.6).

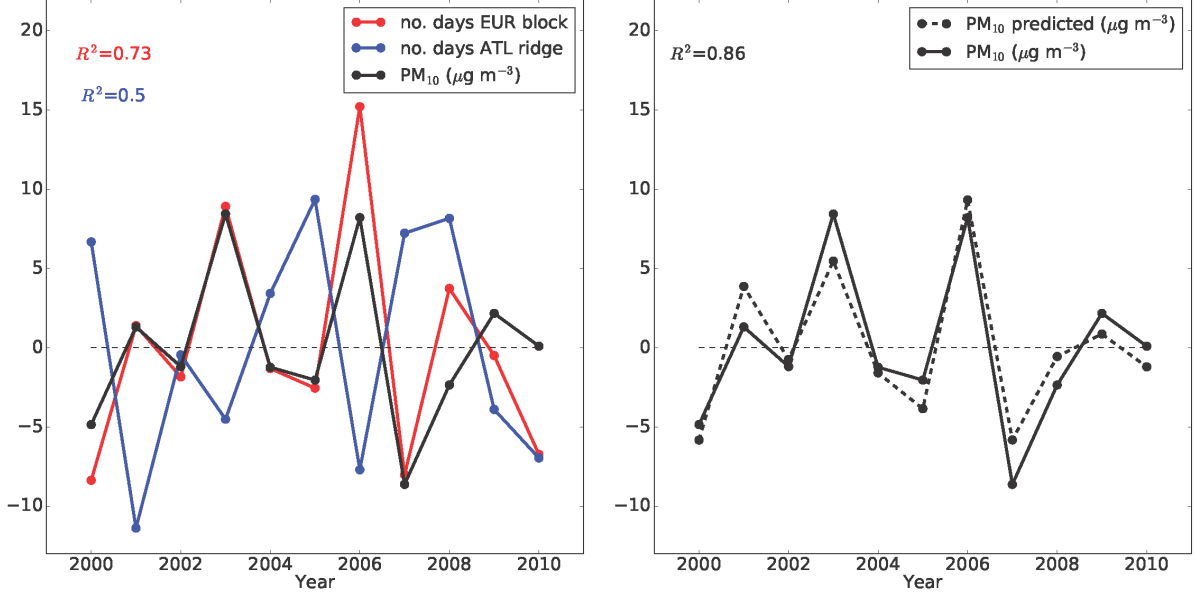


Figure 5.11: Left panel: Anomalies of both the observed winter (DJF) mean PM_{10} concentrations in southern Germany (averages over all sites within the blue box from Figure 5.6, black line) and the frequency of occurrence of EUR blocks (red line) and ATL ridges (blue line). Right panel: Anomalies of winter mean PM_{10} within the region as derived from the observations (solid line, same as in left panel) and by a multiple linear model on the frequency of occurrence of EUR blocks and ATL ridges (dashed line). The long-term trend has been removed from all data.

To put our results into a broader perspective, we have compared them to those from other studies which have examined the impact of atmospheric circulation on the interannual variability of the PM concentrations. Examples of previous findings for Europe, China and the US are mentioned here. Pausata et al. (2013) compared modelled winter $PM_{2.5}$ anomalies in Europe with the NAO index from 1980 to 2005, finding positive correlations (R^2 from 0.21 to 0.46) for locations in the south of the continent and negative correlations for sites in central ($R^2 = 0.06$) and northern ($R^2=0.18$) Europe. Jia et al. (2015) created a new Siberian High position index whose interannual variability is strongly linked to that of wintertime AOD over Northern China ($R^2 = 0.42 - 0.62$). Tai

et al. (2012b) showed that the median mid-latitude cyclone period controls the interannual variability of annual average $PM_{2.5}$ in the Midwest of US ($R^2 = 0.58$). More recently, Shen et al. (2017) combined local meteorological parameters and synoptic circulation patterns as predictors in a multiple linear regression model to reproduce the monthly mean $PM_{2.5}$ concentrations across the US, finding R^2 values of 0.50–0.65 around the Midwest. Our results also show evidence of the impact of mid-latitude large-scale circulation on the interannual variability of PM. The impact of EUR blocks on PM_{10} over the south of Germany ($R^2 = 0.73$, left panel of Figure 5.11) is particularly strong compared to the figures reported by the previous studies and the explained variance rises up to 86 % if ATL ridges are also considered (right panel of the figure). In addition, the interannual variability of the PM_{10} concentrations at a considerable number of sites over a broader region comprising Belgium, Germany, Switzerland and the Czech Republic follows the frequency of occurrence of EUR blocks and/or ATL ridges (Figure 5.6).

5.5 Main findings and discussion

In this chapter we have examined the regional responses of winter PM_{10} to the occurrence, position and persistence of blocks and ridges in the Euro-Atlantic region. The strongest impact on the PM_{10} concentrations has been found in central Europe and, to a lesser extent, north-western Europe, for EUR blocks and ATL ridges. EUR blocks are associated with poor ventilation of the boundary layer as well as reduced vertical mixing and precipitation over those regions, eventually yielding positive PM_{10} anomalies, which average $12 \mu g m^{-3}$ and even reach $50 \mu g m^{-3}$ at some locations. The enhanced zonal flow and increase in the occurrence of precipitation over north-western Europe on days with ATL ridges favour the horizontal and vertical dispersion as well as the washout of pollutants, decreasing PM_{10} concentrations on average by $8 \mu g m^{-3}$ and up to $45 \mu g m^{-3}$ at some locations. The large PM_{10} anomalies are therefore induced by changes in the meteorology, although they are also likely enhanced by changes in emissions from residential heating, as these are expected to increase under the colder than average conditions that prevail during blocking situations in winter and decrease with the milder

temperatures often found under the influence of ridges.

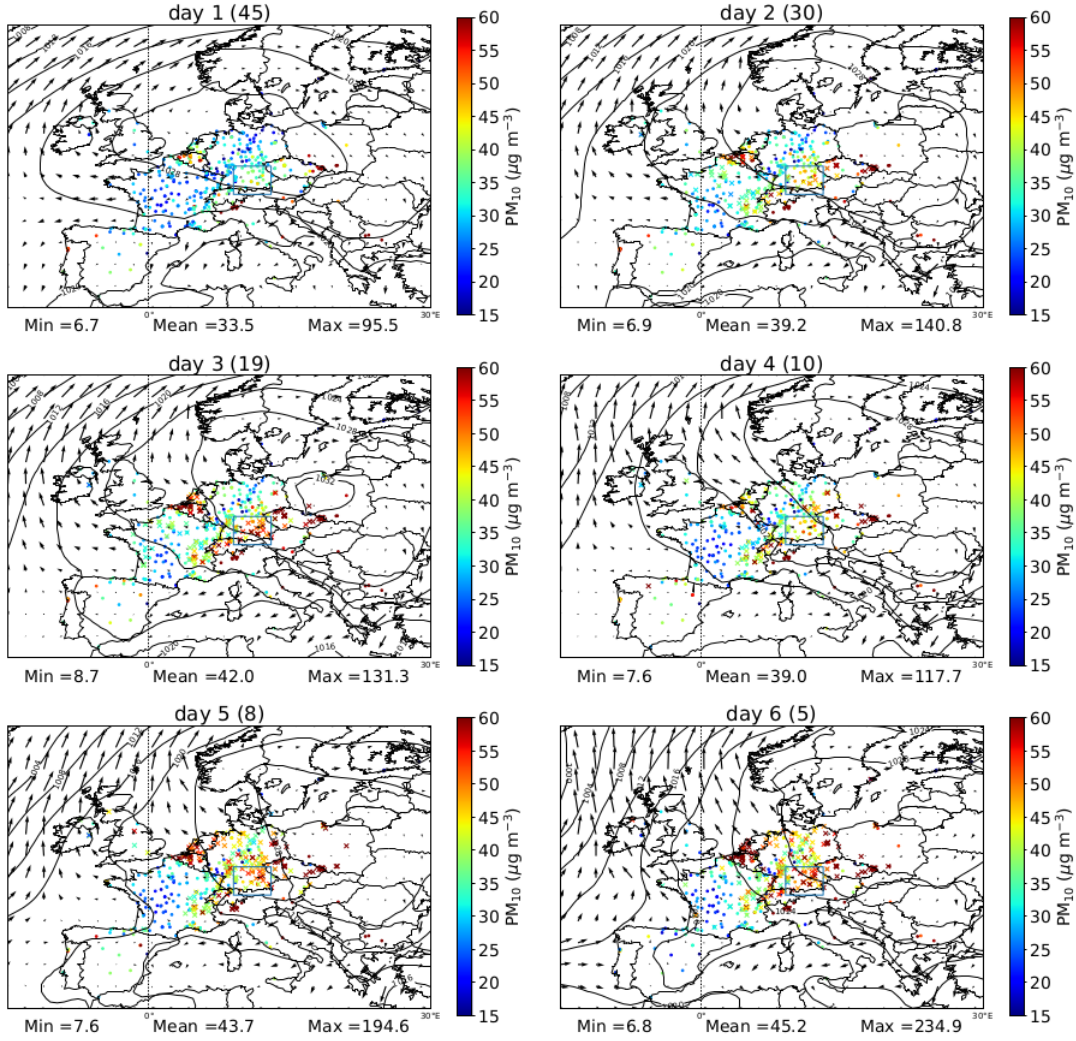


Figure 5.12: Evolution of PM_{10} concentrations under the influence of EUR blocking in winter. The panels show, from left to right and from top to bottom, the average concentrations on each of the first six days a blocking centre is in the sector. The total number of blocks considered is given in brackets on the top of each panel. Crosses indicate stations where the PM_{10} composite under blocking exceeds the 90th of the winter distribution at each location.

These synoptic patterns not only affect the mean PM_{10} concentrations but also the whole range of the PM_{10} distribution, with EUR blocks (ATL ridges) increasing (reducing) the occurrence of exceedances of the $50 \mu\text{g m}^{-3}$ AQ threshold, and more than 35 % of the days with EUR blocks recording exceedances of the local 90th percentile of the winter PM_{10} distribution at many sites in central Europe. Overall, the impact of these

patterns on PM_{10} is stronger than that found by Ordóñez et al. (2017) for O_3 in the same season. Both studies also indicate that the persistence of blocks is more relevant than that of ridges for the evolution of the pollutant concentrations. This has potential implications for the predictability of elevated PM_{10} concentrations and PM_{10} extremes during winter, as both of them increase day after day during the occurrence of blocks within the EUR sector. This occurs not only for sites located in southern Germany (Figure 5.10) but also over a larger region that comprises most of Germany and part of the surrounding countries (Figure 5.12). The latter figure shows that, from the first to the sixth day blocks stay in the EUR sector, there is a notable increase in the number of stations exceeding $\sim 45 \mu g m^{-3}$ (orange and red colours) and the 90th percentile of the winter concentrations (crosses). This result should be interpreted with caution due to the small data sample (only 5 cases of blocking centres remaining 6 days in the EUR sector). Future work on this could benefit from the use of ensembles of long simulations by chemical transport models (CTMs) or chemistry–climate models (CCMs), which would provide long enough datasets to assess the impact of the meteorological persistence of blocks on the build-up of pollution under controlled conditions (e.g. unchanged emissions).

Finally, we have shown that the interannual variability of winter PM_{10} at many sites in southern Germany can be explained by the combined effect of the frequency of occurrence of EUR blocks and ATL ridges ($R^2 > 80 \%$), while other locations of the continent are more sensitive to only one of these patterns. In particular, the interannual variability of winter PM_{10} at many sites in western Germany, Switzerland and the Czech Republic is linked to that of EUR blocks ($R^2 = 40\text{--}70\%$), while ATL ridges have some effect at locations in the western part of the continent as well as in northern and eastern Germany. Although one must be cautious due to the relatively short time series used here, overall, the impact of blocks and ridges on the interannual variability of the winter PM concentrations in Europe is considerably larger than that previously reported by Pausata et al. (2013) for the NAO index. To summarize, the occurrence of EUR blocks and, to a lesser extent, ATL ridges, is closely related to the day-to-day and interannual variability of the winter PM_{10} concentrations over western and central Europe. Thus, these synoptic patterns serve as dynamical indicators of the evolution of PM_{10} at different time scales.

6 The differing impact of air stagnation on summer ozone across Europe

As presented in the Introduction, a previous study has reported that the ozone response to stagnation appears to be weak over some regions of the US (Kerr and Waugh, 2018). In Chapter 3, we have shown a strong build-up of ozone during widespread stagnant episodes, but there is considerable spatial heterogeneity across Europe and further analyses are needed. Since daily maximum temperature is the most correlated meteorological variable with summer daily ozone maxima (Bloomfield et al., 1996; Xu et al., 1996; Kuebler et al., 2001; Tarasova and Karpetchko, 2003; Ordóñez et al., 2005), this chapter examines the joint impact of daily maximum temperature and air stagnation on ozone over eight regions of Europe (BRIT, NCE, NSC, BALT, IBE, WE, SCE, EE; see Section 2.4) for the 18 summers (JJA) during the period 1998 – 2015. For that purpose, we have used the simplified ASI defined by Horton et al. (2012). The choice of HO_ASI instead of WA_ASI or HU_ASI is justified by the fact that the latter are specifically adapted to particulate matter (Wang et al., 2016, 2018; Huang et al., 2018). In addition, as seen in Chapter 4, the former index outperforms both WA_ASI and HU_ASI in the case of PM during summer. The results of this chapter can be found in Garrido-Perez et al. (2019).

6.1 Relationship between *MDA8 O₃*, temperature and stagnation

Table 6.1 shows the Pearson correlation coefficients (R) between the daily time series of average Tmax, average *MDA8 O₃* and the percentage of the area under stagnant conditions for each region in summer. The significance of these correlations has been determined through two-tailed t-tests as indicated in von Storch and Zwiers (1999), taking into account that the data exhibit serial correlation, i.e. the daily values of these variables are not independent of their own future and past values because of the effect of the meteorological persistence (see e.g. Wilks, 2011). This implies that the effective number of degrees of freedom (ν_{eff}) is lower than that directly determined from the sample size, increasing the p-value of the test and reducing the level of statistical significance. Accordingly, we have calculated ν_{eff} following equation 1 of Hu et al. (2017) before assessing significance. This way, the three fields significantly correlate at the 95% confidence level for all regions, with the exception of the stagnation – *MDA8 O₃* correlation in NSC. However, there is considerable spatial heterogeneity across Europe, with higher correlations in the central/southern clusters (IBE, WE, SCE and EE) than in the northern clusters (BRIT, NCE, NSC and BALT). The correlations are above 0.5 over the central/southern regions, with the exception of Tmax – *MDA8 O₃* in IBE and Tmax – stagnation in EE, while they tend to be well below that value for the northern regions. As expected, the correlations of *MDA8 O₃* with Tmax are higher than with the percentage of stagnant area for most regions, although the latter can be considered as a good predictor of ozone in central/southern Europe. On the other hand, Tmax and stagnation present high correlations in the southern clusters as well as in NCE, evidencing the strong covariability between both variables. Hence, it is unclear whether the high correlations between *O₃* and stagnation in the southern regions reflect the ozone–temperature relationship or are due to other processes.

Table 6.1: Pearson product-moment correlation coefficients (R) between the daily time series of average Tmax, average *MDA8 O₃* and the percentage of stagnant area (AS) for each region during summer (JJA) 1998 – 2015. The geographical locations of the regions are displayed in Figure 2.3 (right panel). All values are statistically significant at the 95% confidence level, except where noted by asterisk (*).

	BRIT	NCE	NSC	BALT	IBE	WE	SCE	EE
Tmax – <i>MDA8 O₃</i>	0.18	0.52	0.35	0.48	0.42	0.70	0.77	0.73
AS – <i>MDA8 O₃</i>	0.24	0.39	0.06*	0.27	0.56	0.62	0.70	0.50
Tmax – AS	0.23	0.47	0.24	0.33	0.51	0.53	0.58	0.44

To try to understand the influence of air stagnation in the Tmax – *MDA8 O₃* relationship, we have evaluated if this relationship changes with the occurrence of stagnation. For this purpose, we have first computed the correlation coefficients between the daily time series of Tmax and *MDA8 O₃* for each grid cell, considering stagnant and non-stagnant days separately (Figure 6.1). The spatial distribution of the correlations displayed in the figure is consistent with that shown in Table 6.1, as the highest values are generally found for WE, SCE and EE. Nevertheless, Figure 6.1 presents a complex picture of the effect of stagnation on the Tmax – *MDA8 O₃* relationship across Europe. On the one hand, stagnation seems to contribute to strengthening this relationship over large parts of the three regions that present high correlations. Regions characterized by relatively low ozone levels and stagnation frequency during summer (e.g. the UK and NCE, see Figure 2.3 and top panels of Figure 4.3) also present higher correlations when stagnation occurs. These results are in line with a previous study that has highlighted the contribution of stagnation to increasing the probability of occurrence of a high ozone day given a high-temperature day in the US (Sun et al., 2017). On the other hand, there are some parts of the south and east of the continent where these correlations do not increase with the occurrence of stagnation. The correlations even decrease over an area roughly covering the southeastern half of IBE, where stagnation is relatively common in summer (see top panels of Figure 4.3) and the day-to-day ozone variability – as measured by the relative standard deviation of summer *MDA8 O₃* – is lower than in the rest of the continent.

From these results, no clear conclusions can be drawn on the contribution of stagnation to the ozone–temperature relationship. Actually, these correlations may depend on a number of factors whose effects are difficult to disentangle. First, the range of variability of both daily temperature and ozone differs considerably across Europe. Second, the ozone–temperature relationship tends to be linear only within specific temperature ranges (e.g. Bloomer et al., 2009), high enough to favour photochemical production but below some high thresholds that may lead to ozone suppression at some locations (Steiner et al., 2010; Shen et al., 2016; Meehl et al., 2018). Finally, the strengthening of the O_3 –Tmax correlations under stagnant conditions found for some regions might partly occur because elevated temperatures often coincide with stagnant days. Henceforth, to remove as much as possible the influence of the different factors that limit our understanding of the impact of stagnation on ozone, we will perform composite analyses within specific temperature bins separately for each region.

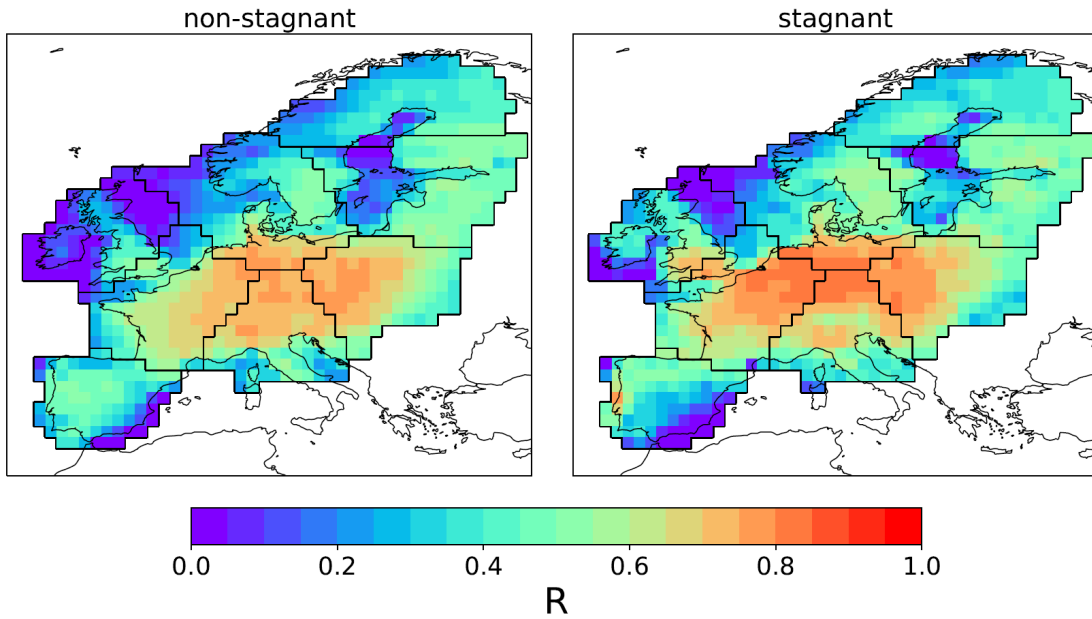


Figure 6.1: Pearson product-moment correlation coefficient (R) between the 1998 – 2015 summer (JJA) daily time series of Tmax and $MDA8\ O_3$ for days without (left) and with (right) stagnation in each grid cell.

Figure 6.2 shows boxplots of $MDA8\ O_3$ within $3\ ^\circ\text{C}$ temperature bins for days with (red) and without (blue) stagnation, considering every grid cell within each region. Overall, the relationship of ozone with temperature starts to be linear above ~ 16

°C, with R^2 values above 0.93 for all regions. The ozone distributions under stagnant and non-stagnant conditions are significantly different at the 95% confidence level for most temperature bins and regions, as determined through the two-sample Kolmogorov-Smirnov test and indicated by stars on top of the pairs of boxes. In central/southern Europe, the presence of stagnant conditions causes consistently higher *MDA8 O₃* mixing ratios regardless of the temperature bin (around 4–6 ppb on average considering the mean values of each bin), but this is not always the case for the northern regions. For instance, ozone is significantly reduced on stagnant days within 24–27 °C in BRIT or above ~21 °C in NSC, and there is a minor impact of stagnation on ozone within 21–30 °C in BALT. Furthermore, stagnation does not seem to exert a significant impact within 27–30 °C in that region and 24–27 °C in NCE.

To understand these results we have compared the typical circulation patterns in the lower troposphere for stagnant and non-stagnant days in all regions. As stagnant conditions in the reanalysis are determined on a grid cell by grid cell basis, we have first identified a representative location for each region and then produced composite maps of daily SLP and 850 hPa wind, considering stagnant and non-stagnant days at each location. For the selection of such locations we have looked for the land grid cells where the correlation between the daily time series of standardized anomalies of summer *MDA8 O₃* and that of the respective centroid (i.e. time series of the average standardized anomalies within the cluster) maximize. The choice of standardized anomalies instead of absolute values of *MDA8 O₃* is justified by the fact that the former were used for the identification of the regions used here (Carro-Calvo et al., 2017). The eight representative locations are displayed as circles in Figure 2.3 (right panel). Then we have composited SLP and 850 hPa wind data for stagnant and non-stagnant days at each location with *T_{max}* within 20–25 °C. This temperature interval has been chosen because it is typical of fair weather conditions favourable for ozone production in northern Europe. Moreover, around 22–44% of the summer days lay within this temperature range at 7 out of the 8 locations, with the exception of only ~3% of the days for the grid cell in BRIT. Consequently, this temperature interval also guarantees a representative enough number of occurrences to draw solid conclusions for most locations.

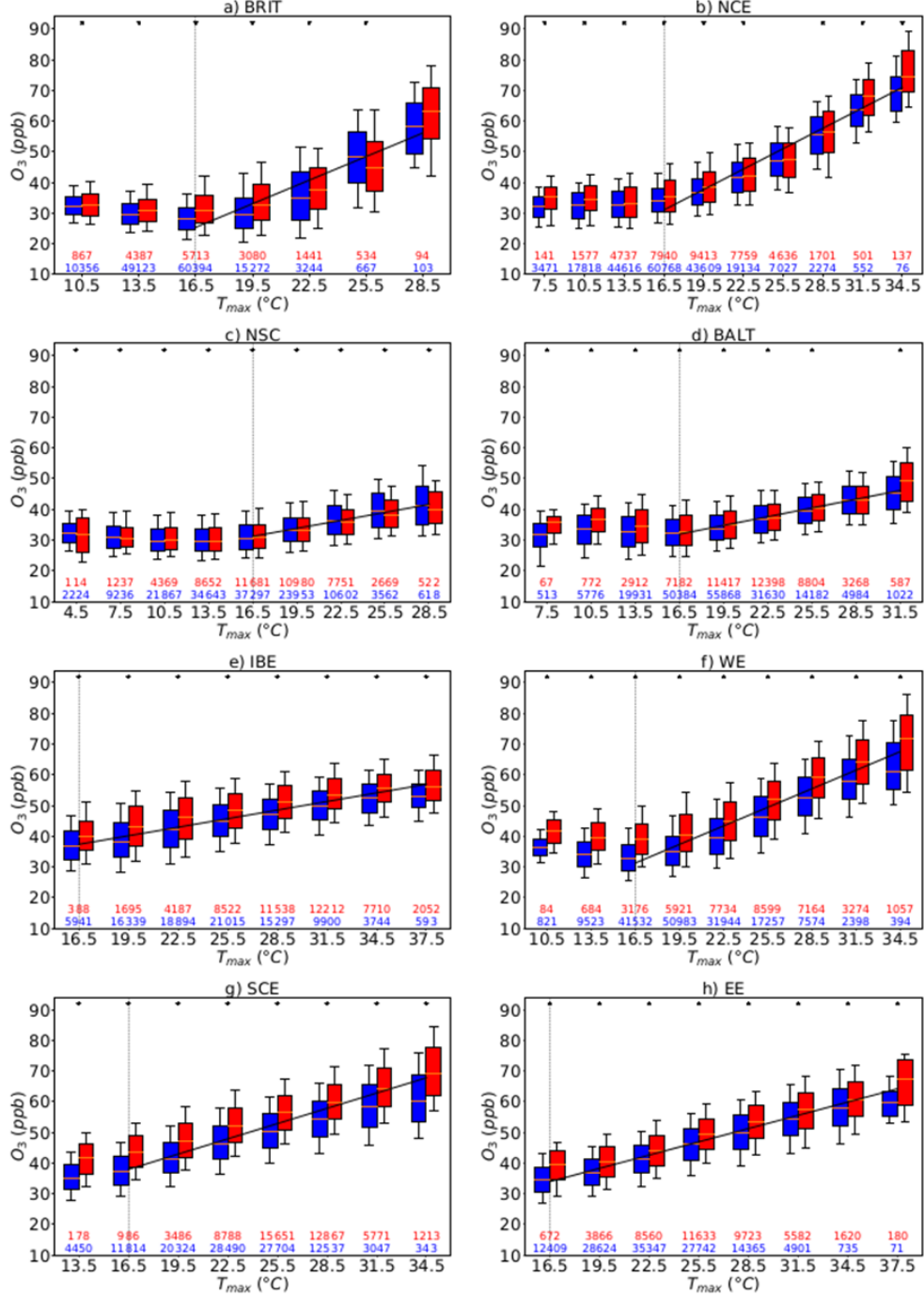


Figure 6.2: Boxplots of 1998 – 2015 summer $MDA8 O_3$ in 3 °C bins of T_{max} , considering all grid cells in each region. Blue (red) boxes represent days classified as non-stagnant (stagnant). The boxes extend from the lower (Q1) to the upper (Q3) quartile values of the data, with a horizontal line indicating the position of the median (Q2). The whiskers extend from the boxes to show the range of the data between the 10th and 90th percentiles. The x-axis tick labels represent the middle point for each temperature bin. Temperature bins are only shown if they include at least 50 cases (number of cases = number of days × number of sites) for both stagnant and non-stagnant conditions; as a result, the range of temperatures shown on the x-axis varies with the region. The numbers of stagnant (red) and non-stagnant (blue) cases are indicated below the corresponding temperature bins. Black stars are shown over each pair of boxes if their $MDA8 O_3$ distributions are significantly different at the 95% confidence level (determined through the two-sample Kolmogorov-Smirnov test). The vertical dotted lines indicate the temperature bins with centres at 16.5°C. Linear regressions of the mean $MDA8 O_3$ within each temperature bin (considering both stagnant and non-stagnant cases) on T_{max} (mid-points of the intervals) have been drawn for the temperature bins $\geq 16.5^\circ\text{C}$.

Figures 6.3 and 6.4 respectively illustrate the circulation patterns on stagnant and non-stagnant days within the mentioned 20–25 °C temperature range in the northern locations (BRIT, NCE, NSC and BALT). As expected, air stagnation situations are characterized by anticyclonic circulation and weak wind in the lower troposphere over the affected regions (Figure 6.3). The composite for NCE during non-stagnant days (Figure 6.4b) displays westerly to southwesterly flow from the North Sea to the region. This situation enhances the transport of relatively clean marine air masses to the receptor region, resulting in ozone levels somewhat below those of stagnant days (Figure 6.2b). On the other hand, BRIT, NSC and BALT are under the effect of southerly advection during non-stagnant days (Figure 6.4, a, c, d) and, as shown above, do not display clear enhancements of $MDA8\ O_3$ (Figure 6.2, a, c, d) despite the low wind speeds found on stagnant days (Figure 6.3, a, c, d). The results for these three regions are in line with the findings by Carro-Calvo et al. (2017), who reported that ozone extremes (exceedances of the summer 95th percentile) in the north of the continent tend to be at least partly caused by the advection of polluted, warm air masses from central/southern regions. This is consistent with the strong meridional gradient of summer $MDA8\ O_3$ in Europe (see Figure 2.3). In the receptor regions, wind speeds are relatively high under such situations, which means that high ozone days often concur with non-stagnant days. This explains the unclear impact of stagnation on $MDA8\ O_3$ within some temperature bins in northern Europe. However, as anticipated before, the results for BRIT should be interpreted with caution because of the reduced data sample (only around 3% of the summer days with temperatures within 20–25 °C, less than one third of them with stagnation). In the case of central-southern Europe, stagnant days are associated with lower wind speeds than non-stagnant days for all regions, as well as with a suppression of westerly advection over WE and EE (see Figures 6.5 and 6.6).

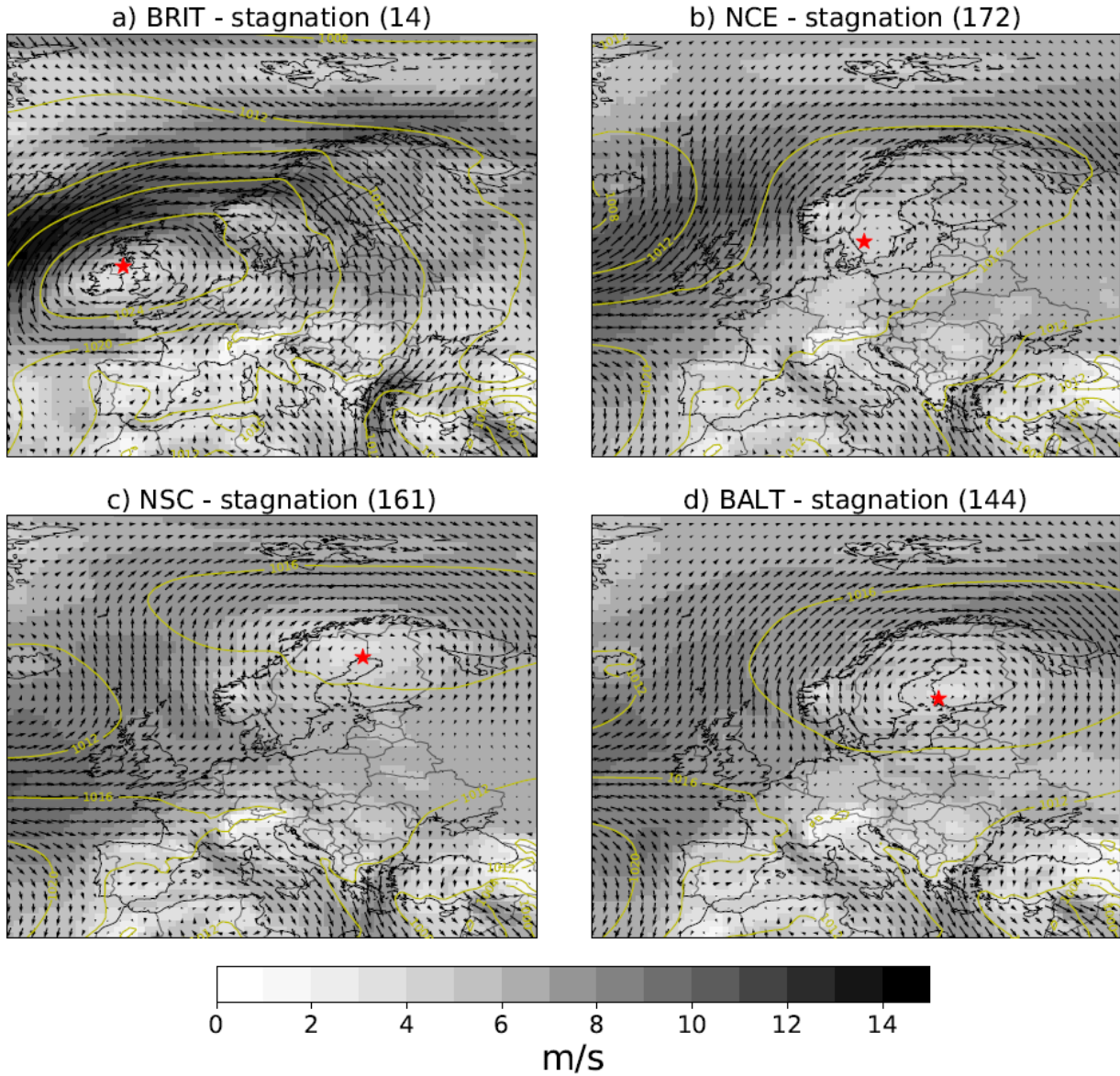


Figure 6.3: Composites of SLP and 850 hPa wind speed on days with stagnant conditions and T_{\max} within $20 - 25^{\circ}\text{C}$, at the representative locations (red stars) of BRIT, NCE, NSC and BALT, during the summer months from 1998 to 2015. The yellow contour lines, grey shading and arrows respectively represent SLP (hPa), and module and vectors of 850 hPa wind speed (m/s). The numbers in brackets represent the number of days considered in each composite.

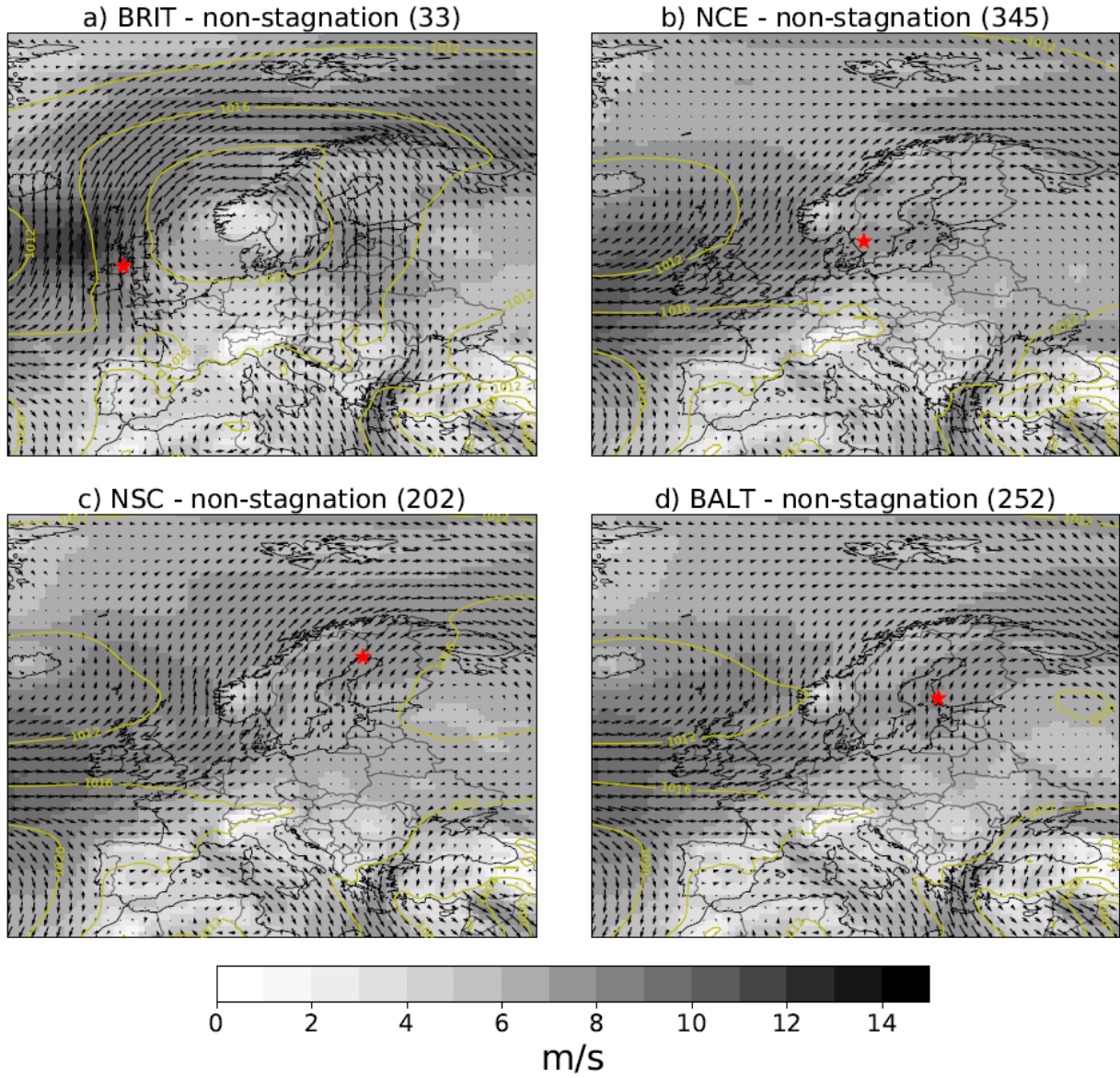


Figure 6.4: As Figure 6.3 but for non-stagnant days.

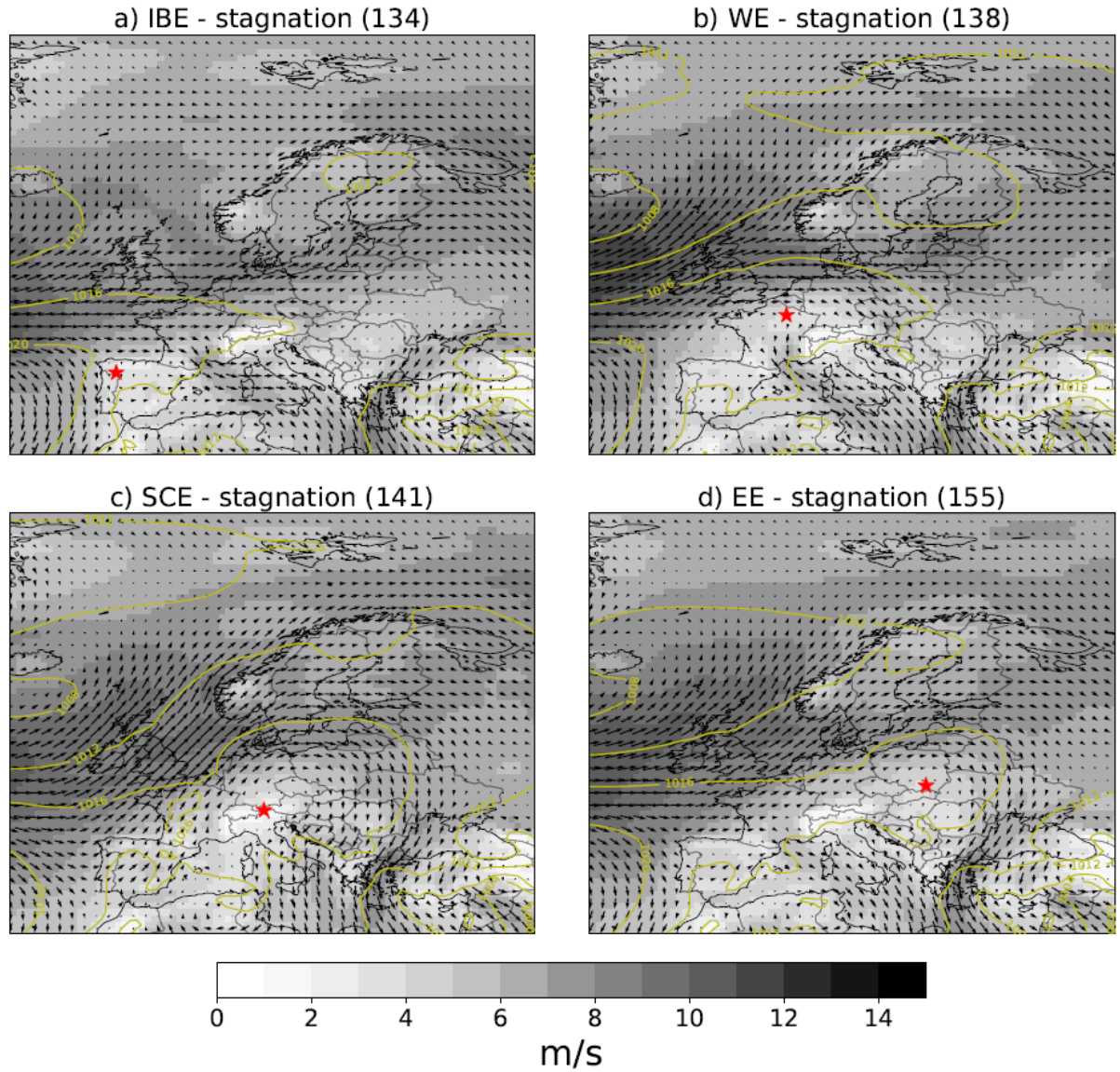


Figure 6.5: As Figure 6.3 but for stagnant days at the representative locations of IBE, WE, SCE and EE.

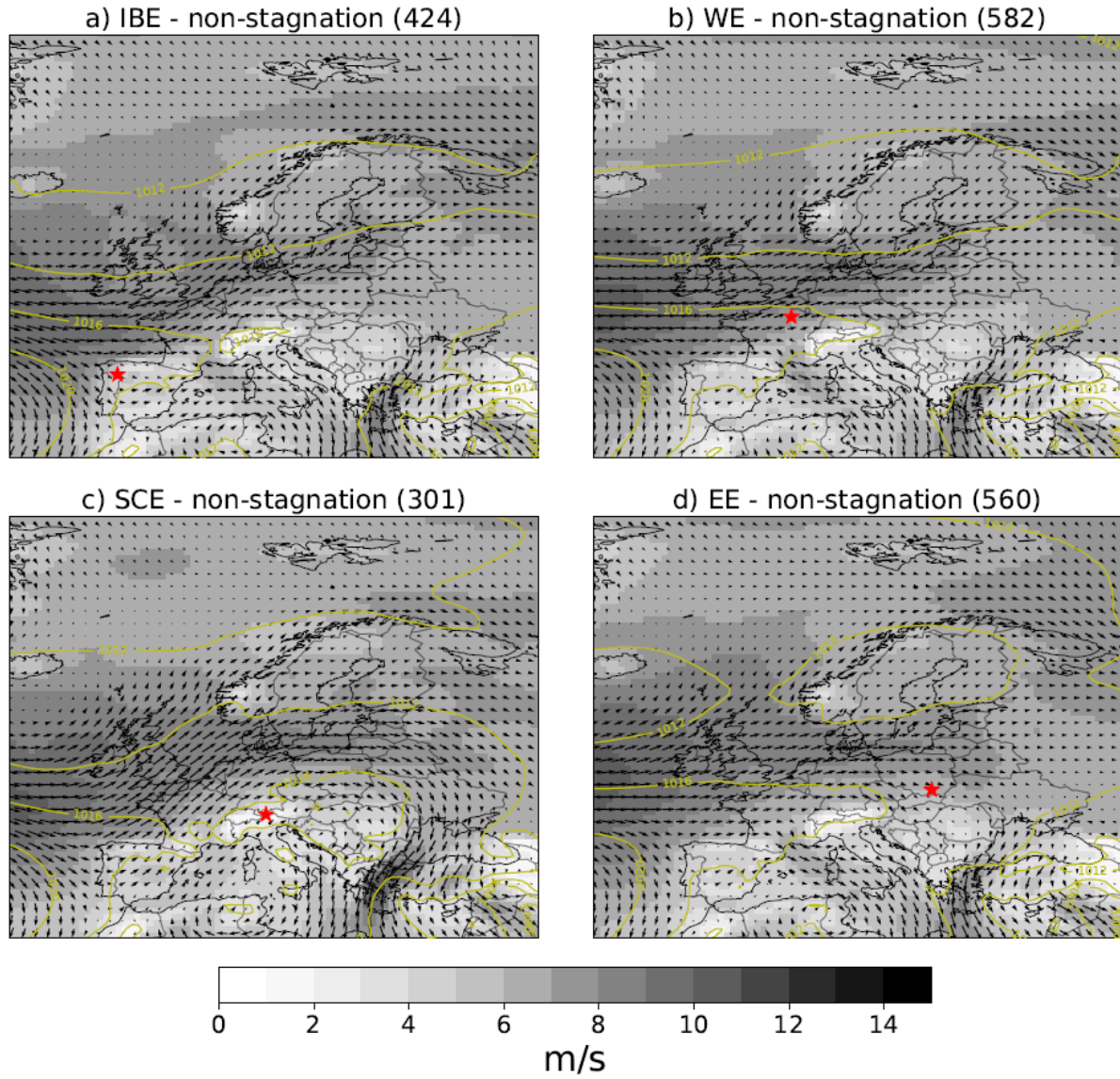


Figure 6.6: As Figure 6.5 but for non-stagnant days.

6.2 Impact of stagnation on the O_3 diurnal cycle

To better understand the ozone response to stagnation, we have compared the diurnal cycles of this pollutant in each region for stagnant and non-stagnant days. Our analyses are inspired by those of Pyrgou et al. (2018), who examined the effect of heatwave conditions on the diurnal cycle of ozone on a Mediterranean island. As in that study, the main limitation of our approach is that the evaluation of diurnal cycles is done based on average or accumulated values of meteorological variables (wind speed and precipitation in our particular case) during the whole day. We have also examined the impact of the persistence of stagnation on these diurnal cycles to investigate if the day-to-day evolution of ozone is affected by stagnation. As before, for the sake of simplicity, these analyses have been carried out for a single land grid cell in each cluster (blue circles in Figure 2.3) considering days with T_{\max} within 20–25 °C. Results are reported in Figure 6.7 for BALT and SCE as two representative regions of northern and central/southern Europe, respectively, and for the rest of clusters in Figure 6.8 in the case of the northern regions and Figure 6.9 for the central/southern regions.

It is well known that O_3 diurnal cycles are characterized by high concentrations during daylight hours and low values during the late night and early morning, as seen on the left and middle panels of Figures 6.7 to 6.9. Both the entrainment of ozone-rich air from aloft during the development of the well-mixed PBL and photochemical production lead to the build-up of the ozone mixing ratios at daytime, with a daily maximum in the afternoon. On the other hand, O_3 mixing ratios decrease during the night because of the cease of production as well as the destruction by dry deposition to surfaces and titration by NO in the shallow nocturnal PBL (e.g. Petetin et al., 2016, and references therein). The daily ozone minimum often occurs at a time with low PBL and elevated NO_x emissions from traffic during the morning rush hour. The amplitude of the diurnal cycle (defined as the difference between the maximum and the minimum hourly O_3 mixing ratios) is geographically dependent due to differences in the emission patterns and climates of each region.

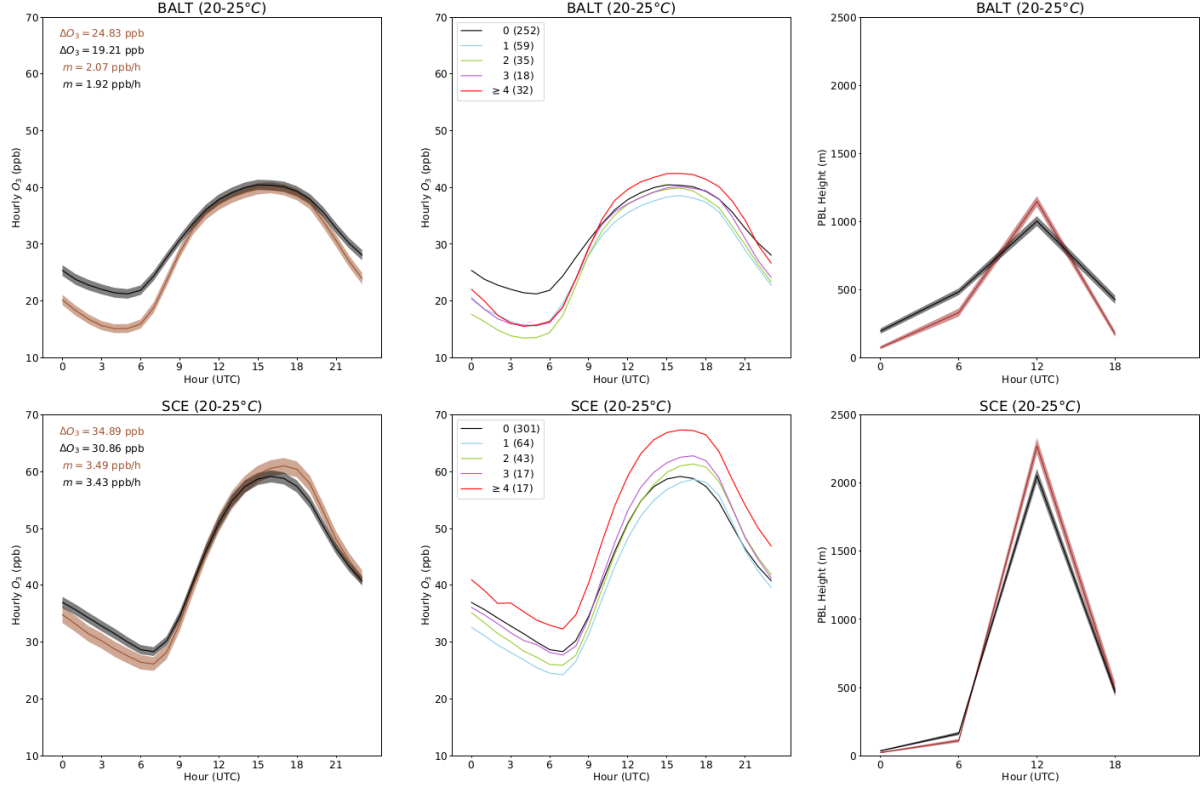


Figure 6.7: Composites of the diurnal cycles of hourly O_3 and PBL height at two representative locations in BALT and SCE on stagnant and non-stagnant days with T_{max} within 20 – 25 °C. The times displayed on the x-axes are UTC while summer local time is UTC+3 for BALT and UTC+2 for SCE. Left panels: Average diurnal ozone profiles for the summer (JJA) 1998 – 2015 days with (brown) and without (black) stagnation in BALT (top) and SCE (bottom). Shadings cover the 95% confidence interval. The amplitudes and increase rates of the stagnant (brown) and non-stagnant (black) diurnal cycles are displayed as ΔO_3 and m on the upper-left corners of the panels. Middle panels: Average diurnal ozone profiles for summer days based on the persistence of stagnation in BALT (top) and SCE (bottom). The black line represents non-stagnation, while the blue, green, purple and red lines represent one, two, three and four or more consecutive days with stagnation, respectively. The numbers in brackets indicate the total number of days considered for each case. Right panels: Evolution of PBL height (using data at 0, 6, 12 and 18 UTC from the ERA-Interim reanalysis) at both locations for stagnant (brown) and non-stagnant (black) days.

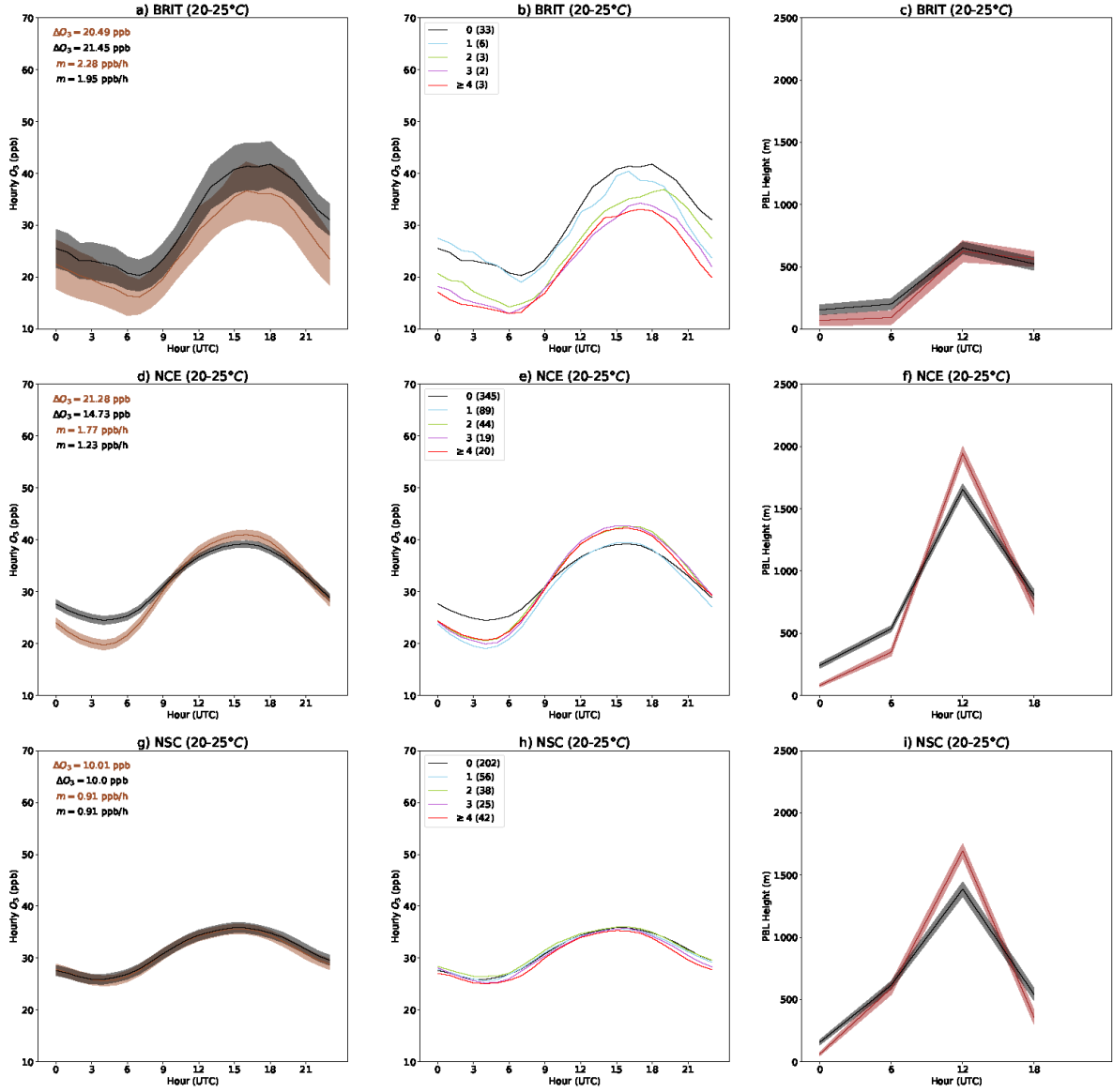


Figure 6.8: As Figure 6.7, but for representative grid cells in BRIT (top), NCE (middle) and NSC (bottom). Note that time on the x-axes is UTC while summer local time is UTC+1 for the grid cell in BRIT and UTC+2 for the other two locations.

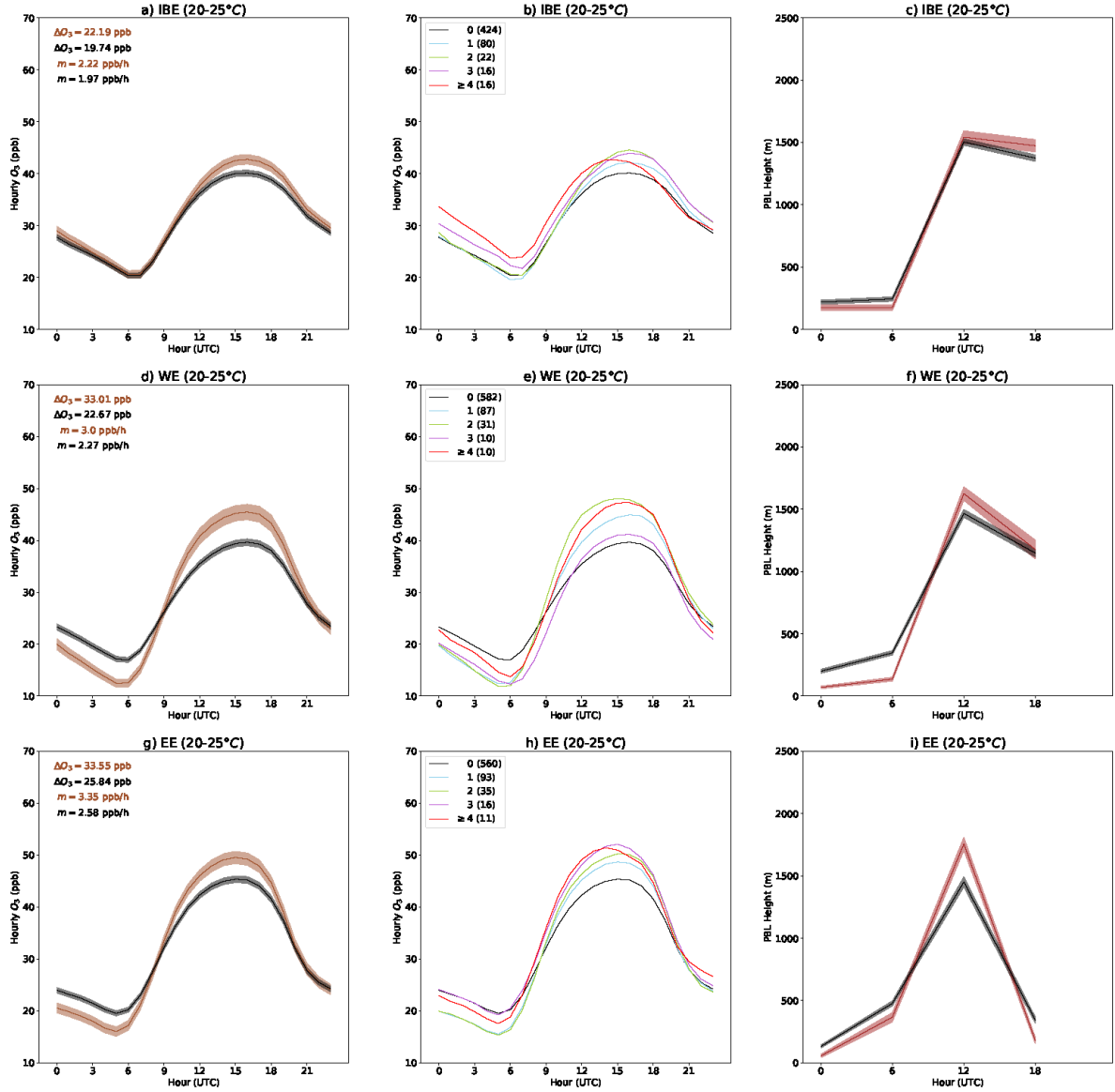


Figure 6.9: As Figure 6.7, but for representative grid cells in IBE (top), WE (middle) and EE (bottom). Note that time on the x-axes is UTC while summer local time is UTC+2 for the three locations.

The left panels of Figures 6.7 to 6.9 illustrate the average diurnal cycles of the hourly O_3 mixing ratios at the selected locations in the 8 regions, considering stagnant (brown) and non-stagnant (black) days, with 95% uncertainty estimates. The confidence intervals have been calculated using standard t-statistics (von Storch and Zwiers, 1999). Generally, the diurnal amplitude is significantly larger on stagnant days, as it increases by 2.5 to 10 ppb in 6 out of 8 selected grid cells (see ΔO_3 values at the upper left corners of

the panels). The only exceptions are the locations in BRIT and NSC, where the amplitude hardly changes. In the former location, the number of days with T_{\max} within $20 - 25\text{ }^{\circ}\text{C}$ is not high enough to draw solid conclusions (see Figure 6.8 a, b), whereas NSC is by far the cluster with the lowest sensitivity of $MDA8\text{ }O_3$ to stagnation (Table 6.1).

The differences between stagnant and non-stagnant O_3 diurnal cycles are often due to the above-average daytime increase and/or nighttime decrease of O_3 during stagnant days, again with the exception of BRIT and NSC. The low nighttime ozone mixing ratios on stagnant days may be caused by enhanced chemical destruction and dry deposition under a stable nocturnal PBL. Indeed, the right panels of Figures 6.7 to 6.9 prove that the average PBL height at 6 UTC is often lower than usual during stagnant nights. That is particularly the case for the locations with the strongest ozone decrease under stagnant conditions at that time of the day (grid cells in BALT, NCE, WE and EE). This results in a reduced O_3 baseline at the beginning of the day for these four locations and, to a lesser extent, for those in SCE and BRIT, while no clear effect is found for the grid cells in NSC and IBE. Thus at most locations the occurrence of stagnation leads to below-average early morning PBL height and ozone on the same day.

By contrast, the stronger build-up of daytime ozone on stagnant days could be related to the accumulation of primary pollutants and subsequent photochemical production as well as to enhanced subsidence and accumulation of ozone under the stable anticyclonic conditions that characterize those days. The afternoon ozone maxima tend to be higher than average on stagnant days for the central/southern locations, in particular for the grid cells in WE and EE, and to lesser extent for those in IBE and SCE. The most noticeable effect of stagnation on daytime ozone for the grid cell in SCE is the shift of the highest mixing ratios to later hours in the evening, consistent with a synchronous shift in temperature under stagnant conditions at the same location (Figure A7). The average afternoon ozone maxima are also higher on stagnant than on non-stagnant days for the grid cell in NCE, while there is no clear impact or even a decrease for the other northern locations in BALT, BRIT and NSC. This is consistent with the unclear impact of stagnation on the $MDA8\text{ }O_3$ – temperature relationship (Figure 6.2, a, c, d) and the effect of

southerly advection during non-stagnant days (Figure 6.4, a, c, d) shown previously for those regions.

We have also computed the daily ozone increase rate (defined as the daily amplitude divided by the period of time between the maximum and the minimum O_3 mixing ratios) at each location under stagnant and non-stagnant days. These values are displayed as m at the upper left corners of the left panels in Figures 6.7 to 6.9. This rate changes from 2.0–2.6 $ppb\ h^{-1}$ under non-stagnant conditions to 2.2–3.4 $ppb\ h^{-1}$ during stagnant days at three of the central/southern locations, IBE, WE and EE (Figure 6.9). The largest increases of this rate are found for WE and EE (above 0.7 $ppb\ h^{-1}$). However, the increase at the grid cell in SCE is negligible (below 0.1 $ppb\ h^{-1}$), because of the mentioned late afternoon ozone maxima at this location under stagnant conditions. The daily ozone increase rate also rises at most of the northern locations under stagnant conditions, but the typical values are lower than those shown above, ranging from 0.9 $ppb\ h^{-1}$ in NSC to 2.0–2.3 $ppb\ h^{-1}$ in BRIT. These results suggest higher photochemical production in the central/southern than in the northern locations, in line with expectations, as well as an enhancement of photochemical activity during stagnant days. Nevertheless, some of the processes previously mentioned (e.g. decrease of the early morning ozone baseline followed by enhanced vertical mixing and subsidence at daytime on stagnant days, southerly advection to northern regions under non-stagnant conditions) may be relevant to explain these differences.

Previous studies have considered four or more consecutive days with air stagnation at a given location as an air stagnation episode (Wang and Angell, 1999; Huang et al., 2017). Such episodes are not common in northern Europe (see Chapter 3), but it is still possible to examine changes in the diurnal evolution of ozone during successive stagnation days. The middle panels of Figures 6.7 to 6.9 display composites of O_3 diurnal cycles for non-stagnant days (black) as well as for one (blue), two (green), three (purple) and four or more (red) consecutive days with stagnation. Despite some limitations due to the small number of consecutive stagnant days at some locations, especially the grid cell in BRIT, the figures indicate that daytime ozone mixing ratios tend to increase with the persistence

of air stagnation. The only exceptions are that location in BRIT and the one selected in NSC. Our results are in the same line as previous analyses which found the number of successive stagnation days as a good indicator of the build-up of $MDA8\ O_3$ in most regions of the US (Sun et al., 2017). In addition, a number of studies have related the persistence of air stagnation or the associated stable anticyclonic conditions to the build-up of summer daily O_3 maxima and $MDA8\ O_3$ in some regions of Europe (Ordóñez et al., 2005, 2017). This also seems to be consistent with the well-known persistence of elevated $MDA8\ O_3$ in Europe (e.g. Otero et al., 2016). However, this increase does not necessarily apply to the whole diurnal cycle. In fact, the first days with stagnation consistently show a lower daily O_3 minimum than non-stagnant days, but this minimum gradually increases with the persistence of stagnation, as found during daylight hours, again with the exception of BRIT and NSC. If air stagnation persists long enough, the early morning O_3 baseline can recover and even exceed the typical levels found during non-stagnant days at the locations in SCE and IBE. BALT, NCE, WE and EE present a similar build-up, but the early morning O_3 baseline during the most persistent stagnation episodes remains below that of non-stagnant days. Hence, it appears that the nighttime destruction of O_3 is enhanced under the shallow PBL during the first stagnant days at most locations and that this destruction is at least partially compensated by the accumulation of O_3 when consecutive days with stagnation occur. The increase in the early morning baseline at some locations, together with mixing of boundary layer air with ozone-rich air from the residual layer after sunrise as well as daytime photochemical production, will favor the occurrence of elevated $MDA8\ O_3$ in the afternoon.

6.3 Main findings and discussion

The main results from this chapter are as follows:

- *MDA8 O₃* mixing ratios consistently increase over central/southern Europe (IBE, WE, SCE, EE) and, to a lesser extent, NCE under stagnant conditions, but this has not been found for some temperature bins in three of the northern regions (BRIT, NSC, BALT). Under non-stagnant conditions and Tmax within 20–25 °C (typical temperatures of fair weather conditions that allow photochemical production in northern Europe), such regions are affected by southerly advection, which is a known mechanism for the occurrence of ozone extremes in the north of the continent (Carro-Calvo et al., 2017).
- The ozone diurnal cycle in the central/southern regions and NCE exhibits larger amplitudes than usual when stagnation occurs, with low nighttime and high daytime mixing ratios in most of these regions. Stagnant nights are associated with stable shallow PBL and, presumably, enhanced dry deposition and chemical destruction of ozone. After sunrise, with the development of the PBL, mixing with air from the residual layer, accumulation of ozone and precursors, and photochemical production seem to be the main mechanisms involved in the build-up of daytime ozone.
- Low nighttime ozone mixing ratios during stagnant days are also a feature of BALT and BRIT, while afternoon ozone and consequently *MDA8 O₃* are not clearly affected by stagnation. In particular, for the 20–25 °C temperature range considered here, afternoon ozone can even decrease under stagnant conditions in BRIT. However, these results should be interpreted with caution considering the limited number of occurrences observed and the fact that *MDA8 O₃* in the same region increases on stagnant days for other temperature ranges.
- NSC is the region with the weakest sensitivity of ozone to stagnation. This is firstly evidenced from the poor correlation between the daily time series of average *MDA8 O₃* and the percentage of stagnant area in the region (R=0.06). Moreover,

the occurrence of stagnation hardly affects the ozone diurnal cycles for T_{\max} within 20–25 °C and even yields decreases in the $MDA8\ O_3$ mixing ratios for T_{\max} above ~ 20 °C. Nonetheless, we note the results for this region are based on relative fewer surface ozone observations as compared to those in central/southern regions (i.e. less than 30 sites north of 62.5° N).

In short, we have been able to identify regions with different responses of summer ozone to the occurrence of air stagnation. It is remarkable that some of the central/southern European regions where stagnation has a clear impact on ozone have already undergone significant upward trends in stagnation over the last decades (see Chapter 3) and are also likely to experience increases in the future (Horton et al., 2014). On the other hand, stagnation seems to exert a minor control on summer ozone over most of northern Europe. Consequently, observations of air stagnation occurrence and projections of increases in air stagnation should not directly be translated into enhanced summer ozone pollution if the sensitivity of this pollutant to stagnation has not been proved for a particular region.

Another relevant result of this chapter is that the occurrence of air stagnation amplifies the diurnal cycles of summer ozone over some regions. While simulations of surface ozone by CTMs are often evaluated against observations of $MDA8\ O_3$ or other relevant cumulative metrics (e.g. Lupășcu and Butler, 2019), understanding the differences in the performance of a set of model simulations for such metrics would require assessing the skill to reproduce the diurnal cycle of ozone. In fact, current global and regional CTMs present limitations at night and under stable conditions, partly because of the difficulty in resolving the stratified conditions near the surface and the depletion of ozone through surface deposition (Travis and Jacob, 2019, and references therein). Nighttime PBL dynamics and chemistry are crucial because they will determine the early morning ozone baseline and also influence morning radical chemistry, with important implications for the formation of daytime ozone (e.g. Brown and Stutz, 2012). On the other hand, following the development of the PBL at daytime, the entrainment of ozone-rich air from the upper levels to the ground has been proved to be an important transport mechanism of summer

ozone smog (e.g. Hu et al., 2018, and references therein). Therefore, special attention should be given to quantifying the contribution of individual processes such as horizontal and vertical advection, vertical diffusion, dry deposition and chemistry to the ozone budget under different meteorological conditions. This can be achieved through the use of probing techniques like Integrated Process Rate analysis (IPR), which provides detailed mass balance information for the aforementioned processes in some regional CTMs (e.g. Liu et al., 2007; Gonçalves et al., 2009; Lyu et al., 2019). Our findings about the differing impacts of air stagnation on the ozone diurnal cycles across Europe provide good observational constraints for the evaluation of such processes under stagnant vs. non-stagnant conditions. Furthermore, periods of persistent stagnant situations can be very appropriate to test the ability of CTMs to reproduce PBL dynamics and the evolution of ozone concentrations.

7 A storyline view of the projected role of remote drivers on summer air stagnation in Europe and the US

In the previous chapters we have characterized the past spatiotemporal variability of air stagnation over the Euro-Mediterranean area and analyzed its impact on PM_{10} and O_3 . Now we will explore how stagnation may change in the future. Using a storyline framework and a CMIP6 multi-model ensemble, this chapter develops for the first time plausible storylines of regional changes in air stagnation by the end of the century over Europe and the contiguous US. Note that these analyses are not limited to Europe as the previous chapters because the contiguous US is another region where the CMIP3 and CMIP5 multi-model ensemble means have consistently projected regional stagnation increases (Horton et al., 2012, 2014) and its climate shares common remote drivers with Europe. We focus our investigation on stagnation changes in summer (JJA) as this is the season with the largest projected changes (Figure 7.3). Our study also provides further insights into potential remote drivers of stagnation changes and associated components of the mid-latitude circulation during summer, which has received less scientific attention than in winter (Coumou et al., 2018). The results of this chapter can be found in Garrido-Perez et al. (2022).

7.1 The computation of the air stagnation index in climate models

In order to characterize stagnation in the climate models, we have used the simplified ASI defined by Horton et al. (2012). As indicated in Chapter 3, this index considers a day as stagnant for a given location when three conditions are fulfilled simultaneously: Wsp10 is lower than 3.2 m/s, Wsp500 is below 13.0 m/s and daily total precipitation is under 1.0 mm. These fixed thresholds may not be appropriate for all climate models due to potential biases in the different meteorological variables. Therefore, we have defined new stagnation thresholds locally (i.e. one value per each grid cell) for each model based on the corresponding percentiles derived from reanalysis. For that purpose, daily mean fields of 500hPa wind speed and near-surface wind speed, as well as daily accumulated precipitation from the ERA5 reanalysis (Hersbach et al., 2020) at $2.5^\circ \times 2.5^\circ$ horizontal resolution (similar to that used in climate models) have been used. Figure 7.1 shows the ERA5 percentiles of the 1981–2010 precipitation, near-surface and mid-tropospheric wind speed distributions corresponding to the respective stagnation thresholds (i.e. 1 mm for precipitation, 3.2 m/s for Wsp10 and 13.0 m/s for Wsp500). As expected, the highest (lowest) percentile values are found in regions where these fields are usually low (high). For example, high wind speed percentiles can be seen in western US, where low winds are relatively common because of the presence of topographic barriers such as the Sierra Nevada mountains and the Columbia and Colorado Plateaus. In a second stage, we have computed the values of the meteorological fields that correspond to the ERA5 percentiles for each CMIP6 model and grid cell, resulting in new ASI thresholds. The multi-model ensemble mean values are displayed in Figure 7.2. Overall, the new thresholds are close to the original ones. Although they are regionally dependent, the new near-surface wind speed (precipitation) thresholds tend to be somewhat higher than 3.2 m/s (1 mm) both in Europe and the US, indicating a positive bias in the CMIP6 models. Conversely, mid-tropospheric wind speed is negatively biased in these regions since their thresholds are consistently lower than 13.0 m/s across Europe and the US. Finally, the new thresholds are used to compute the daily values of ASI in climate models.

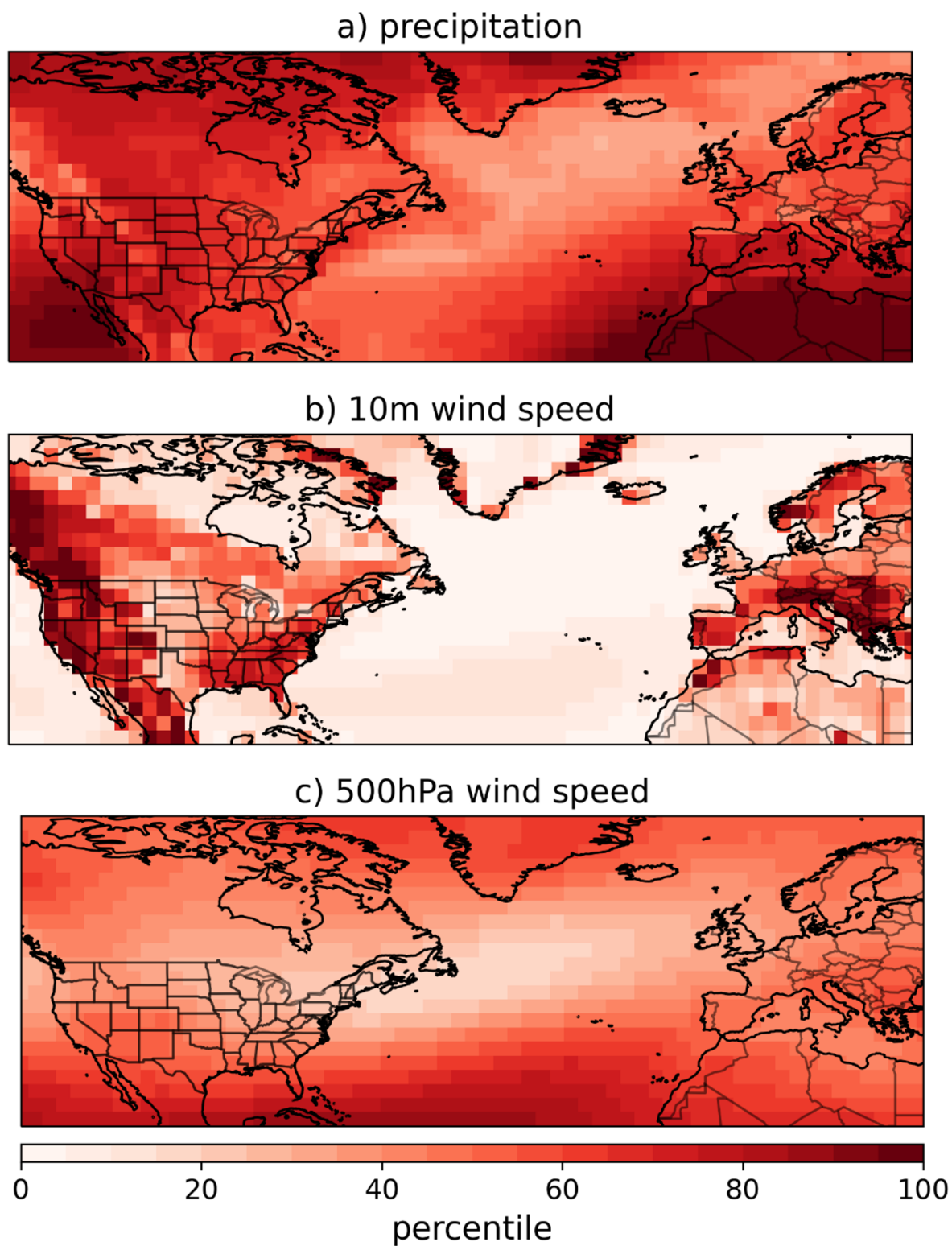


Figure 7.1: Percentiles of the 1981–2010 (a) precipitation, (b) surface wind speed and (c) 500-hPa wind speed distributions corresponding to the respective stagnation thresholds (1 mm, 3.2 m/s and 13.0 m/s). Data source: ERA5 reanalysis.

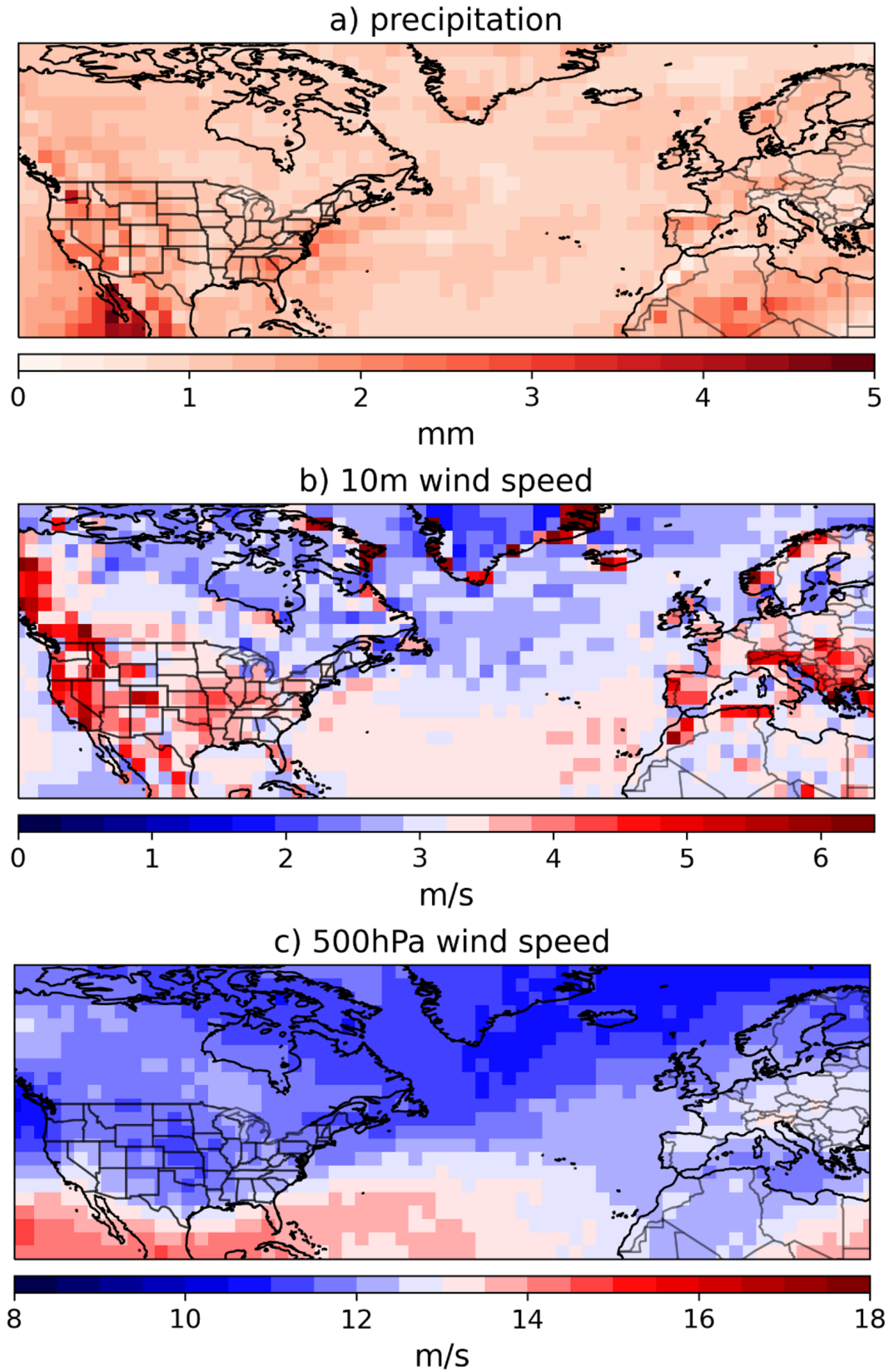


Figure 7.2: CMIP6 multi-model mean values of (a) precipitation, (b) surface wind speed and (c) 500-hPa wind speed corresponding to the ERA5 percentiles illustrated in Figure 7.1. Data source: CMIP6 models (see Table 2.2).

Figure 7.3a-d shows the multi-model ensemble mean percentage of air stagnation days (%) for each season during 1981–2010. Overall, there is considerable spatial heterogeneity. The highest stagnation centres in the US are located over western US and southeastern US, whereas stagnation is more frequent in the south than in the north of Europe. This spatial distribution resembles that displayed by Wang and Angell (1999) for the US and that found in Chapter 3 for Europe using reanalysis products. Figure 7.4a-c displays the ensemble-mean percentage of days that stagnation conditions are met separately for each component used in the ASI definition during summer 1981–2010. Although near-surface wind speed (Figure 7.4b) is the ASI component showing the most similar spatial pattern to that of the frequency of air stagnation, mid-tropospheric wind and precipitation conditions are also key to understand the behaviour of stagnation. As an illustration, the low frequency of the mid-tropospheric wind condition associated with the presence of the mid-latitude jet stream (Figure 7.4c) is clearly limiting the occurrence of stagnation in northern US and, to a lesser extent, northwestern Europe. On the other hand, the precipitation condition is the main limiting factor over some regions such as Scandinavia or southeastern US, where regional conditions favour rainfall (Figure 7.4a).

7.2 Regionalization of air stagnation

As there is considerable spatial heterogeneity in future air stagnation over Europe and the US, a detailed regional assessment is required. For that purpose, as in Chapter 3, we have divided both Europe and the US into regions where air stagnation presents consistent patterns. For that purpose, we have applied the k-means clustering technique on the gridded monthly frequency of stagnant days in the multi-model ensemble during 1981–2010. The choice of the final number of clusters has been made using the ‘elbow criteria’, by which one can stop introducing new clusters when the increase in explained variance does not worth the additional cost of more clusters (see e.g. Carro-Calvo et al., 2017). Figure 7.5a displays the spatial division of the nine resulting regions (four in the US and five in Europe): northwest US, central and northeast US, southwest US, southeast US, Scandinavia, northern Europe, central Europe, southwest Europe, and southeast Europe.

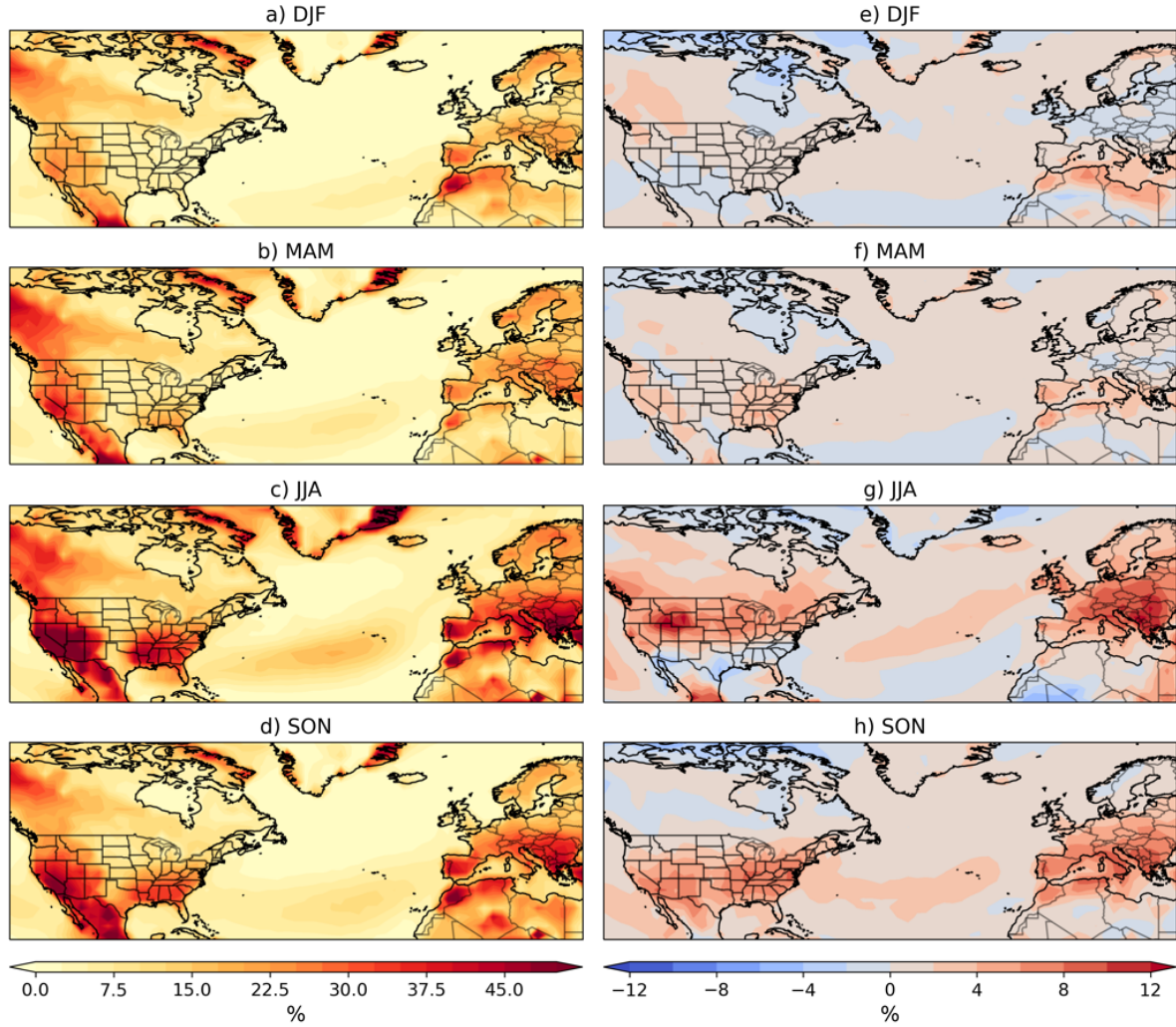


Figure 7.3: Multi-model ensemble mean stagnation for winter (DJF), spring (MAM), summer (JJA) and autumn (SON). (a-d): percentage of stagnation days (%) during the period 1981–2010. (e-h): Absolute change in stagnation occurrence (%) from 1981–2010 to 2071–2100 under the SSP5–8.5 scenario.

The four US clusters are consistent with the spatial distribution of air stagnation shown in Figure 7.3a-d. Southwest US is basically made of California, Nevada, Arizona and Utah, the area with the maximum frequency of stagnation. Central and northeast US covers a large part of The Great Plains, The Great Lakes and Northeast US, where stagnation is less frequent. Although some of these regions are quite distant, they are part of the same cluster because wind speed tends to be relatively high here, limiting the occurrence of stagnation compared to the surrounding regions. While southeast US corresponds to the states around the Gulf of Mexico, northwest US includes the states of Oregon, Washington,

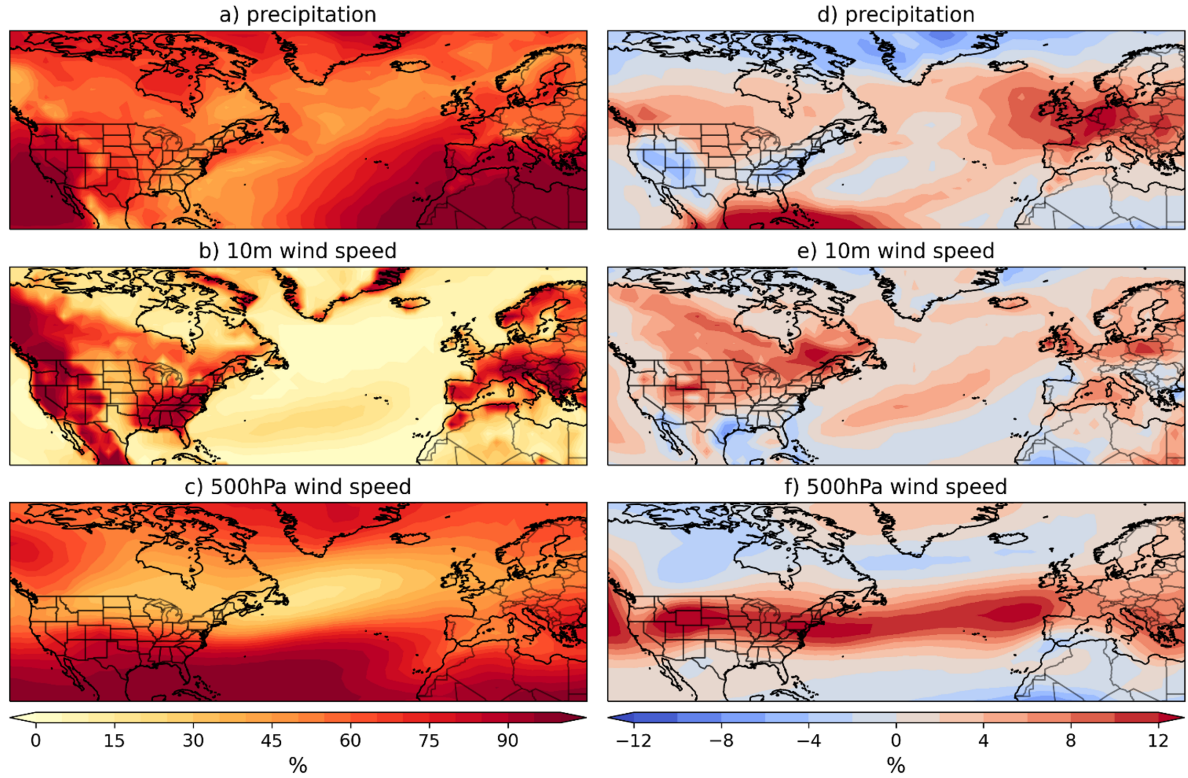


Figure 7.4: (a-c) Ensemble mean JJA percentage (%) of days that fulfil the stagnation condition for (a) precipitation, (b) surface wind speed and (c) mid-tropospheric wind speed during the period 1981–2010. (d-f) Absolute change (%) from 1981–2010 to 2071–2100.

Idaho, Montana and surroundings, both regions with moderate stagnation. On the other hand, the European regionalization agrees well with that presented in Chapter 3 for the ERA-Interim reanalysis (see Figure 3.3). Note that we used a reduced European domain here to match the one of that chapter (i.e. continental areas within the range $33^{\circ}\text{N} - 75^{\circ}\text{N}$ and $12^{\circ}\text{W} - 26.25^{\circ}\text{E}$).

This regionalization could be sensitive to air stagnation changes associated with global warming. In order to investigate whether we can consider the regionalization as time-invariant, we have repeated the analyses considering the period 2071–2100. Overall, only minor differences have been found in the spatial coverage of the clusters (Figure 7.5b). Hence, we can use the regionalization to evaluate the response of stagnation frequency to climate change over time.

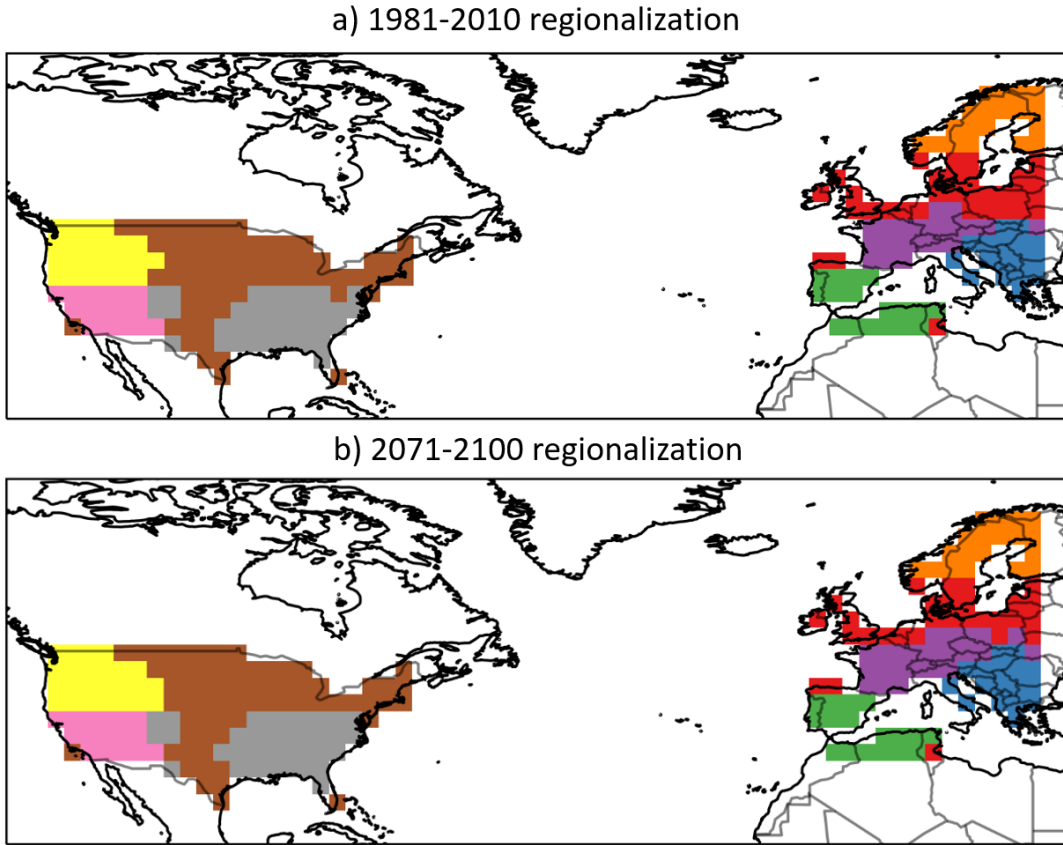


Figure 7.5: Regionalization of monthly stagnation frequency during a) 1981–2010 and b) 2071–2100 in the US and Europe, as derived from the multi-model ensemble. Coloured shading identifies the clustered regions, which broadly correspond to northwest US (yellow), central and northeast US (brown), southwest US (pink), southeast US (grey), Scandinavia (orange), northern Europe (red), central Europe (purple), southwest Europe (green), and southeast Europe (blue).

7.3 Spatial and inter-model variability of projected changes in air stagnation occurrence

By the end of the 21st century, under a high emission scenario, stagnant conditions are projected to be more common in summer over most of the US and Europe (Figure 7.3g). In Europe, the greatest changes are projected in the southeast and to a lesser extent, the centre of the continent (Figure 7.3g), areas that have historically experienced high summer stagnation (Figure 7.3c). In the US, the largest changes are located over the northwest, with average increases in the absolute frequency of air stagnation of

around 7–12% (6–11 days).

Figures 7.4 and 7.6 assess the projected changes in the frequency of stagnant conditions separately for each ASI component. Although the pattern of projected changes for stagnant near-surface wind is heterogeneous, most of the US and Europe show comparatively small increases (below 8%) in the frequency of this condition (Figure 7.4e). For mid-tropospheric winds, the spatial pattern suggests a generalized poleward shift of the North Atlantic westerlies, with the 35–50°N (50–65°N) latitudinal band exhibiting a 10–14% increase (1–4% decrease) in the frequency of stagnant mid-tropospheric wind conditions, more pronounced in the US than in Europe (Figure 7.4f). The change in the frequency of dry days is small for the US, but exhibits substantial increases over most of Europe, with the exception of Scandinavia (Figure 7.4d). Therefore, the projected increases in stagnation days over Europe and the US are largely caused by enhanced frequency of dry days and stagnant mid-tropospheric winds, respectively.

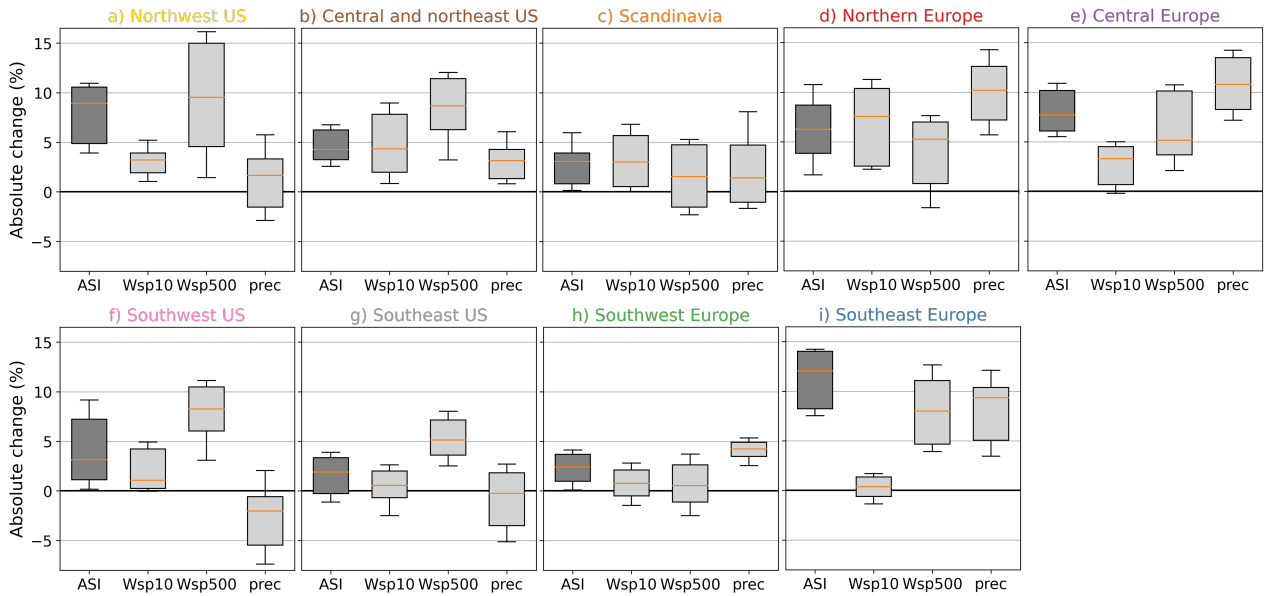


Figure 7.6: (a) – (i) Absolute change in the summer frequency (%) of stagnation days (dark grey) and of days that fulfil each of the stagnation conditions (light grey), calculated as the difference between the future (2071–2100) and historical (1981–2010) periods under the SSP5–8.5 scenario. The boxes extend from the lower to the upper quartile values of the data, with a horizontal line indicating the position of the median. The whiskers extend from the boxes to show the range of the data between the 10th and 90th percentiles. The colours in the headings of panels correspond to those used to depict each region in Figure 7.5. Abbreviations: ASI — air stagnation index, Wsp10 — 10m wind speed, Wsp500 — 500hPa wind speed, and prec — precipitation.

The boxplots in Figure 7.6 illustrate the inter-model spread for the projected changes in stagnation frequency and its components. Increases in stagnation are projected for most regions, with the only interquartile range indicating lesser stagnation in the southeast US. However, the interquartile ranges still show considerable spread among the models and therefore large uncertainty in the projections of stagnation. This indicates that there are regions where model projections are not robust and the multi-model mean blurs the large range of potential responses. To investigate this in more detail and constrain the dynamical uncertainty, a storyline approach for plausible future regional stagnation changes is presented in the next sections.

7.4 Remote driver responses and sensitivity of stagnation

Remote drivers of regional circulation change define the storylines. We construct stagnation storylines by investigating the forced response (future minus baseline) of three remote drivers with known influences on summer weather patterns over Europe and the US: (1) Ratio between the tropical and Arctic warming (RTAW): it measures the differential warming rate between tropical and Arctic latitudes. A higher Arctic than tropical warming is associated with a decrease in equator-to-pole temperature gradients, which leads to a weakened storm track and a southward shift in the mid-latitude jet, with notable implications for European and US climates (Coumou et al., 2018). Following Zappa and Shepherd (2017) and Peings et al. (2018), this driver is computed from regional averages of temperature change in the tropical upper troposphere (30°S – 30°N at 250hPa) and Arctic lower troposphere (60 – 90°N at 850hPa). (2) North Atlantic warming (NATLW): anomalously cold SSTs around the subpolar gyre associated with the slowdown of the Atlantic Meridional Overturning Circulation (AMOC) during the last few decades have been related to weakened westerlies in summer over the North Atlantic sector and persistent dry hot extremes in Europe (Haarsma et al., 2015; Rahmstorf et al., 2015). Following this, NATLW is defined as the SST change averaged in the $[50^{\circ}$ – 65°N , 40° – $10^{\circ}\text{W}]$ domain, which is the area with the lowest projected warming by the end of the 21st century in

the multi-model ensemble mean (Atlantic box in Figure 7.7), resembling that considered by Rahmstorf et al. (2015) as the most sensitive region to a reduction in the AMOC. (3) North Pacific warming (NPACW): studies have linked extratropical North Pacific SSTs with atmospheric circulation anomalies over the contiguous US (Ting and Wang, 1997; Alexander et al., 2002; Lau et al., 2004; Wang et al., 2014; Eden et al., 2015; Jia et al., 2016; McKinnon et al., 2016; Chen et al., 2020), and more specifically, with high pressure systems, which are symptomatic of air stagnation conditions (e.g. McKinnon et al., 2016). NPACW is defined here as the SST change averaged in the $[30^{\circ}\text{--}50^{\circ}\text{N}, 150^{\circ}\text{E}\text{--}150^{\circ}\text{W}]$ domain. This region is influenced by the Pacific Decadal Oscillation (PDO; Deser and Trenberth (2016)) and is expected to experience high SST increases (Pacific box in Figure 7.7). Additional analyses confirm that the results presented here are not sensitive to the choice of the domains over the North Atlantic and North Pacific oceans. All spatial averages are area-weighted. The computation of the remote drivers and stagnation responses has been made for each individual model realization prior to the regression analysis involved in the storyline approach.

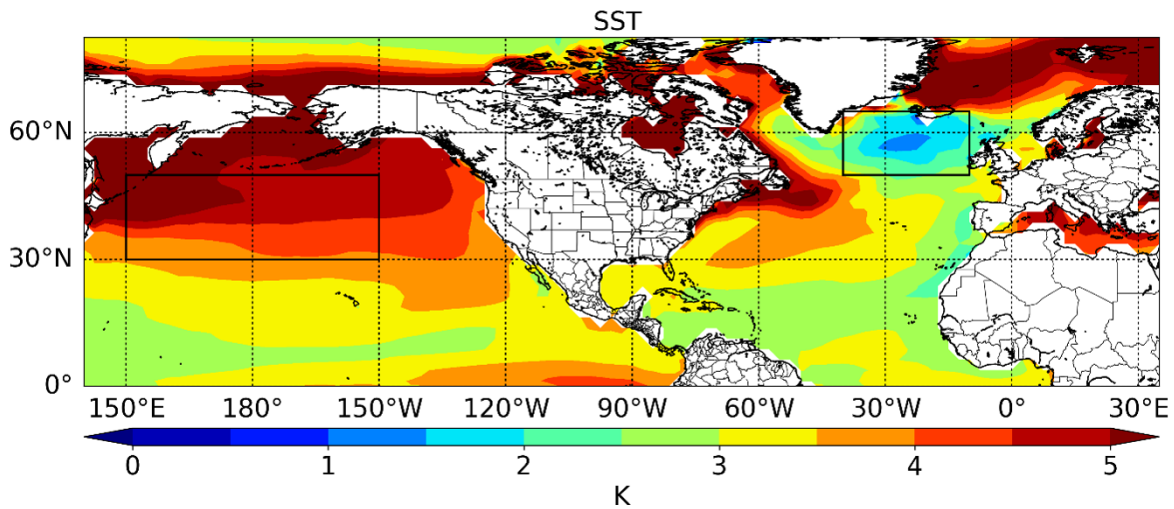


Figure 7.7: Multi-model mean change in sea surface temperature (K), expressed as the difference between the future (2071–2100) and historical (1981–2010) JJA periods. Boxes denote the spatial domains employed for the definition of SST-based drivers over the North Pacific and North Atlantic oceans.

Figure 7.8 shows the spread of near-surface global warming (GW) and driver responses (2071–2100 minus 1981–2010) among the model simulations. The driver re-

sponses are characterized by large uncertainty, with interquartile ranges exceeding 2°C for NATLW. Although the tropics and the Arctic will warm at a faster rate than the rest of the globe, the projected warming is larger in the tropics than in the Arctic ($\text{RTAW} > 1$), leading to an increase in the pole-to-equator temperature gradient. The fact that RTAW ranges from 1 to 1.4 (10^{th} – 90^{th} percentiles) indicates that models with large tropical warming do not necessarily show strong Arctic amplification. On the other hand, the warming (and spread) over the North Pacific is only slightly higher than GW. This occurs because land areas warm faster than oceans, although the North Pacific is among the oceanic regions that will experience the highest increase in SSTs (Lauvset et al., 2017; Mamalakis et al., 2021). Conversely, the projected warming over the North Atlantic is considerably lower (albeit more uncertain) than GW.

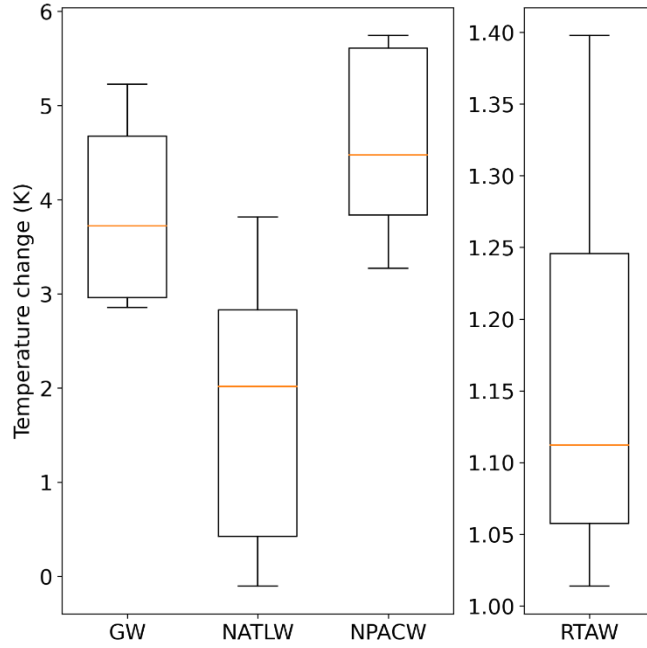


Figure 7.8: Spread of climate change responses (2071–2100 minus 1981–2010) simulated by the CMIP6 models under the SSP5–8.5 scenario: global near-surface warming (GW), North Atlantic warming (NATLW), North Pacific warming (NPACW) and ratio between tropical and Arctic warming (RTAW). GW is evaluated based on annual means, while the other quantities are evaluated for summer (JJA). See caption of Figure 7.6 for the definition of boxplots.

To better understand the influence of these driver responses on stagnation, we use the storyline regression framework of Zappa and Shepherd (2017). We assess the stagna-

tion response separately for each grid cell by applying multi-linear regression analysis on the responses of the three remote drivers for all models. For each model, the driver and stagnation changes are scaled by GW. The resulting regression coefficients give the sensitivity per degree of GW of the regional stagnation response to anomalies (with respect to the multi-model ensemble mean) in the remote driver responses. The general form of the model used is as follows:

$$\frac{\Delta ASI_{xm}}{\Delta T_m} = a_x + b_x \cdot \left(\frac{RTAW}{\Delta T} \right)'_m + c_x \cdot \left(\frac{NATLW}{\Delta T} \right)'_m + d_x \cdot \left(\frac{NPACW}{\Delta T} \right)'_m \quad (7.1)$$

where the vertical dash ' indicates the standardized anomaly relative to the multi-model mean. While the intercept a_x represents the multi-model mean stagnation response, the b_x , c_x , and d_x regression coefficients give the sensitivity of the regional response to anomalies in the remote driver responses: RTAW, NATLW and NPACW. These regression coefficients are illustrated in Figure 7.9 for air stagnation and in Figures 7.10 to 7.12 for each of its components. Although some of the drivers are highly correlated, scaling by global warming substantially decreases correlations (Table 7.1), allowing to separate the uncertainty due to global warming from that in the pattern of the atmospheric circulation response.

Table 7.1: Pearson correlation coefficients (R) between the driver responses of the CMIP6 models from JJA 1981–2010 to JJA 2071–2100 under the SSP5–8.5 scenario. They have been computed using as many points as models listed in Table 2.2. The numbers in parentheses represent the resulting correlations after scaling each model driver response by global warming.

	RTAW	NATLW	NPACW
RTAW	1.00		
NATLW	-0.20 (-0.33)	1.00	
NPACW	-0.45 (-0.05)	0.66 (0.04)	1.00

An anomalously high RTAW in the multi-model ensemble tends to reduce (enhance) the frequency of stagnation over the northern (southern) regions of the US and Europe (Figure 7.9a). The associated strengthening and poleward shift of the wester-

lies decrease the days fulfilling the wind conditions for stagnation over most of Europe and northern US, while the opposite occurs over southwest Europe and the southeast US (Figure 7.10). Nevertheless, the differing effects of this driver on precipitation and winds may cancel out over the US. On the other hand, enhanced warming of the North Pacific is associated with an increase in the frequency of stagnation over a large part of the US, with the most notable exception being the southwest (Figure 7.9b). This is mainly due to an increase in the frequency of days fulfilling stagnant wind conditions, while the influence of North Pacific warming on precipitation over the US is small (Figure 7.11). Finally, NATLW negatively correlates with the stagnation responses over most of Europe (Figure 7.9c), indicating that reduced sea surface warming associated with a slowdown of the AMOC would lead to enhanced stagnation over Europe. This is mainly explained by the negative association of this driver with the occurrence of dry days in Europe (Figure 7.12).

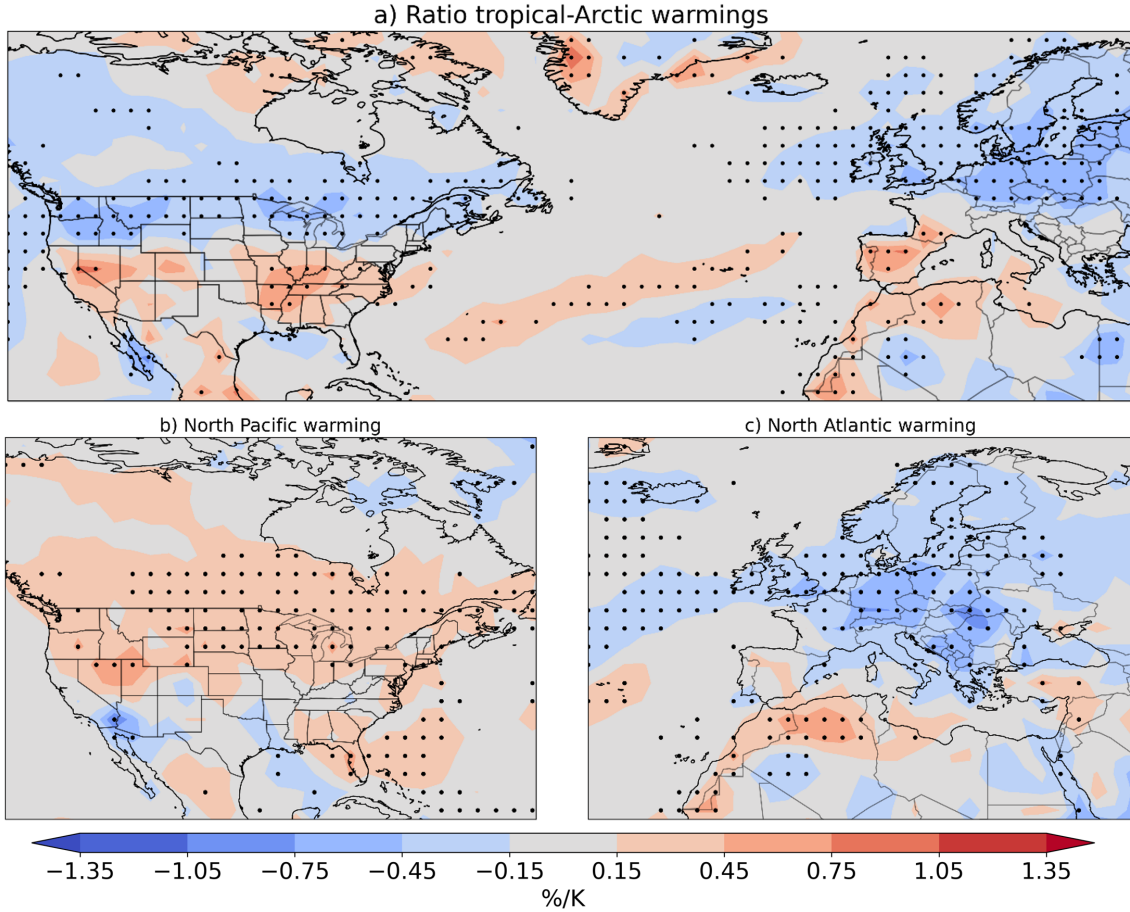


Figure 7.9: Sensitivities of summer stagnation changes (2071–2100 minus 1981–2010) associated with the uncertainties in the climate change driver responses: a) ratio between the tropical and Arctic warming (RTAW), b) North Pacific warming (NPACW) and c) North Atlantic warming (NATLW). These sensitivities correspond to the coefficients obtained from Equation 7.1 (b_x for RTAW, c_x for NATLW and d_x for NPACW). Colours show the air stagnation index (ASI) responses scaled by global warming (%/K) due to one sigma positive anomaly of the driver with respect to the multi-model mean. Stippling indicates regions where the regression coefficients are statistically significant at the 90%.

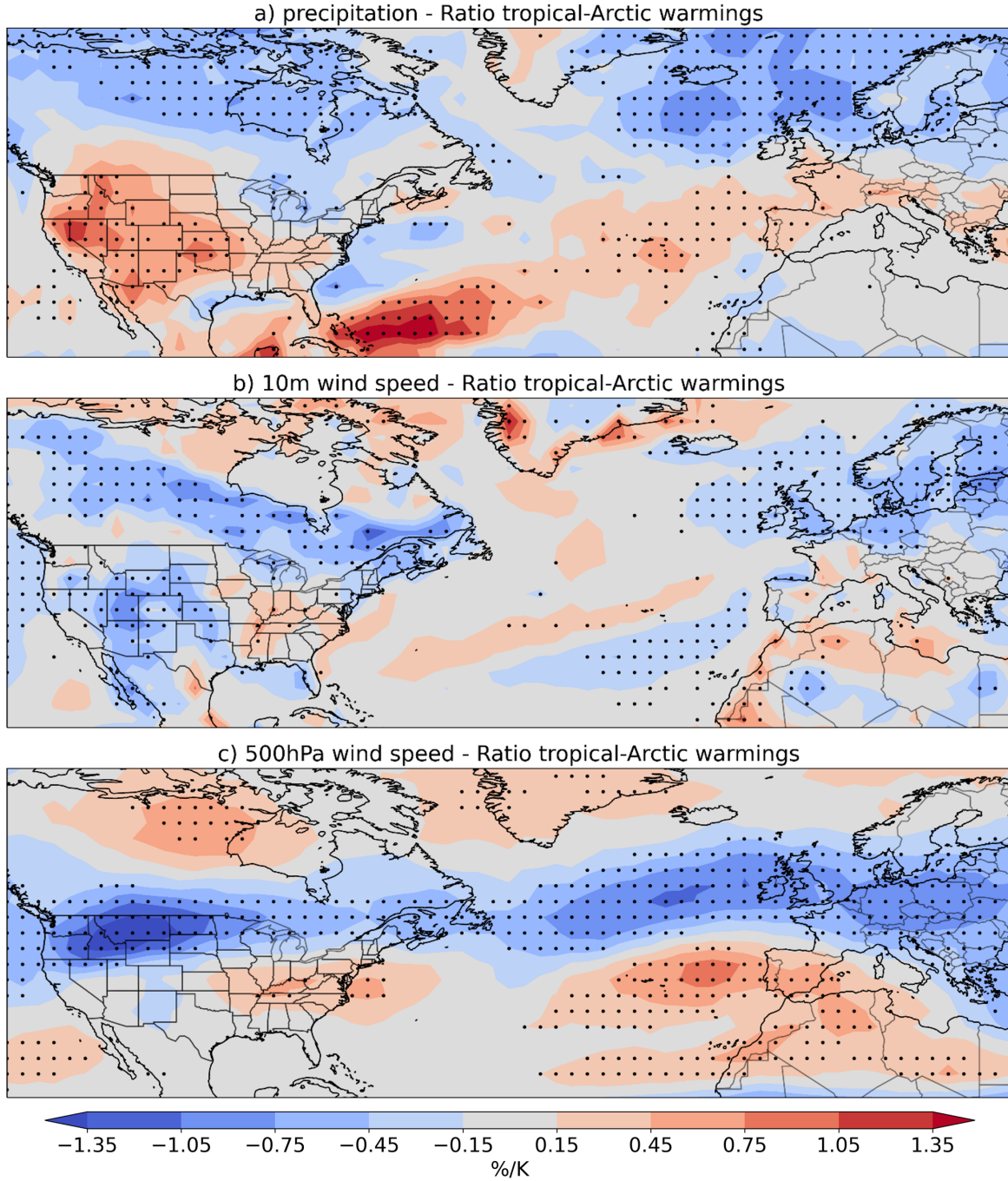


Figure 7.10: Sensitivities of the atmospheric circulation response associated with the uncertainties in the RTAW response from JJA 1981–2010 to JJA 2071–2100. Responses of the frequency of (a) precipitation, (b) near-surface wind and (c) mid-tropospheric wind stagnant conditions scaled by global warming (%/K) associated with a one sigma positive anomaly of RTAW in the CMIP6 inter-model spread. Note that these sensitivities correspond to the coefficient b_x of Equation 7.1. Stippling indicates regions where the regression coefficients are statistically significant at the 90%.

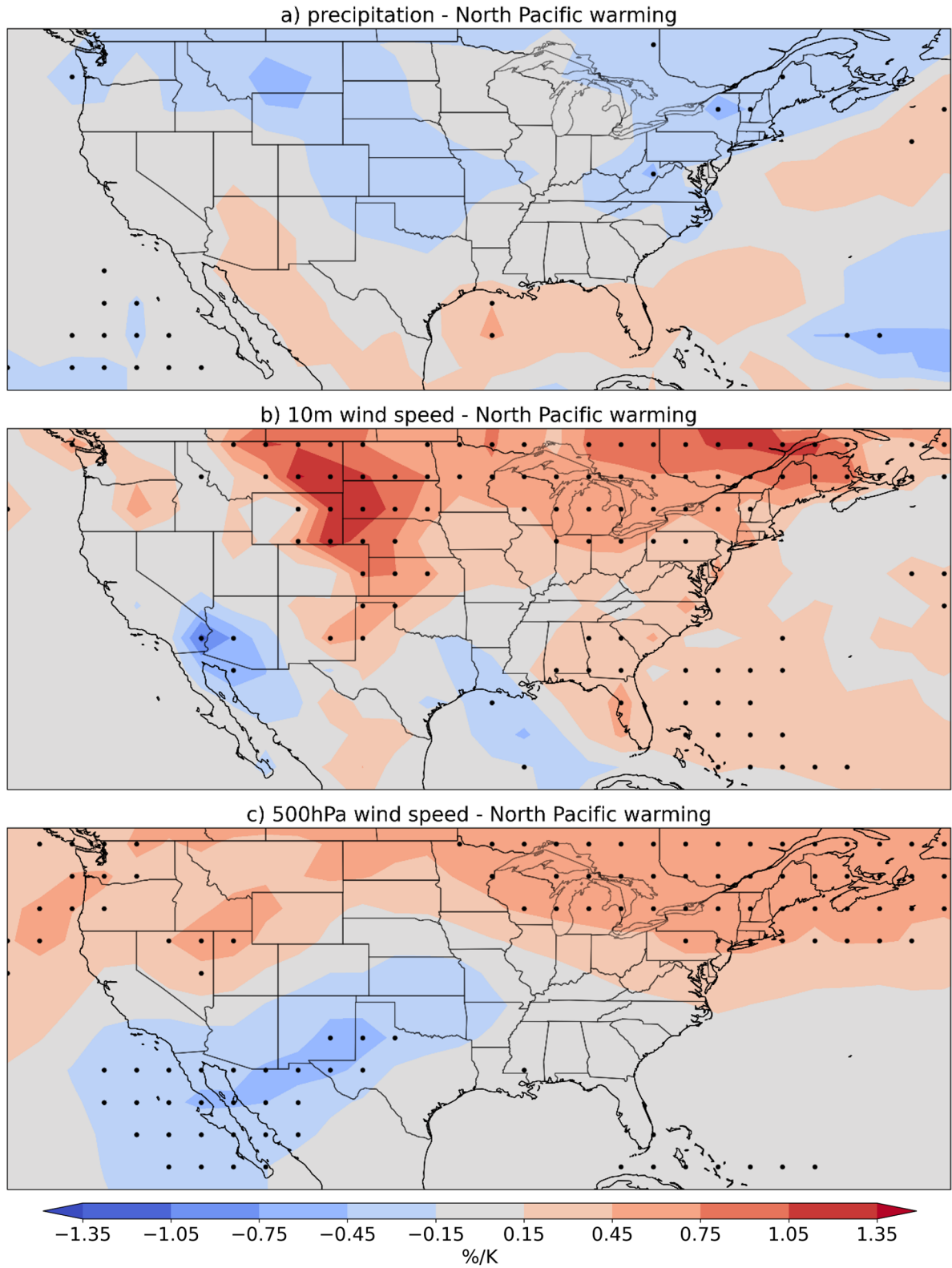


Figure 7.11: As Figure 7.10 but for the uncertainty associated with a one sigma positive anomaly of NPACW (coefficient d_x of Equation 7.1).

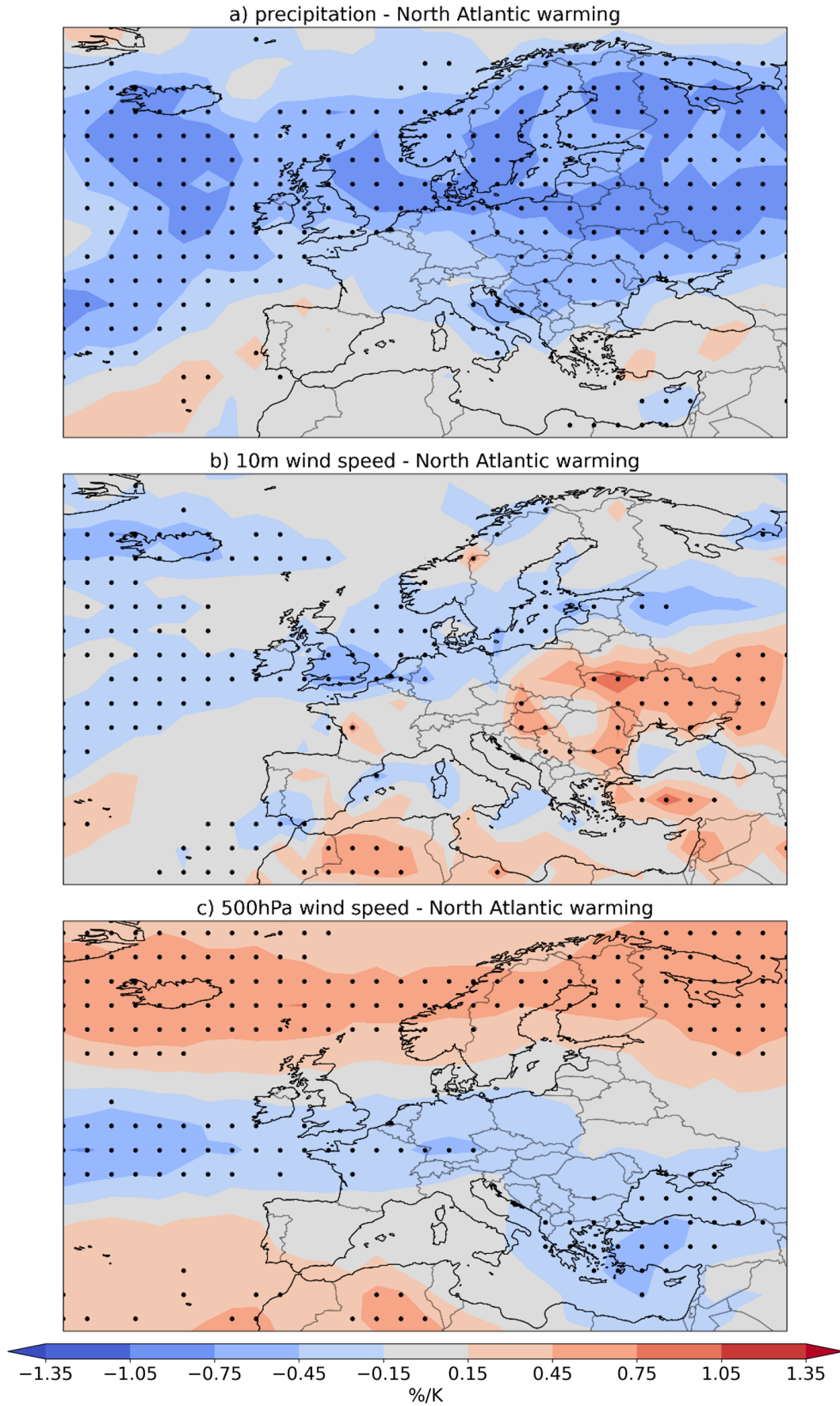


Figure 7.12: As Figure 7.10 but for the uncertainty associated with a one sigma positive anomaly of NATLW (coefficient c_x of Equation 7.1).

Figure 7.13 displays the spatial distribution of the variance explained by the MLRM. There is considerable spatial variability in the coefficients of determination (R^2) across the US and Europe. Although the explained variance might be low over large areas of southern Europe and the US, there are other regions where a large fraction of the variance in the multi-model spread of the stagnation response can be related to the combined effect of the three remote drivers and global warming. In particular, the best performance is found over a wide area covering northwest/central Europe, with values up to 0.7 around the British Isles, Germany and the surrounding countries. Despite the weak atmospheric circulation in summer and the complexity of considering fixed thresholds of three different meteorological fields in the ASI definition, these values indicate that the three drivers control a large fraction of the inter-model variability of regional stagnation projections over some regions of Europe.

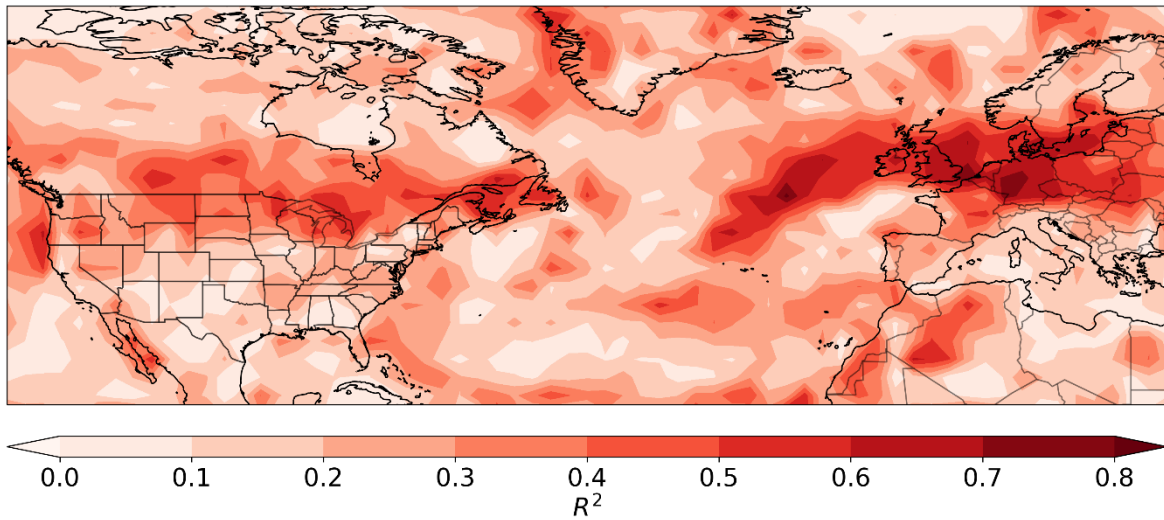


Figure 7.13: Fraction of variance (R^2) of the CMIP6 inter-model spread in summer (JJA) stagnation responses that can be related to the remote driver uncertainty using the regression framework (Equation 7.1).

7.5 Storylines of future regional changes in air stagnation

Based on the identified driver responses, we have generated a range of extreme but plausible storylines of future changes in stagnation. To do so, we use equal standardized

amplitudes for two of the driver responses corresponding to the anomalies that lie on the 80% confidence region of the joint distribution (see black stars in Figure 7.14; Zappa and Shepherd (2017)). In particular, the storylines are based on the combination of RTAW and NPACW for the US and of RTAW and NATLW for Europe. The stagnation response can thus be expressed as:

$$US : \quad \frac{\Delta ASI_x}{\Delta T} = a_x \pm b_x \cdot t \pm d_x \cdot t \quad (7.2)$$

$$Europe : \quad \frac{\Delta ASI_x}{\Delta T} = a_x \pm b_x \cdot t \pm c_x \cdot t \quad (7.3)$$

where $t = \sqrt{\chi^2(0.8, 2)/2} \sim 1.27$, with $\chi^2(p, k)$ being the quantile function of the chi-squared distribution with k degrees of freedom evaluated at probability p .

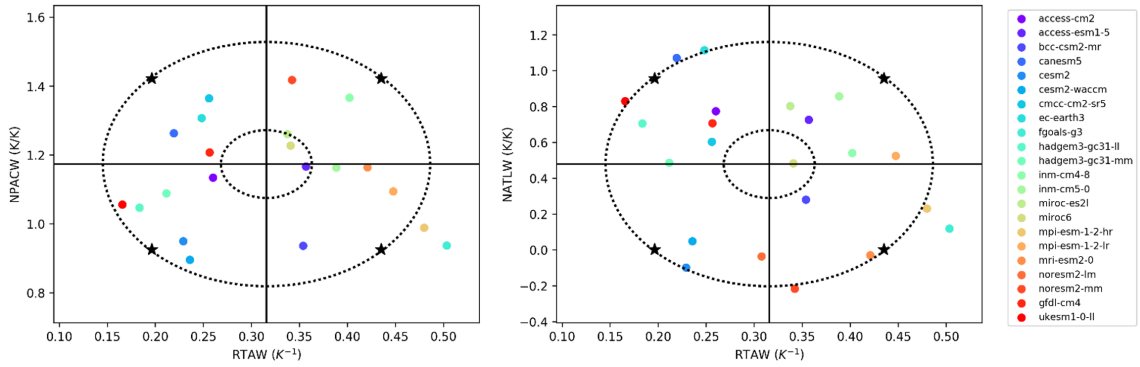


Figure 7.14: Individual CMIP6 model responses in NPACW (left) and NATLW (right) against RTAW (colour dots). The three driver responses are scaled by global warming. The black stars indicate the selected four storylines that combine anomalies in the driver responses. The dashed ellipses show the 80% confidence region obtained by fitting a bivariate normal distribution to the model responses. In each panel, the quadrants delimited by the inner ellipse and by the four straight lines define the regions used to group the models according to the four storylines.

Figure 7.15 illustrates the resulting regional stagnation responses for each storyline. In the US, stagnation seems to increase for all storylines, but with considerable uncertainty. In particular, the northwest US has the largest stagnation changes projected across the storylines considered (i.e. the strongest sensitivity to the driver responses). The combination of low RTAW and high NPACW is associated with an increase in stagnation

frequency of $\sim 3\%/K$ in contrast to $\sim 1\%/K$ when the opposite occurs. This difference (~ 2 days/ K) is mostly caused by a large uncertainty in the mid-tropospheric wind response, with an inter-storyline variability close to $4\%/K$ (~ 4 days/ K). The storyline uncertainty is comparatively low for the stagnation projections in the rest of US, though some stagnation components deserve attention. In particular, the decrease in frequency of dry days over the southwest US projected by the multi-model mean could intensify substantially under low RTAW or turn to a small increase in the opposite case. This component tends to dominate the ASI responses over the southwest US. In general, the storyline uncertainty of air stagnation is moderate (as compared to that of some of the components) for the US. This occurs because the stagnation components respond differently to the driver changes and therefore such responses tend to cancel out. For example, while low RTAW and high NPACW promote stagnant winds and yield stagnation increases in the northwest US, this storyline also decreases the frequency of dry days (and vice-versa for the opposite storyline). Therefore, the ASI responses to the driver changes are compensated by opposite effects in the stagnant components, reducing storyline uncertainty. Despite this, there is large regional heterogeneity in the stagnation response to a given storyline, suggesting that the spatial patterns of stagnation changes depend substantially on the storyline.

Figure 7.15 also displays relevant storylines of future stagnation in Europe. Overall, the European regions present higher sensitivity to the storyline uncertainty than those in the US. This is partially due to the reinforcement of the individual responses in the stagnation components, which contrasts with the opposing effects of the storylines reported for the US. In all regions except southwest Europe, the highest stagnation increases are expected in the low RTAW and weak NATLW storyline, which is associated with larger precipitation and wind decreases than in the multi-model mean. The opposite occurs for the high RTAW and NATLW storyline, which yields the largest rise in stagnant days over southwest Europe but the lowest increase for the rest of Europe.

We have also repeated the analyses shown in Figure 7.15 but using a composite approach rather than the regression framework. For that purpose, we have grouped the

climate models based on their remote driver responses by averaging the scaled circulation response of the models that are delimited by the four quadrants of Figure 7.14. The models in the inner ellipse have been discarded due to their proximity to the multi-model mean. The resulting spatial distributions resemble those derived with the regression framework (see Annex Figures A8 to A11), supporting the previous findings.

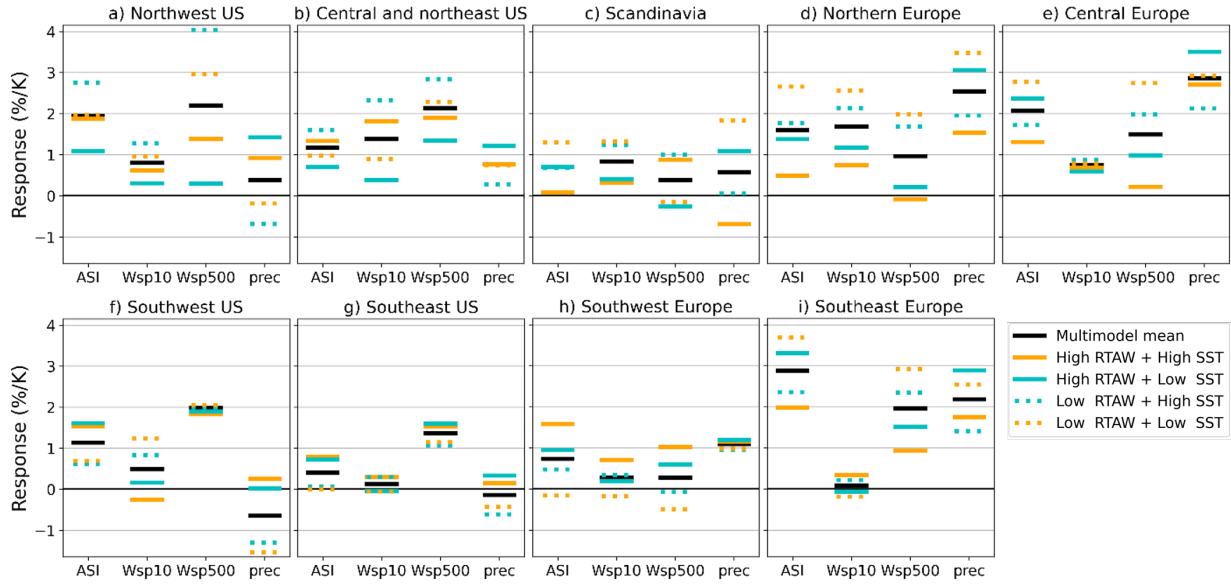


Figure 7.15: Summer stagnation response (JJA 2071–2100 minus JJA 1981–2010) per degree of global warming (%/K) according to four plausible storylines of climate change. These are conditioned on the ratio between the tropical and Arctic warming (RTAW) for all regions as well as the North Pacific warming (NPACW) responses in the US and the North Atlantic warming (NATLW) responses in Europe. Abbreviations: ASI — air stagnation index, Wsp10 — 10m wind speed, Wsp500 — 500hPa wind speed, and prec — precipitation.

The amplitude of the projected stagnation increases also follows that of GW. Figure 7.16 displays the regional stagnation change as a function of GW and a storyline index that represents the standardized anomaly in the driver responses (Zappa and Shepherd, 2017). In other words, the storyline index measures how large the responses of the remote drivers are. High values indicate strong responses, while zero values mean absence of changes. This storyline index has been chosen for the combination of driver responses leading to the highest storyline uncertainty in ASI for each region. This way, positive values of this index represent high RTAW and low NPACW for northwest, central, and northeast US, high RTAW for southwest and southeast US, and high RTAW and NATLW

for the European regions, with the opposite driver responses for negative values. Note that we only use RTAW for the southern regions of the US because the effect of NPACW is negligible there (see Figure 7.15). Overall, the panels show similar spread of stagnation responses across the range of values of global warming and the storyline index. In the US, for a 3°C global warming, the increase in stagnation frequency ranges from 3 to 9% (3–8 days) in northwest US depending on the storyline, while the width of this range drops below 4% (3–4 days) for the rest of US regions.

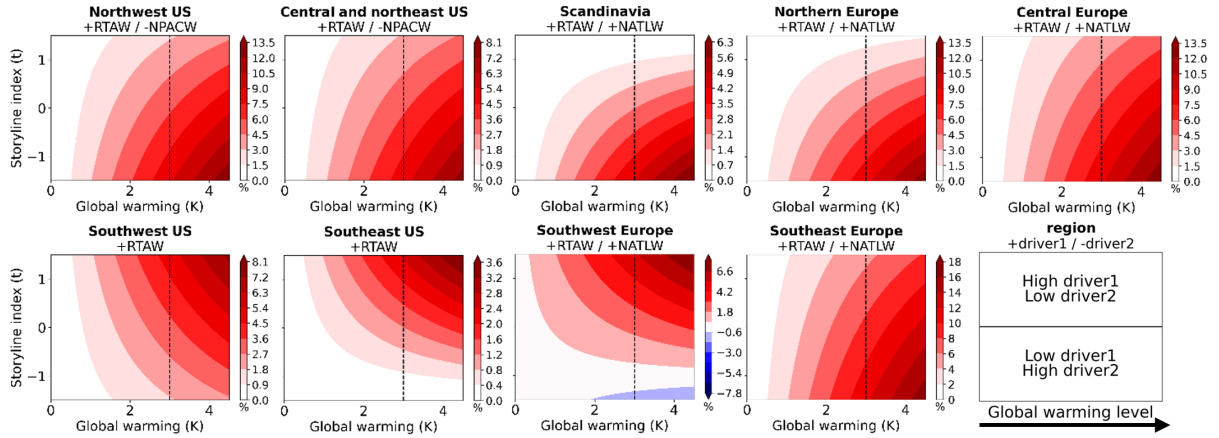


Figure 7.16: Projected changes of regional stagnation frequency as a function of global warming and storyline index. The index represents the standardized anomaly of the combined driver responses. The text on the top of each panel indicates the drivers used to generate the storylines in each region, with the signs specifying how they are combined. For example, positive values of the storyline index represent high RTAW and low NPACW for northwest US, and vice versa. The vertical dashed lines indicate a global warming of 3°C . The right bottom panel shows a schematic diagram to interpret the plots. Note the different colour scales for each region.

On the other hand, the strongest sensitivity to the responses of RTAW and NATLW in Europe is found in northern and, to a lesser extent, southeast and southwest regions (Figure 7.16). For a 3°C global warming, the increase in stagnation frequency ranges from 1 to 9% (1–8 days) in northern Europe, from 5 to 12% (5–11 days) in southeast Europe and from -1 to 5% (-1–5 days) in southwest Europe depending on the storyline. Although stagnation frequency is projected to increase in the multi-model mean for these regions, the magnitude of the changes seems uncertain and might be rather moderate for Scandinavia and southwest Europe. This illustrates the difficulty of establishing a global warming threshold to limit future stagnation increases.

7.6 Main findings and discussion

Recent studies have investigated the influence that climate change could exert on the frequency of air stagnation in different regions of the globe throughout the 21st century (Horton et al., 2012, 2014; Caserini et al., 2017; Han et al., 2017; Gao et al., 2020; Lee et al., 2020). Although they provide a probabilistic view based on multi-model means, there are still large discrepancies among climate model projections. For instance, under the SSP5-8.5 forcing scenario, the interquartile ranges of the changes in summer stagnation frequency can be as high as 8% (7 days) for some regions by the end of the 21st century (see Figure 7.17). While different sources of uncertainty (e.g. internal variability, model formulation) potentially contribute to these differences, previous analyses have shown that the careful examination of the circulation response to external forcings may provide some constraints on model projections (e.g. Shepherd, 2014; Zappa and Shepherd, 2017).

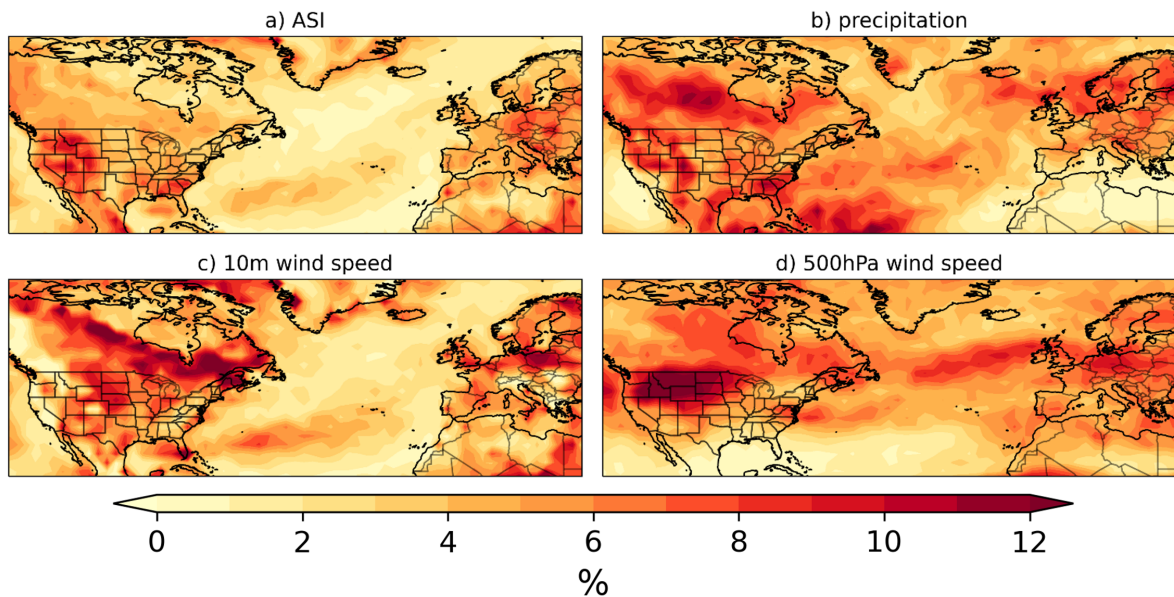


Figure 7.17: Interquartile range of the summer absolute change (2071–2100 minus 1981–2010, %) in the occurrence of (a) air stagnation, (b) dry days, (c) near-surface wind stagnation and (d) mid-tropospheric wind stagnation.

In this chapter we have explored the relationship between stagnation changes in the US and Europe and three different remote drivers of the mid-latitude atmospheric cir-

ulation in summer, when the projected stagnation changes are the highest. While models consistently report future increases in stagnation for the high forcing scenario considered here, the magnitude and spatial distribution of these changes vary substantially across the model ensemble depending on the driver responses. Overall, our results indicate that strong tropical warming relative to Arctic warming is associated with a strengthening and poleward shift of the upper westerlies, which in turn would lead to decreases in stagnation over the northern regions of North America and Europe, as well as increases in some southern regions, as compared to the multi-model mean. Opposite responses occur for larger Arctic warming levels, consistent with the projected weakening and equatorward shift of the mid-latitude jets associated with the Arctic amplification (Screen, 2013; Coumou et al., 2018; Zappa et al., 2018). On the other hand, North Pacific warming tends to increase the frequency of stagnation over some regions of the US by enhancing the frequency of stagnant winds, while reduced North Atlantic warming does the same over Europe by promoting the frequency of dry days. The latter finding is consistent with Jackson et al. (2015), who reported summer precipitation deficits over most Europe for a decline of the AMOC. One could expect that moderate surface warming will limit evaporation over the North Atlantic, although dynamical processes might play a role too due to the influence of North Atlantic SSTs on the eddy-driven jet and the storm track (Woollings et al., 2012; Hall et al., 2016; Baker et al., 2019; Ruggieri et al., 2021).

Given the response of stagnation to these remote drivers, their evolution in future projections will substantially determine the magnitude of the stagnation increases. Following this, we have generated extreme but plausible storylines based on the modelled response of the three remote drivers. The results show differences up to $2\%/K$ (~ 2 stagnant days in summer per degree of global warming) between the storylines for some regions. As an illustration, for a 3°C global warming, the uncertainty in northern Europe is high (around 8%, i.e. ~ 7 days) compared to the observed 1981–2010 frequency of stagnation ($\sim 20\%$). This high inter-storyline variability implies that future projections of stagnation depend substantially on the atmospheric circulation and cannot be well constrained based on multi-model means, even for specific global warming levels. The most sensitive regions to the driver responses are not necessarily those with the highest

inter-model variability. In fact, European regions present higher storyline uncertainty than those in the US, except for northwest US, despite displaying comparable inter-model variability. This is at least partially due to the reinforcement of the individual responses in the stagnation components over Europe as opposed to the offsetting effects of the storylines generated for the US.

The resulting storylines have also shown that the worst-case scenario for one region can be the best-case scenario for another. For instance, the storyline characterized by the combination of a high ratio between tropical and Arctic warming with strong North Atlantic warming is associated with the largest stagnation increase in southwest Europe and the lowest in the rest of the continent. These regional differences may imply uneven impacts of future stagnation changes on air quality. Although the projections of increases in stagnation cannot always be translated into enhanced air pollution (see Chapter 6), they are valuable indicators in the absence of air quality output from climate models, especially for those regions where the sensitivity of air pollution to stagnation has been proven. Interestingly, we have previously reported high increases in summer near-surface ozone concentrations on stagnant days over southeast and central Europe (see Chapter 4 and Chapter 6), where we now project some of the highest stagnation increases and considerable spread among the storylines. This suggests that future air pollution in these and other regions could be especially sensitive to mid-latitude dynamical changes associated with climate change. Thus, the analysis of plausible storylines of future regional changes in stagnation could be instrumental in understanding divergent model responses when assessing future changes in weather conditions conducive to poor air quality in those regions.

Despite the underlying assumptions (i.e. the amplitude of the atmospheric response depends on global warming but not on the chosen scenario) and approaches (percentile-based bias correction), our results show substantial spread in future regional stagnation as mediated by the considered drivers. Additional studies are encouraged to uncover the physical mechanisms linking these drivers with regional stagnation as well as to explore potential remote drivers not considered herein.

8 Conclusions and outlook

8.1 Main conclusions

In this thesis, we have addressed several questions that remained open in the literature. In particular, 1) we have carried out the first characterization of the spatiotemporal variability of air stagnation in Europe and 2) the first comparison of stagnation as derived from meteorological reanalysis and observations. In addition, 3) we have also identified synoptic patterns leading to seasonal stagnation extremes in Europe. Then, we have critically assessed the effect of stagnation on the concentrations of two major air pollutants: 4) particulate matter and 5) ozone. Finally, 6) we have provided a quantitative analysis of future changes in stagnation for different storylines and levels of warming. The main conclusions of each of these topics are summarized next:

Spatiotemporal variability

- There is considerable spatial heterogeneity across Europe, with more stagnation in the south than in the north. Thus, we have regionalized the monthly frequency of stagnant days, resulting five regions with consistent spatiotemporal patterns: Scandinavia (SCAN), Northern-Europe (NEU), Central-Europe (CEU), South-West (SW) and South-East (SE).
- The northern regions (SCAN and NEU), which are affected by moderately strong near-surface winds and ample precipitation, present low frequency and temporal variability in stagnation compared to the southern regions (SW and SE). CEU presents moderate stagnation and small interannual variability.
- We have found significant positive trends in the number of air stagnation days for the period 1979–2016 over a large area including SE and CEU. This is in line with the increase in air stagnation frequency reported by Horton et al. (2014) for a similar region north of the Mediterranean throughout the 21st century, suggesting that the projected increase might have already started in some parts of Europe.

Reanalysis vs observations

- There is a good agreement in both the percentage frequency of stagnant days and the number of stagnation events per year at the continental scale as derived from meteorological reanalysis and observations using HO_ASI. Mean biases (MB) for these benchmarks are relatively low in the reanalysis compared to the observations (-1.4% and 2.1 events respectively).
- The main differences arise from the surface wind speed, as this field depends on the local setting of the observational sites and imperfect parameterizations within the reanalysis model. The correlation between reanalysis and observations is considerably lower for stagnant surface winds (0.64) than for the other two ASI components (0.95 for precipitation and 0.93 for upper-air wind speed).

Typical synoptic patterns

- The winters and summers with the highest stagnation frequency often concur with positive Z500 anomalies over the regions, with the exception of negative Z500 anomalies and a displacement of the extratropical jet to the south in the case of SCAN and NEU during winter.

Air stagnation – particulate matter relationship

- The occurrence of air stagnation, as measured by three different indices (HO_ASI, WA_ASI and HU_ASI) is associated with PM_{10} enhancements. However, the response of the PM_{10} concentrations to stagnation varies with the ASI. While winter PM_{10} anomalies under stagnant conditions are of the same order of magnitude for the three ASIs (on average 17.2 to 18.6 $\mu g m^{-3}$, around 60 % of the mean values), HO_ASI outperforms WA_ASI and HU_ASI at most locations in summer, when the anomalies are considerably smaller (3.8–5.7 $\mu g m^{-3}$, around 19–28 %).
- Our results show that there is some room for improving the performance of HO_ASI and HU_ASI over Europe. This might require revising the 500 hPa wind speed condition for the former and replacing the ventilation condition by an appropriate transport wind speed threshold in the latter.
- The consideration of a meteorological variable representing the large-scale flow consistently contributes to reproducing PM_{10} variability. This is especially true in summer, possibly explaining the highest skill of HO_ASI during this season. In addition, the response of PM_{10} concentrations to large-scale circulation patterns is stronger than previously reported for Europe and other mid-latitude regions. While EUR blocking yields large positive anomalies which average 12 $\mu g m^{-3}$ over a large part of the continent, the occurrence of ATL ridges reduces PM_{10} concentrations on average by around 8 $\mu g m^{-3}$. Furthermore, the occurrence of these anticyclonic situations can explain a large fraction of the interannual variability of PM_{10} over some parts of central Europe, with $R^2 = 0.86$ in Southern Germany during an 11-year

period.

- The ASIs tested here are based on fixed thresholds of meteorological fields. Therefore, they cannot deal with non-linear relationships between the variables that characterize the dilution capacity of the atmosphere and the PM_{10} concentrations, limiting their ability to explain the variability of this pollutant. Non-linear statistical models based on the local selection of air pollution-related variables might be more suited to reproduce the day-to-day variability of PM.

Air stagnation – ozone relationship

- The effects of stagnation on summer ozone are regionally dependent across Europe. $MDA8\ O_3$ mixing ratios consistently increase over central/southern Europe under stagnant conditions (around 4–6 ppb on average), but this has not been found for some temperature ranges in the north. Under non-stagnant situations and relatively high temperatures (20–25 °C), southerly advection often brings warm aged air masses from relatively more polluted areas to the receptor regions in northern Europe. This yields $MDA8\ O_3$ mixing ratios as high as those during stagnant days in such regions. This regional dependency of the ozone – stagnation relationship across Europe indicates that climate model projections of increases in stagnation should not directly be translated into degraded air quality without a proper assessment of the regional impacts.
- The occurrence of stagnation tends to amplify the ozone diurnal cycles in the centre/south of the continent, yielding lower nighttime to early morning mixing ratios and higher daytime mixing ratios than on non-stagnant days, again with a less clear effect in the north. Changes in PBL dynamics, accumulation of ozone and precursors, and subsequent photochemical production during stagnant days are the presumed underlying mechanisms for the amplification of the diurnal cycles.

Future air stagnation

- Under a high radiative forcing scenario (SSP5-8.5), models consistently project increases in stagnation over Europe and the US, which are largely caused by enhanced frequency of dry days and stagnant mid-tropospheric winds, respectively. However, the magnitude and spatial distribution of changes vary substantially across CMIP6 ensemble members, suggesting that future projections are not well-constrained when using the ensemble mean alone.
- We find that the diversity of projected stagnation changes depends on the forced response of remote drivers in individual models. Overall, our results indicate that strong tropical warming relative to Arctic warming is associated with a strengthening and poleward shift of the upper westerlies, which in turn would lead to decreases in stagnation over the northern regions of North America and Europe, as well as increases in some southern regions, as compared to the multi-model mean. On the other hand, North Pacific warming tends to increase the frequency of stagnation over some regions of the US by enhancing the frequency of stagnant winds, while reduced North Atlantic warming does the same over Europe by promoting the frequency of dry days.
- In Europe, differences of ~ 2 stagnant days per degree of global warming are found for summer amongst the different storyline combinations. In addition, the resulting storylines have also shown that the worst-case scenario for one region can be the best-case scenario for another. For example, the storyline characterized by the combination of a high ratio between tropical and Arctic warming with high North Atlantic warming is associated with the highest stagnation increase in southwest Europe and the lowest in the rest of the continent. In the US, only the atmosphere over the northern Rocky Mountain states demonstrates comparable stagnation projection uncertainty, due to opposite influences of remote drivers on the meteorological conditions that lead to stagnation.

8.2 Outlook

Some knowledge gaps have been filled in this thesis, but still several issues deserve further research. The work presented here has shown strong links between stagnation situations and the large-scale circulation. However, no systematic study of the large-scale dynamics associated with stagnation events has been carried out. In Europe there are several dynamical features such as the eddy-driven jet or the large-scale subsidence in the Hadley cell that could be relevant for stagnation. The North Atlantic jet stream modulates the trajectories and strength of extratropical storms and cyclones propagating towards Europe (e.g. Woollings et al., 2010). It has recently been shown that the latitudinal position of the jet controls the regional distribution of PM_{10} concentrations in Europe (Ordóñez et al., 2019), in a similar fashion as found by previous analyses for near-surface ozone in the US (Barnes and Fiore, 2013; Shen et al., 2015). Other studies have shown that the low frequency of summertime mid-latitude cyclones and frontal passages are closely related to stagnation and poor AQ, both in the US (Leibensperger et al., 2008; Tai et al., 2010) and in Europe (Ordóñez et al., 2005; Pope et al., 2016). Some analyses have projected a poleward shift of mid-latitude jets in the future (e.g. Barnes and Polvani, 2013), but there is considerable uncertainty in the future evolution of the North Atlantic jet (e.g. Zappa and Shepherd, 2017; Peings et al., 2018). On the other hand, the characteristic anticyclonic circulations and dry conditions produced by the large-scale subsidence in the Hadley cell are also associated with stagnation. In fact, Horton et al. (2014) have linked the projected increases in air stagnation over the Mediterranean and southern China to enhanced mid-tropospheric subsidence and strengthening / northward shift in the descending branch of the Hadley circulation, respectively. There are also evidences for an expansion of the tropical belt both in the past and in the future (e.g. Hu and Fu, 2007; Lu et al., 2007; Seidel and Randel, 2007; Tao et al., 2016; Grise and Davis, 2020).

We have investigated the link between European air stagnation, air pollution and the synoptic- to large-scale circulation in Maddison et al. (2021) across all seasons and the 1979–2018 period. Dynamical indices identifying atmospheric blocking, Rossby wave

breaking, subtropical ridges, and the North Atlantic eddy-driven and subtropical jets are used in this work to describe the synoptic- to large-scale circulation as predictors in statistical models of air stagnation and pollutant variability. It is found that the large-scale circulation can explain approximately 60% of the variance in monthly air stagnation, ozone and wintertime PM in the five European regions defined in Chapter 3. The variance explained by the model does not vary strongly across regions and seasons, except for PM when the skill is highest in winter. However, the dynamical indices most related to air stagnation do depend on region and season. The blocking and Rossby wave breaking predictors tend to be the most important for describing air stagnation and pollutant variability in northern regions, whereas ridges and the subtropical jet are more important to the south. The demonstrated correspondence between air stagnation, pollution and the large-scale circulation can be used to assess the representation of stagnation in climate models, which is key for understanding how air stagnation and its associated climatic impacts may change in the future. Following this, we are now exploiting the statistical model used in the previous work to provide an alternative approach to ASIs for describing air stagnation in GCMs. This allows for an investigation into projected air stagnation trends, what is driving them, and to what extent they are a result of changes to the dynamics (Maddison et al., 2022).

Regarding the potential of ASIs, we have shown that there is some room for improving their ability to represent the meteorological conditions conducive to enhanced pollution in Europe. Hence, future work could modify these indices by using different meteorological variables or adapting their thresholds, based on some of the results and suggestions presented in this thesis. On the one hand, the 13.0 m s^{-1} wind speed threshold used in HO_ASI is often exceeded during the cold seasons, reducing the occurrence of stagnation in winter for HO_ASI compared to other indices; the links of upper wind speeds to dilution conditions close to the surface should closely be examined before attempting to adapt that condition. On the other hand, ventilation values peak during summer because of the high boundary layers at that time of the year, potentially yielding an artificially low stagnation frequency in summer as compared with winter when HU_ASI is used; our results suggest that the transport wind speed could be used instead to measure the

average strength of horizontal dilution within the boundary layer regardless of its depth. One should also bear in mind that the three indices considered here can only measure the frequency but not the intensity of stagnation. Moreover, they are limited by the use of fixed thresholds in their definitions. Consequently, the possibility of developing new indices should be explored. In this sense, Feng et al. (2018) have introduced a new ASI that provides information about the intensity of air stagnation, allowing the quantification of extreme events in terms of their severity. They have recently extended their index to also include fixed emission information, which improves the ability to capture the spatial distribution of the $PM_{2.5}$ concentrations in China (Feng et al., 2020). Such efforts have not been carried out for Europe yet.

9 Publications

Most of the results presented in this PhD thesis are included in the following publications:

- **Garrido-Perez J.M.**, Ordóñez C., García-Herrera R. (2017): Strong signatures of high-latitude blocks and subtropical ridges in winter over Europe. *Atmospheric Environment*, 167, 49-60. doi:10.1016/j.atmosenv.2017.08.004.
- **Garrido-Perez J.M.**, Ordóñez C., García-Herrera R., Barriopedro D. (2018): Air stagnation in Europe: spatiotemporal variability and impact on air quality, *Science of the Total Environment*, 645, 1238-1252.
- **Garrido-Perez J.M.**, Ordóñez C., García-Herrera R., Schnell, J.L. (2019): The differing impact of air stagnation on summer ozone across Europe. *Atmospheric Environment*. <https://doi.org/10.1016/j.atmosenv.2019.117062>.
- **Garrido-Perez J.M.**, García-Herrera R., Ordóñez C. (2021): Assessing the value of air stagnation indices to reproduce PM_{10} variability in Europe. *Atmospheric Research*, 248, 105258. doi: 10.1016/j.atmosres.2020.105258.
- **Garrido-Perez J.M.**, Ordóñez C., Barriopedro D., , García-Herrera R., Schnell J.L., Horton D.E. (2022): A storyline view of the projected role of remote drivers on summer air stagnation in Europe and the United States. *Environmental Research Letters*, 17, 014026. doi: 10.1088/1748-9326/ac4290.

In addition, during the development of this thesis, the author has also contributed to the following publications:

- Ayarzagüena B., Barriopedro D., **Garrido-Perez J.M.**, Abalos M., de la Cámara A., García-Herrera R., Calvo N., Ordóñez C. (2018): Stratospheric Connection to the Abrupt End of the 2016/2017 Iberian Drought, *Geophysical Research Letters*, 45(22), 12-639.
- García-Herrera R., **Garrido-Perez J.M.**, Barriopedro D., Ordóñez C., Vicente-Serrano S.M., Nieto R., Gimeno L., Sori R., Yiou P. (2019): The European 2016/2017 drought, *Journal of Climate*. doi: 10.1175/JCLI-D-18-0331.1.
- **Garrido-Perez J.M.**, Barriopedro D., García-Herrera R., Ordóñez C. (2021): Impact of climate change on Spanish electricity demand, *Climatic Change*, 165:50, doi: 10.1007/s10584-021-03086-0.
- **Garrido-Perez J.M.**, Ordóñez C., Barriopedro D., García-Herrera R., Paredes D., (2020): Impact of weather regimes on wind power variability in western Europe, *Applied Energy*, 264, 114731. doi: 10.1016/j.apenergy.2020.114731.
- **Garrido-Perez J.M.** et al. (2022) Modulation of European air quality by Euro-Atlantic weather regimes. *Atmospheric Research*. Under Review.
- Ordóñez C., **Garrido-Perez J.M.**, García-Herrera R. (2020): Early spring near-surface ozone in Europe during the COVID-19 shutdown: Meteorological effects outweigh emission changes, *Science of The Total Environment*, 747, 141322. doi: 10.1016/j.scitotenv.2020.141322.
- Maddison J., Abalos M., Barriopedro D., García-Herrera R., **Garrido-Perez J.M.**, Ordóñez C. (2021): Linking air stagnation in Europe with the synoptic-to large-scale atmospheric circulation, *Weather and Climate Dynamics*, 2, 675–694, doi:10.5194/wcd-2-675-2021.
- Maddison J. et al. (2022): Assessing the uncertainty in projected changes in Euro-

pean air stagnation. *Journal of Climate*. Under Review.

- Vicente-Serrano S.M., Juez C., Potopová V., Boincean B., Murphy C., Domínguez-Castro F., Eklundh L., Peña-Angulo D., Noguera I., Jin H., Conradt T., García-Herrera R., **Garrido-Pérez J.M.**, Barriopedro D., Gutiérrez J.M., Iturbide M., Lorenzo-Lacruz J., El Kenawy A. (2022): Drought severity under global warming endangers crop yields in agricultural areas of Eastern Europe: the case of Moldova. *Agricultural and Forest Meteorology*. Under Review.

Bibliography

- Aksoyoglu, S., Keller, J., Barmpadimos, I., Oderbolz, D., Lanz, V. A., Prévât, A. S., and Baltensperger, U. (2011). Aerosol modelling in Europe with a focus on Switzerland during summer and winter episodes. *Atmospheric Chemistry and Physics*, 11(14):7355–7373.
- Alexander, M. A., Bladé, I., Newman, M., Lanzante, J. R., Lau, N. C., and Scott, J. D. (2002). The atmospheric bridge: The influence of ENSO teleconnections on air-sea interaction over the global oceans. *Journal of Climate*, 15(16):2205–2231.
- Aurenhammer, F. (1991). Voronoi diagrams—a survey of a fundamental geometric data structure. *ACM Computing Surveys*, 23(3):345–405.
- Bador, M., Naveau, P., Gilleland, E., Castellà, M., and Arivelo, T. (2015). Spatial clustering of summer temperature maxima from the CNRM-CM5 climate model ensembles & E-OBS over Europe. *Weather and Climate Extremes*, 9:17–24.
- Baker, H. S., Woollings, T., Forest, C. E., and Allen, M. R. (2019). The linear sensitivity of the north atlantic oscillation and eddy-driven jet to SSTs. *Journal of Climate*, 32(19):6491–6511.
- Barkhordarian, A., Bhend, J., and von Storch, H. (2012). Consistency of observed near surface temperature trends with climate change projections over the Mediterranean region. *Climate Dynamics*, 38(9-10):1695–1702.
- Barmpadimos, I., Hueglin, C., Keller, J., Henne, S., and Prévôt, A. S. (2011). Influ-

- ence of meteorology on PM_{10} trends and variability in Switzerland from 1991 to 2008. *Atmospheric Chemistry and Physics*, 11(4):1813–1835.
- Barnpadimos, I., Keller, J., Oderbolz, D., Hueglin, C., and Prévôt, A. (2012). One decade of parallel fine ($PM_{2.5}$) and coarse ($PM_{10} - PM_{2.5}$) particulate matter measurements in Europe: Trends and variability. *Atmospheric Chemistry and Physics*, 12(7):3189–3203.
- Barnes, E. A. and Fiore, A. M. (2013). Surface ozone variability and the jet position: implications for projecting future air quality. *Geophysical Research Letters*, 40:2839–2844.
- Barnes, E. A. and Polvani, L. (2013). Response of the midlatitude jets, and of their variability, to increased greenhouse gases in the CMIP5 models. *Journal of Climate*, 26:7117–7135.
- Barriopedro, D., García-Herrera, R., Lupo, A. R., and Hernández, E. (2006). A climatology of Northern Hemisphere blocking. *Journal of Climate*, 19(6):1042–1063.
- Barriopedro, D., García-Herrera, R., and Trigo, R. M. (2010). Application of blocking diagnosis methods to General Circulation Models. Part I: A novel detection scheme. *Climate Dynamics*, 35(7):1373–1391.
- Bedi, H. S. and Parthasarathy, B. (1967). Cold Waves over northwest India and neighbourhood. *Indian Journal of Meteorology and Geophysics*, 54(551.55.4):371–378.
- Begum, B. A., Biswas, S. K., Pandit, G. G., Saradhi, I. V., Waheed, S., Siddique, N., Seneviratne, M. C., Cohen, D. D., Markwitz, A., and Hopke, P. K. (2011). Long-range transport of soil dust and smoke pollution in the South Asian region. *Atmospheric Pollution Research*, 2(2):151–157.
- Bencala, K. E. and Seinfeld, J. H. (1976). On frequency distributions of air pollutant concentrations. *Atmospheric Environment (1967)*, 10(11):941–950.
- Bloomer, B. J., Stehr, J. W., Piety, C. A., Salawitch, R. J., and Dickerson, R. R. (2009). Observed relationships of ozone air pollution with temperature and emissions. *Geophysical Research Letters*, 36(9).

- Bloomfield, P., Royle, J., Steinberg, L., and Yang, Q. (1996). Accounting for meteorological effects in measuring urban ozone levels and trends. *Atmospheric Environment*, 30(17):3067–3077.
- Boleti, E., Hueglin, C., and Takahama, S. (2018). Ozone time scale decomposition and trend assessment from surface observations in Switzerland. *Atmospheric Environment*, 191:440–451.
- Bosilovich, M. G., Chen, J., Robertson, F. R., and Adler, R. F. (2008). Evaluation of global precipitation in reanalyses. *Journal of Applied Meteorology and Climatology*, 47:2279–2299.
- Brown, B. G., Gilleland, E., and Ebert, E. E. (2012). Forecasts of spatial fields. In: Jolliffe, I.T., Stephenson, D.B. (Eds.), *Forecast verification: A practitioner’s guide in atmospheric science*, Second Edition. John Wiley and Sons. New Jersey, United States. ISBN: 978-0-470-66071-3.
- Brown, S. S. and Stutz, J. (2012). Nighttime radical observations and chemistry. *Chemical Society Reviews*, 41(19):6405–6447.
- Brunner, D., Savage, N., Jorba, O., Eder, B., Giordano, L., Badia, A., Balzarini, A., Baró, R., Bianconi, R., Chemel, C., Curci, G., Forkel, R., Jiménez-Guerrero, P., Hirtl, M., Hodzic, A., Honzak, L., Im, U., Knote, C., Makar, P., Manders-Groot, A., van Meijgaard, E., Neal, L., Pérez, J. L., Pirovano, G., San Jose, R., Schröder, W., Sokhi, R. S., Syrakov, D., Torian, A., Tuccella, P., Werhahn, J., Wolke, R., Yahya, K., Zabkar, R., Zhang, Y., Hogrefe, C., and Galmarini, S. (2015). Comparative analysis of meteorological performance of coupled chemistry-meteorology models in the context of AQMEII phase 2. *Atmospheric Environment*, 115:470–498.
- Cai, W., Li, K., Liao, H., Wang, H., and Wu, L. (2017). Weather conditions conducive to Beijing severe haze more frequent under climate change. *Nature Climate Change*, 7(4):257–262.
- Carro-Calvo, L., Ordóñez, C., García-Herrera, R., and Schnell, J. L. (2017). Spatial

- clustering and meteorological drivers of summer ozone in Europe. *Atmospheric Environment*, 167:496–510.
- Carvalho, M. J., Melo-Gonçalves, P., Teixeira, J. C., and Rocha, A. (2016). Regionalization of Europe based on a K-Means Cluster Analysis of the climate change of temperatures and precipitation. *Physics and Chemistry of the Earth*, 94:22–28.
- Caserini, S., Giani, P., Cacciamani, C., Ozgen, S., and Lonati, G. (2017). Influence of climate change on the frequency of daytime temperature inversions and stagnation events in the Po Valley: historical trend and future projections. *Atmospheric Research*, 184:15–23.
- Chang, L., Xu, J., Tie, X., and Wu, J. (2016). Impact of the 2015 El Nino event on winter air quality in China. *Scientific Reports*, 6(34275).
- Chen, X., Zhou, T., Wu, P., Guo, Z., and Wang, M. (2020). Emergent constraints on future projections of the western North Pacific Subtropical High. *Nature Communications*, 11(1):1–10.
- Cohen, A. J., Brauer, M., Burnett, R., Anderson, H. R., Frostad, J., Estep, K., Balakrishnan, K., Brunekreef, B., Dandona, L., Dandona, R., Feigin, V., Freedman, G., Hubbell, B., Jobling, A., Kan, H., Knibbs, L., Liu, Y., Martin, R., Morawska, L., Pope, C. A., Shin, H., Straif, K., Shaddick, G., Thomas, M., van Dingenen, R., van Donkelaar, A., Vos, T., Murray, C. J., and Forouzanfar, M. H. (2017). Estimates and 25-year trends of the global burden of disease attributable to ambient air pollution: an analysis of data from the Global Burden of Diseases Study 2015. *The Lancet*, 389(10082):1907–1918.
- Coumou, D., Di Capua, G., Vavrus, S., Wang, L., and Wang, S. (2018). The influence of Arctic amplification on mid-latitude summer circulation. *Nature Communications*, 9(1):1–12.
- Dawson, J. P., Adams, P. J., and Pandis, S. N. (2007). Sensitivity of $PM_{2.5}$ to climate in the Eastern US: A modeling case study. *Atmospheric Chemistry and Physics*, 7(16):4295–4309.

- Dawson, J. P., Bloomer, B. J., Winner, D. A., and Weaver, C. P. (2014). Understanding the meteorological drivers of U.S. particulate matter concentrations in a changing climate. *Bulletin of the American Meteorological Society*, 95(4):521–532.
- de Sherbinin, A. (2014). Climate change hotspots mapping: What have we learned? *Climatic Change*, 123:23–37.
- Dee, D. P., Uppala, S. M., Simmons, A. J., Berrisford, P., Poli, P., Kobayashi, S., Andrae, U., Balmaseda, M. A., Balsamo, G., Bauer, P., Bechtold, P., Beljaars, A. C., van de Berg, L., Bidlot, J., Bormann, N., Delsol, C., Dragani, R., Fuentes, M., Geer, A. J., Haimberger, L., Healy, S. B., Hersbach, H., Hólm, E. V., Isaksen, L., Kållberg, P., Köhler, M., Matricardi, M., McNally, A. P., Monge-Sanz, B. M., Morcrette, J. J., Park, B. K., Peubey, C., de Rosnay, P., Tavolato, C., Thépaut, J. N., and Vitart, F. (2011). The ERA-Interim reanalysis: Configuration and performance of the data assimilation system. *Quarterly Journal of the Royal Meteorological Society*, 137(656):553–597.
- Demetillo, M. A. G., Anderson, J. F., Geddes, J. A., Yang, X., Najacht, E. Y., Herrera, S. A., Kabasares, K. M., Kotsakis, A. E., Lerda, M. T., and Pusede, S. E. (2019). Observing severe drought influences on ozone air pollution in California. *Environmental Science and Technology*, 53(9):4695–4706.
- Deser, C. and Trenberth, K. (2016). The Climate Data Guide: Pacific Decadal Oscillation (PDO): Definition and Indices. Retrived from: <https://climatedataguide.ucar.edu/climate-data/pacific-decadal-oscillation-pdo-definition-and-indices>.
- Diffenbaugh, N. S. and Giorgi, F. (2012). Climate change hotspots in the CMIP5 global climate model ensemble. *Climatic Change*, 114(3-4):813–822.
- Dimitriou, K. (2015). The dependence of PM size distribution from meteorology and local-regional contributions, in Valencia (Spain) – A CWT model approach. *Aerosol and Air Quality Research*, 15(5):1979–1989.

- Doche, C., Dufour, G., Foret, G., Eremenko, M., Cuesta, J., Beekmann, M., and Kalabokas, P. (2014). Summertime tropospheric-ozone variability over the Mediterranean basin observed with IASI. *Atmospheric Chemistry and Physics*, 14(19):10589–10600.
- Dominici, F., McDermott, A., Zeger, S. L., and Samet, J. M. (2002). On the use of generalized additive models in time-series studies of air pollution and health. *American Journal of Epidemiology*, 156(3):193–203.
- Durre, I., Vose, R. S., and Wuertz, D. B. (2006). Overview of the integrated global radiosonde archive. *Journal of Climate*, 19(1):53–68.
- Eden, J. M., Van Oldenborgh, G. J., Hawkins, E., and Suckling, E. B. (2015). A global empirical system for probabilistic seasonal climate prediction. *Geoscientific Model Development*, 8(12):3947–3973.
- Edwards, P. J., Wood, F., and Kochenderfer, J. N. (1991). Characterization of ozone during consecutive drought and wet years at a rural West Virginia site. *Journal of the Air and Waste Management Association*, 41(11):1450–1453.
- EEA (2019). Air quality in Europe – 2019 report. European Environment Agency. Available at: <https://www.eea.europa.eu/publications/air-quality-in-europe-2019>.
- EU (2008). Directive 2008/50/EC of the European Parliament and of the Council of 21 May 2008 on ambient air quality and cleaner air for Europe. Official Journal of the European Union. OJ L 152, 11.6.2008. Available at: <https://eur-lex.europa.eu/legal-content/EN/TXT/PDF/?uri=CELEX:32008L0050&from=en>.
- EU (2016). Directive 2016/2284/EC of the European Parliament and of the Council of 14 December 2016 on the reduction of national emissions of certain atmospheric pollutants. Amending Directive 2003/35/EC and Repealing Directive 2001/81/EC. Official Journal of the European Union. Available at: https://eur-lex.europa.eu/legal-content/EN/TXT/?uri=uriserv:OJ.L_.2016.344.01.0001.01.ENG&toc=OJ:L.
- Eyring, V., Bony, S., Meehl, G. A., Senior, C. A., Stevens, B., Stouffer, R. J., and Taylor, K. E. (2016). Overview of the Coupled Model Intercomparison Project Phase

- 6 (CMIP6) experimental design and organization. *Geoscientific Model Development*, 9(5):1937–1958.
- Fehsenfeld, F., Calvert, J., Fall, R., Goldan, P., Guenther, A. B., Hewitt, C. N., Lamb, B., Trainer, M., Westberg, H., and Zimmerman, P. (1992). Emissions of volatile organic compounds from vegetation and the implications for atmospheric chemistry. *Global Biogeochemical Cycles*, 6(4):389–430.
- Felzer, B. S., Cronin, T., Reilly, J. M., Melillo, J. M., and Wang, X. (2007). Impacts of ozone on trees and crops. *Comptes Rendus - Geoscience*, 339(11-12):784–798.
- Feng, J., Liao, H., Li, Y., Zhang, Z., and Tang, Y. (2020). Long-term trends and variations in haze-related weather conditions in north China during 1980–2018 based on emission-weighted stagnation intensity. *Atmospheric Environment*, 240(117830).
- Feng, J., Quan, J., Liao, H., Li, Y., and Zhao, X. (2018). An air stagnation index to qualify extreme haze events in northern China. *Journal of the Atmospheric Sciences*, 75(10):3489–3505.
- Fiore, A. M., Naik, V., and Leibensperger, E. M. (2015). Air quality and climate connections. *Journal of the Air and Waste Management Association*, 65(6):645–685.
- Fiore, A. M., Naik, V., Spracklen, D. V., Steiner, A., Unger, N., Prather, M., Bergmann, D., Cameron-Smith, P. J., Cionni, I., Collins, W. J., Dalsøren, S., Eyring, V., Folberth, G. A., Ginoux, P., Horowitz, L. W., Josse, B., Lamarque, J.-F., MacKenzie, I. A., Nagashima, T., O’Connor, F. M., Righi, M., Rumbold, S. T., Shindell, D. T., Skeie, R. B., Sudo, K., Szopa, S., Takemura, T., and Zeng, G. (2012). Global air quality and climate. *Chemical Society Reviews*, 41(19):6663–6683.
- Fortelli, A., Scafetta, N., and Mazzarella, A. (2016). Influence of synoptic and local atmospheric patterns on PM_{10} air pollution levels: a model application to Naples (Italy). *Atmospheric Environment*, 143:218–228.
- Fowler, D., Brunkreef, B., Fuzzi, S., Monks, P., Sutton, M., Brasseur, G., Friedrich, R., Passante, L., and Jimenez-Mingo, J. (2013). Research findings in support of the EU

- Air Quality Review. Publications Office of the European Union, Luxembourg. Available at: <https://op.europa.eu/en/publication-detail/-/publication/2c4a737c-fc83-11e5-b713-01aa75ed71a1/language-en>.
- Fraedrich, K., Bantzer, C., and Burkhardt, U. (1993). Winter climate anomalies in Europe and their associated circulation at 500 hPa. *Climate Dynamics*, 8(4):161–175.
- Francis, J. A. and Vavrus, S. J. (2015). Evidence for a wavier jet stream in response to rapid Arctic warming. *Environmental Research Letters*, 10(014005).
- Freund, R. and Wilson, W. (1998). Regression analysis: Statistical modeling of a response variable, First edition. Academic Press, San Diego and London. ISBN: 978-0122674754.
- Friedman, J. H. (2001). Greedy function approximation: A gradient boosting machine. *Annals of Statistics*, 29(5):1189–1232.
- Gao, Y., Zhang, L., Zhang, G., Yan, F., Zhang, S., Sheng, L., Li, J., Wang, M., Wu, S., Fu, J. S., Yao, X., and Gao, H. (2020). The climate impact on atmospheric stagnation and capability of stagnation indices in elucidating the haze events over North China Plain and Northeast China. *Chemosphere*, 258(127335).
- García-Herrera, R. and Barriopedro, D. (2018). Climate of the Mediterranean region. Oxford Research Encyclopedia of Climate Science. Oxford University Press USA. <https://doi.org/10.1093/acrefore/9780190228620.013.509>.
- Garrido-Perez, J. M., García-Herrera, R., and Ordóñez, C. (2021). Assessing the value of air stagnation indices to reproduce PM_{10} variability in Europe. *Atmospheric Research*, 248(105258).
- Garrido-Perez, J. M., Ordóñez, C., Barriopedro, D., García-Herrera, R., Schnell, J., and Horton, D. (2022). A storyline view of the projected role of remote drivers on summer air stagnation in Europe and the United States. *Environmental Research Letters*, Under review.

- Garrido-Perez, J. M., Ordóñez, C., and García-Herrera, R. (2017). Strong signatures of high-latitude blocks and subtropical ridges in winter PM_{10} over Europe. *Atmospheric Environment*, 167:49–60.
- Garrido-Perez, J. M., Ordóñez, C., García-Herrera, R., and Barriopedro, D. (2018). Air stagnation in Europe: Spatiotemporal variability and impact on air quality. *Science of the Total Environment*, 645:1238–1252.
- Garrido-Perez, J. M., Ordóñez, C., García-Herrera, R., and Schnell, J. L. (2019). The differing impact of air stagnation on summer ozone across Europe. *Atmospheric Environment*, 219:117062.
- Gatey, D., Isyumov, N., Case, P., Ho, T.E., and Miller, C. (2011). Design wind climates for very tall structures. *Proceedings of the 13th International Conference on Wind Engineering, Amsterdam, The Netherlands, 10–15 June 2011*.
- Georgoulias, A. K., Van Der, R. A., Stammes, P., Folkert Boersma, K., and Eskes, H. J. (2019). Trends and trend reversal detection in 2 decades of tropospheric NO_2 satellite observations. *Atmospheric Chemistry and Physics*, 19(9):6269–6294.
- Gietl, J. K. and Klemm, O. (2009). Analysis of traffic and meteorology on airborne particulate matter in Münster, Northwest Germany. *Journal of the Air and Waste Management Association*, 59(7):809–818.
- Giorgi, F. and Lionello, P. (2008). Climate change projections for the Mediterranean region. *Global and Planetary Change*, 63(2-3):90–104.
- Gonçalves, M., Jiménez-Guerrero, P., and Baldasano, J. M. (2009). Contribution of atmospheric processes affecting the dynamics of air pollution in South-Western Europe during a typical summertime photochemical episode. *Atmospheric Chemistry and Physics*, 9(3):849–864.
- Grise, K. M. and Davis, S. M. (2020). Hadley cell expansion in CMIP6 models. *Atmospheric Chemistry and Physics*, 20:5249–5268.

- Guerreiro, C. B., Foltescu, V., and de Leeuw, F. (2014). Air quality status and trends in Europe. *Atmospheric Environment*, 98:376–384.
- Guo, J., Lou, M., Miao, Y., Wang, Y., Zeng, Z., Liu, H., He, J., Xu, H., Wang, F., Min, M., and Zhai, P. (2017). Trans-Pacific transport of dust aerosols from East Asia: Insights gained from multiple observations and modeling. *Environmental Pollution*, 230:1030–1039.
- Haarsma, R. J., Selten, F. M., and Drijfhout, S. S. (2015). Decelerating Atlantic meridional overturning circulation main cause of future west European summer atmospheric circulation changes. *Environmental Research Letters*, 10(9).
- Hall, R. J., Jones, J. M., Hanna, E., Scaife, A. A., and Erdélyi, R. (2016). Drivers and potential predictability of summer time North Atlantic polar front jet variability. *Climate Dynamics*, 48(11-12):3869–3887.
- Hamburger, T., McMeeking, G., Minikin, A., Birmili, W., Dall’Osto, M., O’Dowd, C., Flentje, H., Henzing, B., Junninen, H., Kristensson, A., De Leeuw, G., Stohl, A., Burkhardt, J. F., Coe, H., Krejci, R., and Petzold, A. (2011). Overview of the synoptic and pollution situation over Europe during the EUCAARI-LONGREX field campaign. *Atmospheric Chemistry and Physics*, 11(3):1065–1082.
- Han, Z., Zhou, B., Xu, Y., Wu, J., and Shi, Y. (2017). Projected changes in haze pollution potential in China: An ensemble of regional climate model simulations. *Atmospheric Chemistry and Physics*, 17(16):10109–10123.
- Haylock, M., Hofstra, N., Klein Tank, A., Klok, E., Jones, P., and New, M. (2008). A European daily higher-resolution gridded data set of surface temperature and precipitation for 1950-2006. *Journal of Geophysical Research: Atmospheres*, 113(D20).
- Heald, C. L., Henze, D. K., Horowitz, L. W., Feddema, J., Lamarque, J. F., Guenther, A., Hess, P. G., Vitt, F., Seinfeld, J. H., Godstein, A. H., and Fung, I. (2008). Predicted change in global secondary organic aerosol concentrations in response to future

- climate, emissions, and land use change. *Journal of Geophysical Research Atmospheres*, 113(D05211).
- Hersbach, H., Bell, B., Berrisford, P., Hirahara, S., Horányi, A., Muñoz-Sabater, J., Nicolas, J., Peubey, C., Radu, R., Schepers, D., Simmons, A., Soci, C., Abdalla, S., Abellan, X., Balsamo, G., Bechtold, P., Biavati, G., Bidlot, J., Bonavita, M., De Chiara, G., Dahlgren, P., Dee, D., Diamantakis, M., Dragani, R., Flemming, J., Forbes, R., Fuentes, M., Geer, A., Haimberger, L., Healy, S., Hogan, R. J., Hólm, E., Janisková, M., Keeley, S., Laloyaux, P., Lopez, P., Lupu, C., Radnoti, G., de Rosnay, P., Rozum, I., Vamborg, F., Villaume, S., and Thépaut, J. N. (2020). The ERA5 global reanalysis. *Quarterly Journal of the Royal Meteorological Society*, 146(730).
- Hong, C., Zhang, Q., Zhang, Y., Davis, S. J., Tong, D., Zheng, Y., Liu, Z., Guan, D., He, K., and Schellnhuber, H. J. (2019). Impacts of climate change on future air quality and human health in China. *Proceedings of the National Academy of Sciences of the United States of America*, 116(35):17193–17200.
- Horton, D. E., Harshvardhan, and Diffenbaugh, N. S. (2012). Response of air stagnation frequency to anthropogenically enhanced radiative forcing. *Environmental Research Letters*, 7(044034).
- Horton, D. E., Skinner, C. B., Singh, D., and Diffenbaugh, N. S. (2014). Occurrence and persistence of future atmospheric stagnation events. *Nature Climate Change*, 4(8):698–703.
- Hu, J., Emile-Geay, J., and Partin, J. (2017). Correlation-based interpretations of paleoclimate data – where statistics meet past climates. *Earth and Planetary Science Letters*, 459:362–371.
- Hu, J., Li, Y., Zhao, T., Liu, J., Hu, X. M., Liu, D., Jiang, Y., Xu, J., and Chang, L. (2018). An important mechanism of regional O_3 transport for summer smog over the Yangtze River Delta in eastern China. *Atmospheric Chemistry and Physics*, 18(22):16239–16251.

- Hu, Y. and Fu, Q. (2007). Observed poleward expansion of the Hadley circulation since 1979. *Atmospheric Chemistry and Physics*, 7:5229–5236.
- Huang, Q., Cai, X., Song, Y., and Zhu, T. (2017). Air stagnation in China (1985 – 2014): climatological mean features and trends. *Atmospheric Chemistry and Physics*, 17(12):7793–7805.
- Huang, Q., Cai, X., Wang, J., Song, Y., and Zhu, T. (2018). Climatological study of the Boundary-layer air Stagnation Index for China and its relationship with air pollution. *Atmospheric Chemistry and Physics*, 18(10):7573–7593.
- IPCC (2021). Climate Change 2021: The Physical Science Basis. Contribution of Working Group I to the Sixth Assessment Report of the Intergovernmental Panel on Climate Change [Masson-Delmotte V, Zhai P, Pirani A, Connors S L, Péan C, Berger S, Caud N, Chen Y, Goldfarb L, Gomis M I, Huang M, Leitzell K, Lonnoy E, Matthews J B R, Maycock T K, Waterfield T, Yelekçi O, Yu R and Zhou B (eds.)]. *Cambridge University Press*.
- Jackson, L. C., Kahana, R., Graham, T., Ringer, M. A., Woollings, T., Mecking, J. V., and Wood, R. A. (2015). Global and European climate impacts of a slowdown of the AMOC in a high resolution GCM. *Climate Dynamics*, 45(11-12):3299–3316.
- Jackson, L. S., Carslaw, N., Carslaw, D. C., and Emmerson, K. M. (2009). Modelling trends in OH radical concentrations using generalized additive models. *Atmospheric Chemistry and Physics*, 8(4):14607–14642.
- Jacob, D., Logan, J., Gardner, G., Yevich, R., Spivakovsky, C., and Wofsy, S. (1993). Factors regulating ozone over the United States and its export to the global atmosphere. *Journal of Geophysical Research*, 98(D8):817–826.
- Jacob, D. J. and Winner, D. A. (2009). Effect of climate change on air quality. *Atmospheric Environment*, 43(1):51–63.

- Janssen, N. A. H., Fischer, P., Marra, M., Ameling, C., and Cassee, F. R. (2013). Short-term effects of $PM_{2.5}$, PM_{10} and $PM_{2.5-10}$ on daily mortality in the Netherlands. *Science of the Total Environment*, 463-464:20–26.
- Jia, B., Wang, Y., Yao, Y., and Xie, Y. (2015). A new indicator on the impact of large-scale circulation on wintertime particulate matter pollution over China. *Atmospheric Chemistry and Physics*, 15(20):11919–11929.
- Jia, L., Vecchi, G. A., Yang, X., Gudgel, R. G., Delworth, T. L., Stern, W. F., Paffendorf, K., Underwood, S. D., and Zeng, F. (2016). The roles of radiative forcing, sea surface temperatures, and atmospheric and land initial conditions in U.S. summer warming episodes. *Journal of Climate*, 29(11):4121–4135.
- Jiménez-Guerrero, P., Montávez, J. P., Gómez-Navarro, J. J., Jerez, S., and Lorente-Plazas, R. (2012). Impacts of climate change on ground level gas-phase pollutants and aerosols in the Iberian Peninsula for the late XXI century. *Atmospheric Environment*, 55:483–495.
- Kalnay, E., Kanamitsu, M., Kistler, R., Collins, W., Deaven, D., Gandin, L., Iredell, M., Saha, S., White, G., Woollen, J., Zhu, Y., Chelliah, M., Ebisuzaki, W., Higgins, W., Janowiak, J., Mo, K., Ropelewski, C., Wang, J., Leetmaa, A., Reynolds, R., Jenne, R., and Joseph, D. (1996). The NCEP NCAR 40-Year Reanalysis Project. *Bulletin of the American Meteorological Society*, 77(3):437–472.
- Kerr, G. H. and Waugh, D. W. (2018). Connections between summer air pollution and stagnation. *Environmental Research Letters*, 13(084001).
- Kim, J. H., Kim, M. K., Ho, C. H., Park, R. J., Kim, M. J., Lim, J., Kim, S. J., and Song, C. K. (2019). Possible link between Arctic Sea ice and January PM_{10} concentrations in South Korea. *Atmosphere*, 10(10).
- Koelemeijer, R. B. A., Homan, C. D., and Matthijsen, J. (2006). Comparison of spatial and temporal variations of aerosol optical thickness and particulate matter over Europe. *Atmospheric Environment*, 40(27):5304–5315.

- Kollanus, V., Tiittanen, P., Niemi, J. V., and Lanki, T. (2016). Effects of long-range transported air pollution from vegetation fires on daily mortality and hospital admissions in the Helsinki metropolitan area, Finland. *Environmental Research*, 151:351–358.
- Kornhuber, K. and Tamarin-Brodsky, T. (2021). Future Changes in Northern Hemisphere Summer Weather Persistence Linked to Projected Arctic Warming. *Geophysical Research Letters*, 48(4):1–12.
- Kuebler, J., Van Den Bergh, H., and Russell, A. G. (2001). Long-term trends of primary and secondary pollutant concentrations in Switzerland and their response to emission controls and economic changes. *Atmospheric Environment*, 35(8):1351–1363.
- Lau, W. K., Lee, J. Y., Kim, K. M., and Kang, I. S. (2004). The North Pacific as a regular of summertime climate over Eurasia and North America. *Journal of Climate*, 17(4):819–833.
- Laurila, T. (1999). Observational study of transport and photochemical formation of ozone over northern Europe. *Journal of Geophysical Research*, 104(D21):26235.
- Lauvset, K. S., Tjiputra, J., and Muri, H. (2017). Climate engineering and the ocean: Effects on biogeochemistry and primary production. *Biogeosciences*, 14(24):5675–5691.
- Lecoeur, E. and Seigneur, C. (2013). Dynamic evaluation of a multi-year model simulation of particulate matter concentrations over Europe. *Atmospheric Chemistry and Physics*, 13(8):4319–4337.
- Lecoeur, È., Seigneur, C., Pagé, C., and Terray, L. (2014). A statistical method to estimate $PM_{2.5}$ concentrations over Europe from meteorology and its application to the effect of climate change. *Journal of Geophysical Research: Atmospheres*, 119:3537–3585.
- Lee, D., Wang, S., Zhao, L., Kim, H., Kim, K., and Yoon, J. (2020). Long-term increase in atmospheric stagnant conditions over Northeast Asia and the role of greenhouse gases-driven warming. *Atmospheric Environment*, 117772(241).

- Leibensperger, E. M., Mickley, L. J., and Jacob, D. J. (2008). Sensitivity of US air quality to mid-latitude cyclone frequency and implications of 1980–2006 climate change. *Atmospheric Chemistry and Physics*, 8(23):7075–7086.
- Leung, D. M., Tai, A. P. K., Mickley, L. J., Moch, J. M., van Donkelaar, A., Shen, L., and Martin, R. V. (2018). Synoptic meteorological modes of variability for fine particulate matter ($PM_{2.5}$) air quality in major metropolitan regions of China. *Atmospheric Chemistry and Physics*, 18:6733–6748.
- Leung, L. R. and Gustafson, W. I. (2005). Potential regional climate change and implications to U.S. air quality. *Geophysical Research Letters*, 32(16).
- Liao, H., Chen, W. T., and Seinfeld, J. H. (2006). Role of climate change in global predictions of future tropospheric ozone and aerosols. *Journal of Geophysical Research Atmospheres*, 111(12).
- Liao, T., Gui, K., Jiang, W., Wang, S., Wang, B., Zeng, Z., Che, H., Wang, Y., and Sun, Y. (2018). Air stagnation and its impact on air quality during winter in Sichuan and Chongqing, southwestern China. *Science of the Total Environment*, 635:576–585.
- Liu, L., Andreani-Aksoyoglu, S., Keller, J., Ordóñez, C., Junkermann, W., Hak, C., Braathen, G. O., Reimann, S., Astorga-Llorens, C., Schultz, M., Prévôt, A. S., and Isaksen, I. S. (2007). A photochemical modeling study of ozone and formaldehyde generation and budget in the Po basin. *Journal of Geophysical Research Atmospheres*, 112:D22303.
- Lu, J., Vecchi, G. A., and Reichler, T. (2007). Expansion of the Hadley cell under global warming. *Geophysical research letters*, 34(L06805).
- Lupaşcu, A. and Butler, T. (2019). Source attribution of European surface O_3 using a tagged O_3 mechanism. *Atmospheric Chemistry and Physics*, 19(23):14535–14558.
- Lyapina, O., Schultz, M. G., and Hense, A. (2016). Cluster analysis of European surface ozone observations for evaluation of MACC reanalysis data. *Atmospheric Chemistry and Physics*, 16(11):6863–6881.

- Lyu, X., Wang, N., Guo, H., Xue, L., Jiang, F., Zeren, Y., Cheng, H., Cai, Z., Han, L., and Zhou, Y. (2019). Causes of a continuous summertime O_3 pollution event in Jinan, a central city in the North China Plain. *Atmospheric Chemistry and Physics*, 19:3025–3042.
- Maddison, J. W., Abalos, M., Barriopedro, D., García-Herrera, R., Garrido-Perez, J. M., and Ordóñez, C. (2021). Linking air stagnation in Europe with the synoptic- to large-scale atmospheric circulation. *Weather and Climate Dynamics*, 2:675–694.
- Maddison, J. W., Abalos, M., Barriopedro, D., García-Herrera, R., Garrido-Perez, J. M., and Ordóñez, C. (2022). Assessing the uncertainty in projected changes in European air stagnation.
- Mamalakis, A., Randerson, J. T., Yu, J. Y., Pritchard, M. S., Magnusdottir, G., Smyth, P., Levine, P. A., Yu, S., and Fofoula-Georgiou, E. (2021). Zonally contrasting shifts of the tropical rain belt in response to climate change. *Nature Climate Change*, 11(2):143–151.
- Masato, G., Hoskins, B. J., and Woollings, T. J. (2012). Wave-breaking characteristics of midlatitude blocking. *Quarterly Journal of the Royal Meteorological Society*, 138(666):1285–1296.
- McClure, C. D. and Jaffe, D. A. (2018). US particulate matter air quality improves except in wildfire-prone areas. *Proceedings of the National Academy of Sciences of the United States of America*, 115(31):7901–7906.
- McKinnon, K. A., Rhines, A., Tingley, M. P., and Huybers, P. (2016). Long-lead predictions of eastern United States hot days from Pacific sea surface temperatures. *Nature Geoscience*, 9(5):389–394.
- Meehl, G. A., Tebaldi, C., Tilmes, S., Lamarque, J. F., Bates, S., Pendergrass, A., and Lombardozzi, D. (2018). Future heat waves and surface ozone. *Environmental Research Letters*, 13(064004).

- Mindlin, J., Shepherd, T. G., Vera, C. S., Osman, M., Zappa, G., Lee, R. W., and Hodges, K. I. (2020). Storyline description of Southern Hemisphere midlatitude circulation and precipitation response to greenhouse gas forcing. *Climate Dynamics*, 54(9-10):4399–4421.
- Monks, P. S., Archibald, A. T., Colette, A., Cooper, O., Coyle, M., Derwent, R., Fowler, D., Granier, C., Law, K. S., Mills, G. E., Stevenson, D. S., Tarasova, O., Thouret, V., Von Schneidemesser, E., Sommariva, R., Wild, O., and Williams, M. L. (2015). Tropospheric ozone and its precursors from the urban to the global scale from air quality to short-lived climate forcer. *Atmospheric Chemistry and Physics*, 15(15):8889–8973.
- Myhre, G., Shindell, D., Bréon, F.-M., Collins, W., Fuglestvedt, J., Huang, J., Koch, D., Lamarque, J.-F., Lee, D., Mendoza, B., Nakajima, T., Robock, A., Stephens, G., Takemura, T., and Zhang, H. (2013). Anthropogenic and natural radiative forcing. In: *Climate Change 2013: The physical science basis. Contribution of Working Group I to the Fifth Assessment Report of the Intergovernmental Panel on Climate Change. Cambridge University Press, Cambridge, United Kingdom and New York, NY, USA.*
- Nel, A. (2005). Air Pollution-Related Illness: Effects of Particles. *Science*, 5723:804–806.
- Nogueira, M. (2020). Inter-comparison of ERA-5, ERA-interim and GPCP rainfall over the last 40 years: Process-based analysis of systematic and random differences. *Journal of Hydrology journal*, 583(124632).
- Nygård, T., Valkonen, T., and Vihma, T. (2014). Characteristics of Arctic low-tropospheric humidity inversions based on radio soundings. *Atmospheric Chemistry and Physics*, 14(4):1959–1971.
- Ordóñez, C., Barriopedro, D., and García-Herrera, R. (2019). Role of the position of the North Atlantic jet in the variability and odds of extreme PM_{10} in Europe. *Atmospheric Environment*, 210:35–46.
- Ordóñez, C., Barriopedro, D., García-Herrera, R., Sousa, P. M., and Schnell, J. L. (2017).

- Regional responses of surface ozone in Europe to the location of high-latitude blocks and subtropical ridges. *Atmospheric Chemistry and Physics*, 17(4):3111–3131.
- Ordóñez, C., Garrido-Perez, J. M., and García-Herrera, R. (2020). Early spring near-surface ozone in Europe during the COVID-19 shutdown: Meteorological effects outweigh emission changes. *Science of The Total Environment*, 747(141322).
- Ordóñez, C., Mathis, H., Furger, M., Henne, S., Hüglin, C., Staehelin, J., and Prévôt, A. S. H. (2005). Changes of daily surface ozone maxima in Switzerland in all seasons from 1992 to 2002 and discussion of summer 2003. *Atmospheric Chemistry and Physics*, 5:1187–1203.
- Orlando, J. J., Tyndall, G. S., and Calvert, J. G. (1992). Thermal decomposition pathways for peroxyacetyl nitrate (PAN): Implications for atmospheric methyl nitrate levels. *Atmospheric Environment Part A, General Topics*, 26(17):3111–3118.
- Otero, N., Sillmann, J., Mar, K. A., Rust, H. W., Solberg, S., Andersson, C., Engardt, M., Bergström, R., Bessagnet, B., Colette, A., Couvidat, F., Cuvelier, C., Tsyro, S., Fagerli, H., Schaap, M., Manders, A., Mircea, M., Briganti, G., Cappelletti, A., Adani, M., D’Isidoro, M., Pay, M. T., Theobald, M., Vivanco, M. G., Wind, P., Ojha, N., Raffort, V., and Butler, T. (2018). A multi-model comparison of meteorological drivers of surface ozone over Europe. *Atmospheric Chemistry and Physics*, 18(16):12269–12288.
- Otero, N., Sillmann, J., Schnell, J. L., Rust, H. W., and Butler, T. (2016). Synoptic and meteorological drivers of extreme ozone concentrations over Europe. *Environ. Res. Lett*, 11(024005).
- Paoletti, E., De Marco, A., Beddows, D. C., Harrison, R. M., and Manning, W. J. (2014). Ozone levels in European and USA cities are increasing more than at rural sites, while peak values are decreasing. *Environmental Pollution*, 192:295–299.
- Pateraki, S., Asimakopoulou, D. N., Flocas, H. A., Maggos, T., and Vasilakos, C. (2012). The role of meteorology on different sized aerosol fractions (PM_{10} , $PM_{2.5}$, $PM_{2.5-10}$). *Science of the Total Environment*, 419:124–135.

- Pausata, F. S. R., Pozzoli, L., Dingenen, R. V., Vignati, E., Cavalli, F., and Dentener, F. J. (2013). Impacts of changes in North Atlantic atmospheric circulation on particulate matter and human health in Europe. *Geophysical Research Letters*, 40(15):4074–4080.
- Peings, Y., Cattiaux, J., Vavrus, S. J., and Magnusdottir, G. (2018). Projected squeezing of the wintertime North-Atlantic jet. *Environmental Research Letters*, 13(074016).
- Petetin, H., Thouret, V., Athier, G., Blot, R., Boulanger, D., Cousin, J.-M., Gaudel, A., Nédélec, P., and Cooper, O. (2016). Diurnal cycle of ozone throughout the troposphere over Frankfurt as measured by MOZAIC-IAGOS commercial aircraft. *Elementa: Science of the Anthropocene*, 4(000129).
- Pey, J., Querol, X., Alastuey, A., Forastiere, F., and Stafoggia, M. (2013). African dust outbreaks over the Mediterranean Basin during 2001-2011: PM_{10} concentrations, phenomenology and trends, and its relation with synoptic and mesoscale meteorology. *Atmospheric Chemistry and Physics*, 13(3):1395–1410.
- Pope, R. J., Butt, E. W., Chipperfield, M. P., Doherty, R. M., Fenech, S., Schmidt, A., Arnold, S. R., and Savage, N. H. (2016). The impact of synoptic weather on UK surface ozone and implications for premature mortality. *Environmental Research Letters*, 11(124004).
- Pope III, C. A., Burnett, R. T., Thun, M. J., Calle, E. E., Krewski, D., and Thurston, G. D. (2002). Lung cancer, cardiopulmonary mortality and long-term exposure to fine particulate air pollution. *The Journal of the American Medical Association*, 287(9):1132–1141.
- Porter, W. C. and Heald, C. L. (2019). The mechanisms and meteorological drivers of the summertime ozone-temperature relationship. *Atmospheric Chemistry and Physics*, 19(21):13367–13381.
- Putaud, J. P., Van Dingenen, R., Alastuey, A., Bauer, H., Birmili, W., Cyrys, J., Flentje, H., Fuzzi, S., Gehrig, R., Hansson, H. C., Harrison, R. M., Herrmann, H., Hitzenberger, R., Hüglin, C., Jones, A. M., Kasper-Giebl, A., Kiss, G., Kousa, A., Kuhlbusch, T. A.,

- Löschau, G., Maenhaut, W., Molnar, A., Moreno, T., Pekkanen, J., Perrino, C., Pitz, M., Puxbaum, H., Querol, X., Rodriguez, S., Salma, I., Schwarz, J., Smolik, J., Schneider, J., Spindler, G., ten Brink, H., Tursic, J., Viana, M., Wiedensohler, A., and Raes, F. (2010). A European aerosol phenomenology - 3: Physical and chemical characteristics of particulate matter from 60 rural, urban, and kerbside sites across Europe. *Atmospheric Environment*, 44(10):1308–1320.
- Pyrgou, A., Hadjinicolaou, P., and Santamouris, M. (2018). Enhanced near-surface ozone under heatwave conditions in a Mediterranean island. *Scientific Reports*, 8(9191).
- Querol, X., Pey, J., Pandolfi, M., Alastuey, A., Cusack, M., Pérez, N., Moreno, T., Viana, M., Mihalopoulos, N., Kallos, G., and Kleanthous, S. (2009). African dust contributions to mean ambient PM_{10} mass-levels across the Mediterranean Basin. *Atmospheric Environment*, 43(28):4266–4277.
- Rahmstorf, S., Box, J. E., Feulner, G., Mann, M. E., Robinson, A., Rutherford, S., and Schaffernicht, E. J. (2015). Exceptional twentieth-century slowdown in Atlantic Ocean overturning circulation. *Nature Climate Change*, 5(5):475–480.
- REVIHAAP (2013). Review of evidence on health aspects of air pollution - REVIHAAP Project. Technical Report. World Health Organization Regional Office for Europe, Bonn. Available at: http://www.euro.who.int/__data/assets/pdf_file/0004/193108/REVIHAAP-Final-technical-report-final-version.pdf. Technical report.
- Rex, D. (1950). Blocking action in the middle troposphere and its effect upon regional climate. *Tellus*, 4(2):275–301.
- Ruggieri, P., Bellucci, A., Nicolí, D., Athanasiadis, P. J., Gualdi, S., Cassou, C., Castruccio, F., Danabasoglu, G., Davini, P., Dunstone, N., Eade, R., Gastineau, G., Harvey, B., Hermanson, L., Qasmi, S., Ruprich-Robert, Y., Sanchez-Gomez, E., Smith, D., Wild, S., and Zampieri, M. (2021). Atlantic multidecadal variability and north atlantic jet: A multimodel view from the decadal climate prediction project. *Journal of Climate*, 34(1):347–360.

- Russo, A., Gouveia, C., Levy, I., Dayan, U., Jerez, S., Mendes, M., and Trigo, R. (2016). Coastal recirculation potential affecting air pollutants in Portugal: The role of circulation weather types. *Atmospheric Environment*, 135:9–19.
- Sacks, J. D., Stanek, L. W., Luben, T. J., Johns, D. O., Buckley, B. J., Brown, J. S., and Ross, M. (2011). Particulate matter-induced health effects: Who is susceptible? *Environmental Health Perspectives*, 119(4):446–454.
- Salvador, P., Alonso-Pérez, S., Pey, J., Artíñano, B., De Bustos, J. J., Alastuey, A., and Querol, X. (2014). African dust outbreaks over the western Mediterranean Basin: 11-year characterization of atmospheric circulation patterns and dust source areas. *Atmospheric Chemistry and Physics*, 14(13):6759–6775.
- Santos, J. A., Pinto, J. G., and Ulbrich, U. (2009). On the development of strong ridge episodes over the eastern North Atlantic. *Geophysical Research Letters*, 36(L17804).
- Schnell, J. L., Holmes, C. D., Jangam, A., and Prather, M. J. (2014). Skill in forecasting extreme ozone pollution episodes with a global atmospheric chemistry model. *Atmospheric Chemistry and Physics*, 14(15):7721–7739.
- Schnell, J. L. and Prather, M. J. (2017). Co-occurrence of extremes in surface ozone, particulate matter, and temperature over eastern North America. *Proceedings of the National Academy of Sciences*, 114(11):2854–2859.
- Schnell, J. L., Prather, M. J., Josse, B., Naik, V., Horowitz, L. W., Cameron-Smith, P., Bergmann, D., Zeng, G., Plummer, D. A., Sudo, K., Nagashima, T., Shindell, D. T., Faluvegi, G., and Strode, S. A. (2015). Use of North American and European air quality networks to evaluate global chemistry-climate modeling of surface ozone. *Atmospheric Chemistry and Physics*, 15(18):10581–10596.
- Screen, J. A. (2013). Influence of Arctic sea ice on European summer precipitation. *Environmental Research Letters*, 8(4).
- Seidel, D. J. and Randel, W. J. (2007). Recent widening of the tropical belt: Evidence from tropopause observations. *Journal of geophysical research*, 112(D20113).

- Seinfeld, J. and Pandis, S. (2016). *Atmospheric chemistry and physics: from air pollution to climate change, Third edition. John Wiley and Sons. New Jersey, United States. ISBN: 978-1-118-94740-1.*
- Servén, D. and Brummitt, C. (2018). pyGAM: Generalized additive models in Python. *Zenodo*.
- Sfetsos, A. and Vlachogiannis, D. (2010). A new approach to discovering the causal relationship between meteorological patterns and PM_{10} exceedances. *Atmospheric Research*, 98(2-4):500–511.
- Shen, L., Mickley, L. J., and Gilleland, E. (2016). Impact of increasing heat waves on U.S. ozone episodes in the 2050s: Results from a multimodel analysis using extreme value theory. *Geophysical Research Letters*, 43(8):4017–4025.
- Shen, L., Mickley, L. J., and Murray, L. T. (2017). Influence of 2000-2050 climate change on particulate matter in the United States: Results from a new statistical model. *Atmospheric Chemistry and Physics*, 17(6):4355–4367.
- Shen, L., Mickley, L. J., and Tai, A. P. K. (2015). Influence of synoptic patterns on surface ozone variability over the eastern United States from 1980 to 2012. *Atmospheric Chemistry and Physics*, 15:10925–10938.
- Shepherd, T. G. (2014). Atmospheric circulation as a source of uncertainty in climate change projections. *Nature Geoscience*, 7(10):703–708.
- Shepherd, T. G., Boyd, E., Calel, R. A., Chapman, S. C., Dessai, S., Dima-West, I. M., Fowler, H. J., James, R., Maraun, D., Martius, O., Senior, C. A., Sobel, A. H., Stainforth, D. A., Tett, S. F., Trenberth, K. E., van den Hurk, B. J., Watkins, N. W., Wilby, R. L., and Zenghelis, D. A. (2018). Storylines: an alternative approach to representing uncertainty in physical aspects of climate change. *Climatic Change*, 151(3-4):555–571.
- Shindell, D., Kuylenstierna, J. C. I., Vignati, E., Dingenen, R. V., Amann, M., Klimont, Z., Anenberg, S. C., Muller, N., Janssens-maenhout, G., Raes, F., Schwartz, J., Faluvegi, G., Pozzoli, L., Kupiainen, K., Höglund-isaksson, L., Emberson, L., Streets, D.,

- Ramanathan, V., Hicks, K., Oanh, N. T. K., Milly, G., and Williams, M. (2012). Simultaneously mitigating near-term climate change and improving human health and food security. *Science*, 335(6065):183–189.
- Sicard, P., De Marco, A., Troussier, F., Renou, C., Vas, N., and Paoletti, E. (2013). Decrease in surface ozone concentrations at Mediterranean remote sites and increase in the cities. *Atmospheric Environment*, 79:705–715.
- Simpson, D. (1995). Biogenic emissions in Europe: 2. Implications for ozone control strategies. *Journal of Geophysical Research*, 100(D11):22891–22906.
- Smirnov, N. (1939). On the estimation of the discrepancy between empirical curves of distribution for two independent samples. *Moscow University Mathematics Bulletin*, 2(2).
- Smith, A., Lott, N., and Vose, R. (2011). The integrated surface database: Recent developments and partnerships. *Bulletin of the American Meteorological Society*, 92(6):704–708.
- Sousa, P. M., Trigo, R. M., Barriopedro, D., Soares, P. M., Ramos, A. M., and Liberato, M. L. (2016). Responses of European precipitation distributions and regimes to different blocking locations. *Climate Dynamics*, 48(3-4):1141–1160.
- Sousa, P. M., Trigo, R. M., Barriopedro, D., Soares, P. M. M., and Santos, J. A. (2017). European temperature responses to blocking and ridge regional patterns. *Climate Dynamics*, 50(1-2):457–477.
- Stein, A. F., Draxler, R. R., Rolph, G. D., Stunder, B. J., Cohen, M. D., and Ngan, F. (2015). NOAA’s HYSPLIT atmospheric transport and dispersion modeling system. *Bulletin of the American Meteorological Society*, 96(12):2059–2077.
- Steiner, A. L., Davis, A. J., Sillman, S., Owen, R. C., Michalak, A. M., and Fiore, A. M. (2010). Observed suppression of ozone formation at extremely high temperatures due to chemical and biophysical feedbacks. *Proceedings of the National Academy of Sciences of the United States of America*, 107(46):19685–19690.

- Sun, W., Hess, P., and Liu, C. (2017). The impact of meteorological persistence on the distribution and extremes of ozone. *Geophysical Research Letters*, 44(3):1545–1553.
- Tai, A. P. K., Mickley, L. J., and Jacob, D. J. (2010). Correlations between fine particulate matter ($PM_{2.5}$) and meteorological variables in the United States: Implications for the sensitivity of $PM_{2.5}$ to climate change. *Atmospheric Environment*, 44(32):3976–3984.
- Tai, A. P. K., Mickley, L. J., and Jacob, D. J. (2012a). Impact of 2000–2050 climate change on fine particulate matter ($PM_{2.5}$) air quality inferred from a multi-model analysis of meteorological modes. *Atmospheric Chemistry and Physics*, 12(23):11329–11337.
- Tai, A. P. K., Mickley, L. J., Jacob, D. J., Leibensperger, E. M., Zhang, L., Fisher, J. A., and Pye, H. O. T. (2012b). Meteorological modes of variability for fine particulate matter ($PM_{2.5}$) air quality in the United States: Implications for $PM_{2.5}$ sensitivity to climate change. *Atmospheric Chemistry and Physics*, 12(6):3131–3145.
- Tao, L., Hu, Y., and Liu, J. (2016). Anthropogenic forcing on the Hadley circulation in CMIP5 simulations. *Climate Dynamics*, 46:3337–3350.
- Tarasova, O. A. and Karpetchko, A. Y. (2003). Accounting for local meteorological effects in the ozone time-series of Lovozero (Kola Peninsula). *Atmospheric Chemistry and Physics*, 3(4):941–949.
- Taszarek, M., Brooks, H. E., Czernecki, B., Szuster, P., and Fortuniak, K. (2018). Climatological aspects of convective parameters over Europe: A comparison of ERA-interim and sounding data. *Journal of Climate*, 31(11):4281–4308.
- Ting, M. and Wang, H. (1997). Summertime U.S. precipitation variability and its relation to Pacific sea surface temperature. *Journal of Climate*, 10(8):1853–1873.
- Torrence, C. and Compo, G. P. (1998). A practical guide to wavelet analysis. *Bulletin of the American Meteorological Society*, 79(1):61–78.
- Tørseth, K., Aas, W., Breivik, K., Fjæraa, A. M., Fiebig, M., Hjellbrekke, A. G., Lund Myhre, C., Solberg, S., and Yttri, K. E. (2012). Introduction to the European Monitor-

- ing and Evaluation Programme (EMEP) and observed atmospheric composition change during 1972-2009. *Atmospheric Chemistry and Physics*, 12(12):5447–5481.
- Travis, K. R. and Jacob, D. J. (2019). Systematic bias in evaluating chemical transport models with maximum daily 8h average (MDA8) surface ozone for air quality applications: A case study with GEOS-Chem v9.02. *Geoscientific Model Development*, 12(8):3641–3648.
- Trigo, R. M., Trigo, I. F., DaCamara, C. C., and Osborn, T. J. (2004). Climate impact of the European winter blocking episodes from the NCEP/NCAR reanalyses. *Climate Dynamics*, 23(1):17–28.
- Vautard, R., Cattiaux, J., Yiou, P., Thépaut, J. N., and Ciais, P. (2010). Northern Hemisphere atmospheric stilling partly attributed to an increase in surface roughness. *Nature Geoscience*, 3(11):756–761.
- Vautard, R., Colette, A., van Meijgaard, E., Meleux, F., van Oldenborgh, G. J., Otto, F., Tobin, I., and Yiou, P. (2018). Attribution of wintertime anticyclonic stagnation contributing to air pollution in western Europe. *Bulletin of the American Meteorological Society*, 99:S70–S75.
- Vautard, R., Honoré, C., Beekmann, M., and Rouil, L. (2005). Simulation of ozone during the August 2003 heat wave and emission control scenarios. *Atmospheric Environment*, 39(16):2957–2967.
- Velchev, K., Cavalli, F., Hjorth, J., Marmer, E., Vignati, E., Dentener, F., and Raes, F. (2011). Ozone over the Western Mediterranean Sea - Results from two years of shipborne measurements. *Atmospheric Chemistry and Physics*, 11(2):675–688.
- Vlachogianni, A., Kassomenos, P., Karppinen, A., Karakitsios, S., and Kukkonen, J. (2011). Evaluation of a multiple regression model for the forecasting of the concentrations of NO_x and PM_{10} in Athens and Helsinki. *Science of the Total Environment*, 409(8):1559–1571.

- von Storch, H. and Zwiers, F. W. (1999). *Statistical Analysis in Climate Research, First Edition*. Cambridge University Press Cambridge, UK. ISBN: 0511010184 .
- Waked, A., Sauvage, S., Borbon, A., Gauduin, J., Pallares, C., Vagnot, M. P., Léonardis, T., and Locoge, N. (2016). Multi-year levels and trends of non-methane hydrocarbon concentrations observed in ambient air in France. *Atmospheric Environment*, 141:263–275.
- Wang, H., Schubert, S., Koster, R., Ham, Y. G., and Suarez, M. (2014). On the role of SST forcing in the 2011 and 2012 extreme U.S. heat and drought: A study in contrasts. *Journal of Hydrometeorology*, 15(3):1255–1273.
- Wang, J. X. L. and Angell, J. K. (1999). Air Stagnation Climatology for the United States. NOAA/Air Resources Laboratory ATLAS. Available at: <https://www.nrc.gov/docs/ML0722/ML072260075.pdf>.
- Wang, X., Dickinson, R. R. E., Su, L., Zhou, C., and Wang, K. (2018). $PM_{2.5}$ pollution in China and how it has been exacerbated by terrain and meteorological conditions. *Bulletin of the American Meteorological Society*, 99(1):105–120.
- Wang, X., Wang, K., and Su, L. (2016). Contribution of atmospheric diffusion cConditions to the recent improvement in air quality in China. *Scientific Reports*, 6(36404).
- Watson, J. G. (2002). Visibility: Science and regulation. *Journal of the Air and Waste Management Association*, 52(9):973–999.
- Webber, C. P., Dacre, H. F., Collins, W. J., and Masato, G. (2017). The dynamical impact of Rossby wave breaking upon UK PM_{10} concentration. *Atmospheric Chemistry and Physics*, 17(2):867–881.
- Wesely, M. (1989). Parametrization of surface resistances to gaseous dry deposition in regional-scale numerical models. *Atmospheric Environment*, 23(6):1293–1304.
- Wilks, D. S. (2011). *Statistical Methods in the Atmospheric Sciences, Third edition*. Academic Press, Oxford, UK. ISBN: 9780123850225.

- Wise, E. K. and Comrie, A. C. (2005). Meteorologically adjusted urban air quality trends in the Southwestern United States. *Atmospheric Environment*, 39(16):2969–2980.
- Wood, S. (2017). Generalized Additive Models: An Introduction with R, Second edition. Chapman and Hall/CRC press, Boca Raton, USA. ISBN: 9781498728331.
- Woollings, T. (2010). Dynamical influences on European climate: An uncertain future. *Philosophical Transactions of the Royal Society A: Mathematical, Physical and Engineering Sciences*, 368(1924):3733–3756.
- Woollings, T., Gregory, J. M., Pinto, J. G., Reyers, M., and Brayshaw, D. J. (2012). Response of the North Atlantic storm track to climate change shaped by ocean-atmosphere coupling. *Nature Geoscience*, 5(5):313–317.
- Woollings, T., Hannachi, A., and Hoskins, B. (2010). Variability of the North Atlantic eddy-driven jet stream. *Quarterly Journal of the Royal Meteorological Society*, 136(649):856–868.
- Worden, H. M., Deeter, M. N., Frankenberg, C., George, M., Nichitiu, F., Worden, J., Aben, I., Bowman, K. W., Clerbaux, C., Coheur, P. F., De Laat, A. T., Detweiler, R., Drummond, J. R., Edwards, D. P., Gille, J. C., Hurtmans, D., Luo, M., Martínez-Alonso, S., Massie, S., Pfister, G., and Warner, J. X. (2013). Decadal record of satellite carbon monoxide observations. *Atmospheric Chemistry and Physics*, 13(2):837–850.
- Xu, D., Yap, D., and Taylor, P. A. (1996). Meteorologically adjusted ground level ozone trends in Ontario. *Atmospheric Environment*, 30(7):1117–1124.
- Young, I. T. (1977). Proof without prejudice: use of the Kolmogorov Smirnov test for the analysis of histograms from flow systems and other sources. *Journal of Histochemistry and Cytochemistry*, 25(7):935–941.
- Zanis, P., Hadjinicolaou, P., Pozzer, A., Tyrllis, E., Dafka, S., Mihalopoulos, N., and Lelieveld, J. (2014). Summertime free-tropospheric ozone pool over the eastern Mediterranean/middle east. *Atmospheric Chemistry and Physics*, 14(1):115–132.

- Zappa, G. (2019). Regional climate impacts of future changes in the mid-latitude atmospheric circulation: a storyline view. *Current Climate Change Reports*, 5:358–371.
- Zappa, G., Pithan, F., and Shepherd, T. G. (2018). Multimodel Evidence for an Atmospheric Circulation Response to Arctic Sea Ice Loss in the CMIP5 Future Projections. *Geophysical Research Letters*, 45(2):1011–1019.
- Zappa, G. and Shepherd, T. G. (2017). Storylines of atmospheric circulation change for European regional climate impact assessment. *Journal of Climate*, 30(16):6561–6577.
- Zhao, S., Feng, T., Tie, X., Long, X., Li, G., Cao, J., Zhou, W., and An, Z. (2018). Impact of climate change on Siberian high and wintertime air pollution in China in past two decades. *Earth’s Future*, 6(2):118–133.
- Zou, Y., Wang, Y., Xie, Z., Wang, H., and J. Rasch, P. (2020). Atmospheric teleconnection processes linking winter air stagnation and haze extremes in China with regional Arctic sea ice decline. *Atmospheric Chemistry and Physics*, 20(8):4999–5017.
- Zou, Y., Wang, Y., Zhang, Y., and Koo, J. H. (2017). Arctic sea ice, Eurasia snow, and extreme winter haze in China. *Science Advances*, 3(3):e1602751.

Annex

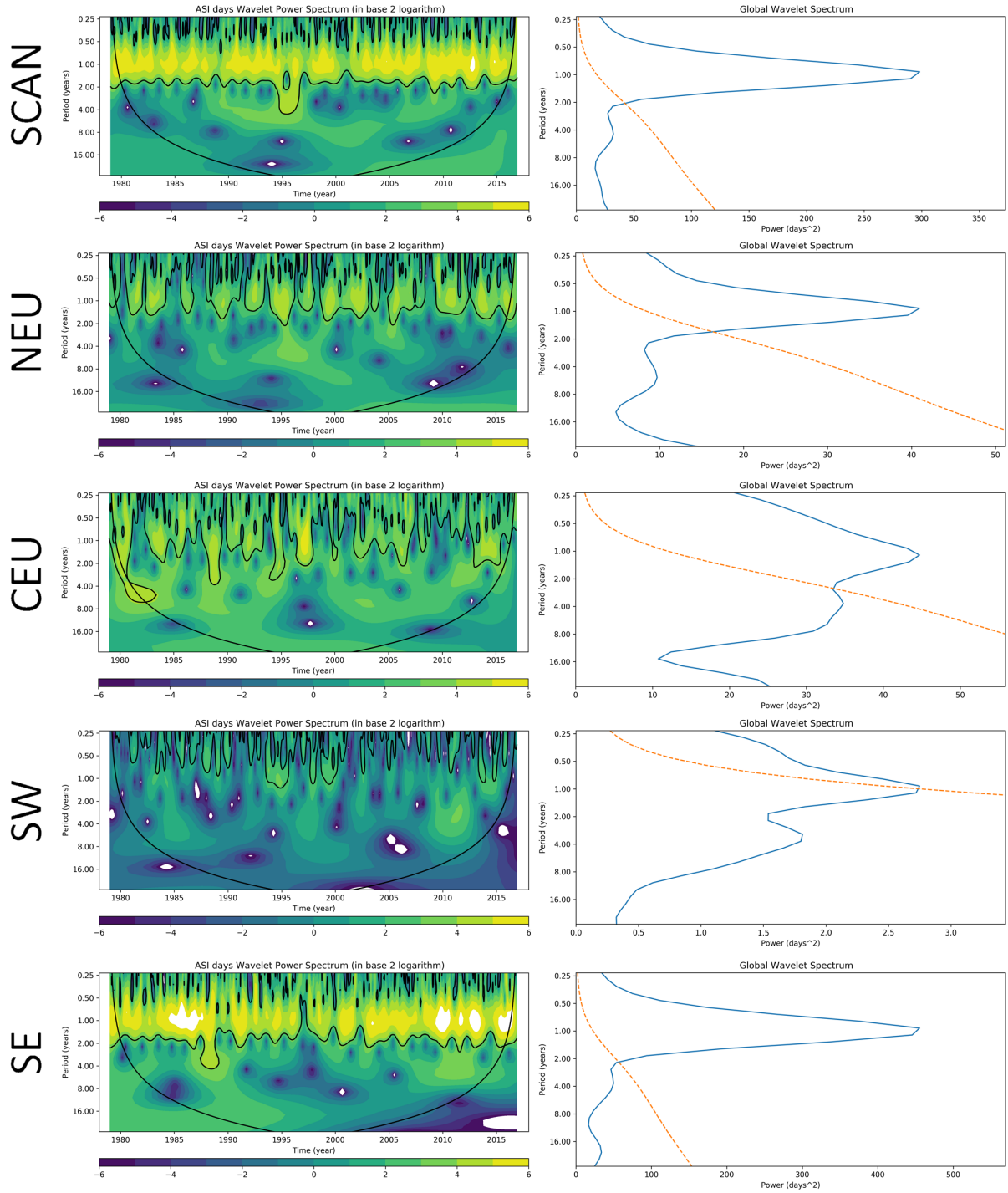


Figure A1: Left panels: Wavelet power spectrum for the monthly frequency of stagnant days during the period 1979 – 2016. The wavelet power spectrum has been computed using the Morlet wavelet. The x-axis is the wavelet location in time. The y-axis is the wavelet period in years. The black contours are the 5% significance regions, using a red-noise background spectrum. Right panels: Global wavelet spectrum as a function of Fourier period for the monthly frequency of stagnant days during the period 1979 – 2016 (blue line). The dotted line is the 5% significance level.

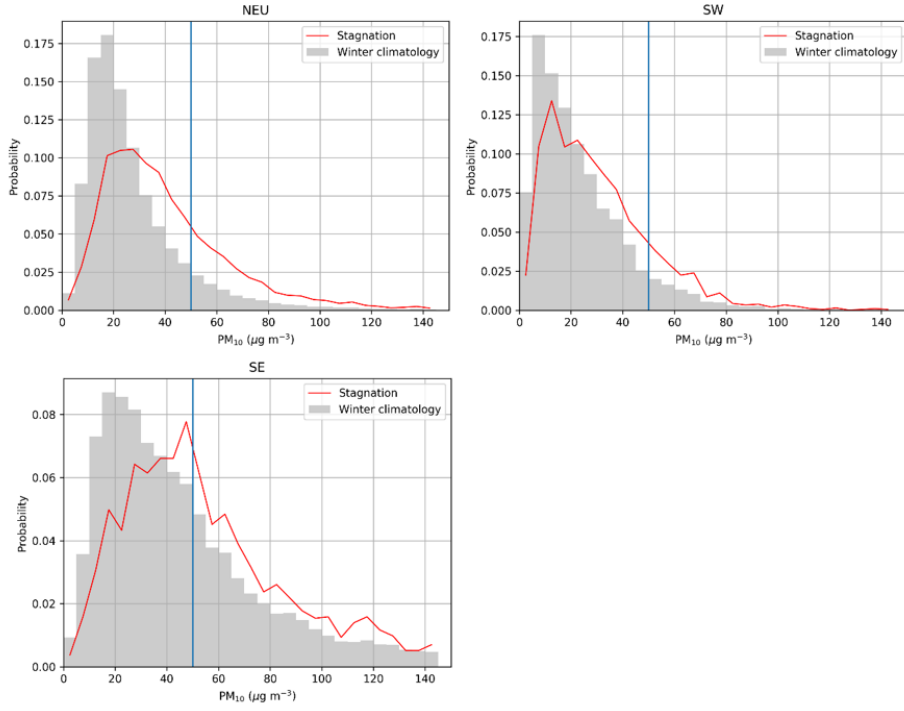


Figure A2: As Figure 3.8 but for winter daily PM_{10} in NEU, SW and SE. Results for SCAN are not shown due to the lack of PM_{10} data there. The PDF under stagnant conditions is more smoothed for NEU than for SE and, to a lesser extent, SW, as a consequence of the considerably larger number of sites in the first region.

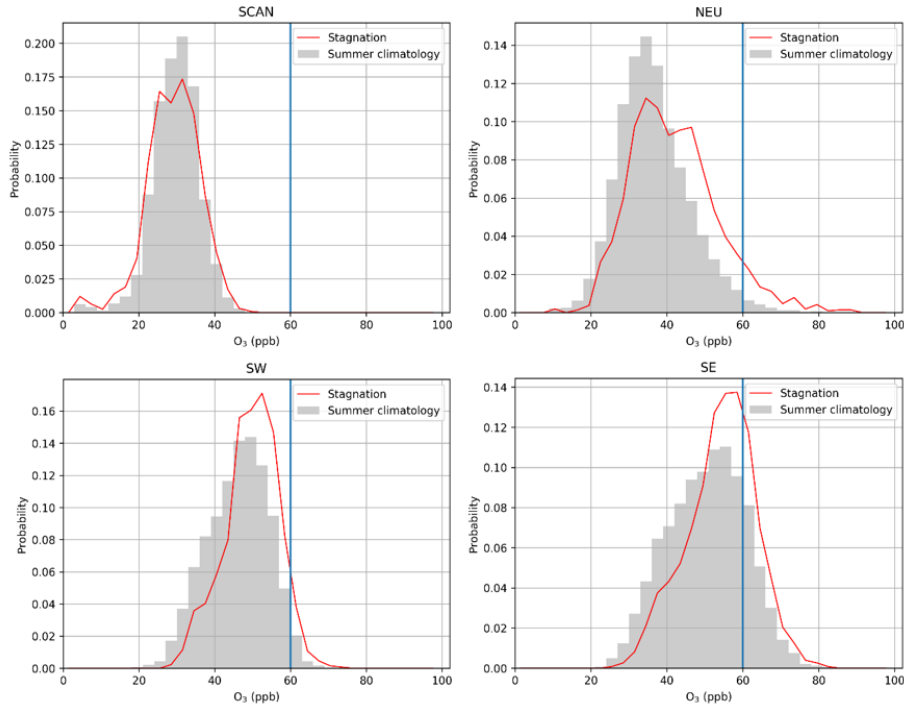


Figure A3: As Figure 3.8 of the main text but for summer MDA8 O_3 in SCAN, NEU, SW and SE.

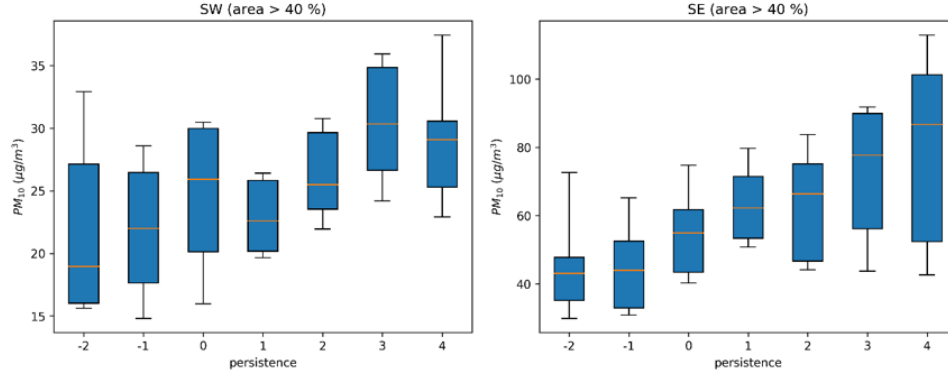


Figure A4: As Figure 3.9 but for winter PM_{10} in SW and SE. In the case of SW, stagnation episodes have been selected by considering only the portion of that region located in Iberia, because of the lack of air quality observations in Northern Africa. Results for SCAN are not shown due to the lack of PM_{10} data there.

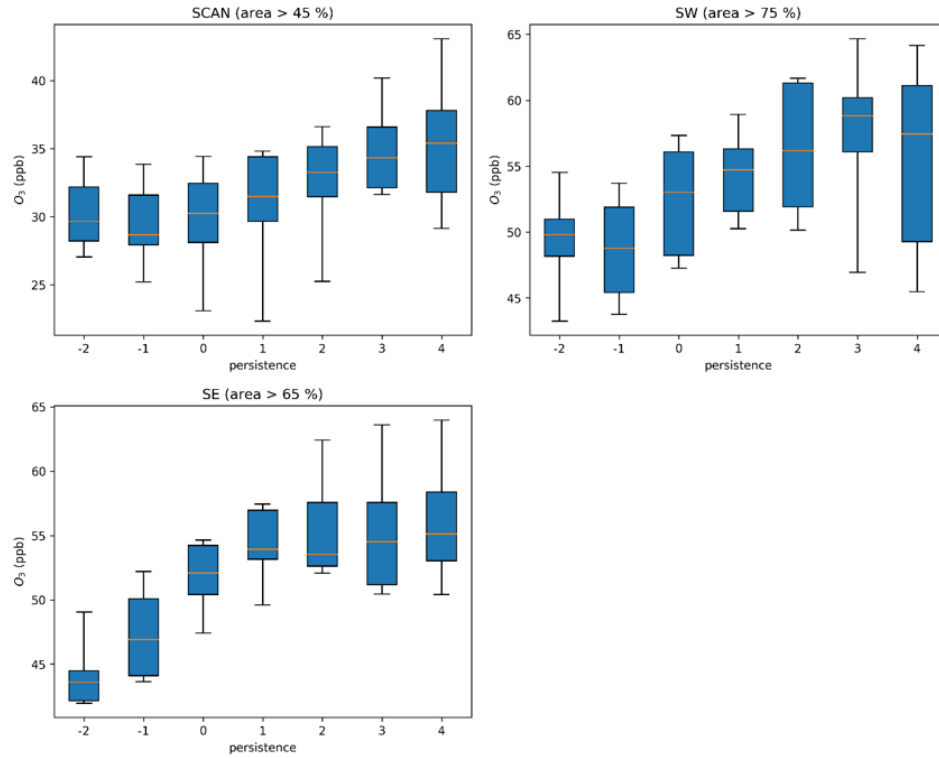


Figure A5: As Figure 3.9 of the main text but for summer $MDA8 O_3$ in SCAN, SW and SE. In the case of SW, stagnation episodes have been considered only for the portion of the region located in Iberia due to the lack of air quality observations in Northern Africa; note this is particularly relevant in summer as during that season Northern Africa is under stagnant conditions a large portion of the time, which would introduce biases in the analyses for SW. For SE, stagnation episodes have been considered since 2004 because of some inhomogeneities in the ozone data within the region before that year (see Section 3.4 for details).

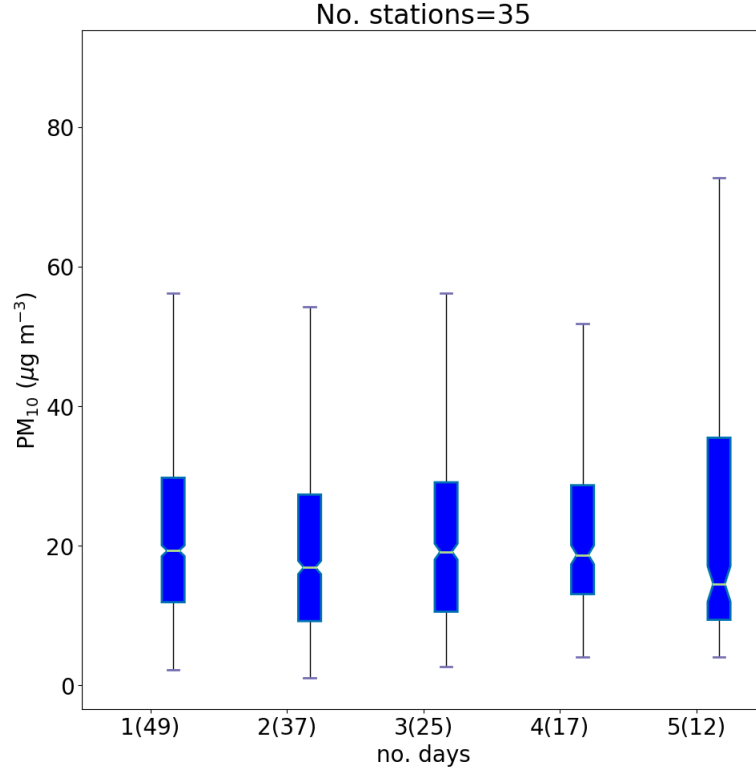


Figure A6: As Figure 5.10 but for ATL ridges.

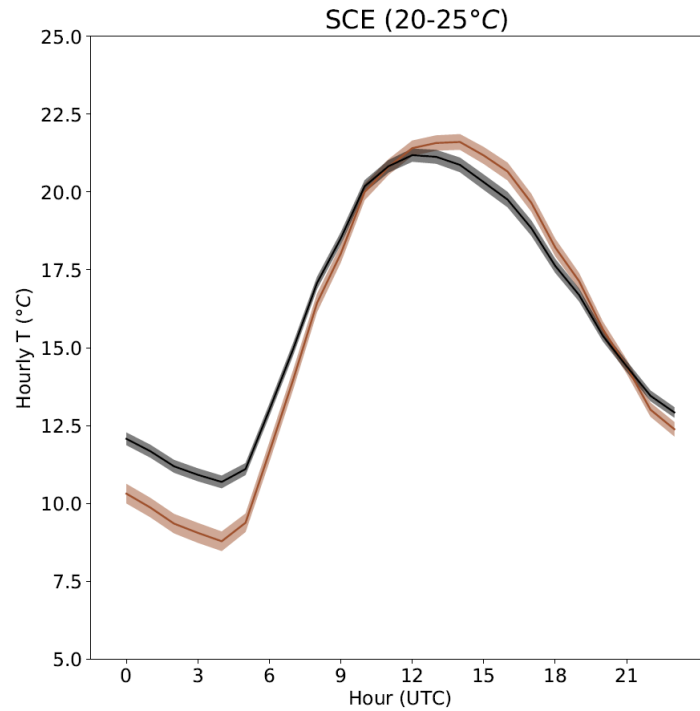


Figure A7: Composites of the diurnal cycles of hourly temperature at a representative location in SCE on stagnant (brown) and non-stagnant (black) days with T_{max} within 20 – 25 $^{\circ}C$ during summer. The times displayed on the x-axes are UTC. Shadings cover the 95% confidence interval.

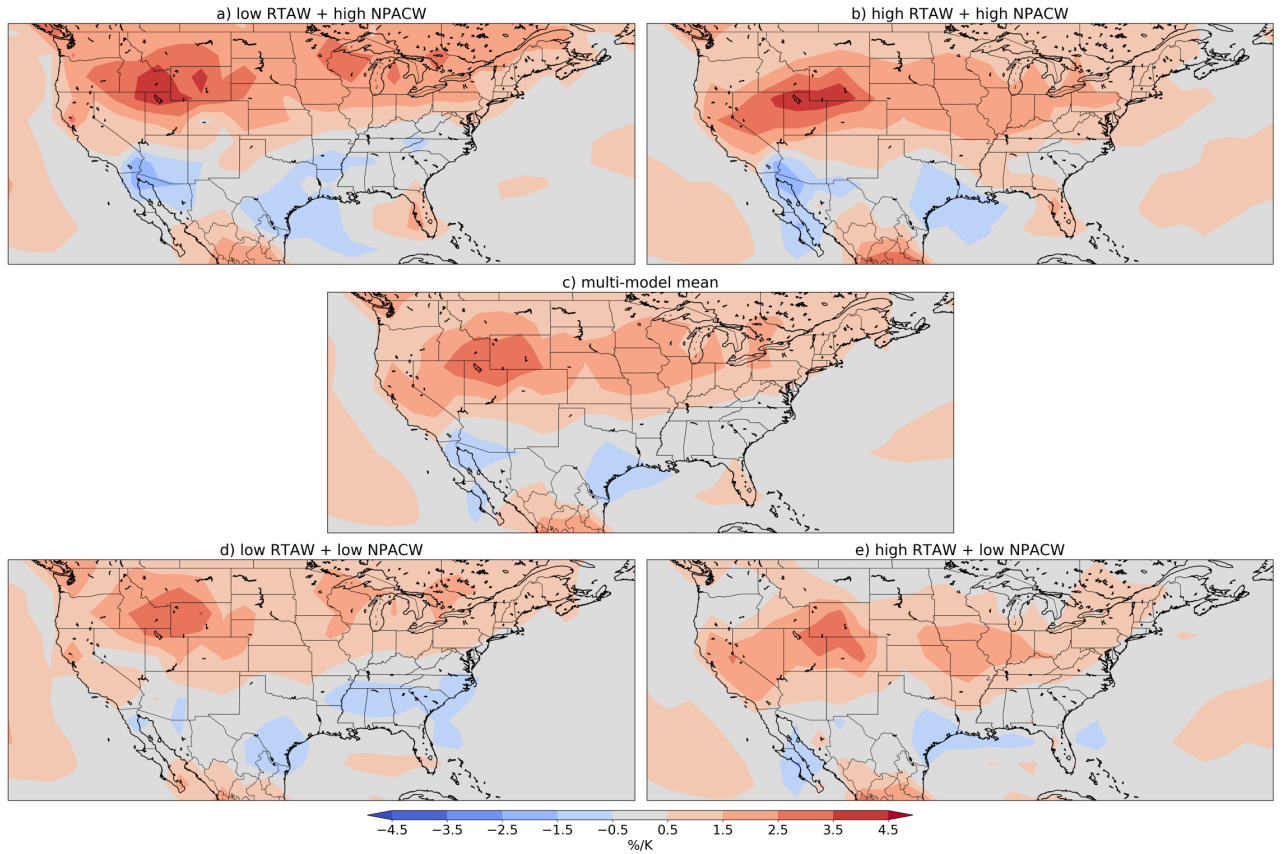


Figure A8: JJA stagnation response per degree of global warming (%/K) according to (a,b,d,e) four plausible storylines of climate change that are conditioned on the RTAW and NPACW responses over the US. The storylines in (a) and (b) are characterized by a high NPACW, while those in (d) and (e) have low NPACW. The storylines in (b) and (e) are characterized by high RTAW, while those in (a) and (d) have low RTAW. (c) The multi-model mean response scaled by global warming. The corresponding driver responses in each storyline are indicated by the four black stars in Figure 7.14.

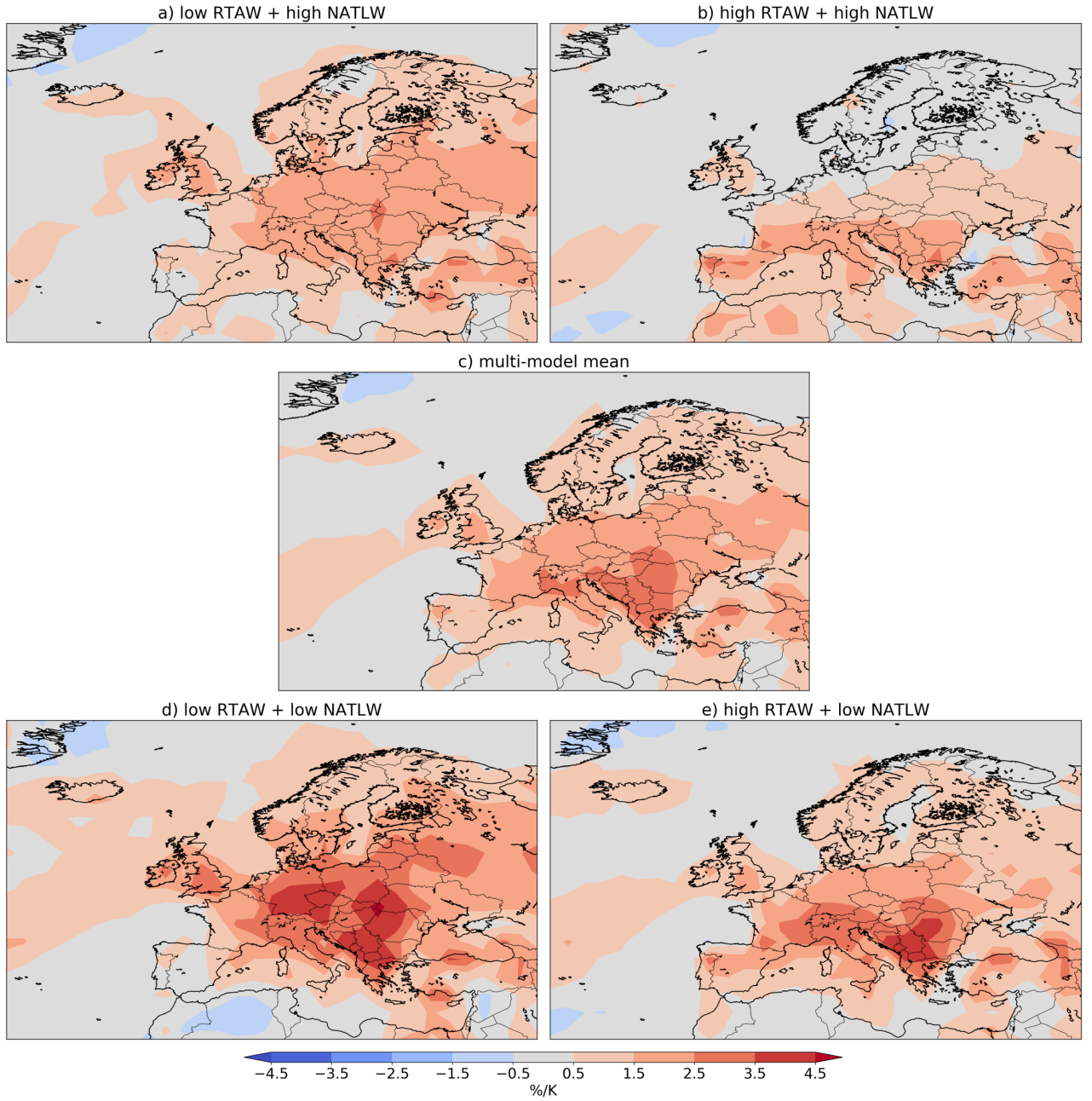


Figure A9: As Figure A8 but conditioned on the RTAW and NATLW responses over Europe.

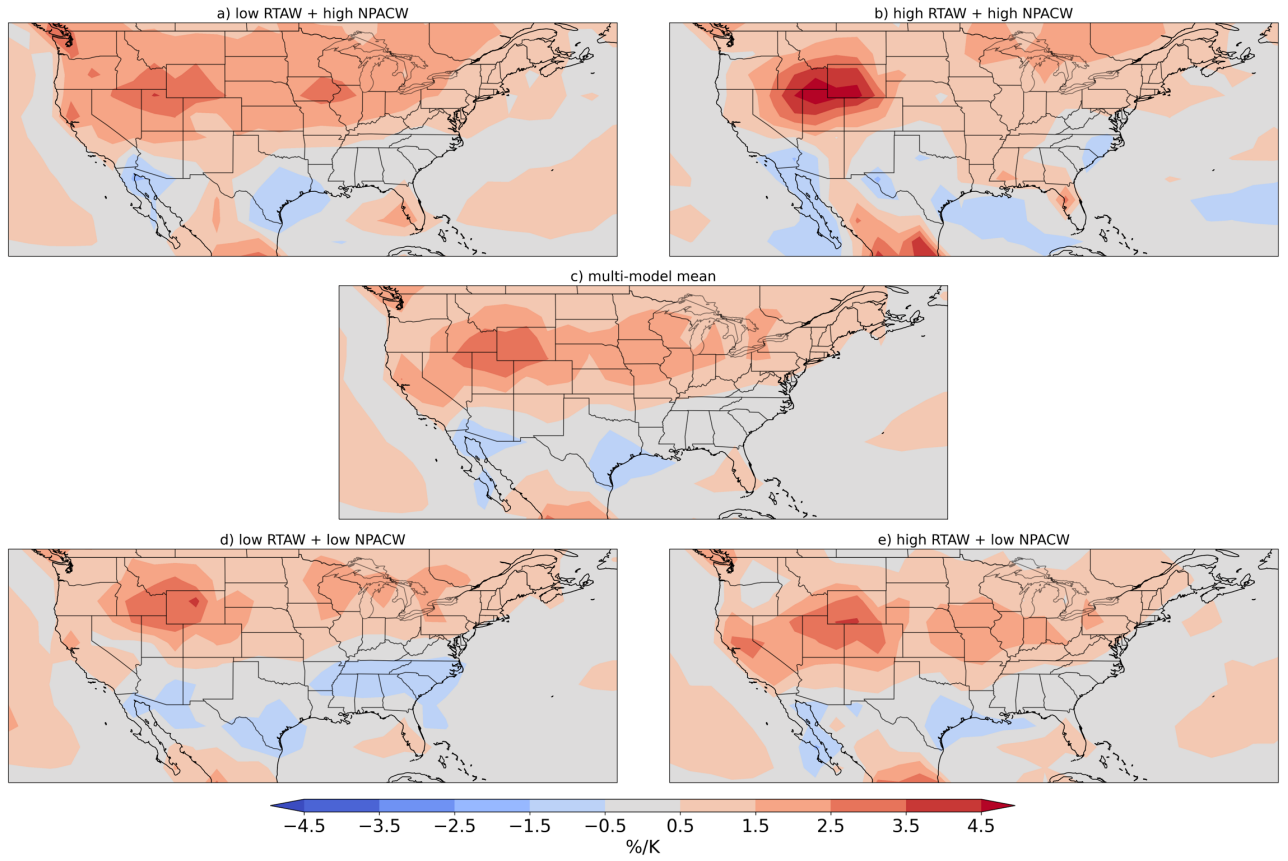


Figure A10: As Figure A8 but computed using the composite approach (grouping models in the four quadrants delimited by the inner and outer ellipses of Figure 7.14 left) rather than the regression framework.

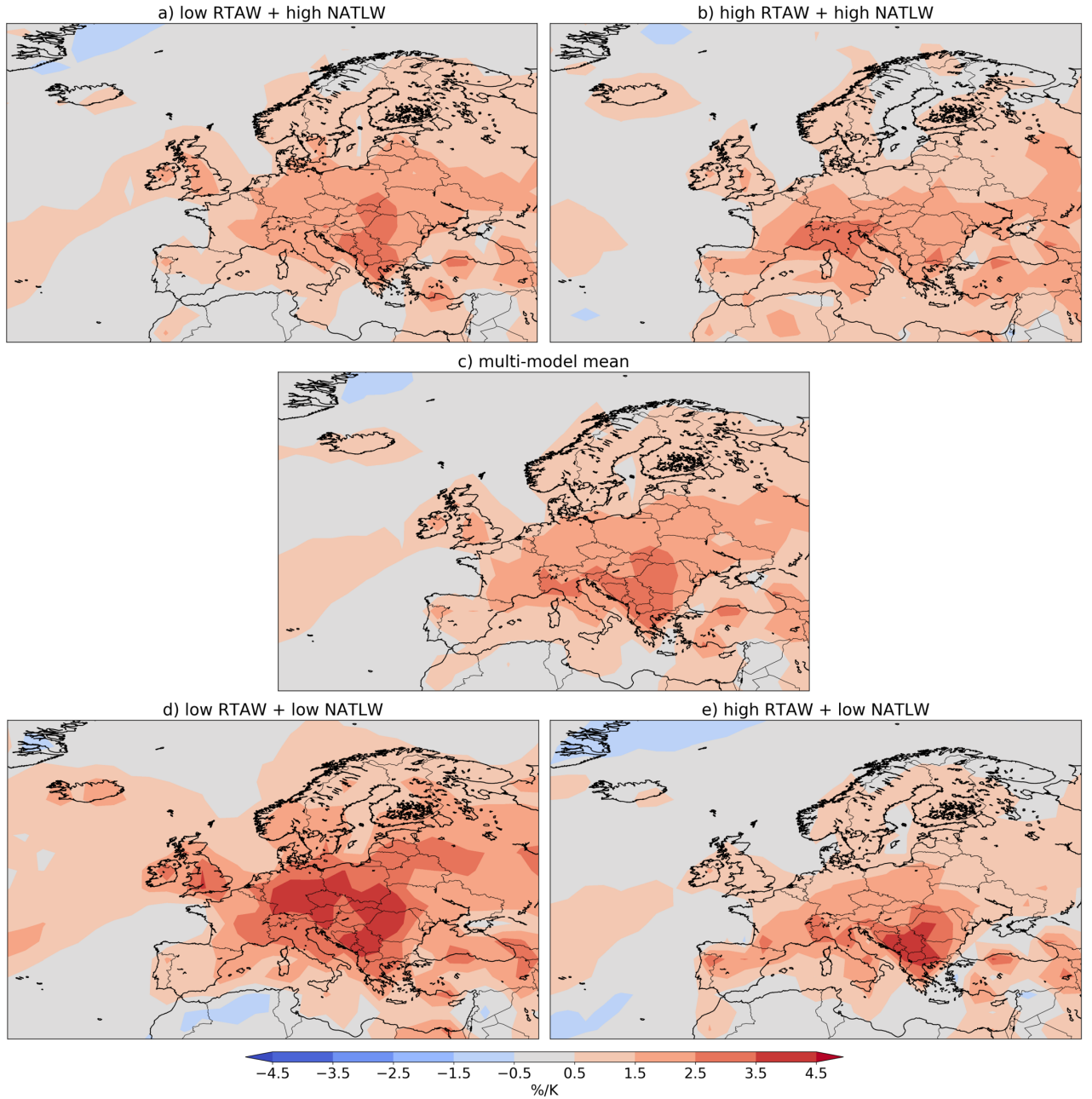


Figure A11: As Figure A9 but computed using the composite approach (grouping models as in the four quadrants of Figure 7.14 right) rather than the regression framework.

Table A1: Explanatory variables selected at each location in winter (selected = 1, not selected = 0). The first column refers to the codes of the AirBase measurement sites.

	Wsp10	Wsp500	Vent	BLH	Twsp	Prec	PTD	Z500	SLP
AT0ILL1	1	1	1	0	0	0	0	1	1
AT10001	1	1	1	0	0	0	0	1	0
AT10002	1	1	1	0	0	0	0	0	0
AT10003	1	1	1	0	0	0	0	0	1
BETB011	1	1	0	1	0	1	0	0	1
BETH201	0	1	1	0	0	0	1	0	1
BETN029	0	1	1	0	0	1	0	0	1
BETN045	1	1	0	0	0	0	0	0	1
BETR012	1	1	0	0	0	0	0	0	1
BETR701	0	1	1	0	0	1	0	0	1
BG0051A	1	1	0	1	0	1	0	1	1
BG0052A	0	1	1	0	0	1	0	1	0
CH0002R	0	1	0	1	1	1	1	1	1
CH0003R	1	1	0	0	1	1	0	1	1
CH0004R	1	1	0	1	0	1	1	1	1
CH0005A	1	1	0	0	1	1	0	1	1
CH0005R	1	1	0	1	1	1	0	1	1
CH0008A	1	1	0	1	0	1	0	1	1
CH0010A	1	1	1	0	1	1	0	1	1
CH0011A	1	0	0	1	0	0	0	1	0
CH0014A	1	1	1	0	1	1	0	1	1
CH0017A	1	1	0	1	0	1	0	1	1
CH0022A	1	0	0	0	1	1	1	0	0
CH0024A	1	1	0	1	0	1	1	1	1
CH0033A	1	1	1	0	1	1	0	1	0
CH0040A	1	1	1	0	0	1	0	1	1
CZ0AKOB	0	1	1	0	0	1	0	1	1
CZ0ALIB	1	1	0	1	0	1	0	1	1
CZ0ARIE	1	1	0	1	0	1	0	1	1
CZ0AVEL	1	0	0	1	1	1	0	1	1
CZ0BBNY	0	1	1	0	1	0	0	1	1
CZ0CCBD	0	1	1	0	0	1	1	1	1
CZ0HSER	1	1	1	0	1	1	0	1	1
CZ0JKOS	1	1	1	0	0	1	0	1	1
CZ0KSOM	0	1	1	0	1	1	0	1	1
CZ0MJES	1	1	0	1	0	1	0	1	1
CZ0MPRR	1	1	0	1	0	1	0	1	1
CZ0MPST	0	1	1	0	1	0	0	1	1
CZ0PPLV	0	1	1	0	0	1	0	1	1
CZ0TFMI	0	1	1	0	1	1	0	1	1
CZ0THAR	1	1	0	1	0	1	0	1	1
CZ0TKAR	1	1	0	1	0	1	0	1	1
CZ0TOFF	1	1	1	0	1	1	0	1	1
CZ0TOVK	0	1	1	0	1	1	0	1	1
CZ0TOZR	0	1	0	1	1	1	0	1	1
CZ0TSTD	1	1	0	1	0	1	0	1	1
CZ0TTRO	1	1	0	1	1	1	0	1	1
CZ0TVER	1	1	1	0	0	1	0	1	1
CZ0UCHM	0	0	0	1	1	1	0	1	0
CZ0UDCM	1	1	1	0	1	1	0	0	0
CZ0UMOM	0	0	1	0	0	1	0	1	0
CZ0URVH	1	1	0	1	0	1	0	1	1
CZ0UULK	0	0	1	0	0	1	0	1	1
CZ0UULM	1	0	0	1	1	1	0	1	1

Annex

	Wsp10	Wsp500	Vent	BLH	Twsp	Prec	PTD	Z500	SLP
DEBB021	0	1	1	0	0	1	0	1	0
DEBE034	0	1	1	0	0	1	0	1	0
DEBE051	0	1	1	0	1	1	0	1	0
DEBW004	1	1	0	1	0	0	0	1	1
DEBW010	0	1	1	0	0	0	0	1	1
DEBW024	1	1	0	1	1	1	0	1	1
DEBW027	1	1	0	0	0	1	0	0	1
DEBW042	1	1	0	1	0	1	0	0	0
DEBW087	0	1	1	0	0	1	0	1	1
DEBY002	0	0	1	0	1	1	0	1	1
DEBY004	0	1	1	0	0	1	0	1	1
DEBY005	0	1	1	0	0	0	0	1	1
DEBY007	0	1	1	0	0	1	0	1	1
DEBY009	0	1	1	0	0	1	0	1	1
DEBY020	0	1	1	0	0	1	0	1	1
DEBY021	0	1	1	0	0	1	0	0	1
DEBY031	0	1	1	0	0	1	0	1	1
DEBY032	0	0	1	0	0	1	0	1	1
DEBY039	1	1	0	0	1	1	0	0	1
DEBY047	0	1	1	0	0	1	0	1	1
DEBY052	0	1	1	0	0	1	0	1	0
DEBY062	0	1	1	0	0	1	0	1	1
DEBY067	0	1	1	0	0	1	0	1	1
DEBY089	1	1	0	0	1	1	0	1	1
DEBY093	0	1	1	1	0	1	0	1	0
DEBY099	1	1	0	1	1	1	0	1	1
DEHB001	0	1	1	0	1	1	0	1	0
DEHE001	1	1	0	1	0	0	0	1	1
DEHE008	0	1	1	0	0	1	0	1	1
DEHE018	0	1	1	0	0	0	0	1	1
DEHE022	0	1	1	0	0	0	0	1	1
DEHE030	0	1	1	0	0	1	0	1	1
DEHE032	0	1	1	0	0	1	0	1	1
DEHE043	0	1	1	0	0	1	0	1	1
DEHE044	0	1	1	0	0	1	0	1	1
DEHE045	0	1	1	0	0	1	0	1	1
DEHE046	0	1	1	0	0	1	0	1	1
DEHE051	1	1	0	1	0	1	1	1	0
DEHH008	0	1	0	1	1	1	0	1	0
DEHH015	0	1	1	0	0	1	0	1	0
DEHH059	0	1	0	1	0	1	0	1	0
DEMV004	0	1	1	0	1	1	0	1	0
DEMV007	1	1	0	1	1	0	0	1	0
DEMV012	0	1	1	0	1	0	0	1	1
DEMV017	0	1	1	0	1	1	0	1	1
DENI011	0	1	1	0	0	1	0	1	1
DENI016	0	1	0	1	1	1	0	1	1
DENI020	0	1	1	0	0	1	0	1	1
DENI028	0	1	1	0	0	1	0	1	1
DENI029	0	1	1	0	1	1	0	1	0
DENI031	0	1	0	1	0	0	0	1	0
DENI038	0	1	1	0	0	0	0	0	1
DENI041	0	1	1	0	0	0	0	1	1
DENI042	0	1	1	0	0	1	0	1	1
DENI043	0	1	1	0	0	1	0	1	0
DENI051	0	0	1	0	0	1	1	0	0
DENI052	0	1	1	0	0	0	0	1	0

Annex

	Wsp10	Wsp500	Vent	BLH	Twsp	Prec	PTD	Z500	SLP
DENI054	0	1	1	0	0	1	0	1	1
DENI058	0	1	1	0	1	0	0	0	1
DENI059	0	1	1	0	1	0	0	1	0
DENI060	1	1	0	1	1	0	0	1	1
DENI062	0	1	0	1	1	1	0	0	1
DENI063	0	1	0	1	1	1	0	1	0
DERP001	0	1	1	0	0	1	0	1	1
DERP007	0	1	1	0	0	0	0	0	1
DERP013	0	1	1	0	0	1	0	1	1
DERP014	1	1	0	1	1	1	0	1	1
DERP015	0	1	1	0	0	1	0	1	1
DERP016	0	0	1	0	1	1	0	0	1
DERP017	0	1	0	1	1	1	0	1	1
DERP021	0	1	1	0	0	1	0	1	1
DERP025	1	1	0	1	1	1	0	1	1
DEST011	0	1	1	0	0	1	0	1	1
DEST063	0	1	1	0	0	1	0	1	0
DEST089	0	1	0	1	1	1	0	1	1
DETH005	0	1	1	0	0	1	0	1	1
DETH009	0	1	1	0	0	1	0	1	1
DETH013	0	1	1	0	0	1	0	1	1
DETH018	0	0	1	0	1	1	0	1	0
DETH026	0	1	1	0	0	1	0	1	1
DETH036	0	1	1	0	0	1	0	1	1
DETH041	0	1	1	0	0	1	0	1	1
DETH060	0	1	1	0	1	1	0	1	0
DEUB005	0	1	1	0	1	1	0	1	0
ES1038A	1	1	0	1	0	1	0	1	1
ES1472A	1	1	0	0	0	1	0	0	1
ES1529A	1	1	0	1	0	0	0	1	1
ES1530A	0	1	1	0	0	1	0	1	0
ES1535A	1	1	0	1	0	1	0	1	1
ES1537A	1	0	0	0	0	0	0	1	0
ES1543A	1	1	0	1	0	0	0	1	1
FI00424	1	1	0	0	0	1	0	1	1
FI00425	0	1	1	1	0	0	0	1	1
FR01001	0	1	0	1	1	1	0	1	1
FR01012	1	1	0	1	0	1	0	0	0
FR01014	0	1	1	0	1	0	0	0	1
FR01015	0	1	1	0	0	1	0	1	1
FR01017	0	1	1	0	0	0	0	1	1
FR01019	1	1	0	0	1	0	0	1	0
FR01020	1	0	0	0	0	0	0	0	1
FR02008	0	0	1	0	1	1	1	0	0
FR02022	0	1	1	0	1	0	0	0	1
FR03014	1	0	0	0	0	0	0	1	0
FR03029	1	0	0	0	0	1	0	0	0
FR03043	1	0	0	0	0	1	0	0	0
FR03062	1	0	0	0	1	0	0	1	0
FR03080	1	1	1	0	0	0	0	0	1
FR03084	1	1	1	0	0	1	0	0	1
FR04001	0	1	1	0	0	1	0	1	0
FR04002	1	1	0	1	0	1	0	1	0
FR04004	0	1	1	0	0	1	0	1	1
FR04023	1	0	0	1	1	1	0	1	0
FR04034	1	1	0	0	0	1	0	1	0
FR04150	1	1	0	1	1	1	0	1	0

Annex

	Wsp10	Wsp500	Vent	BLH	Twsp	Prec	PTD	Z500	SLP
FR04156	0	1	1	0	0	1	0	1	0
FR04319	1	0	0	0	1	1	0	1	0
FR04328	0	1	1	0	0	1	0	1	0
FR05074	0	1	1	0	1	1	0	1	0
FR06001	1	0	0	1	1	1	1	0	1
FR06003	1	1	0	1	1	1	0	1	0
FR06007	1	0	0	1	1	1	0	0	1
FR06009	0	0	1	0	0	1	0	0	1
FR06011	1	0	0	1	1	1	0	0	1
FR07004	0	1	1	0	0	1	0	1	1
FR07008	0	1	1	0	0	1	0	1	1
FR08016	0	0	1	0	1	0	0	1	1
FR08614	0	0	1	0	1	0	0	1	1
FR08713	0	1	1	0	1	1	0	0	0
FR08714	0	0	1	0	0	1	1	0	0
FR09002	1	1	0	0	1	1	0	1	0
FR09003	0	1	1	0	1	1	0	0	1
FR09010	0	1	1	0	1	1	0	0	1
FR09015	1	1	0	1	1	0	0	1	1
FR09016	0	1	1	0	0	1	0	1	1
FR09017	0	1	1	0	0	1	0	1	1
FR09019	0	0	1	0	1	1	0	0	1
FR10007	0	1	1	0	1	1	0	0	1
FR10032	0	0	1	0	0	1	0	0	1
FR11025	0	1	1	0	0	1	0	0	1
FR11027	0	0	1	0	0	1	0	0	1
FR12004	1	0	0	1	1	1	0	1	1
FR12026	1	0	0	1	1	1	0	1	1
FR12027	0	0	1	0	1	1	0	0	1
FR12030	1	0	0	1	1	1	1	0	0
FR13007	1	1	0	1	1	1	1	1	1
FR14031	1	1	0	1	1	1	0	1	1
FR14033	1	1	0	1	1	1	0	0	0
FR15017	1	1	1	0	0	1	0	1	1
FR15038	1	1	1	0	0	1	0	1	1
FR16029	1	0	0	0	0	1	0	1	0
FR16038	1	1	0	0	0	1	0	1	1
FR16053	1	0	0	0	0	1	0	1	0
FR16060	0	1	1	0	0	1	0	1	1
FR16066	1	0	0	0	1	1	1	0	0
FR17009	1	1	0	0	1	1	0	1	0
FR17011	1	1	0	1	0	1	0	1	1
FR18019	0	1	1	0	1	1	0	0	1
FR18035	0	0	1	0	1	1	0	0	1
FR18039	0	1	1	0	1	1	0	0	1
FR20037	1	1	0	1	1	1	0	0	0
FR20045	1	1	0	1	1	1	0	0	0
FR21001	0	0	1	0	0	1	0	1	0
FR21040	0	1	1	0	0	1	0	1	0
FR22004	1	1	0	1	0	1	0	1	1
FR22016	1	0	0	0	0	1	0	0	1
FR23078	0	1	1	0	1	1	0	1	0
FR23120	0	1	1	0	0	1	0	1	0
FR25036	0	0	1	0	0	1	0	1	0
FR25039	0	0	1	0	1	1	0	0	1
FR25043	0	0	1	0	0	1	0	0	0

Annex

	Wsp10	Wsp500	Vent	BLH	Twsp	Prec	PTD	Z500	SLP
FR25045	0	1	1	0	1	1	0	1	0
FR26005	0	1	1	0	0	1	0	1	1
FR26016	1	1	0	1	1	1	0	1	1
FR26017	0	0	1	0	0	1	0	1	1
FR27002	0	0	1	0	0	1	0	1	1
FR29421	0	1	1	0	0	1	0	1	1
FR29423	0	1	1	0	0	1	0	1	1
FR29424	0	1	1	0	0	1	0	1	1
FR29426	0	1	1	0	1	1	0	1	1
FR30020	1	1	0	1	0	1	0	1	1
FR30021	1	0	0	1	1	1	0	1	0
FR31002	0	1	1	0	0	1	0	1	1
FR31007	0	1	1	0	0	1	0	1	1
FR31013	1	1	0	1	0	1	0	0	0
FR31014	1	1	0	0	1	1	0	0	1
FR32005	0	0	1	0	0	1	1	1	1
FR32006	0	1	1	0	0	0	0	0	1
FR33101	1	1	0	0	1	1	0	1	1
FR33102	1	1	0	0	1	1	0	1	1
FR33111	1	1	0	1	1	1	0	1	1
FR33120	0	1	0	0	1	1	0	1	1
FR33121	1	1	0	1	0	1	0	1	1
FR33201	1	1	0	1	1	1	0	1	1
FR33202	1	1	0	1	1	1	0	1	1
FR33212	0	1	1	0	0	1	0	1	1
FR34012	0	0	1	0	0	1	0	1	1
FR34025	1	0	0	1	0	1	0	1	0
FR34032	0	1	1	0	0	1	0	1	1
FR34042	0	0	1	0	0	1	0	0	1
FR34051	1	1	0	1	1	1	0	1	1
FR35002	1	1	0	1	1	1	0	1	1
FR35003	1	1	0	1	1	1	0	1	1
FR35004	1	1	0	0	1	1	0	1	1
FR35005	1	0	0	1	1	1	0	1	1
FR35006	1	1	0	0	1	1	0	0	1
FR35007	0	0	0	1	1	1	0	1	1
FR36001	1	1	1	0	0	1	0	1	1
GB0566A	0	1	1	0	0	1	1	1	0
GB0567A	1	1	0	0	0	1	0	1	0
GB0584A	1	1	0	0	0	0	0	1	0
GB0641A	0	1	1	0	0	1	0	0	1
GB0643A	0	1	1	0	1	1	0	1	0
GB0673A	1	0	0	0	1	1	0	0	0
IE0095A	1	1	0	0	0	0	0	0	1
IT0469A	1	1	1	0	1	1	0	1	1
IT0706A	1	0	1	0	0	1	0	0	1
IT0862A	1	1	0	1	0	1	0	1	0
IT0906A	1	1	0	1	1	0	0	1	0
IT0953A	1	0	1	1	1	0	0	1	0
IT1010A	1	1	0	0	1	1	0	0	1
IT1459A	1	0	0	1	1	1	0	1	0
IT1654A	1	1	0	1	0	0	0	1	1
NL00131	0	1	1	0	0	0	0	0	1
NL00133	1	0	0	0	1	0	0	0	1
NL00230	0	1	1	0	1	0	0	0	1
NL00318	0	1	1	0	0	1	0	1	0
NL00404	0	1	1	0	1	1	0	1	0

	Wsp10	Wsp500	Vent	BLH	Twsp	Prec	PTD	Z500	SLP
NL00418	0	1	1	0	0	0	0	1	0
NL00437	0	1	1	0	0	0	0	1	0
NL00444	0	0	0	1	0	1	0	0	1
NL00538	0	1	1	0	1	0	0	1	0
NL00722	0	1	1	0	0	1	0	1	0
NL00929	0	1	1	0	1	1	0	1	0
PL0010A	0	1	1	0	1	1	0	0	0
PL0039A	0	0	1	0	1	1	0	1	1
PL0045A	0	0	0	1	1	1	0	1	1
PL0046A	0	0	1	0	1	1	0	0	1
PL0047A	0	1	1	0	1	1	0	1	1
PL0048A	0	0	1	0	1	1	0	0	1
PL0049A	0	1	1	0	1	1	0	1	1
PL0050A	0	1	0	1	1	1	0	1	1
PL0051A	0	1	0	1	1	0	0	1	1
PL0052A	0	0	0	1	1	1	0	1	0
PT01021	1	1	0	1	1	1	0	1	0
PT01023	1	0	0	0	0	1	0	0	1
PT01031	0	1	1	0	0	1	0	1	0
PT03071	1	1	0	1	0	0	0	1	0
SE0001A	0	1	1	0	0	1	0	1	0
SE0004A	1	1	0	1	1	1	0	1	0
SE0022A	1	1	0	1	1	1	0	1	1
SI0001A	1	0	0	1	1	1	0	1	1
SK0004A	0	1	1	0	1	0	0	0	1

Table A2: Explanatory variables selected at each location in summer (selected = 1, not selected = 0).

	Wsp10	Wsp500	Vent	BLH	Twsp	Prec	PTD	Z500	SLP
AT0ILL1	0	1	0	1	1	0	0	1	1
AT10001	1	1	0	1	0	0	0	1	1
AT10002	1	1	0	1	0	0	0	1	1
AT10003	0	1	0	1	1	0	0	1	1
BETB011	1	1	0	1	0	0	0	1	1
BETH201	1	1	0	0	0	0	0	1	0
BETN029	1	1	0	1	0	0	0	1	1
BETN045	1	1	1	0	1	0	0	1	1
BETR012	1	1	1	0	0	0	0	1	1
BETR701	1	1	0	0	1	0	0	1	0
BG0051A	1	1	1	0	0	0	0	1	1
BG0052A	0	1	1	1	0	1	0	1	1
CH0002R	0	1	0	1	0	0	0	1	1
CH0003R	0	1	0	1	1	0	0	1	1
CH0004R	1	1	0	1	0	0	0	1	1
CH0005A	1	1	0	1	0	0	0	1	1
CH0005R	1	0	0	1	0	1	0	1	1
CH0008A	1	1	0	1	0	0	0	1	1
CH0010A	1	1	0	1	0	0	0	1	1
CH0011A	1	1	1	1	0	0	0	1	1
CH0014A	1	1	1	0	0	1	0	1	1
CH0017A	1	1	0	1	0	0	0	1	1
CH0022A	1	1	0	1	0	1	0	1	1
CH0024A	0	1	0	1	0	0	0	1	1
CH0033A	1	0	0	1	0	1	0	1	1
CH0040A	1	1	0	1	0	1	0	1	1
CZ0AKOB	1	1	1	0	0	0	0	1	1
CZ0ALIB	1	1	0	1	0	0	0	1	1
CZ0ARIE	1	1	1	0	0	0	0	1	1
CZ0AVEL	1	1	0	1	0	0	0	1	1
CZ0BBNY	1	1	0	1	0	0	0	1	1
CZ0CCBD	1	1	0	1	0	0	0	1	1
CZ0HSER	0	1	0	1	1	0	0	1	1
CZ0JKOS	1	1	1	0	0	0	0	1	1
CZ0KSOM	1	1	1	1	0	0	0	1	1
CZ0MJES	0	1	1	1	1	0	0	1	1
CZ0MPRR	1	1	0	1	0	0	0	1	1
CZ0MPST	0	1	1	0	1	0	0	1	1
CZ0PPLV	1	1	1	0	0	0	0	1	1
CZ0TFMI	1	1	0	0	0	0	0	1	1
CZ0THAR	1	1	0	1	0	0	0	1	1
CZ0TKAR	1	1	0	1	0	0	0	1	1
CZ0TOFF	1	1	1	0	0	0	0	1	1
CZ0TOVK	1	1	0	1	0	0	0	1	1
CZ0TOZR	1	1	0	0	0	0	0	1	0
CZ0TSTD	1	1	0	1	0	0	0	1	1
CZ0TTRO	1	1	0	0	0	0	0	1	1
CZ0TVER	1	1	1	0	0	0	0	1	1
CZ0UCHM	1	1	1	1	0	0	0	1	1
CZ0UDCM	1	1	1	1	0	0	0	1	1
CZ0UMOM	1	1	0	1	0	0	0	1	1
CZ0URVH	1	1	0	1	0	0	0	1	0
CZ0UULK	1	1	1	1	0	0	0	1	1
CZ0UULM	1	0	1	1	0	0	0	1	1
DEBB021	1	1	0	1	0	0	0	1	1

Annex

	Wsp10	Wsp500	Vent	BLH	Twsp	Prec	PTD	Z500	SLP
DEBE034	0	1	1	1	1	0	0	1	1
DEBE051	1	1	0	1	0	0	0	1	1
DEBW004	1	1	1	1	0	0	0	1	0
DEBW010	1	1	0	1	0	0	0	1	1
DEBW024	1	1	1	1	0	0	0	1	1
DEBW027	1	1	0	0	0	0	0	1	1
DEBW042	1	1	0	1	0	0	0	1	1
DEBW087	1	1	1	1	0	0	0	1	1
DEBY002	1	1	1	0	0	0	0	1	1
DEBY004	1	1	0	1	0	0	0	1	1
DEBY005	1	1	0	1	0	0	0	1	1
DEBY007	1	1	0	1	0	0	0	1	1
DEBY009	1	1	0	1	0	0	0	1	1
DEBY020	1	1	1	0	0	0	0	1	1
DEBY021	1	1	0	1	0	0	0	1	1
DEBY031	1	1	0	1	0	0	0	1	1
DEBY032	1	1	1	0	0	0	0	1	1
DEBY039	1	1	0	1	1	0	0	1	1
DEBY047	1	1	1	0	0	0	0	1	1
DEBY052	1	1	0	1	0	0	0	1	1
DEBY062	0	1	0	1	1	0	0	1	1
DEBY067	1	1	0	1	0	0	0	1	1
DEBY089	1	1	0	1	1	0	0	1	0
DEBY093	1	1	0	1	0	0	0	1	1
DEBY099	1	1	1	1	0	0	0	1	1
DEHB001	1	0	1	0	1	0	0	1	1
DEHE001	1	1	1	1	0	0	0	1	1
DEHE008	1	0	1	0	0	0	0	1	1
DEHE018	1	1	0	1	0	0	0	1	1
DEHE022	1	1	0	1	0	0	0	1	1
DEHE030	1	0	0	0	0	0	0	1	1
DEHE032	1	1	0	1	0	0	0	1	1
DEHE043	1	1	1	1	1	0	0	1	1
DEHE044	0	1	0	0	1	0	0	1	0
DEHE045	1	1	1	1	1	0	0	1	1
DEHE046	0	0	0	0	1	0	0	1	1
DEHE051	1	1	1	1	0	0	0	1	1
DEHH008	1	0	0	1	0	0	0	1	1
DEHH015	1	1	0	1	0	0	0	1	1
DEHH059	1	0	1	0	0	0	0	1	1
DEMV004	1	0	0	1	0	0	0	1	1
DEMV007	1	0	0	1	0	0	0	1	1
DEMV012	1	1	0	1	0	0	0	1	1
DEMV017	0	1	1	0	1	0	0	1	1
DENI011	0	0	0	0	1	0	0	1	1
DENI016	0	1	0	0	1	0	0	1	1
DENI020	0	1	1	0	1	0	0	1	1
DENI028	1	1	0	0	1	0	0	1	1
DENI029	0	1	0	0	0	0	0	1	1
DENI031	0	0	0	0	0	0	0	1	1
DENI038	1	0	0	1	0	0	0	1	1
DENI041	0	0	0	0	1	0	0	1	1
DENI042	0	1	0	0	1	0	0	1	1
DENI043	0	0	0	1	1	0	0	1	1
DENI051	0	0	0	0	1	0	0	1	0
DENI052	0	0	0	0	1	0	0	1	1
DENI054	0	0	0	0	1	0	0	1	1
DENI058	1	1	0	1	1	0	0	1	1

Annex

	Wsp10	Wsp500	Vent	BLH	Twsp	Prec	PTD	Z500	SLP
DENI059	0	1	1	0	0	0	0	1	1
DENI060	1	0	1	0	1	0	0	1	1
DENI062	1	0	1	0	1	0	0	1	1
DENI063	0	0	0	0	1	0	0	1	1
DERP001	1	1	0	1	0	0	0	1	1
DERP007	1	1	0	1	0	0	0	1	1
DERP013	1	1	0	1	1	0	0	1	1
DERP014	1	1	1	1	1	0	0	1	1
DERP015	0	1	0	1	1	0	0	1	1
DERP016	0	0	0	0	1	0	0	1	1
DERP017	1	1	1	1	1	0	0	1	1
DERP021	1	1	0	1	1	0	0	1	1
DERP025	1	1	0	1	0	0	0	1	1
DEST011	1	1	1	1	0	0	0	1	1
DEST063	1	0	1	0	1	0	0	1	1
DEST089	1	0	0	1	0	0	1	1	1
DETH005	1	1	0	0	0	0	0	1	1
DETH009	1	1	1	0	0	0	0	1	1
DETH013	1	1	0	0	0	0	0	1	1
DETH018	1	1	0	0	0	0	0	1	1
DETH026	1	1	0	1	0	0	0	1	1
DETH036	1	1	0	0	0	0	0	1	1
DETH041	1	1	0	0	0	0	0	1	1
DETH060	1	1	0	0	0	0	0	1	1
DEUB005	0	0	1	0	1	0	1	1	1
ES1038A	1	1	1	1	0	1	1	1	1
ES1472A	0	0	0	1	1	0	1	1	1
ES1529A	1	1	0	1	0	1	1	1	1
ES1530A	0	1	0	1	1	0	0	1	1
ES1535A	1	1	1	1	0	0	1	1	1
ES1537A	1	0	0	1	0	0	1	1	1
ES1543A	0	1	1	1	0	1	1	1	1
FI00424	1	0	1	1	0	0	0	1	1
FI00425	1	0	0	1	1	0	0	1	1
FR01001	0	1	0	1	1	0	0	1	1
FR01012	1	1	0	1	0	0	0	1	1
FR01014	0	1	1	1	1	0	0	1	1
FR01015	0	1	0	1	0	0	0	1	1
FR01017	0	0	0	0	0	0	0	1	1
FR01019	0	0	0	1	0	0	0	1	1
FR01020	1	1	1	1	0	0	0	1	1
FR02008	1	1	0	1	0	0	1	1	1
FR02022	1	1	0	1	0	0	1	1	1
FR03014	1	0	0	0	0	0	0	1	1
FR03029	0	0	0	0	1	0	0	1	1
FR03043	1	0	0	0	0	0	0	1	1
FR03062	1	0	0	1	0	0	0	1	1
FR03080	1	1	0	1	0	0	0	1	1
FR03084	1	0	0	0	0	0	1	1	1
FR04001	0	1	1	1	0	0	0	1	0
FR04002	1	1	0	1	1	0	0	1	1
FR04004	0	1	0	1	1	0	0	1	0
FR04023	0	1	0	1	1	1	0	1	1
FR04034	0	1	1	1	0	0	0	1	1
FR04150	0	1	1	1	0	0	0	1	1
FR04156	1	1	0	1	0	0	0	1	1
FR04319	1	1	1	1	1	0	0	1	1
FR04328	1	1	0	1	1	0	0	1	1

Annex

	Wsp10	Wsp500	Vent	BLH	Twsp	Prec	PTD	Z500	SLP
FR05074	1	1	0	0	1	1	0	1	1
FR06001	0	1	0	0	1	0	0	1	1
FR06003	0	1	1	1	0	0	0	1	0
FR06007	1	1	0	0	0	0	0	1	0
FR06009	0	1	1	1	0	0	0	1	1
FR06011	0	1	0	1	1	0	0	1	1
FR07004	0	1	0	1	0	0	1	1	1
FR07008	1	1	0	1	0	1	1	1	1
FR08016	0	1	1	0	1	0	1	1	1
FR08614	0	1	1	0	1	0	1	1	1
FR08713	0	1	1	0	1	1	1	1	1
FR08714	0	1	1	0	0	1	1	1	1
FR09002	0	1	1	1	0	0	1	1	1
FR09003	0	1	1	0	0	0	1	1	1
FR09010	0	1	1	0	1	0	0	1	1
FR09015	1	1	1	1	1	0	0	1	1
FR09016	1	1	1	0	1	0	0	1	1
FR09017	1	1	1	0	0	0	1	1	1
FR09019	1	1	1	0	1	0	0	1	1
FR10007	1	0	1	1	0	0	0	1	1
FR10032	1	1	0	1	0	1	0	1	1
FR11025	1	1	1	1	0	0	0	1	0
FR11027	1	1	0	1	0	0	0	1	0
FR12004	1	1	0	0	1	0	0	1	1
FR12026	0	1	1	1	0	1	0	1	1
FR12027	0	1	0	0	1	0	0	1	1
FR12030	0	1	0	0	1	0	1	1	1
FR13007	0	1	0	1	0	0	0	1	1
FR14031	0	1	0	1	1	0	0	1	0
FR14033	0	1	0	1	1	0	0	1	0
FR15017	1	1	1	1	0	0	0	1	1
FR15038	1	1	0	1	0	0	0	1	1
FR16029	1	1	0	1	0	1	0	1	1
FR16038	0	1	1	1	0	1	0	1	0
FR16053	1	1	1	0	0	0	0	1	1
FR16060	0	1	1	1	0	0	0	1	1
FR16066	1	1	0	1	0	0	0	1	1
FR17009	0	1	0	0	0	1	0	1	1
FR17011	1	1	1	0	0	0	0	1	1
FR18019	0	1	1	0	1	0	0	1	0
FR18035	0	1	1	1	0	0	0	1	0
FR18039	1	1	0	1	0	0	0	1	1
FR20037	1	1	0	0	0	0	0	1	1
FR20045	1	1	0	1	0	1	0	1	1
FR21001	0	1	1	0	0	1	0	1	1
FR21040	1	1	0	1	1	0	0	1	1
FR22004	1	1	0	1	1	0	0	1	1
FR22016	1	1	0	1	0	0	0	1	0
FR23078	0	1	1	1	0	0	0	1	1
FR23120	0	1	1	1	1	0	0	1	1
FR25036	1	1	0	0	0	0	0	1	0
FR25039	0	1	1	1	1	0	0	1	1
FR25043	1	1	1	1	0	0	0	1	1
FR25045	1	1	0	1	1	1	0	1	1
FR26005	0	1	0	1	1	0	0	1	1
FR26016	0	1	1	1	0	0	0	1	0
FR26017	1	1	0	1	0	0	0	1	1
FR27002	1	1	0	0	1	0	1	1	1

Annex

	Wsp10	Wsp500	Vent	BLH	Twsp	Prec	PTD	Z500	SLP
FR29421	1	0	0	1	0	0	0	1	1
FR29423	0	1	1	0	0	0	1	1	1
FR29424	1	1	1	0	1	0	0	1	1
FR29426	1	1	0	0	0	0	0	1	1
FR30020	1	1	0	1	0	0	0	1	1
FR30021	1	1	0	1	0	0	0	1	1
FR31002	0	1	1	1	0	0	0	1	1
FR31007	0	1	1	0	0	1	1	1	1
FR31013	1	1	0	0	1	1	1	1	1
FR31014	0	1	0	0	1	0	1	1	1
FR32005	0	1	1	1	0	0	0	1	1
FR32006	0	1	1	1	0	1	0	1	1
FR33101	0	1	1	0	0	0	0	1	1
FR33102	1	1	0	1	0	0	0	1	1
FR33111	1	1	0	1	0	1	0	1	1
FR33120	0	1	0	1	0	0	0	1	1
FR33121	1	1	1	0	0	0	0	1	1
FR33201	1	1	0	1	0	0	0	1	1
FR33202	0	1	1	0	0	0	0	1	1
FR33212	0	1	0	1	0	0	0	1	1
FR34012	1	1	1	0	0	1	0	1	1
FR34025	0	1	1	0	0	0	1	1	1
FR34032	0	1	1	1	0	0	0	1	1
FR34042	0	1	1	1	0	0	0	1	1
FR34051	0	1	1	1	0	0	0	1	1
FR35002	1	1	1	1	0	0	0	1	1
FR35003	1	1	1	0	0	0	0	1	1
FR35004	1	1	1	0	0	0	1	1	1
FR35005	1	1	1	1	0	0	0	1	1
FR35006	1	1	1	0	0	0	0	1	1
FR35007	1	1	1	0	1	0	0	1	1
FR36001	1	1	0	0	0	0	0	1	1
GB0566A	0	1	1	0	0	0	0	1	1
GB0567A	0	1	1	0	1	1	0	1	0
GB0584A	1	1	1	0	0	0	0	1	0
GB0641A	1	1	0	1	1	0	0	1	0
GB0643A	0	1	1	1	0	0	0	1	0
GB0673A	0	1	1	1	1	0	0	1	0
IE0095A	0	1	1	1	0	1	1	0	1
IT0469A	1	1	0	0	1	1	0	1	1
IT0706A	1	1	1	0	0	0	0	1	1
IT0862A	1	1	1	1	0	0	0	1	1
IT0906A	0	1	0	1	0	1	0	1	1
IT0953A	0	1	0	1	1	0	1	1	0
IT1010A	1	0	0	1	0	0	0	1	1
IT1459A	1	1	0	0	0	1	0	1	0
IT1654A	1	1	0	1	1	1	1	1	1
NL00131	0	1	0	1	1	0	0	1	1
NL00133	1	0	1	0	1	0	0	1	1
NL00230	1	1	1	0	0	0	0	1	1
NL00318	1	1	0	1	1	0	0	1	1
NL00404	1	1	0	1	0	1	0	1	1
NL00418	0	1	0	0	1	0	0	1	1
NL00437	1	0	1	0	0	0	0	1	1
NL00444	0	0	1	0	0	0	0	1	1
NL00538	0	1	1	0	0	0	1	1	1
NL00722	0	1	1	1	0	0	0	1	1
NL00929	0	0	1	0	0	0	0	1	1

	Wsp10	Wsp500	Vent	BLH	Twsp	Prec	PTD	Z500	SLP
PL0010A	1	1	1	1	0	0	1	1	1
PL0039A	1	1	0	1	0	0	0	1	1
PL0045A	1	1	1	1	0	0	0	1	1
PL0046A	1	1	1	1	0	0	0	1	1
PL0047A	1	1	0	1	0	0	0	1	1
PL0048A	1	1	0	0	0	0	0	1	1
PL0049A	1	1	0	1	0	0	0	1	1
PL0050A	1	1	0	1	0	0	0	1	1
PL0051A	1	1	1	1	0	1	0	1	1
PL0052A	0	1	0	0	1	0	0	1	1
PT01021	1	1	1	0	0	1	0	1	1
PT01023	0	1	0	1	1	1	0	1	1
PT01031	0	1	0	1	1	1	0	1	1
PT03071	1	1	1	0	0	0	0	1	1
SE0001A	0	1	1	0	1	0	0	1	1
SE0004A	1	0	1	1	0	0	0	1	0
SE0022A	0	1	1	1	1	1	0	1	0
SI0001A	0	1	0	1	0	0	0	1	1
SK0004A	1	1	1	1	0	0	0	1	1
